ACTUATION FATIGUE CHARACTERIZATION METHODS AND LIFETIME PREDICTIONS OF SHAPE MEMORY ALLOY ACTUATORS

A Dissertation

by

ROBERT WARREN WHEELER III

Submitted to the Office of Graduate and Professional Studies of
Texas A&M University
in partial fulfillment of the requirements for the degree of

DOCTOR OF PHILOSOPHY

Chair of Committee,	Dimitris C. Lagoudas
Committee Members,	Darren J. Hartl
	Ibrahim Karaman
	Amine Benzerga
Head of Department,	Rodney Bowersox

May 2017

Major Subject: Aerospace Engineering

Copyright 2017 Robert Warren Wheeler III

ABSTRACT

Shape Memory Alloys (SMAs) are a class of intermetallic alloys that possess the ability to repeatedly sustain large amounts of deformation and recover a designed geometry through a thermal-induced, diffusionless, solid-to-solid phase transformation. Due to their high actuation energy density and ability to recover large strains, SMAs have many promising engineering applications in the aerospace, automotive, biomedical, and energy industries. In recent years, the interest in high temperature SMAs (HTSMAs) has increased dramatically due to their potential applications in harsh environments, such as those commonly seen in the aerospace industry. However, the lack of standard testing methods which accurately characterize and model thermomechanical fatigue in SMA actuators frequently limits their use to non-structural/non-critical components or results in actuators being severely overdesigned.

While many actuation fatigue studies have been completed over the last three decades, the vast majority have only considered isobaric loading paths with full or partial degrees of transformation. However, many potential applications, such as morphing aerostructures or deployable space structures, require more complex thermomechanical loading paths. In order for SMAs to be used in such applications, existing testing standards and actuation fatigue lifetime prediction methods must be improved.

The four objectives of this study are: First, the fatigue behavior of equiatomic NiTi is investigated in order to develop methods for studying actuation fatigue and provide a baseline actuation fatigue response for constant force biasing loads. Second, the actuation

fatigue behavior of equiatomic Nickel-Titanium and the HTSMA $Ni_{50.3}Ti_{29.7}Hf_{20}$ is studied to create a fatigue database for the purpose of actuator design. Third, improved testing and data collection methods and processes are developed for characterizing the actuation fatigue response of SMAs for complex thermomechanical loading paths. Fourth, the axial actuation fatigue data collected and the provided torsional fatigue data are utilized to analyze and evaluate the capabilities of the previously proposed actuation fatigue lifetime predictions. These actuation fatigue lifetime prediction methods are modified, as needed, to account for minor loops and variable loading conditions. This research will enhance future testing methods and understanding of actuation fatigue and improve the design of SMA-based solid state actuator systems.

ACKNOWLEDGEMENTS

I would like to thank my committee chair, Dr. Dimitris Lagoudas, and my committee members, Dr. Amine Benzerga, Dr. Darren Hartl, and Dr. Ibrahim Karaman for their guidance and support throughout my graduate course work and research.

Thanks also go to the entire faculty and staff of the Aerospace Engineering and Material Science and Engineering Department for making my time at Texas A&M University a worthwhile and enlightening experience.

A special debt of gratitude is owed to Boeing for their financial support and specifically to Jim Mabe for going beyond what was required to encourage and mentor me throughout the course of my research.

CONTRIBUTORS AND FUNDING SOURCES

This work was supervised by a dissertation committee consisting of Dr. Dimitris Lagoudas, Dr. Darren Hartl, and Dr. Amine Benzerga of the Department of Aerospace Engineering and Dr. Ibrahim Karaman of the Department of Material Science and Engineering.

All work for the dissertation was completed by the student, under the advisement of Dr. Dimitris Lagoudas of the Department of Aerospace Engineering.

Graduate study was supported by a fellowship from Texas A&M University. This work was made possible in part by The Boeing Company. The contents of this dissertation are solely the responsibility of the author and do not necessarily represent the official views of The Boeing Company.

TABLE OF CONTENTS

Page

LIST OF FIGURES

Page

LIST OF TABLES

Page

1 INTRODUCTION AND PROBLEM STATEMENT

Shape Memory Alloys (SMAs) are metals which possess the ability to sustain large amounts of deformation and recover a designed geometry when heated above a critical temperature. SMAs recover these strains, induced by mechanical or thermal loading, by transforming between martensite and austenite. This diffusionless, solid-to-solid phase transformation can be utilized in numerous ways and makes SMAs a multifunctional material, as one component can provide both structural support and an additional function, such as actuation stroke or damping. The necessary conditions for initiating this transformation, which can be induced by either mechanical or thermal loading, are shown, schematically, in the stress-temperature phase diagram in Figure 1.1. Two common ways this repeatable transformation is utilized are isobaric thermal actuation under a mechanical bias load and isothermal pseudoelastic loading, which consists of cyclic mechanical loading in a constant temperature environment. These two thermomechanical loading paths are shown in Figure 1.1 as a solid and dashed line, respectively.

The actuation loading path, shown in Figure 1.2 in temperature-strain space, results in thermal-induced strain recovery, and these recoverable or actuation strains range between 1% and 10%, depending largely on the applied mechanical load, material, and processing. The four critical temperatures which describe the onset and completion of this thermal induced transformation, shown as M_s^σ, M_f^σ, A_s^σ, and A_f^σ in Figure 1.1 and 1.2, are the martensite and austenite start and finish temperatures under an applied mechanical load, respectively. When the SMA is under a sufficient mechanical load and cooled below

M_f^σ, the material will develop strain resulting from detwinned martensite. As the SMA is heated above A_s^σ, it will begin to recover the strain until the SMA reaches A_f^σ. To complete the actuation loading path, the SMA is cooled and develops inelastic strain between M_s^σ and M_f^σ. Depending on the material selection and processing, these temperatures can be shifted below freezing or, in the case of High Temperature Shape Memory Alloys (HTSMAs), above 100°C. The fact that this thermal-induced strain recovery is highly repeatable, coupled with its high actuation energy density, makes SMAs viable actuators for many engineering applications, such as morphing aerostructures. The actuation energy densities, which are found by multiplying the actuation stress by the strain, for common active materials are shown in Figure 1.3 [1–10]. This actuation energy density represents the useful work performed by the SMA component per unit volume.

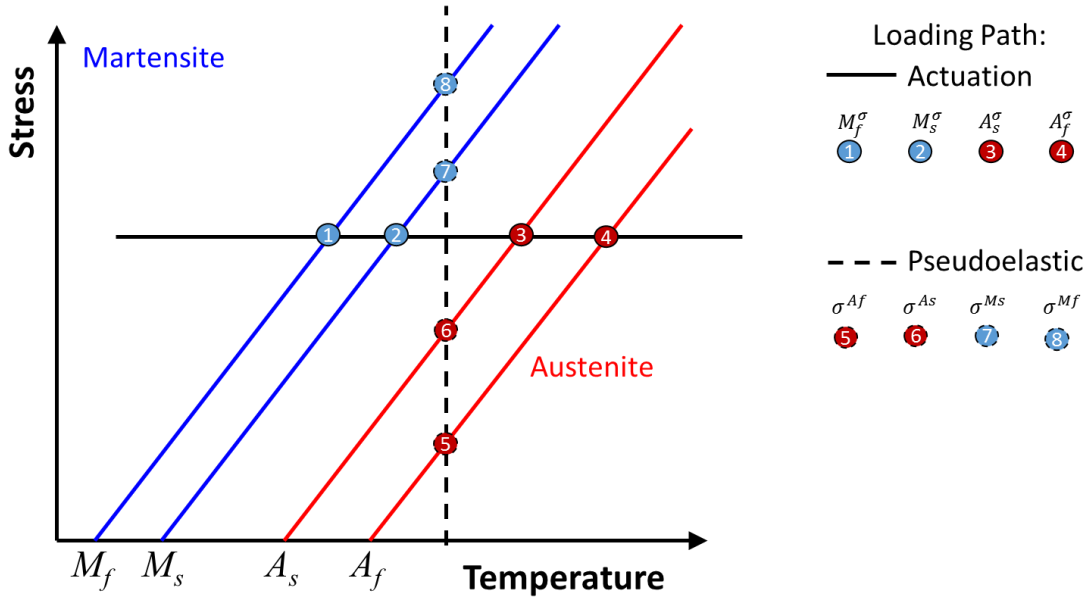

Figure 1.1: Schematic of SMA phase diagram.

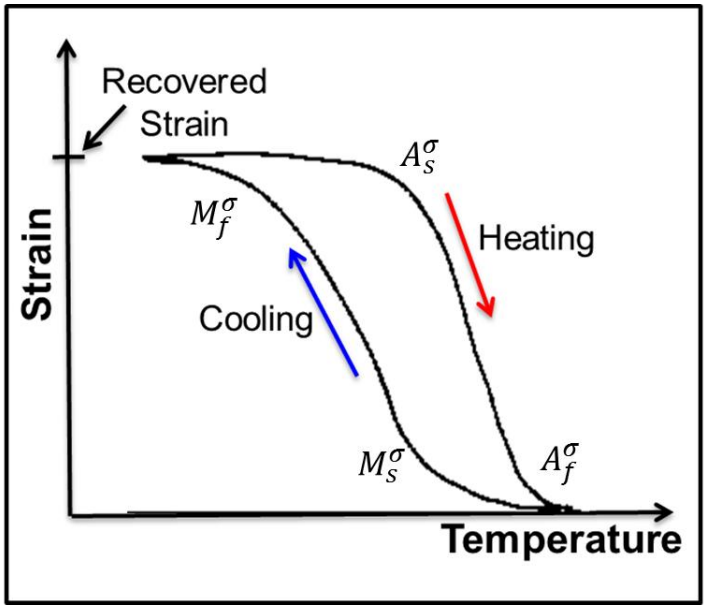

Figure 1.2: Thermal induced strain recovery experimentally observed in NiTi wire under actuation loading.

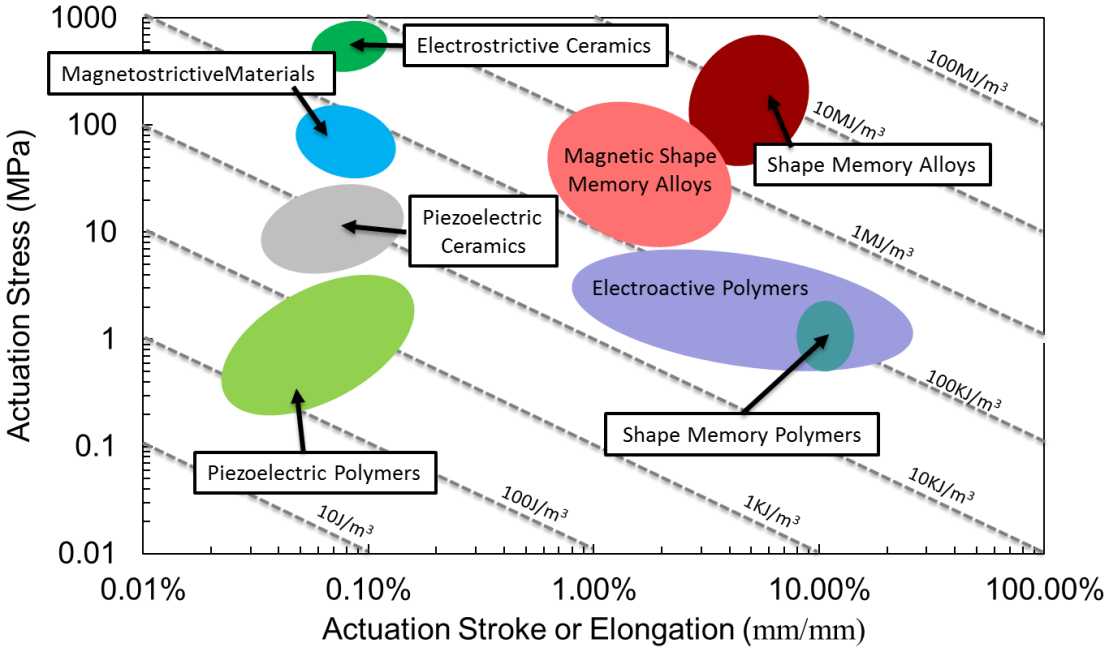

Figure 1.3: Actuation stresses and strains for common active materials. The actuation energy density is the product of the actuation strain with the applied isobaric load.

For most actuator applications, the SMA is loaded mechanically and then heated in order to recover strain in the direction of the loading [1–8]. SMA-based actuators have been used in a wide variety of deployable structures such as hingeless ailerons and spanwise wing twisting in aircraft, as well as solar array deployment mechanisms and actuating hinges [1–4]. The designs which incorporate active materials have targeted improving fuel efficiency, noise reduction [11], and providing increased performance or previously unobtainable capabilities.

The commercial applications which take advantage of the actuation strain recovery have mostly focused on improving aircraft efficiency and noise reduction, which are some of the primary research efforts within the aviation industry.[1] These applications include the Chevron on the Boeing 777 engine outlet [11, 12], an inductively heated twisting wing [13], and an adaptive trailing edge [14].

The Chevron is designed to actuate between a configuration which reduces noise for takeoff and landing and a configuration which increases engine efficiency when the aircraft is at cruising altitude. This motion is achieved through the passive actuation of SMA strips, which are attached to the inside of the Chevron. More recently, Boeing flight tested an SMA-actuated Adaptive Trailing Edge (ATE), which integrated an SMA torque tube into the hinge of a small trailing edge flap on the wing of a commercial aircraft (737-800). Due to the actuation energy density achievable by the SMA torque tube, the

[1] In 2016, the FAA completed a five year CLEEN (Continuous Lower Energy, Emissions and Noise) Program which, with partner organizations, invested over $250 million to encourage the development of quieter and lower emission engines.

actuation system was able to fit along the hinge-line whereas conventional actuators proved to be too bulky [11–14].

In addition to the Chevron, several research efforts have also targeted improving engine performance and safety by using SMAs to actuate components within or directly connected to the engine. These designs include varying the cross-sectional area of the F-15 inlet cowl [15], varying the fan nozzle area in a commercial jet engine [16,17], and opening a vent to allow for cool air to lower the core temperature of a Rolls-Royce jet engine [18].

While the thermal-induced phase transformation of an SMA subjected to the actuation loading path is governed by four critical temperatures, the isothermal pseudoelastic loading path has four critical stresses which dictate the stress-induced transformation: σ^{Ms}, σ^{Mf}, σ^{As}, and σ^{Af}. In order to undergo a pseudoelastic loading cycle, the SMA is heated above A_f prior to mechanical loading. Then, as the mechanical load is increased, the SMA undergoes predominantly elastic deformation until the stress reaches σ^{Ms}. Once in stress induced martensite, the material remains in the pseudoelastic plateau (B→C in Figure 1.4) until it reaches fully detwinned martensite, σ^{Mf}. Upon unloading, the strain is fully recovered if the temperature is kept above A_f.

This pseudoelastic response has been utilized by many biomedical [19–30] and civil engineering applications [31–34]. Biomedical implant applications include deployable stents [19], guide wires [20], thin film flow diverters for wide-neck aneurysms [21,22] and orthopedic bone fillings implants [23]. The biomedical industry has also utilized

SMAs in the development of improved instruments, such as orthodontic devices to repair occlusal defects [24], flexible distal tips, endoscopic stabilizers and graspers [25], martensitic dilatators in various shapes for heart surgery, and biopsy forceps and hinge-less graspers used in laparoscopic surgery [29,30]. These and other biomedical applications frequently utilize SMAs for their ability to recover from large deformations, which allows devices to be compressed prior to insertion, and for their inherent corrosion resistance and biocompatibility.

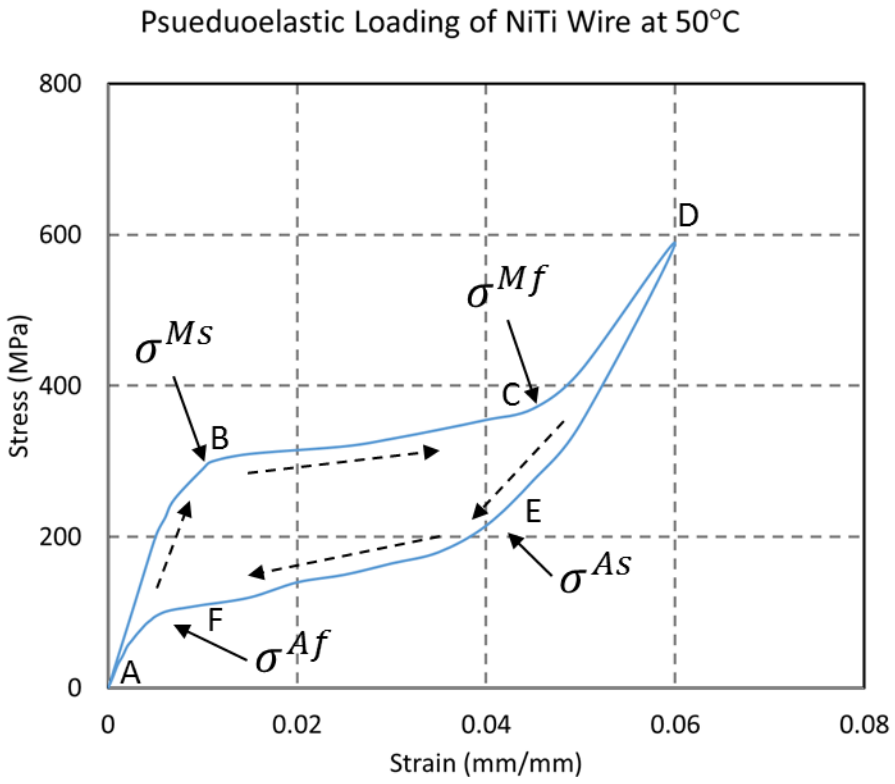

Figure 1.4: Psuedoelastic loading of NiTi Wire at 50°C; dashed arrows indicate loading direction.

In the civil engineering industry, the pseudoelastic response is frequently utilized for its energy dissipation in addition to its ability to recover from large deformations. (Note: In Figure 1.4, the energy density dissipated can be found through calculating the area inside the pseudoelastic loop.) Some applications include shape restoration [31], active structural frequency tuning [32], structural self-sensing and rehabilitation to handle macro-size cracks [33], and passive structural control in ground isolation system and energy dissipation system [34].

1.1 Fatigue of Shape Memory Alloys

While there are many applications which have utilized SMAs to solve engineering challenges that conventional materials and actuation systems could not efficiently solve, and many more potential uses for these active materials, the main drawback to building a system around an SMA is that, after sufficient actuation or pseudoelastic cycles, the SMA component will generate irrecoverable deformation and suffer structural failure. Due to this repeatable stress or temperature induced phase transformation, SMA actuators undergo actuation or thermomechanical fatigue in addition to mechanical or pseudoelastic fatigue.

The fatigue of SMAs can be divided into two categories: pseudoelastic and actuation fatigue (Figure 1.5). Pseudoelastic fatigue under isothermal mechanical loading has been studied extensively relative to the less understood actuation fatigue [10,35–61]. Many of the commercial applications of SMAs undergo pseudoelastic fatigue, such as stents and other applications in the biomedical industry. These applications undergo a stress-induced phase transformation and can exhibit upwards of 10^4 cycles to failure for large strain

amplitudes (10%) and 10^6 cycles to failure for low strain amplitudes (1%). These pseudoelastic lifetimes have been shown to be largely dependent on degree of transformation, alloy composition, material processing (e.g. heat treatment), and surface finish [42–61].

Actuation fatigue, or the effect of repeated thermal-induced phase transformations while under a mechanical biasing load, has been studied significantly less often and is generally limited to actuating against a constant force or isobaric mechanical load. While thermomechanical fatigue in materials without phase transformation has been studied extensively in the past, actuation fatigue introduces cyclic strain recovery as the primary mechanism for inducing damage and failure. When an SMA actuator is cooled below the martensite finish (M_f) temperature and subjected to a mechanical biasing load, the SMA enters a detwinned martensite state; upon heating, the material transforms into austenite and recovers most of the inelastic strain, as shown in Figure 1.2. This recovered strain, or actuation strain, is generally between 1% and 10% for most SMAs, and is largely dependent on the material, processing, and applied loads. Transformation induced plasticity (TRIP) and retained martensite account for the remnant, unrecovered strains [56]. The evolution of this irrecoverable strain can be seen in Figure 1.5 for a NiTi wire subjected to 150MPa load. After the first cycle, there is a relatively large amount of unrecovered strain. By the 10th cycle, the irrecoverable strain generated per cycle has decreased significantly, and by the 100th cycle, the material has stabilized and the hysteresis loop is nearly closed.

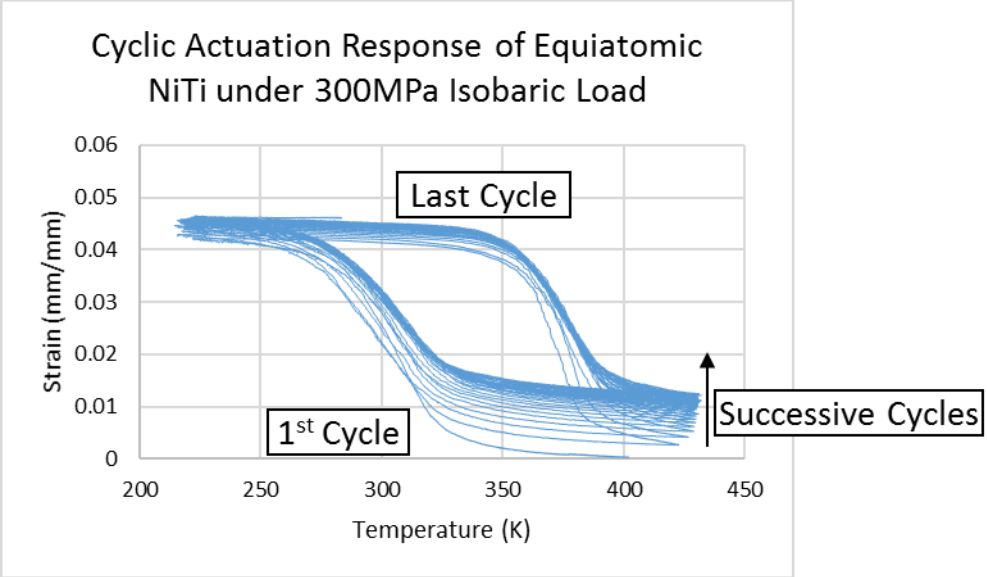

Figure 1.5: Cyclic Thermal Load of a NiTi Wire under a stress of 300MPa.

Bigeon and Morin [50] thermally-cycled SMA wires through complete transformation under an isobaric load until failure, and noted the inverse relationship between applied stress and cycles to failure. Rong et al. [58] found the effect of annealing temperature on transformation temperature, fatigue life, and deformation behavior of SMA wires under constant stress cycled to failure. Expanding upon this, Lagoudas et al. [59] examined the effects of applied load, heat treatment, material processing and degree of transformation on TiNiCu wires. Higher annealing temperatures and a reduction in the amplitude of partial transformation and transformation strain were shown to increase the fatigue life. Bertacchini et al. [56] built upon this study and analyzed the effects of corrosion and composition on the fatigue behavior. Actuation in a corrosive environment

was shown to reduce the fatigue life of SMA wire actuators in both complete and partial transformation cases.

Calhoun *et al.* [36] and Agboola *et al.* [35] also studied Ni-rich, precipitated hardened NiTi alloys and noted the power-law relationship between cycles to failure and actuation work. Additionally, Agboola *et al.* [35] observed a high micro-crack density away from the fracture surface, and indicated that failure of precipitated NiTi may be due to the way in which cracks initiate and propagate while the SMA is transforming. The first actuation fatigue of a plate study on plate actuators was conducted by Schick [62] , who utilized $Ni_{60}Ti_{40}$ material and examined the effect of the alloy's high volume fraction of Ni-rich precipitates on lifetime under the constant stress loading condition for complete transformation. Mammano and Dragoni [43,63] tested commercial NiTi wires (SAES Getters SmartFlex) under varying mechanical loading. Their study, designed to capture application-based loading paths for common wire applications, illustrated that the loading path can have significant effects on the fatigue life of a wire actuator and total work output.

1.2 Determining the Lifetime of SMA Actuators

Numerous previous studies have successfully correlated the number of actuation lifecycles with actuation fatigue characteristics, including stress, actuation strain, irrecoverable strain resulting from transformation, and the mechanical work received. Lagoudas et al. [58] implemented a power-law relationship, similar to the Manson-Coffin law, in order to correlate the accumulated irrecoverable strain to the cycles to failure for wire actuators. The relationship utilized in their study is shown in Equation 1.1:

$$\varepsilon^{tr} = \alpha N_f^{\beta} \tag{1.1}$$

In Equation 1.1, N_f represents the number actuation cycles an SMA is able to sustain while ε^{tr} represents the accumulated plastic strain. The material parameters α and β, referred to as the fatigue ductility constant and exponent, respectively, in standard mechanical low-cycle fatigue of metals, can be determined from fitting the modified Manson-Coffin law to the experimental data.

Similarly, numerous studies have shown a strong correlation between actuation work and cycles to failure for wire actuators [41], dogbone actuators [36,40], and plate or sheet actuators [62]. This relationship has been utilized in both a critical plane model, based on the work of Smith, Watson, and Topper (SWT) [41], and a continuum damage model, proposed by Hartl et al. [61].

While these correlations have been observed in multiple material systems and in independent studies, few attempts have been made to utilize these relationships in order to develop a predictive model which can determine the number of actuation cycles an SMA specimen or component can sustain prior to suffering ultimate failure. Additionally, these correlations have not been validated for non-isobaric or variable loading conditions, and should be tested for new material systems which have been developed in recent years. In the following work, four actuation fatigue life prediction methods are developed and the fatigue response of many different SMAs with various compositions, processing, and geometries have been analyzed so that the fatigue life prediction implementations can be tested and validated.

1.3 Overview of Objectives and Goals

There are four objectives of this study: First, the actuation fatigue behavior of equiatomic Nickel-Titanium (NiTi) will be investigated in order to develop methods for studying actuation fatigue and provide a baseline actuation fatigue response for constant force biasing loads. Second, improved testing and data collection methods and processes will be developed for characterizing the actuation fatigue response of SMAs for isobaric and variable thermomechanical loading paths. Third, the actuation fatigue behavior of equiatomic NiTi, Nickel-Rich $Ni_{60}Ti_{40}$ (atomic weight percentage), and the HTSMA $Ni_{50.3}Ti_{29.7}Hf_{20}$ will be studied in order to create a fatigue database for the purpose of actuator design. Fourth, the actuation fatigue data collected will be used to analyze and evaluate the capabilities of the several actuation fatigue lifetime prediction implementations. These actuation fatigue lifetime prediction methods are developed based on previous work and literature review, and have been adapted to account for any given thermomechanical loading path.

The first objective, developing a baseline actuation fatigue response, will accomplished by performing actuation fatigue tests on equiatomic Nickel-Titanium (NiTi) dogbones. Equiatomic NiTi is an ideal candidate for developing a baseline response as it has been studied extensively in literature, is highly commercially available, and does not form precipitates. The experimental phase of the NiTi actuation fatigue characterization will include a scoping study to select heat treatments which produced promising fatigue responses and an in-depth characterization of selected heat treatments. Specific heat treatments will be deemed promising if they exhibited low accumulated transformation

induced plasticity (TRIP) and high cycles to failure. Out of a test matrix of eight heat treatments, the two most promising will be selected and further characterized.

The second objective, developing improved actuation testing methods, will be accomplished through the development of novel software for testing, data processing, and data management as well as the incorporation of new sensing and measurement techniques. In order to ensure consistent and repeatable fatigue testing, an intelligent state-space machine was built in LabVIEW to control testing and record experimental data. MATLAB and Python scripts were developed for data processing and reporting as well as material characterization, which required inputs from multiple tests. The software suite presented in Chapter 2 and Appendix A encompasses the software necessary to perform an actuation fatigue test, process the experimental measurements, and post-process the data set to determine the necessary material properties.

The third objective, to collect sufficient characterization data to develop an actuation fatigue database, will be accomplished by using the developed testing methods to characterize equiatomic NiTi, $Ni_{60}Ti_{40}$, and NiTiHf. In addition to characterizing their actuation fatigue response when under isobaric loads, the effect of variable loading will also be studied. The experimental data obtained from these tests is reported in Chapter 3.

The fourth objective, to develop and evaluate fatigue lifetime prediction methods, will be accomplished by analyzing the data collected for the actuation fatigue database as well as available literature in order to develop four fatigue lifetime prediction methods, which are discussed and evaluated in Chapter 4. Since many SMA-based actuation systems,

including most of the applications discussed in the previous section, require their SMA components to sustain many actuation cycles with non-constant or evolving thermomechanical loads, the developed implementations will be evaluated for their ability to capture the actuation fatigue response for isobaric as well as more complex variable loading paths.

2 EXPERIMENTAL DESIGN

In this chapter, the experimental methods for studying actuation fatigue will be presented and the capabilities and limitations of the custom thermomechanical loading frames will be discussed. The experimental design consists of four main sections: the design of the test frame, the development of testing and post-processing software, and specimen preparation, and a testing overview. The discussion of the experimental design details how actuation fatigue is induced in actuator specimens and parts through repeatable, controlled, and measured thermomechanical cycles. Section 2.2 summarizes the development and use of the software suite developed for studying and characterizing the fatigue response. Further discussion of the software along with screenshots are available in Appendix A. Section 2.3 provides an overview for specimen preparation, processing and testing. Lastly, Section 2.4 summarizes the tests which were completed for this work.

2.1 Experimental Design Overview

In order to induce actuation fatigue in a controlled and repeatable manner, four custom thermomechanical loading frames were utilized and modified to allow for continuous data collection. For an isobaric fatigue test, an actuator specimen, such as the one schematically shown in Figure 2.1, will be subjected to a constant force mechanical load, while the temperature is cycled. When under a sufficient mechanical load, the thermal cycle will induce an actuation stroke, as shown in Figure 2.2. The actuator is loaded onto the test frame when fully martensite, denoted as point 1 in Figure 2.2, and undergoes

forward transformation. Then, upon heating, the transformation strain is recovered, leaving the system with elastic strain in austenite, shown as point 2. It should be noted that, while the elastic strain is non-zero, it was found to be an order of magnitude lower than the transformation strain and, therefore, was deducted when characterizing the actuation fatigue response.

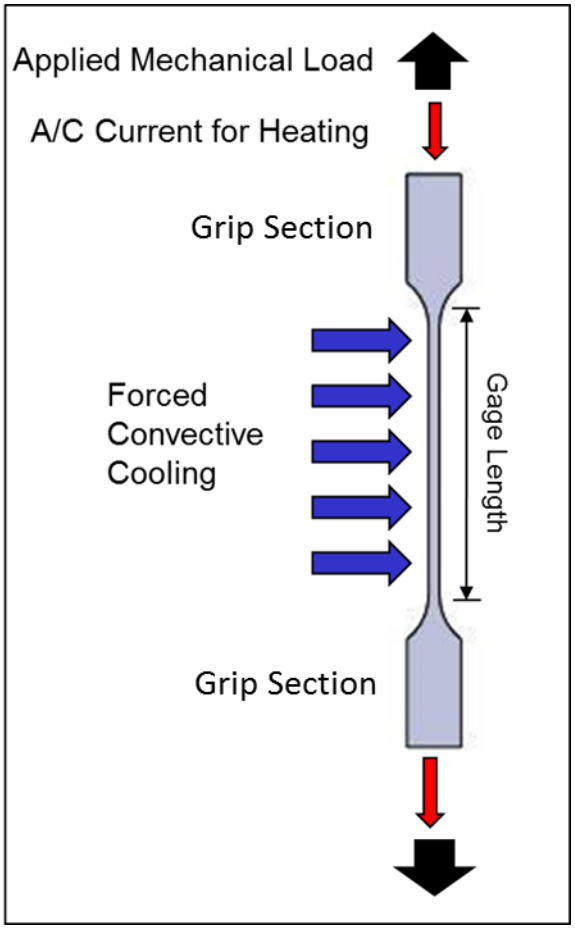

Figure 2.1: Thermomechanical loading schematic for dogbone actuator.

This actuation cycle is induced in the SMA actuator through resistive heating and forced, convective cooling while the specimen was under a biasing mechanical load. This process is shown schematically in Figure 2.1. Both the load and current were applied through the mechanical grips in order to avoid localized effects due to the experimental setup.

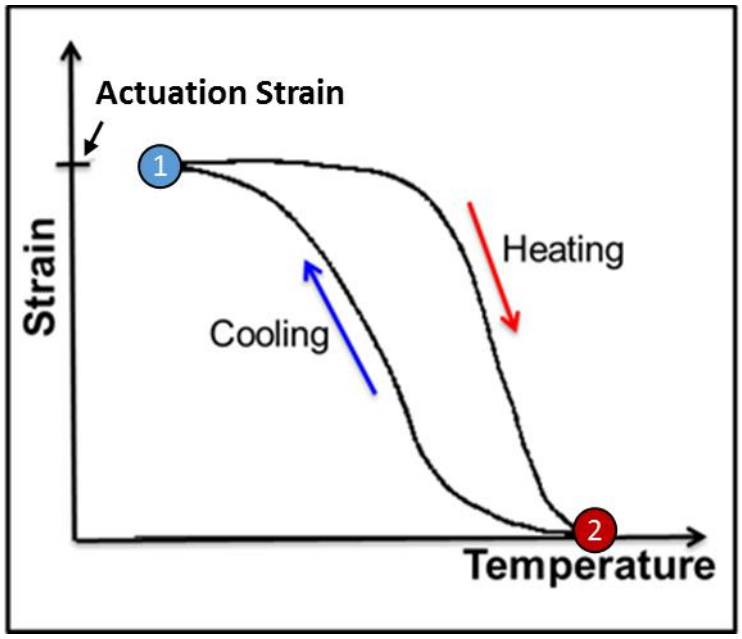

Figure 2.2: Schematic representation of the actuation loading path for an SMA.

Due to the nature of the actuation strain recovery and its evolution over the course of an actuators fatigue life, continuous monitoring of measurable state variables, such as strain and temperature, can provide significant insight into the fatigue process. Because

of this, three non-contact measurement methods for deformation and temperature were tested in addition to a conventional extensometry methods.

Each actuator specimen is subjected to many of the thermal cycles shown in Figure 2.2 over the course of its fatigue life. During these thermal cycles, irrecoverable deformation is generated and must be accounted for in the experimental design. A standard result of the evolution of these hysteresis loops can be seen in Figure 2.3. The nominal stress is utilized to describe the mechanical load (250MPa in Figure 2.3), and the strain is the nominal engineering strain, measured over the length of the gage section.

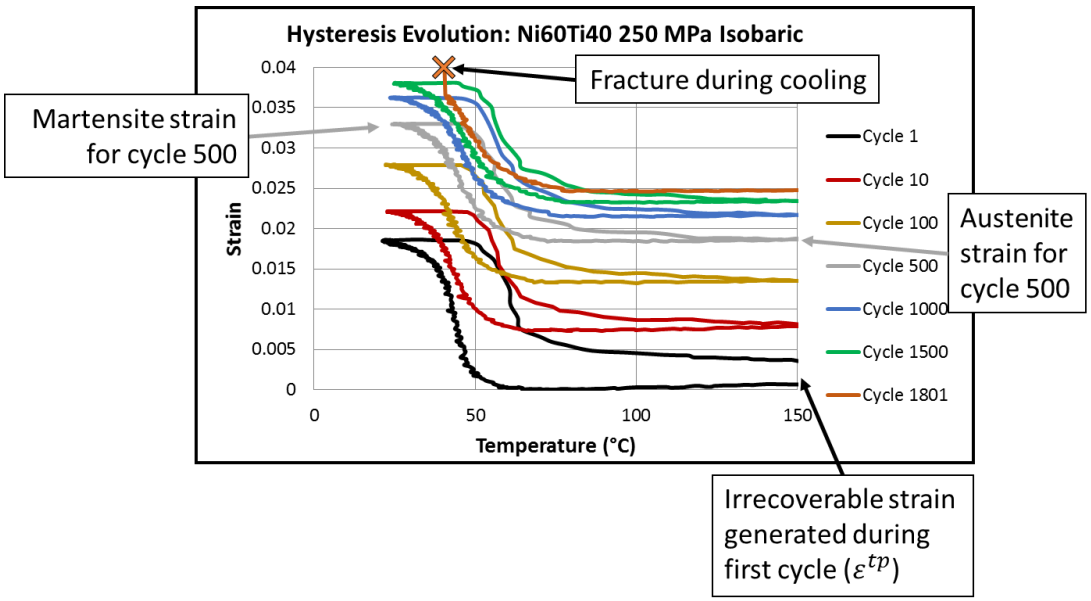

Figure 2.3: Hysteresis evolution for a $Ni_{60}Ti_{40}$ dogbone actuator; irrecoverable strain, martensite strain for cycle 500, austenite strain for cycle 500, and fracture are noted.

Several details can be determined from Figure 2.3:

- Irrecoverable strain is generated during each cycle; however, it is much larger during the first cycle.
- Each cycle has a local minimum and maximum strain, and the difference between them being the actuation strain.
- These strains evolve until catastrophic failure occurs during cooling.

In addition to analyzing the evolution of the hysteresis, the strain evolution can also be utilized to better understand the fatigue response of a dogbone actuator. For each of the tests completed during this work, the engineering strain measured by the extensometer was additively decomposed into two parts: irrecoverable strain and actuation strain. For the same test shown in Figure 2.3, the strain evolution is shown in Figure 2.4. The strain evolution is comprised of the minimum (austenite) and maximum strain (martensite) for each cycle, with the difference being the actuation strain.

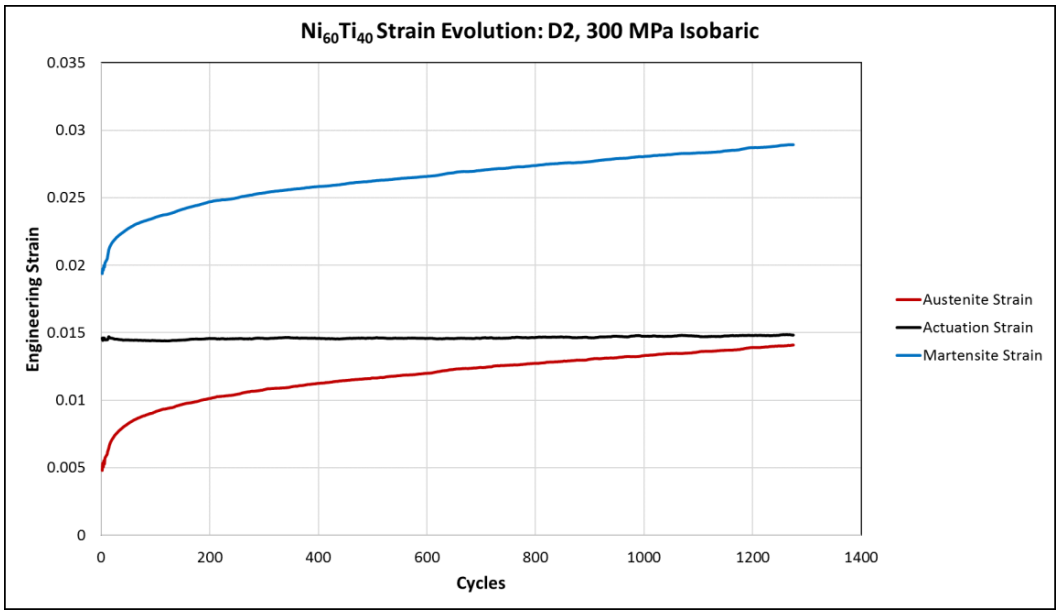

Figure 2.4: Example Strain Evolution for a $Ni_{60}Ti_{40}$ dogbone actuator under 300MPa isobaric loading.

2.1.1 Testing Hardware

The testing setup can be seen in Figure 2.5. The setup is composed of a custom steel frame (black), 3D printed ABS plastic specimen or test chamber (white), an air treatment system with vortex tube cooling, and a data acquisition system consisting of a PC and a National Instruments Data Acquisition Card (NI-DAQ). The actuator specimen is loaded onto the steel frame within the test chamber, and a mechanical load is attached below the actuator.

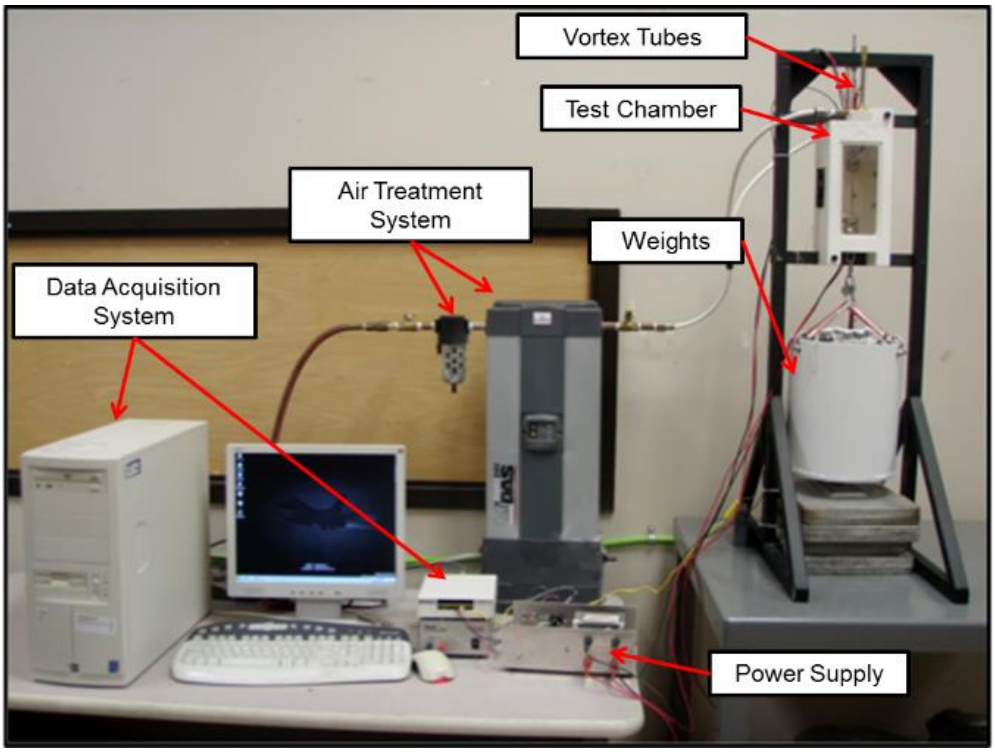

Figure 2.5: Fatigue test frame and experimental setup.

To ensure axial loading with minimal torsion, the load is connected directly to the bottom of the specimen grips with stainless steel hooks. In the case of linear or spring loading, a spring array, such as the one shown in Figure 2.6, is attached to the bottom of the specimen grips and can provide a variable load which is linearly dependent with transformation strain. The setup, as shown in Figure 2.6, can provide up to a 500lbf shift in mechanical load on the actuator for 3mm actuation stroke while remaining in the linear regime of the springs.

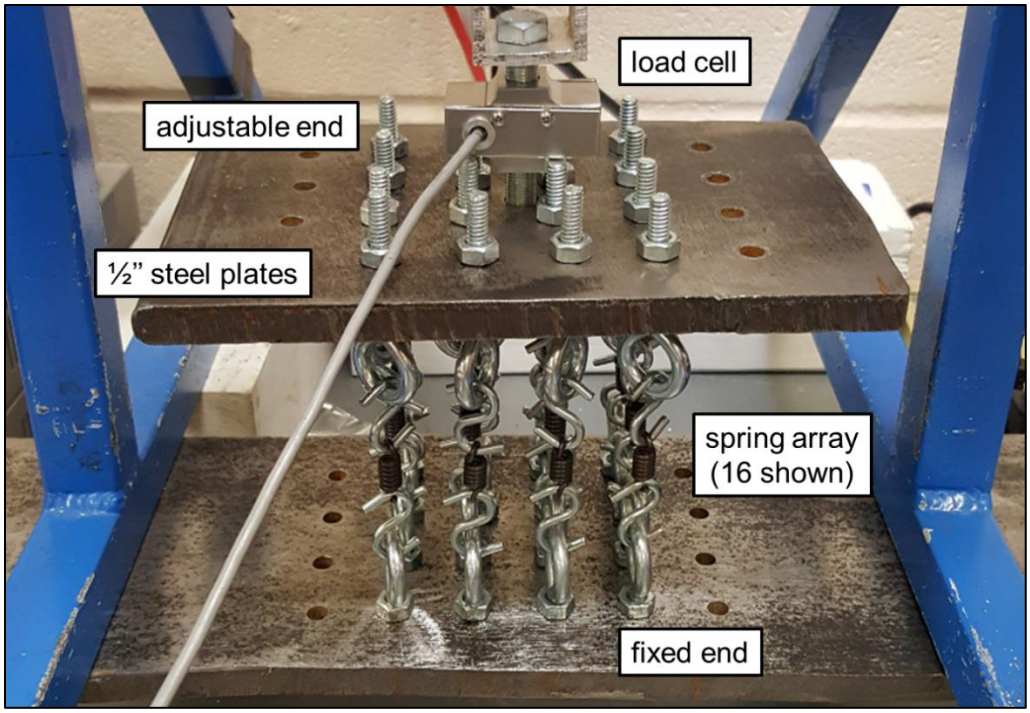

Figure 2.6: Spring array setup used for linear loading paths.

Many actuator applications, such as morphing aerostructures or control surfaces, which are subjected to evolving aerodynamic loading, require actuators to function under loading profiles which evolve with the actuation strain. In addition to providing a load which better simulates the actuation fatigue experienced by actuators in such applications, the load line can also be adjusted mid-test without interruption or unloading the sample. Due to the positioning of the eye bolts, additional springs can be added during a test to increase the load experienced by the specimen.

In addition to linearly varying load lines, the effects of stepwise loading was also studied. Similar to linearly varying load lines, the motivation for stepwise loading also came from actuator applications. While some actuator applications have a range of

deployment positions, others are generally limited to two distinct positions, commonly referred to on/off actuators; examples of these systems include the Active Hinge Pin Actuator developed by Boeing or wire actuated snapping mechanisms. In total, three loading paths were studied: isobaric, linear, and stepwise. These three loading paths are shown, schematically, in Figure 2.7A, and experimental results for a linear loading path are shown in Figure 2.7B. The most well studied and standard is the isobaric loading path, which is shown in red. This was achieved by hanging a constant weight off of the actuator, such as the one shown in Figure 2.5. The spring loading path, shown in blue, has different loading and unloading paths due to the actuation strain recovery: starting in martensite, the actuator is loaded and heated. Once the actuator reaches the austenite start temperature, the SMA begins to contract and extends the spring array, thus increasing the load. Conversely, as the actuator cools to the martensite start temperature, the SMA extends allowing the spring array to relax and the load to decrease. This is similar to an actuator being thermally activated and moving a control surface further into a flow, thus resulting in an increase in load on the actuator. The stepwise loading, shown in purple, was used to simulate an on/off actuator and was achieved by placing a turn-buckle in line with the actuator. This turn-buckle was then adjusted until the weight was set down at the desired percent actuation strain. For this load path, the weight generally set down when the actuator has completed nearly 75% of its transformation stroke and picked back up after 25% of the reverse transformation.

In the experimental setup, two sensors are connected in line with the actuator: a linear variable differential transformer (LVDT) and a load cell. The load cell was calibrated for a 0-500lbf load regime with ±1lbf accuracy and primarily used for the variable loading tests. The LVDT, which is located behind the specimen chamber, is connected to the bottom specimen grip via an aluminum arm and was found to be accurate to 0.1mm. Additionally, two type-j thermocouples were connected to the test frame: one was utilized to sense the temperature of the specimen chamber in order to detect cases of severe overheating and monitor ambient temperatures, while the second was used in system calibration tests.

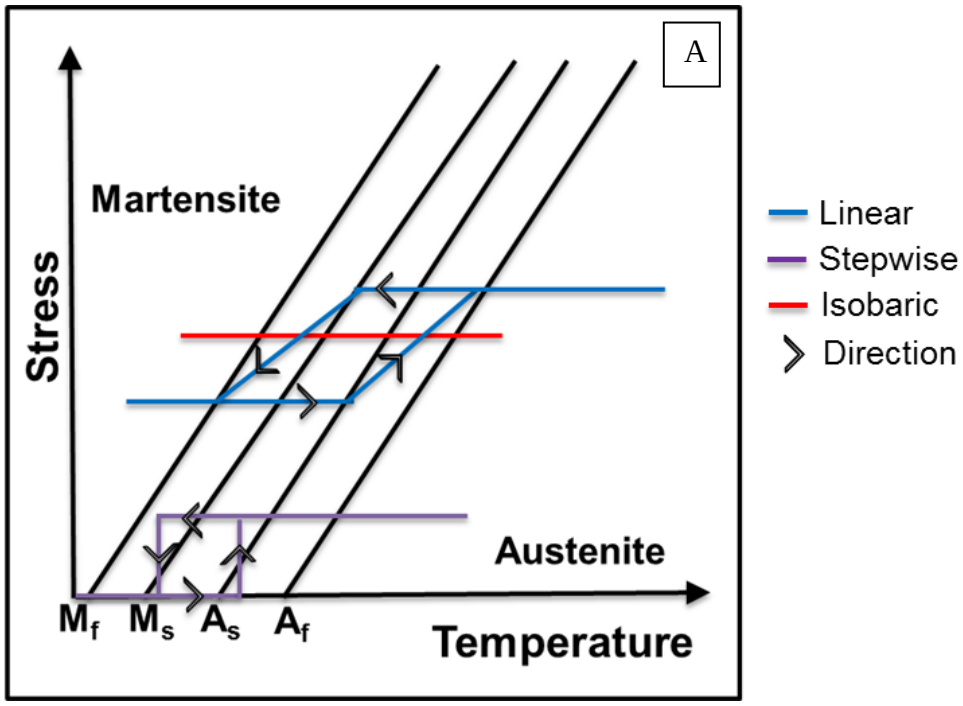

Figure 2.7: (A) Schematic of thermomechanical loading paths studied. (B) Experimental results for an SMA subjected to a linear loading scheme.

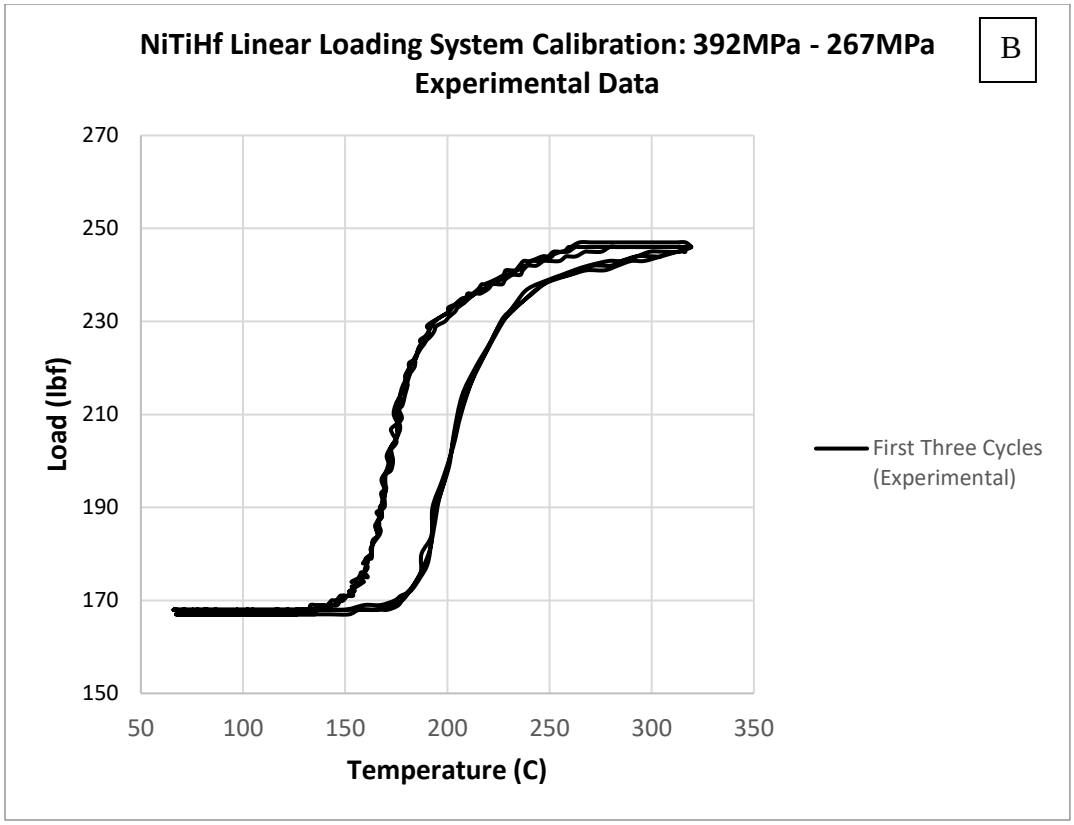

Figure 2.7: Continued.

The power supply system consists of a control box with a solid-state relay (SSR) and a manual shutoff switch, a variable alternating current power supply (VARIAC) with a 130V manually tunable range, a transformer, and two sets of electrical leads which are attached to the specimen grips. This system supplies between 10 and 40A to the actuator at 0.5 to 4V; for each test, the power is closely monitored to ensure repeatable testing.

While the power supply is toggled on and off during testing, it was found that continuous forced convection significantly reduced temperature gradients in the actuator specimens. For regular SMAs, the cooling system shown in Figure 2.3 was utilized as it

could achieve air temperatures of 0-10°C, which ensured full forward transformation. For HTSMAs, where the martensite finish temperatures exceed 100°C, it was found that computer fans provided faster and more even cooling due to the increased flow volume. Additionally, this allowed for the removal of the front of the test chamber to improve the accuracy of non-contact sensors.

2.1.2 Non-Contact Sensors

In addition to the conventional, contact sensors discussed in the previous section, several non-contact measurement systems were utilized in order to further characterize the actuation fatigue response while minimizing the impact on the actuation fatigue test. The addition of these sensors can be seen in Figure 2.8. Note: as pictured, the front of the specimen chamber is removed to allow for accurate IR measurements and a black background is placed in the specimen chamber to improve visual data collection.

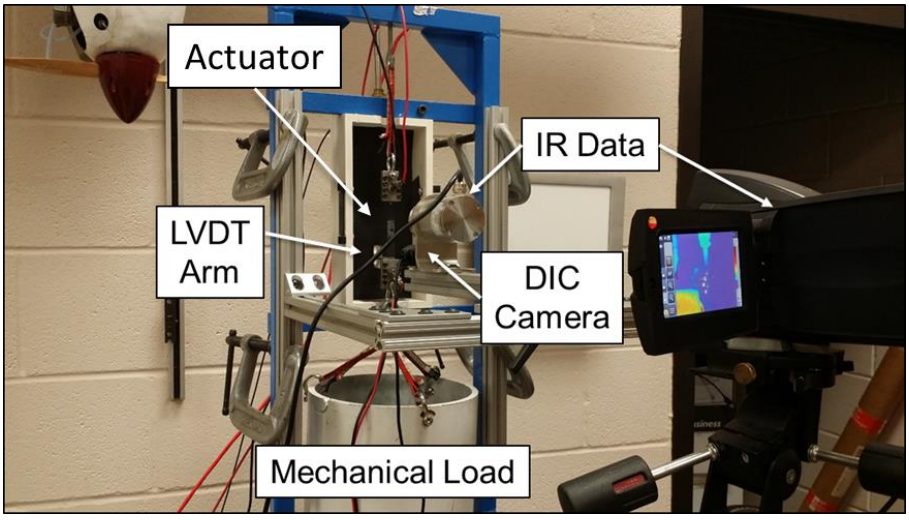

Figure 2.8: Experimental setup showing the implementation of non-contact sensors for full field deformation, displacement, and temperature.

During preliminary testing of equiatomic NiTi, it became apparent that strain localization and necking were a large issue. In order to better quantify the degree of strain localization, a visual extensometry method was developed based on previously conducted research [38, 66] and Digital Image Correlation (DIC) was implemented to increase the spatial resolution.

In addition to an evolving strain field, the resistance of the actuator specimen was also found to evolve due plastic strains and microstructural damage. In order to monitor the current being supplied to the system, AC current sensors were added to the system.

2.1.3 Data Acquisition System

Continuous data was collected from the test frame through a National Instruments Data Acquisition Card, which was connected to a PC that runs the control software and records raw data. For most tests, an NI-DAQ USB 622 system was utilized (shown in Figure 2.9).

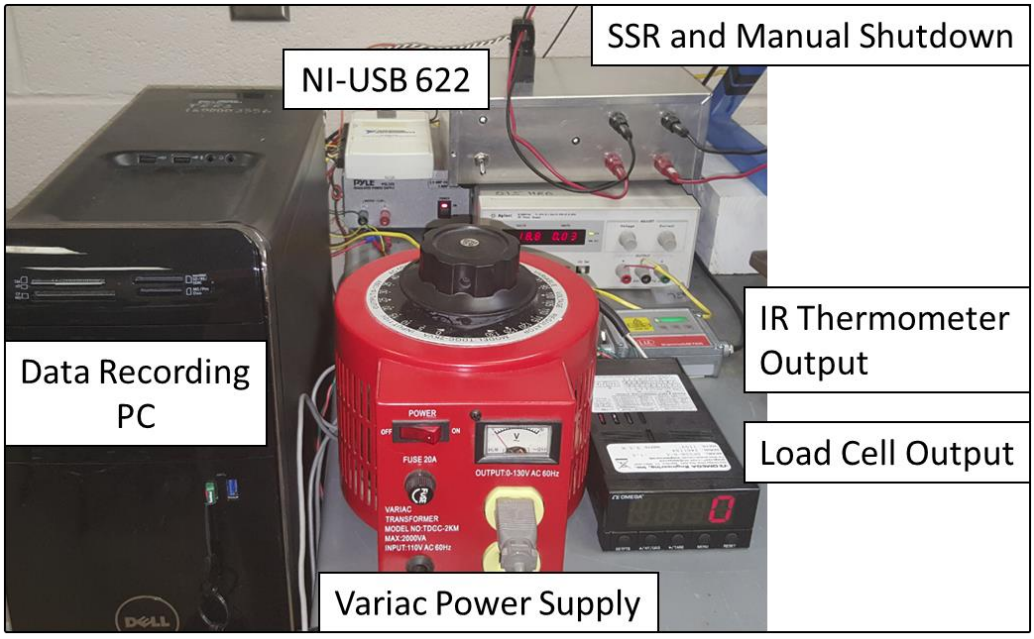

Figure 2.9: Data Acquisition System (DAQ) and manual readouts for test monitoring.

2.2 Actuation Fatigue Software Development

Due to the complexity of the actuation strain recovery and the actuation fatigue response of SMAs/HTSMAs, a new suite of software was developed to control the test frame (Section 2.2.1) and post-process the significant amount of data collected (Section 2.2.2). Data acquisition and testing software was designed to run standard, low-cost research PCs (8GB RAM, 3+GHz quad-core i5 processors); post-processing of data was generally performed on higher power (16GB RAM, hexa/octacore 3+GHz i5+ processors) machines to reduce computational time.

2.2.1 LabVIEW Software Development Overview

In order to ensure consistent cycling, an intelligent state-space controller was developed in LabVIEW. A state space machine, graphically represented as a flowchart in Figure 2.10, updates the state of a system (in this case the actuation fatigue software) by running sensor inputs through the provided control laws and choosing a new system state based on the data available from the previous computational step.

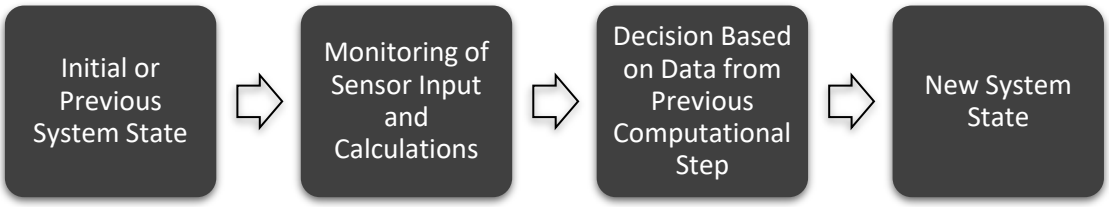

Figure 2.10: Flowchart depicting the general process of the state-space machine utilized by the fatigue testing software.

The control panel, which is shown in Figure 2.11, consists of user inputs (white text boxes), text outputs (gray text boxes) which indicate the live measurements, and trigger lights (dark and light green circles) which indicate whether the test is heating or cooling and if any of the error checks have been tripped. Similar to the code, the front panel is split into functional groups for ease of use.

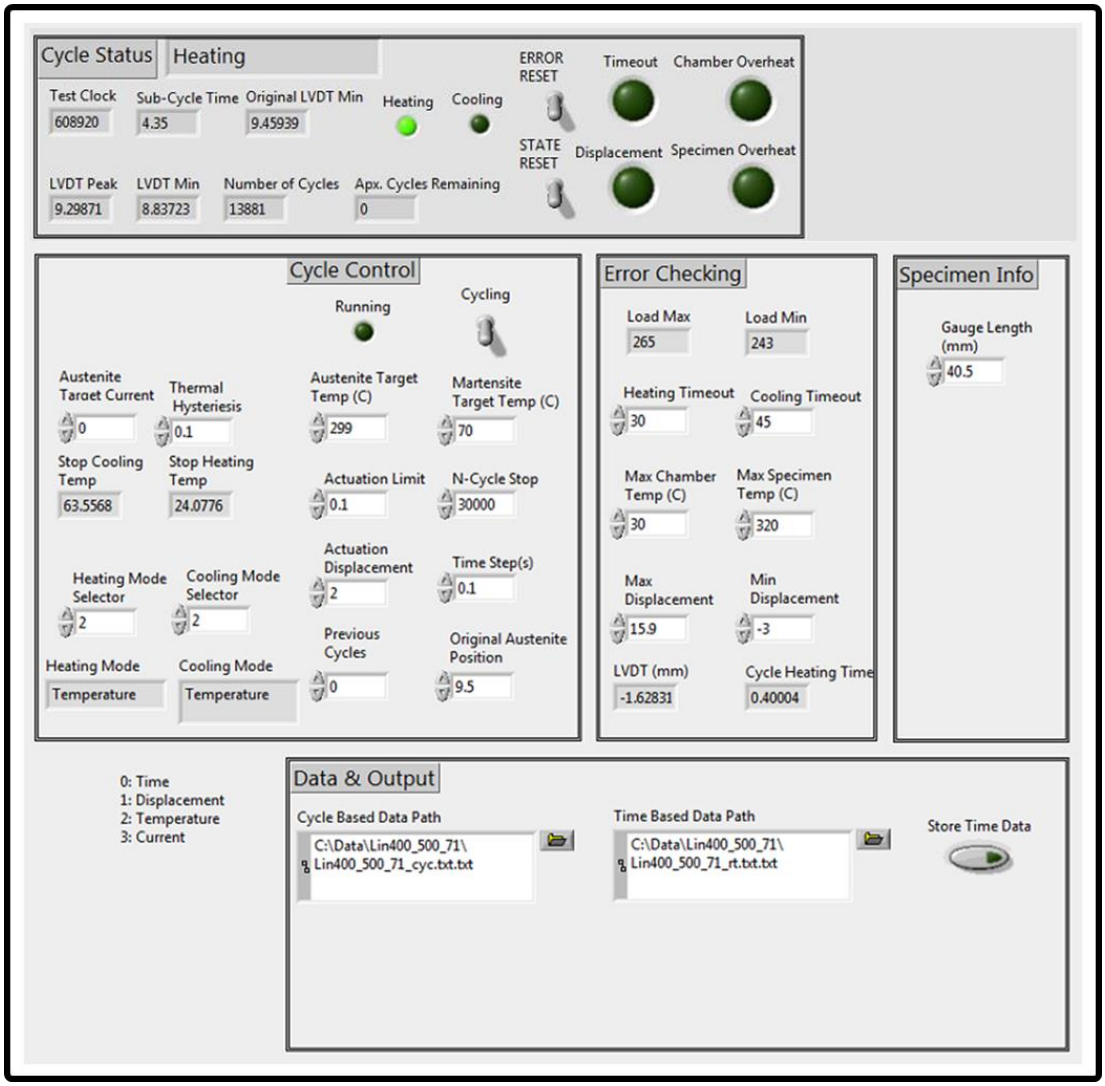

Figure 2.11: Front-panel controls for Fatigue Testing Software.

The top block consists of information pertaining to the current cycle of the test. The large text output next to the Cycle Status label shows the current state of the cycle: for example, Heating, Cooling, Off. Other outputs in this portion of the front panel include the number of cycles, the maximum and minimum grip displacements for the current cycle, and indicator lights for each of the potential system errors.

The left block in the middle row contains the user inputs which control the cycling of the system. The selection modes allow the user to select how they want to control the cycle (e.g. cool to a certain temperature, then heat for a certain time) while the numerical input boxes allow the user to dictate the set-points. The center block in the middle row, labeled Error Checking, contains inputs which dictate when the test halts and an error case is thrown (e.g. if the specimen overheats, halt testing). The Specimen Info block has an input for Gauge Length (in mm) which allows the software to convert displacement to engineering strain or percentage elongation. In the bottom row are text boxes for directory inputs which point the software to the data files. Additional discussion about the software developed for this work can be found in Appendix A.

The other half of the user interface, which is shown in Figure 2.12, consists mostly of graphical outputs which allow the test operator to better monitor the test. The graphical outputs include (from top left, clock-wise): the LVDT measurement of the grip displacement, the current running to the specimen, a secondary current measurement for calibration tests, the strain evolutions for the previous 1,000 cycles, real-time plotting of the hysteresis loops (displacement vs. temperature), and the IR measurement of the specimen. Additional graphs (not shown) include chamber temperature and the load cell.

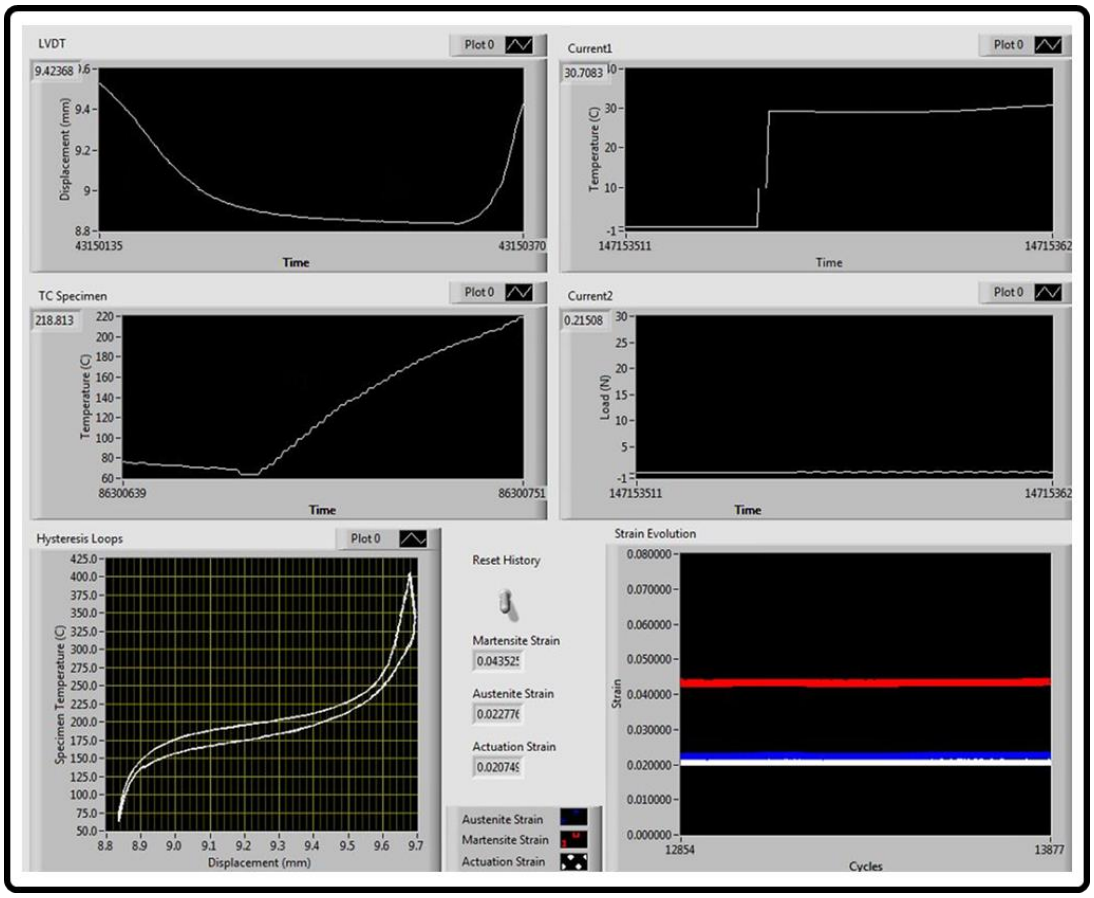

Figure 2.12: Front-panel graphs for Fatigue Testing Software.

2.2.2 Measurements and Data Processing

Over the course of a fatigue test, the actuator will undergo several hundred to tens of thousands of thermomechanical cycles. In order to better understand this process, two main plots were analyzed for each test: the hysteresis evolution and the extension evolution (Figure 2.3 and 2.4 respectively). These results were determined utilizing Equations 2.1-2.4:

$$e_C = \frac{l_{current} - l_{initial}}{l_{initial}} \tag{2.1}$$

$$e_A = \frac{l_{min} - l_{initial}}{l_{initial}} \tag{2.2}$$

$$e_M = \frac{l_{max} - l_{initial}}{l_{initial}} \tag{2.3}$$

$$e_{tr} = \frac{l_{max} - l_{min}}{l_{initial}} \tag{2.4}$$

In these equations, l is the actuator length: $l_{original}$ corresponds to the original gage length, $l_{current}$ is the actuator length at the time of the measurement, and l_{max} and l_{min} are the maximum and minimum length for a given cycle. The engineering strains, e, are calculated for each time-step, e_C, and the austenite, martensite, and transformation strains, e_A, e_M, and e_{tr}, respectively, are determined for each cycle. The actuation strain, e_{tr}, can also be determined by taking the difference between the martensite and austenite strains. The displacements utilized in the calculation for the austenite and transformation strains is also shown schematically in Figure 2.13. The displacement after the first heating cycle is utilized as the reference location in order to remove the austenite elastic strain (labeled as 1st Heating Cycle). For an intermediate cycle (labeled as Nth Cycle), the austenite strain is illustrated by difference between image 1 and 2 (red lines) while the transformation strain is shown as the difference between images 2 and 3 (black). The martensite strain can be determined by comparing images 1 and 3.

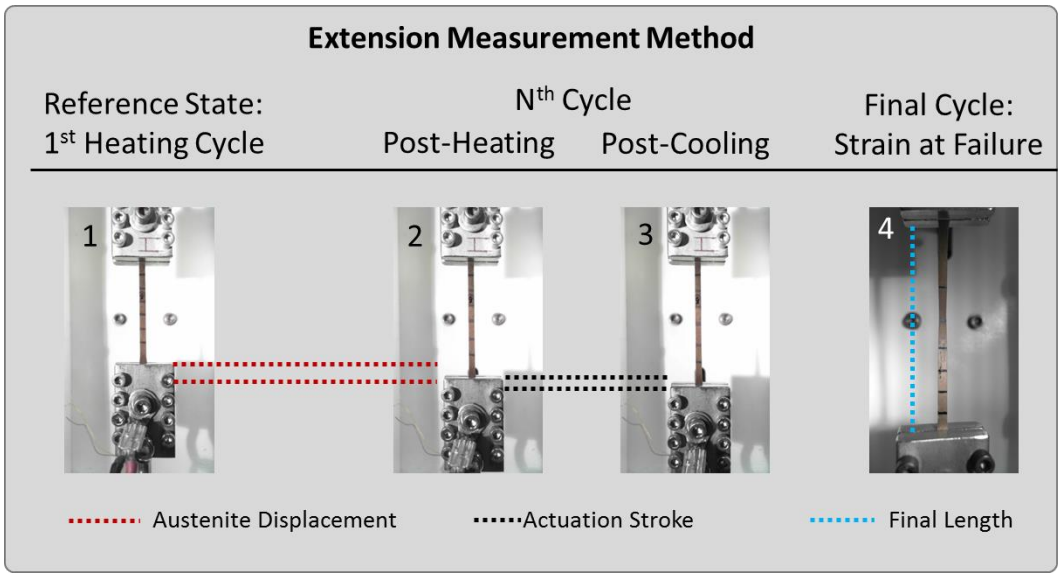

Figure 2.13: Schematic showing displacement measurements; specimen shown is equiatomic NiTi.

While the hysteresis and extension evolutions were the two main sources of data, several other measurements were analyzed. These include determining the resistance of the actuator, resistivity of the material, and transformation temperatures. The MATLAB code developed for this analysis can be found in the supplementary files and is discussed further in Appendix A.

2.3 Specimen Geometries, Processing, and Preparation

2.3.1 Dogbone Specimens and Plate Actuator Component Geometries

Over the course of this study, two sets of geometries were utilized: dogbone and plate actuators. The dogbone actuators consisted of grip sections where the electrical leads and mechanical grips were attached, and gage sections of either 31.75mm (equiatomic NiTi)

or 40.5mm ($Ni_{60}Ti_{40}$, NiTiHf). An example of this geometry can be seen in Figure 2.14, which has the dimensions for the equiatomic NiTi dogbones.

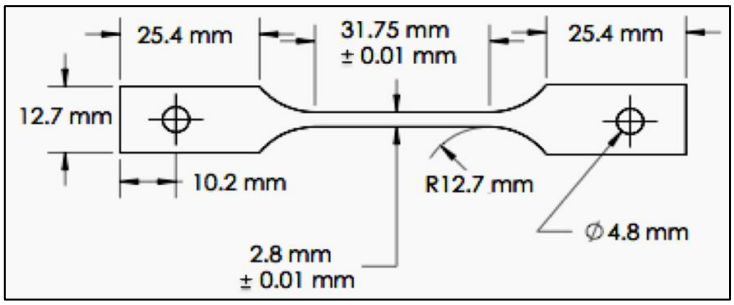

Figure 2.14: Equiatomic NiTi dogbone actuator geometry; two thicknesses were used: 0.25mm and 0.5mm.

Dogbone actuators were chosen for the majority of tests due to the number of available standards for testing of non-active materials which use dogbones, and since they provide a bulk response, unlike wires actuators, while still keeping testing feasible in terms of required mechanical loads and use of expensive SMA materials. From a modeling perspective, they also provide the simplest method for material characterization. However, most actuator applications which implement bulk actuators will require their SMA components to function while under stress concentrations from attachment points, rivet holes, or other system-level requirements. In order to begin to study the effect of stress concentrations as well as analyze the modeling and predictive capabilities for the proposed lifetime prediction methods, three plate actuator geometries were studied. These

geometries, shown in Figure 2.15, consist of plate actuators 100mm x 10mm x 0.5mm (L x W x H) with hole or notch radii of 1mm.

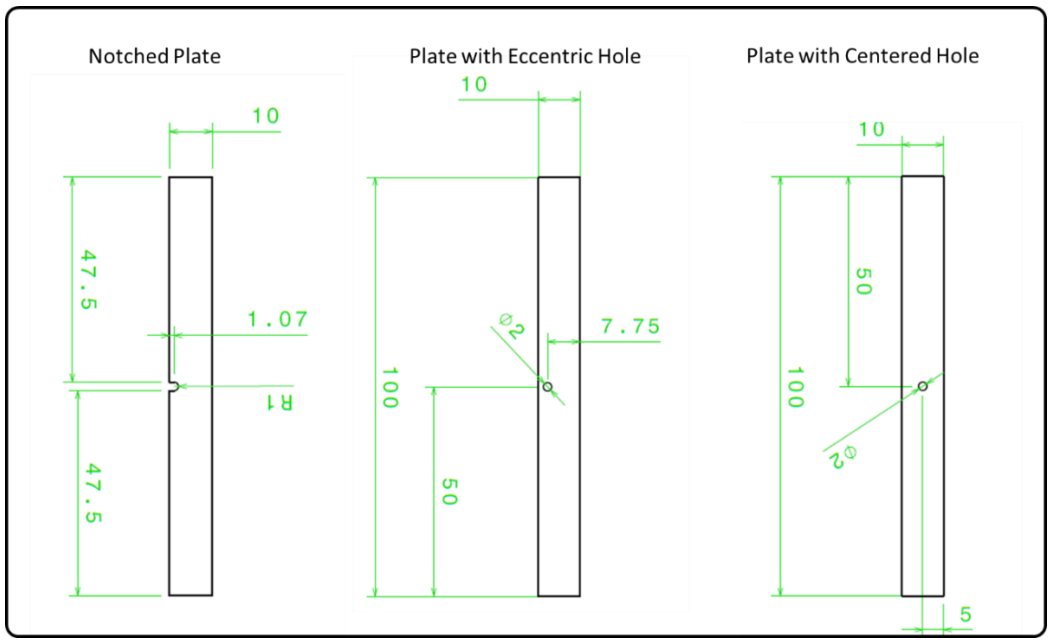

Figure 2.15: Plate actuator geometries; centered hole, eccentric hole, and notched plate (from L to R). Hole dimensions remained constant while position was shift from center (lowest stress concentration) to the edge (highest).

The specimen geometries were selected to satisfy several requirements and constraints: actuation fatigue behavior representative of bulk actuators, material availability, and feasibility of experimental design. In order to obtain an actuation fatigue response which was representative of a bulk actuator undergoing continuous use, dogbone and plate actuators of thicknesses exceeding 0.25mm were utilized. Previous work conducted by Bertacchini *et al*. found that, for certain heat treatment procedures,

specimens with thicknesses below this threshold exhibited a reduction in fatigue life [56]. While wire actuators are generally cheaper and easier to test, they were not considered for this study due to their propensity to develop long, circumferential surface cracks. While cracks in dogbone actuators tend to be short and randomly distributed throughout the actuator [35], the surface crack length were found to exceed the diameter by Bertacchini [56]. Additionally, microstructural damage was found throughout the NiTiHf dogbones tested in this work, while, in literature, non-fatal cracks are frequently limited to regions around the surface/oxide layer in wires.

2.3.2 Heat Treatment Procedures

All actuator test specimens were electro-discharge machined (EDM); the equiatomic NiTi and Nickel-rich $Ni_{60}Ti_{40}$ were cut from sheets while the NiTiHf specimens were cut from extruded rods approximately 20mm in diameter. Equiatomic NiTi sheets, which were 25% cold worked, were heat treated between 350 and 400°C then water quenched prior to being cut via EDM. The $Ni_{60}Ti_{40}$ and NiTiHf actuators were first cut then underwent a solutionizing step (above 850°C) and a heat treatment to develop precipitates. The heat treatment and solutionizing steps were chosen based on previous studies [36,41,68]: 450°C for 20 hours followed by a water quench for the Nickel-rich NiTi, and 550°C for 3 hours followed by a water quench for the NiTiHf.

2.3.3 Speckle Patterning and DIC Preparation

In order to use digital image correlation (DIC) techniques simultaneously with infrared thermography, two high contrast/low glare paints were obtained with approximately identical thermal emissivity. Additionally, these paints needed to survive

50,000 thermal (40-350°C) and actuation cycles. Due to these requirements, black engine block paint was utilized along with a flat white primer. They were found to have thermal emissivites of 0.88 ± 0.01 and 0.88 ± 0.025, respectively and, the black engine block paint, showed no degradation when subjected to thermal cycles under 400°C. For low temperature tests, the white paint was generally used as a base layer and for high temperature tests the black paint was always used as a base layer due to its increased resistance to high temperatures. An example speckle pattern can be seen in Figure 2.16 and a DIC result obtained from commercial software (VIC-2D/VIC-3D) can be seen in Figure 2.17.

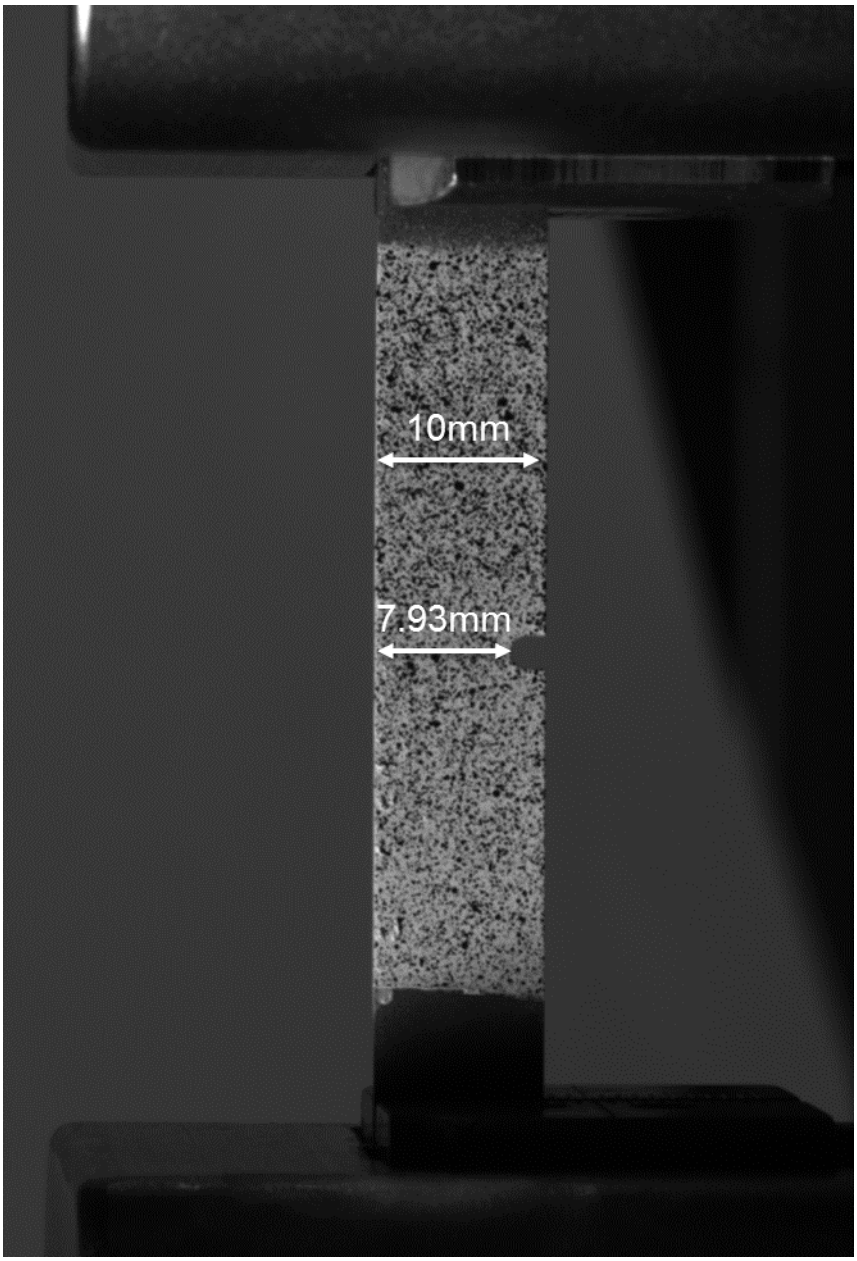

Figure 2.16: Plate actuator with DIC speckle pattern shown in an MTS test frame.

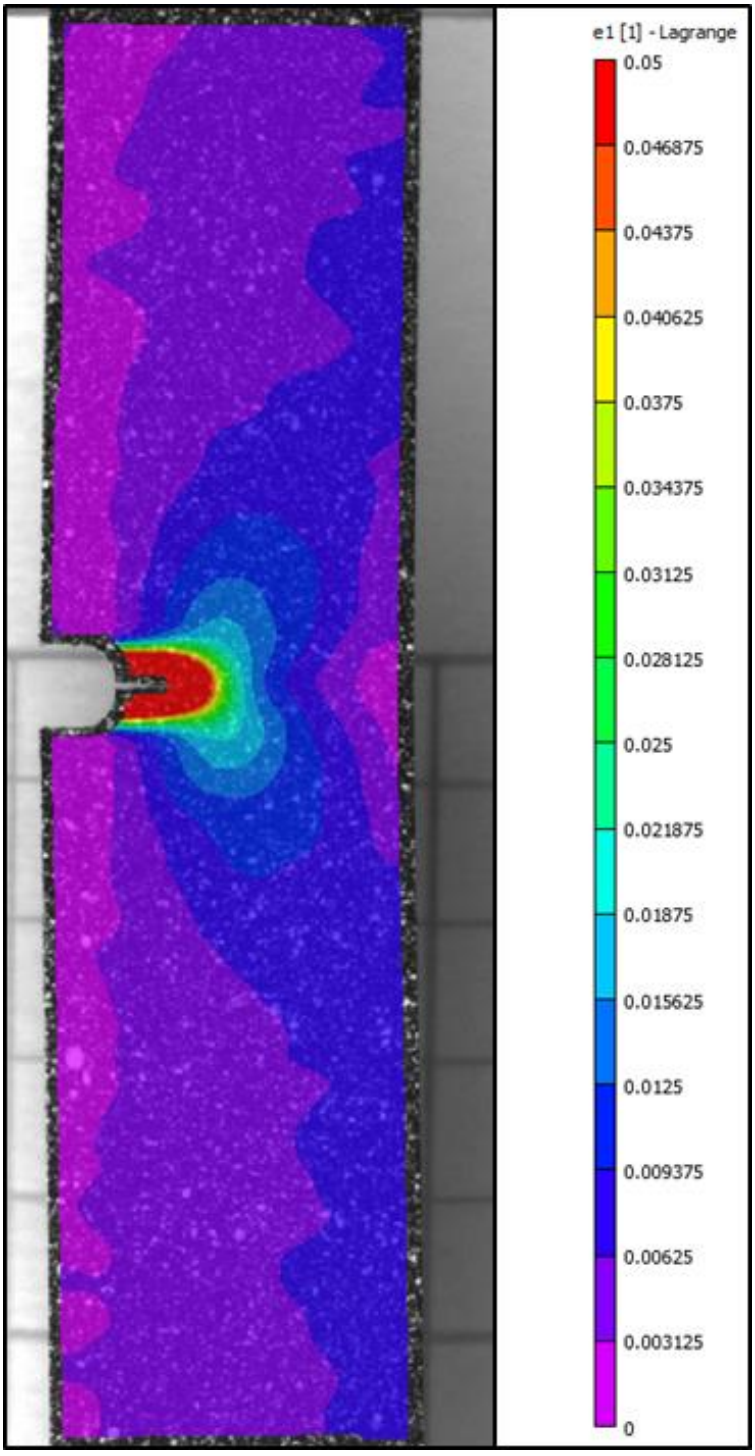

Figure 2.17: DIC result from fatigue test of notched plate actuator; final martensite strain field shown just prior to failure.

2.4 Experimental Testing Overview

In order to accomplish the goals discussed in the first chapter, the actuation fatigue response of five different systems were studied: equiatomic NiTi with two different heat treatments, Nickel-rich NiTi ($Ni_{60}Ti_{40}$), low purity $Ni_{50.3}Ti_{29.7}Hf_{20}$ (NiTiHf 200 series), and high purity $Ni_{50.3}Ti_{29.7}Hf_{20}$ (NiTiHf 500 series)[2]. Due to the high critical temperatures, resistance to TRIP, total work output, and number of potential aerospace applications of the chosen NiTiHf composition, this material will be the focus of this study. However, equiatomic NiTi (not precipitated) and $Ni_{60}Ti_{40}$ (precipitated) were studied due to the availability of data, material, and difference in fatigue response.

Most of the experimental work performed for this study was focused on uniaxial actuation fatigue tests of dogbone specimens. Isobaric tests with full transformation were run until ultimate failure for all material systems in order to calibrate the fatigue life prediction methods. Multiple stress levels were selected for these isobaric calibration tests in order to determine all of the necessary material parameters as well as understand the operational limits of these materials.

Since many of the engineering applications for SMA/HTSMA actuators subject their components to variable loading paths or stress concentrations, two additional loading paths, linear and stepwise, and three plate actuator geometries were also studied. All loading paths considered are shown schematically in Figure 2.7, and the plate geometries can be seen in Figure 2.17. Table 2-1 contains a summary of the data collected for this

[2] Numbers correspond to atomic weight percentage for $Ni_{60}Ti_{40}$ and atomic percentage for $Ni_{50.3}Ti_{29.7}Hf_{20}$. The Nickel-rich NiTi is 55.022% Nickel and 44.978% Titanium by atomic percentage.

study. Each of the material systems was calibrated with isobaric testing and the fatigue lifetime prediction methods were validated with either variable loading or variable geometry tests. In total, five material systems were studied: two heat treatments of equiatomic NiTi, Nickel-rich NiTi, and low and high purity NiTiHf.

Table 2-1: Summary of Data Collection

	Equiatomic NiTi	*$Ni_{60}Ti_{40}$*	*NiTiHf*
Calibration	Isobaric	Isobaric	Isobaric
Validation	Linear	Variable Geom.	Linear & Stepwise

3 ACTUATION FATIGUE CHARACTERIZATION AND DATABASE OF NICKEL-TITANIUM SMAS*+

In this chapter, the experimental results from each of the low temperature material systems studied is presented, analyzed, and discussed. The calibrations for each of the material systems was completed utilizing the phenomenological SMA model presented in Lagoudas *et al.* [1] and the TRIP parameters were determined per Entchev *et al.* [64,65].

3.1 Equiatomic Nickel-Titanium

The purpose of this first test matrix was to determine the effect of heat treatments on the fatigue response of equiatomic Nickel-Titanium (NiTi) actuators and to characterize the variation in the fatigue responses. The results from the first phase of this effort were presented at the ASME conference: Smart Materials, Adaptive Structures and Intelligent Systems (SMASIS) [40]. Due to the large amount of TRIP observed in the equiatomic NiTi actuation fatigue tests, results are reported in extension (change in length normalized by original length). Equations 2.1-2.4 were used to determine the extensions reported in the following experimental results.

---

* Part of the data reported in Chapter Three, Section One is reprinted with permission from Characterization and modeling of thermo-mechanical fatigue in equiatomic NiTi actuators by Wheeler RW, Hartl DJ, Chemisky Y, Lagoudas DC, 2014. Vol. 2 Mech. Behav. Act. Mater. Integr. Syst. Des. Implementation; Bioinspired Smart Mater. Syst. Energy Harvest., Copyright 2014 by ASME.

+ Part of the data reported in Chapter Three, Section Two is reprinted with permission from Actuator lifetime predictions for Ni60Ti40 shape memory alloy plate actuators by Wheeler RW, Ottmers C, Hewling B, Lagoudas DC, 2016. International Society for Optics and Photonics, Copyright 2016 by Society of Photo Optical Instrumentation Engineers.

3.1.1 Test Matrices for Equiatomic NiTi Study

All equiatomic NiTi dogbones were 25% coldworked into sheets of 0.25 and 0.5mm thickness (±0.03mm); specimens were cut via EDM post heat treatment. Since thermal processing is known to have major effects on actuation fatigue responses of NiTi [66], a test matrix consisting of temperatures ranging from 350°C to 400°C and aging times between one and three hours was utilized, as shown in Table 3-1. The heat treatment times and temperatures were based on previous work and literature which indicated that the actuation fatigue properties, specifically resistance to TRIP and actuation strain, could be modified by relieving the residual stresses resulting from coldwork [71-73]. Temperatures were kept below the recrystallization temperature of 500°C [71]. Each data point consisted of six independent fatigue tests: two 0.25mm thick specimens, two 0.5mm thick specimens, and two linearly loaded specimens. Multiple thicknesses were studied in order to ascertain whether there would be a size effect for smaller actuators.

Specimen nomenclature is listed for each test. Past experience had indicated equiatomic NiTi which had been heat treated at 375°C for 2 hours produced promising actuators. Therefore, the test matrix was centered on this value.

Table 3-1: Test Matrix for Equiatomic NiTi Scoping Study

HEAT TREATMENT	*1 HOUR*	*2 HOURS*	*3 HOURS*
350°C (A)		A21, A22, A25, A26, A27, A28	A31, A32, A35, A36, A37, A38

Table 3-1: Continued

HEAT TREATMENT	*1 HOUR*	*2 HOURS*	*3 HOURS*
365°C (B)		B21, B22, B23 B25, B26	
375°C (C)	C11, C12, C15, C16, C17, C18	C21, C22, C25, C26, C27, C28	C31, C32, C35, C36, C37, C38
400°C (E)	E11, E12, E15, E16, E17, E18	E21, E22, E23, E24 E25, E26, E27, E28	

The first two tests for each data point (xx1, xx2) were thin and loaded with a constant weight. The middle two tests (xx5, xx6) were thick and loaded with a constant weight. The last two tests (xx7, xx8) were loaded with a spring array[3]. These final tests were mixed between thick and thin specimens since they were added to the test matrix after it was determined that there was no detectable size effect between the fatigue response of the .25mm and .5mm thick specimens. It should also be noted that heat treatments with temperatures of 365°C or 385°C were not repeated with spring loading since it was determined they did not produce unique results.

The stress levels selected for this study were 200MPa for isobaric tests and approximately 150-250MPa for variable loading tests. The isobaric load was selected as it is a commonly used working stress for NiTi actuators, while the spring loading was

[3] Note: Additional tests (xx3, xx4) were necessary for the calibration of visual extensometry methods. These tests were in agreement with the rest of the test matrix.

selected such that the average load would be the same and each actuation cycle would be approximately energetically equivalent between the isobaric and linear tests.

3.1.2 Experimental Results: Scoping Study

The experimental results for this phase of the study are split into two sections: the initial characterization where nine heat treatments were tested and a more in-depth study of selected heat treatments. A summary of the results from Table 3-1 are presented in this section and organized according to their heat treatment. Further analysis of trends and comparisons between heat treatments can be found in Section 3.1.3.

350°C for 2 hours (A2x)

Specimens with the lowest heat treatment exhibited the most brittle response. They were characterized by low strains and slow irrecoverable strain generation. All tests exhibited discontinuities or jumps in the irrecoverable strain, most likely resulting from crack formation and propagation. An example of the fatigue strain evolution can be seen in Figure 3.1.

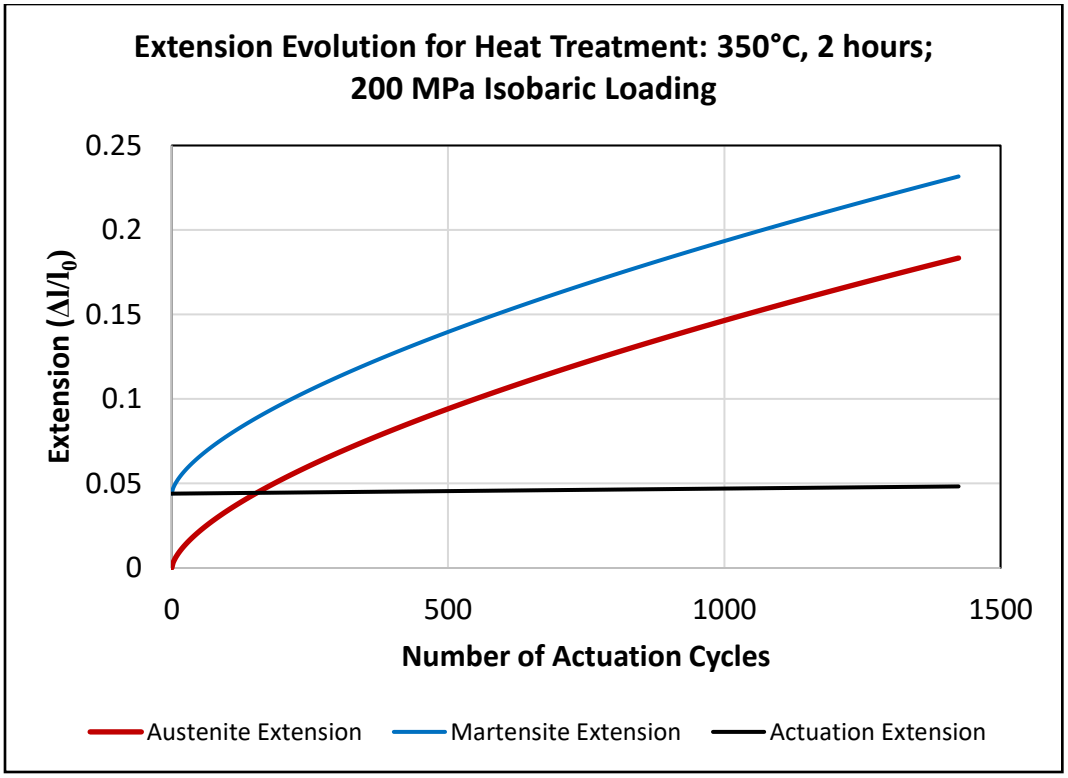

Figure 3.1: Strain evolution for specimen A22; 200 MPa isobaric loading.

Specimens with the 350°C, 2 hours heat treatment also showed significant fatigue improvements when loaded with a spring array, as shown in Figure 3.2. Irrecoverable strain generation was significantly slower and the final irrecoverable strain was marginally[4] lower. Their failure mechanisms were also consistent as they fell victim to seemingly random crack formation and propagation until failure around 17-18% irrecoverable strain. No localized strain was observed for this heat treatment.

[4] Between 0.5% and 3% (normalized)

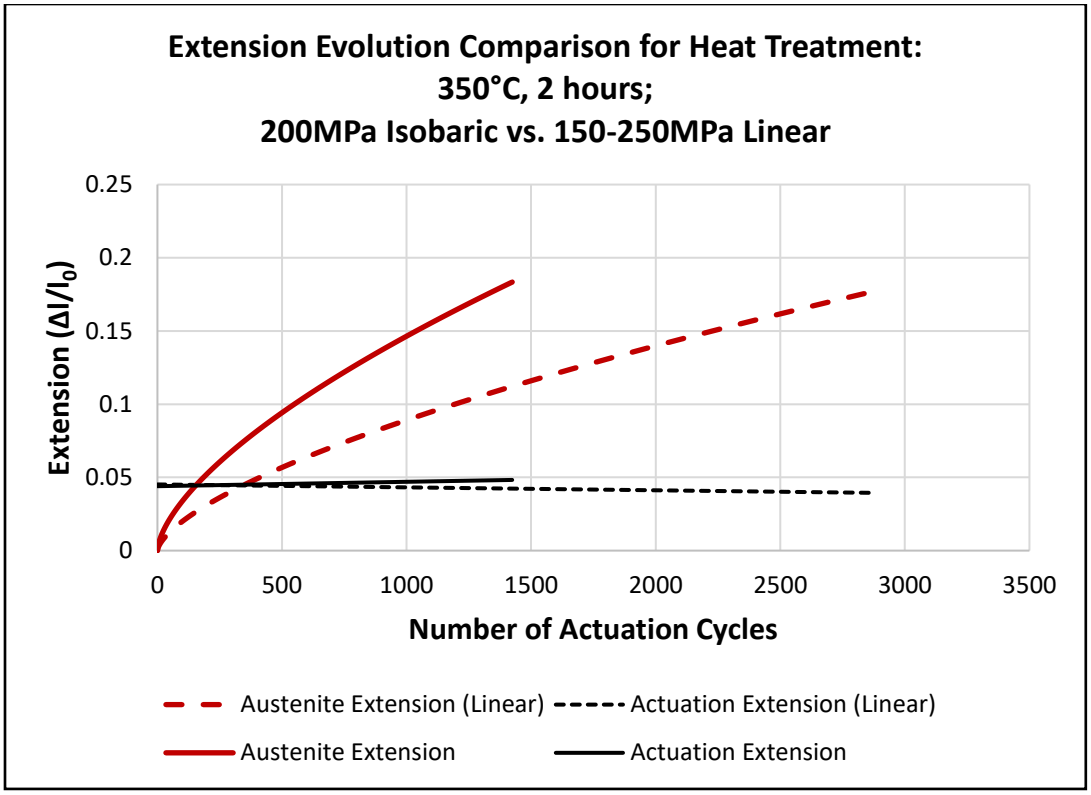

Figure 3.2: Strain evolution for specimen A22 compared with A27; 200 MPa isobaric loading compared with 150-250MPa linearly varying loading.

350°C for 3 hours (A3x)

Specimens with the A3 heat treatment (350°C, 3 hours) exhibited a relatively brittle response similar to that of A2. They were characterized by low strains and slow irrecoverable strain generation. The fatigue life also improved slightly compared with the A2 heat treatment, however the irrecoverable strain or TRIP evolution was less stable. This can be seen in Figure 3.3, where the strain evolution is shown for A31.

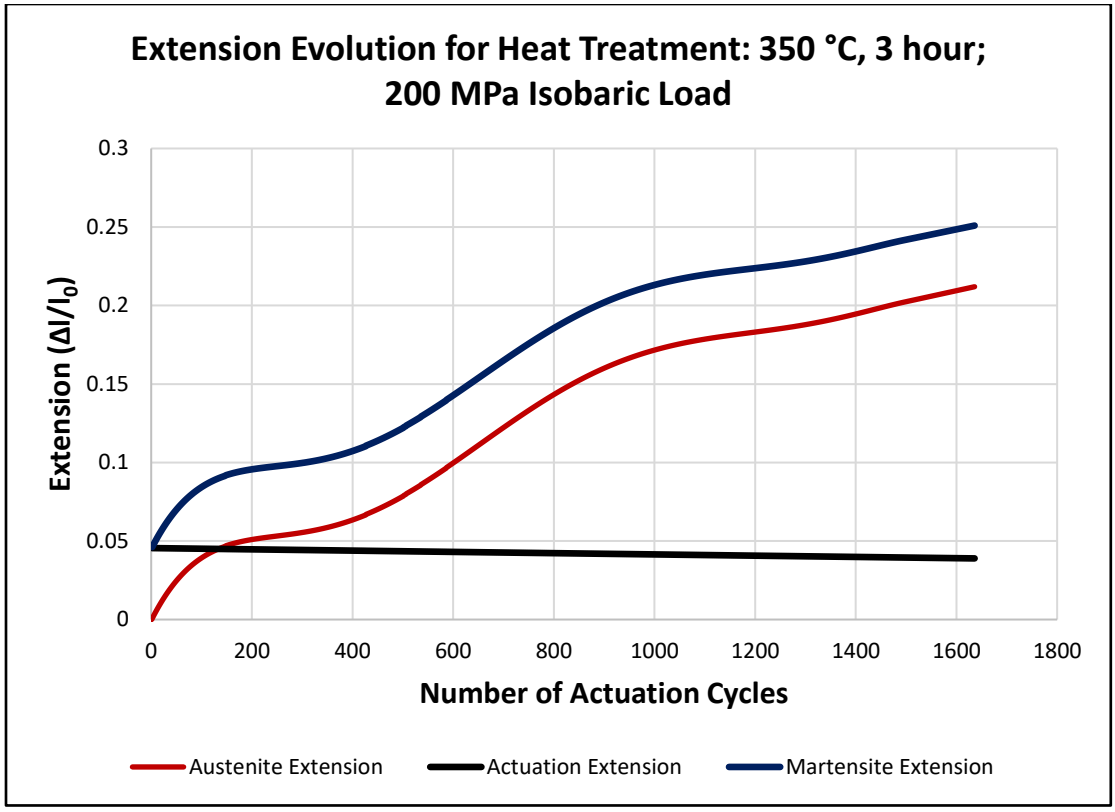

Figure 3.3: Strain evolution for specimen A31; 200 MPa isobaric loading.

Dogbone actuators with the A3 heat treatment showed even more significant fatigue improvements, in terms of TRIP development, when loaded with a spring array, as shown in Figure 3.4. Their failure mechanisms were also consistent as they fell victim to seemingly random crack formation and propagation until failure around 18-22% irrecoverable strain. The main observable difference between the A2 and A3 heat treatments was the actuators loaded with spring arrays developed significantly higher strains towards the end of their fatigue life.

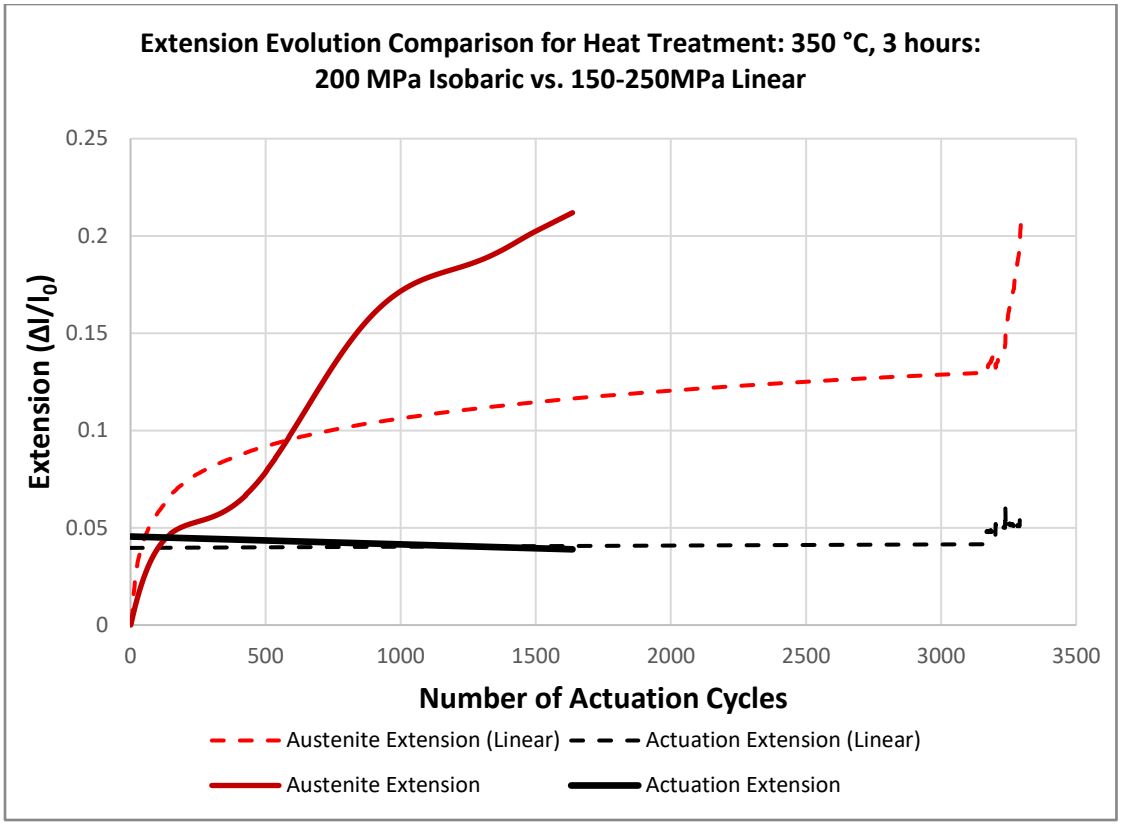

Figure 3.4: Strain evolution for specimen A22 compared with A27; 200 MPa isobaric loading compared with 150-250MPa linearly varying loading.

365°C for 2 hours (B2x)

Specimens with the B2 heat treatment exhibited a fatigue life similar to actuators with the 350°C heat treatment temperatures; however, the strain evolution was noticeably smoother. They were characterized by low overall strains and slow irrecoverable strain generation. A representative strain evolution can be seen in Figure 3.5.

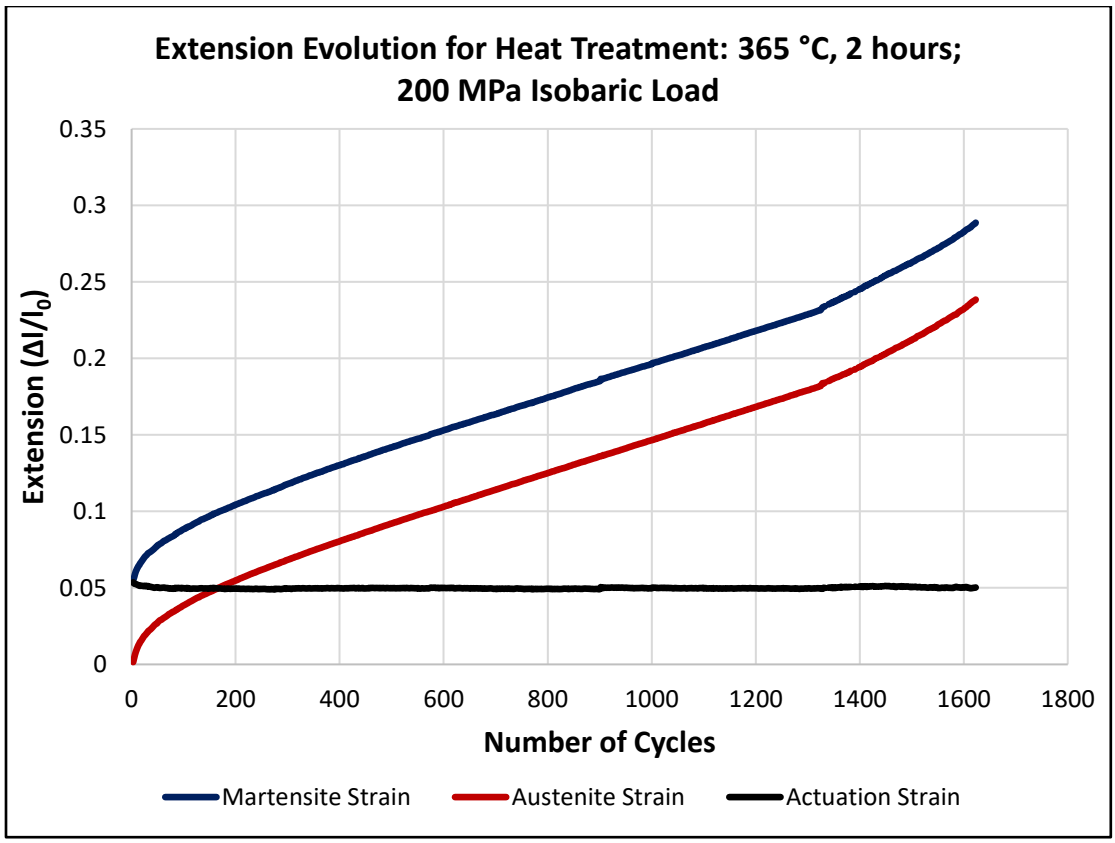

Figure 3.5: Strain evolution for specimen B23; 200 MPa isobaric loading.

While no visible necking occurred in the specimens with the B2 heat treatment, the visual extensometry data for specimen B23, shown in Figure 3.6, indicates that a moderate amount of TRIP localization occurred. Interestingly, this pattern was not detectable when analyzing the transformation strain, which continued to be evenly distributed throughout the test.

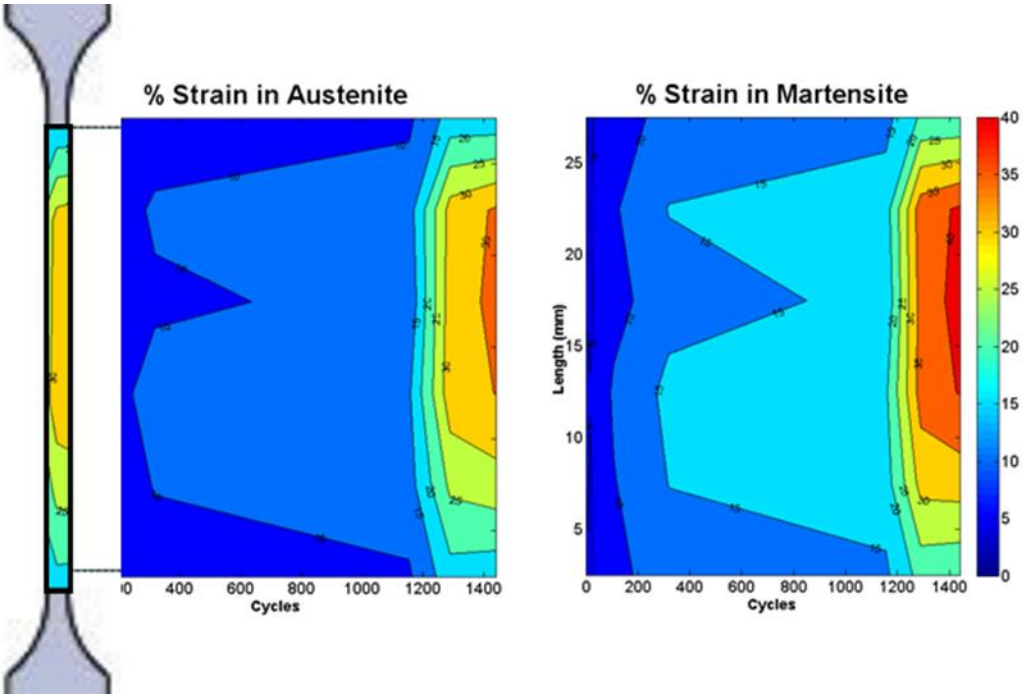

Figure 3.6: Visual extensometry data for specimen B23; 200 MPa isobaric loading.*

375°C for 1 hour (C1x)

Specimens with the C1 heat treatment exhibited a ductile response. They were characterized by large strains and relatively slow irrecoverable strain generation for ductile specimens. All tests exhibited a shape similar to that of a third order polynomial: increasing irrecoverable strain at a decreasing rate (the training phase), a short region which contained an inflection point and relatively stable strain growth (normal or stable fatigue response), and, finally, a region which exhibited increases in irrecoverable

* Figure 3.6 is reprinted with permission from Effect of processing and loading on equiatomic NiTi fatigue life and localized failure mechanisms by Wheeler RW, Santa-Cruz J, Hartl DJ, Lagoudas DC, 2013. Vol. 2 Mech. Behav. Act. Mater. Integr. Syst. Des. Implementation; Bioinspired Smart Mater. Syst. Energy Harvest., Copyright 2013 by ASME.

(austenite) strain at an increasing rate (a degradation or failure phase) near the end of the specimen's life. This was the lowest heat treatment to exhibit this dimensional instability. A representative engineering strain evolution plot can be seen in Figure 3.7.

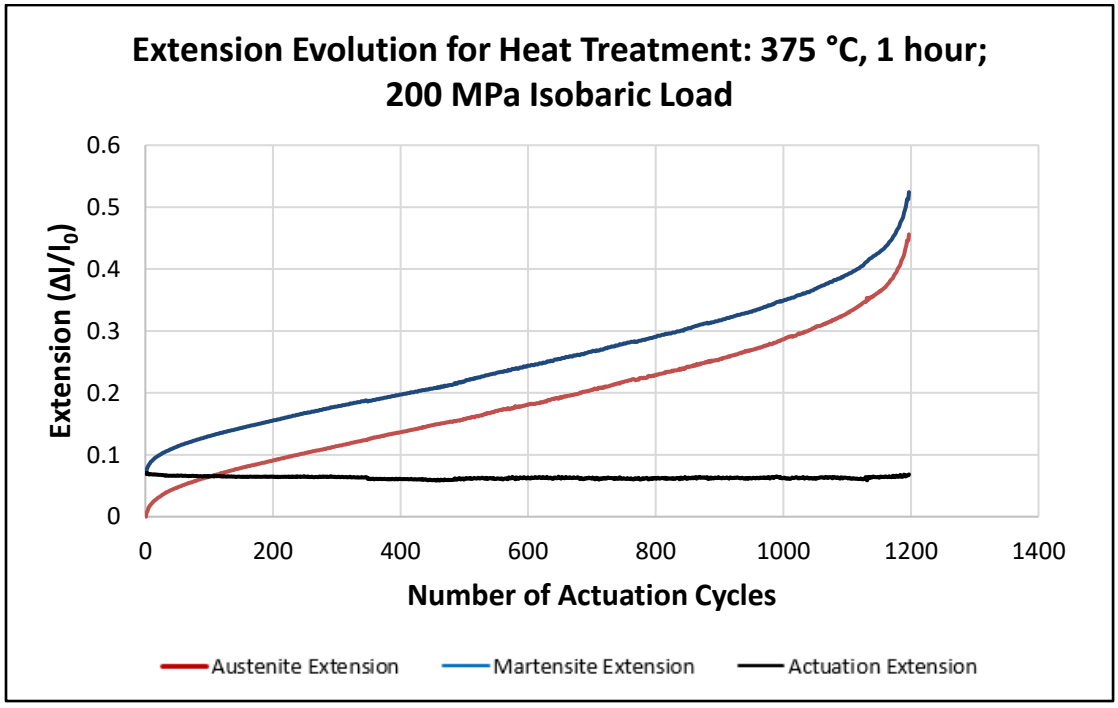

Figure 3.7: Engineering strain evolution for specimen C16; 200 MPa isobaric loading.

The fatigue responses observed for specimens with C1 heat treatment were highly dependent on the loading path. Specimens with a constant weight exhibited an unstable response while those loaded with a spring array appeared significantly more stable, more closely resembling specimens with a lower heat treatment. Due to this difference in response, the irrecoverable strains were significantly lower (20-30%) at failure, as is

evident in Figure 3.8. This severe difference in fatigue response was observed for each of the six tests completed for this heat treatment.

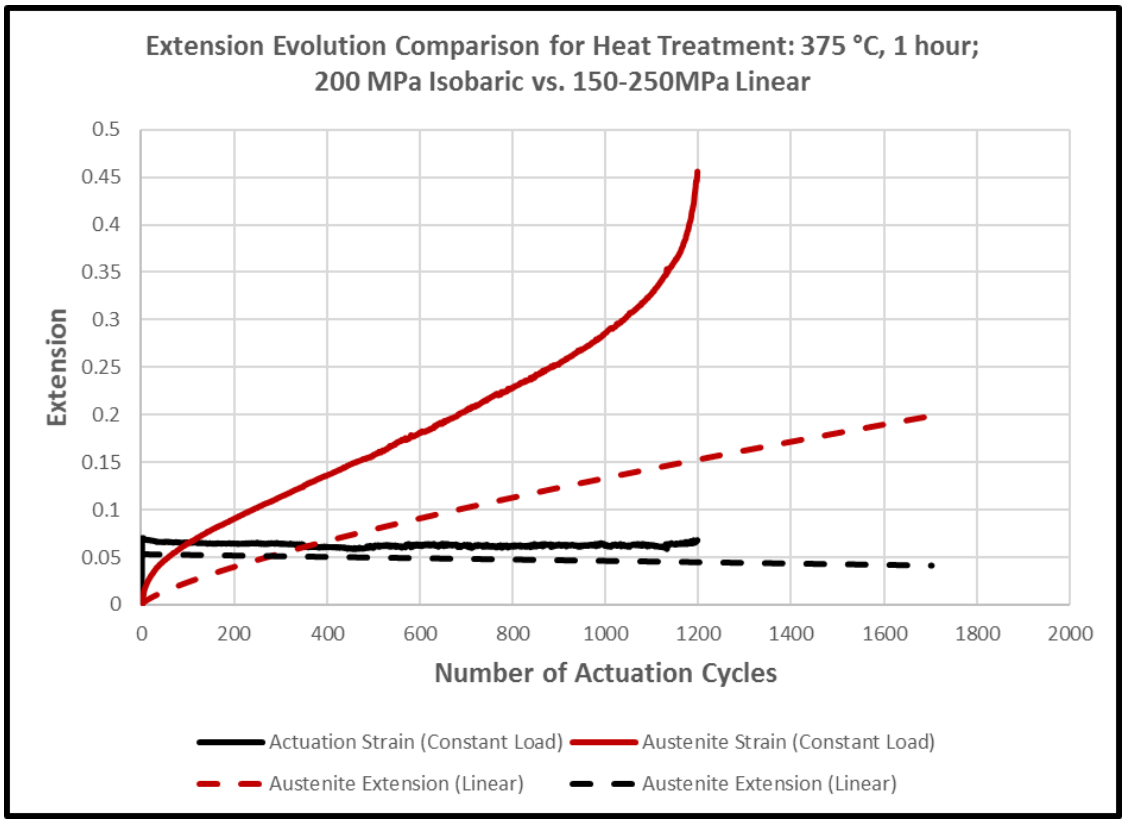

Figure 3.8: Strain evolution for specimen C16 compared with C; 200 MPa isobaric loading compared with 150-250MPa linearly varying loading.

375°C for 2 hours (C2x)

Specimens with the C2 heat treatment exhibited the most promising response, from a fatigue life perspective. They were characterized by moderate final strains and slow irrecoverable strain generation, thus giving rise to the longest fatigue life. They did not exhibit significant changes in slope of the irrecoverable strain post training, which is

indicative of a dimensionally stable response. A representative engineering strain evolution is shown in Figure 3.9.

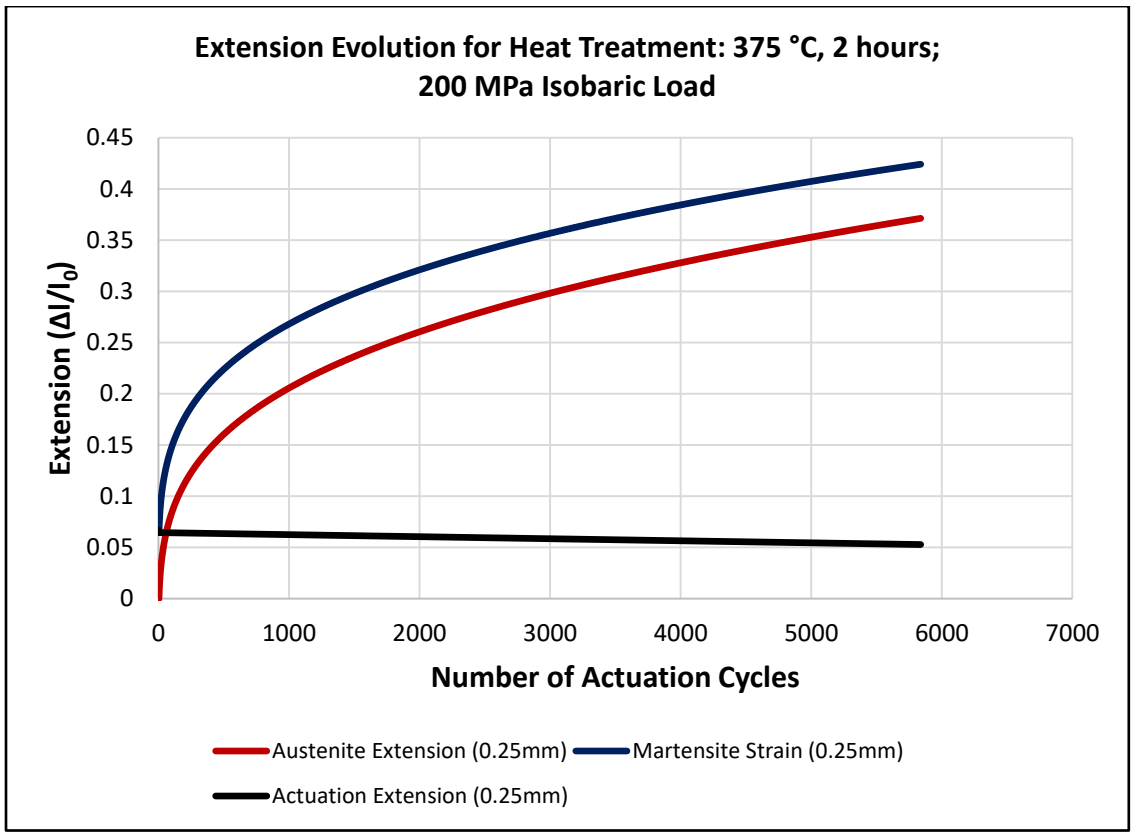

Figure 3.9: Engineering strain evolution for specimen C21; 200 MPa isobaric loading.

As expected, actuators with the C2 heat treatment showed a fatigue life improvement when loaded with a spring array, as shown in Figure 3.10. Irrecoverable strain generation was moderately slower and the final irrecoverable strain was marginally lower (2-5%) for all tests.

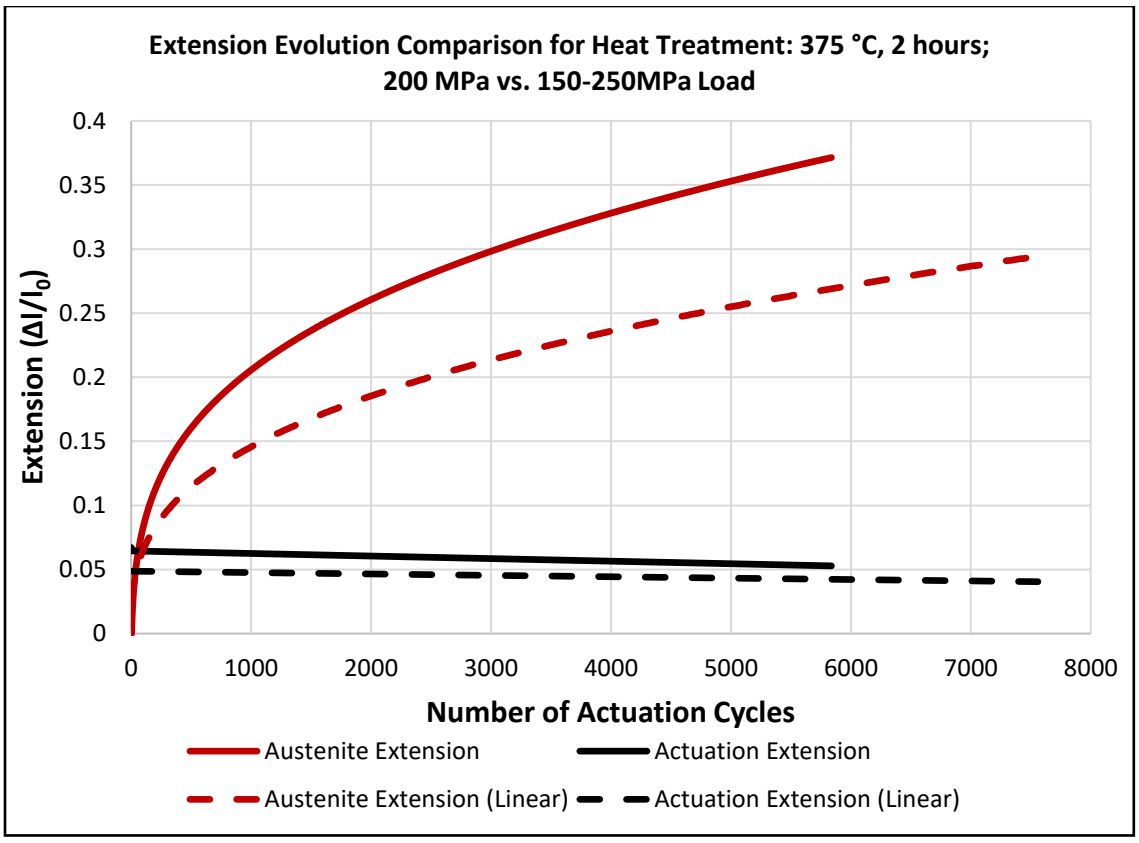

Figure 3.10: Strain evolution for specimen C21 compared with C27; 200 MPa isobaric loading compared with 150-250MPa linearly varying loading.

375°C for 2 hours (C3x)

Specimens with the C3 heat treatment exhibited a more ductile response than C1 and C2. They were characterized by large strains and fast irrecoverable strain generation. All tests exhibited inflection points in the irrecoverable strain generation rate, indicative of a quickly degrading fatigue response. This is observable in Figure 3.11 between cycle 300 and 400.

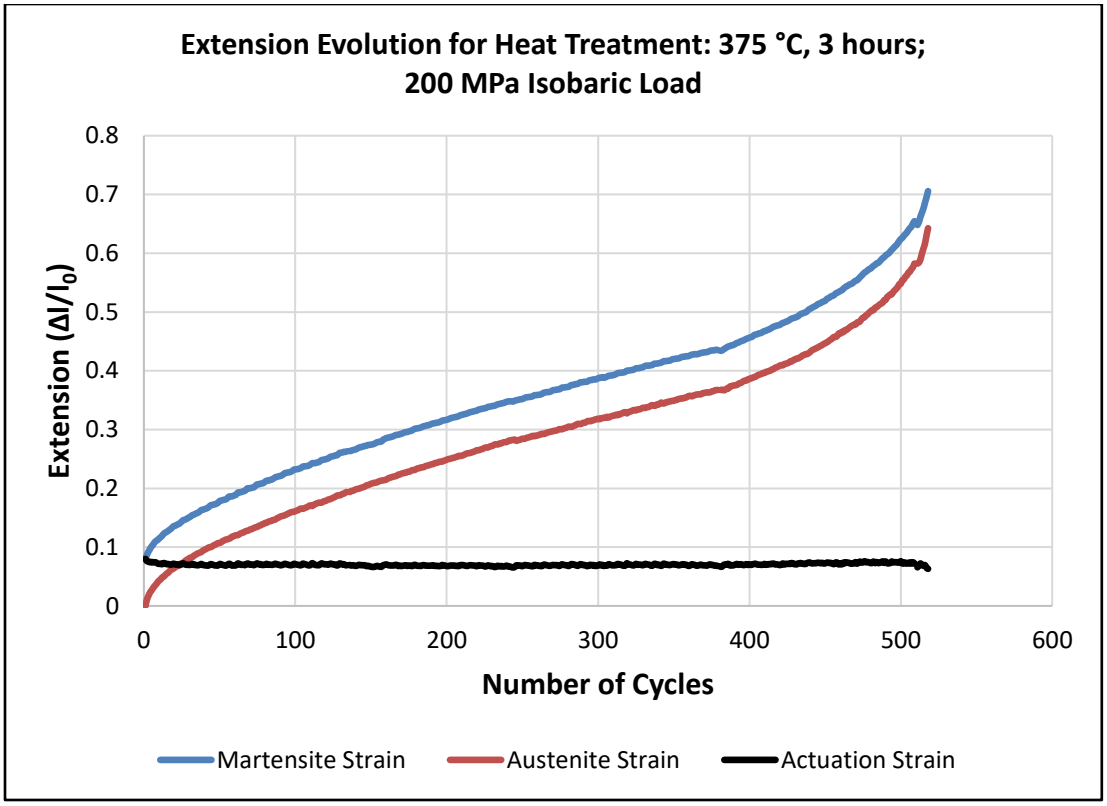

Figure 3.11: Engineering strain evolution for specimen C31; 200 MPa isobaric loading.

Specimens with the C3 heat treatment showed significant fatigue improvements when loaded with a spring array. Irrecoverable strain generation was significantly slower and the final irrecoverable strain, as a result, was significantly (15-18%) lower. This improved actuation fatigue response can be seen in Figure 3.12.

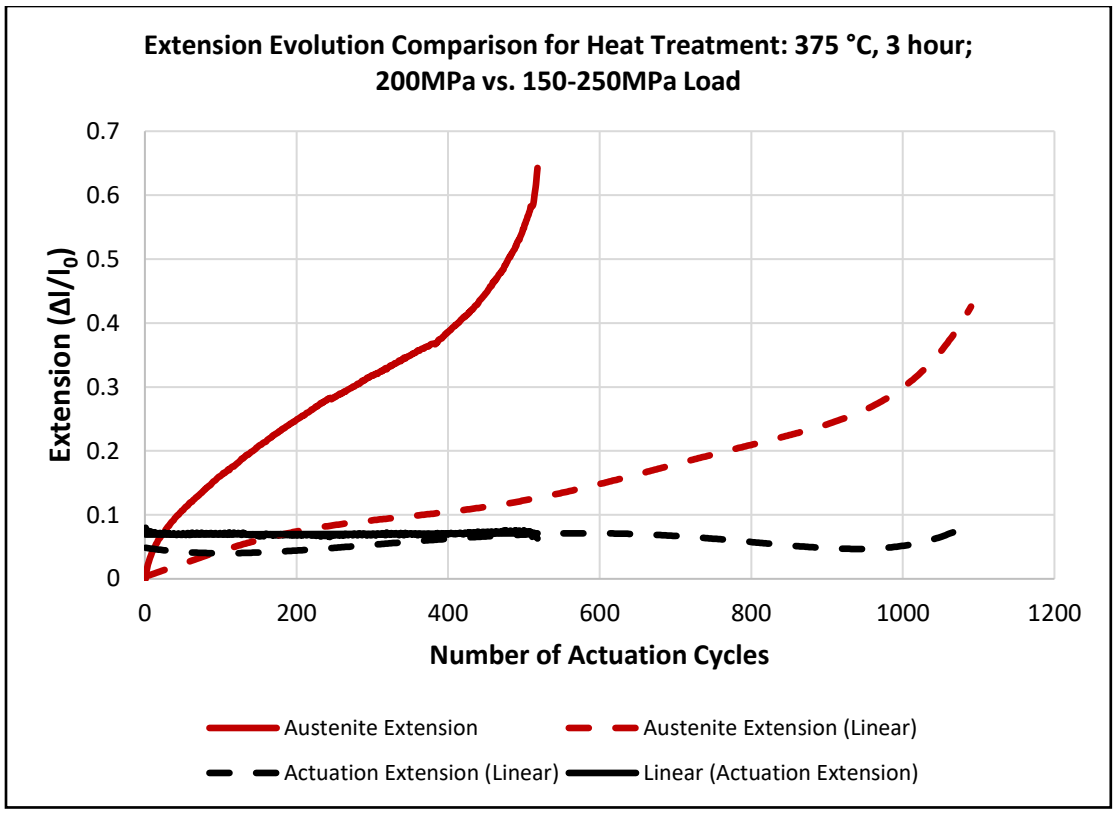

Figure 3.12: Engineering strain evolution for specimen C31 compared with C38; 200 MPa isobaric loading compared with 150-250MPa linearly varying loading.

385°C for 2 hours (D2x)

Specimens with the D2 heat treatment exhibited a fatigue response similar to that of C3, but with a longer fatigue life. They were characterized by large strains and fast irrecoverable strain generation. All tests exhibited relatively smooth irrecoverable strain generations; however, the rates were large enough to prevent a useful fatigue response, when considering most actuator applications, as shown in Figure 3.13.

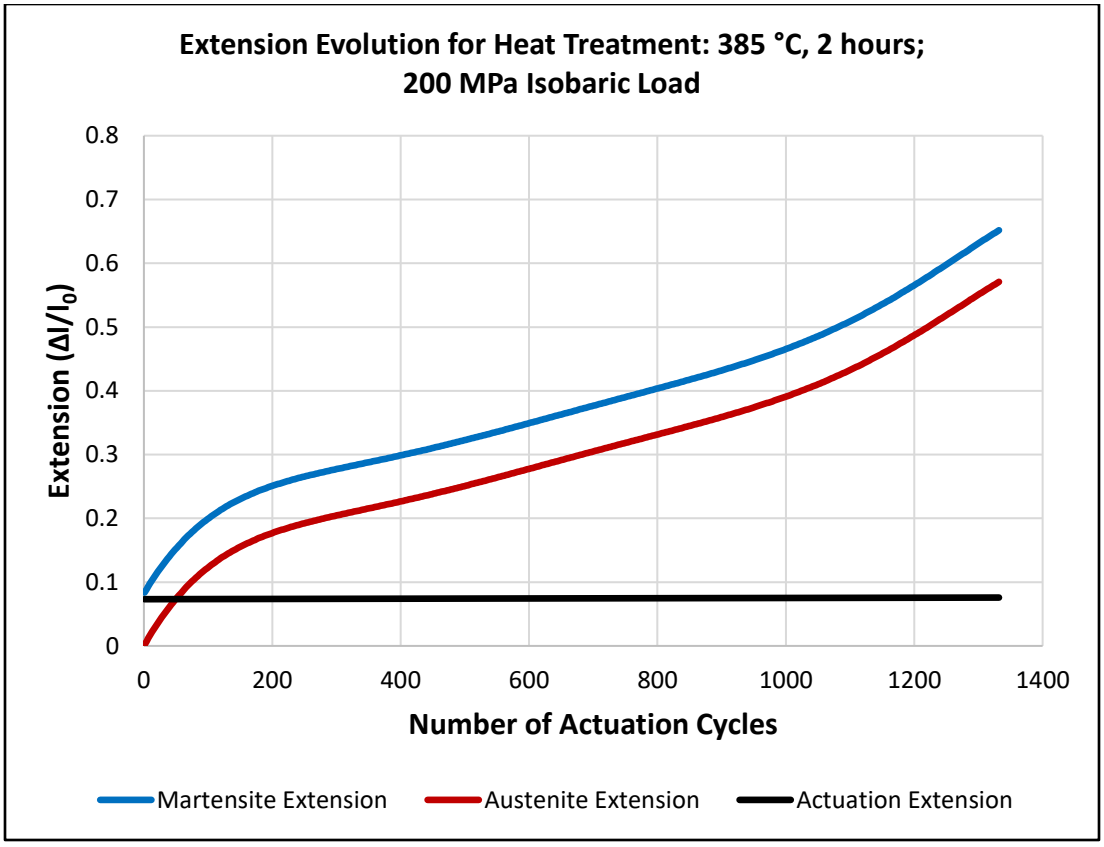

Figure 3.13: Engineering strain evolution for specimen D22; 200 MPa isobaric loading.

400°C for 1 hours (E1x)

Dogbones with the E1 heat treatment exhibited a very ductile response. They were characterized by extremely large strains and fast irrecoverable strain generation. All tests exhibited a smooth strain generation with an inflection point near the midway point in the fatigue test. This type of fatigue response can be observed in Figure 3.14.

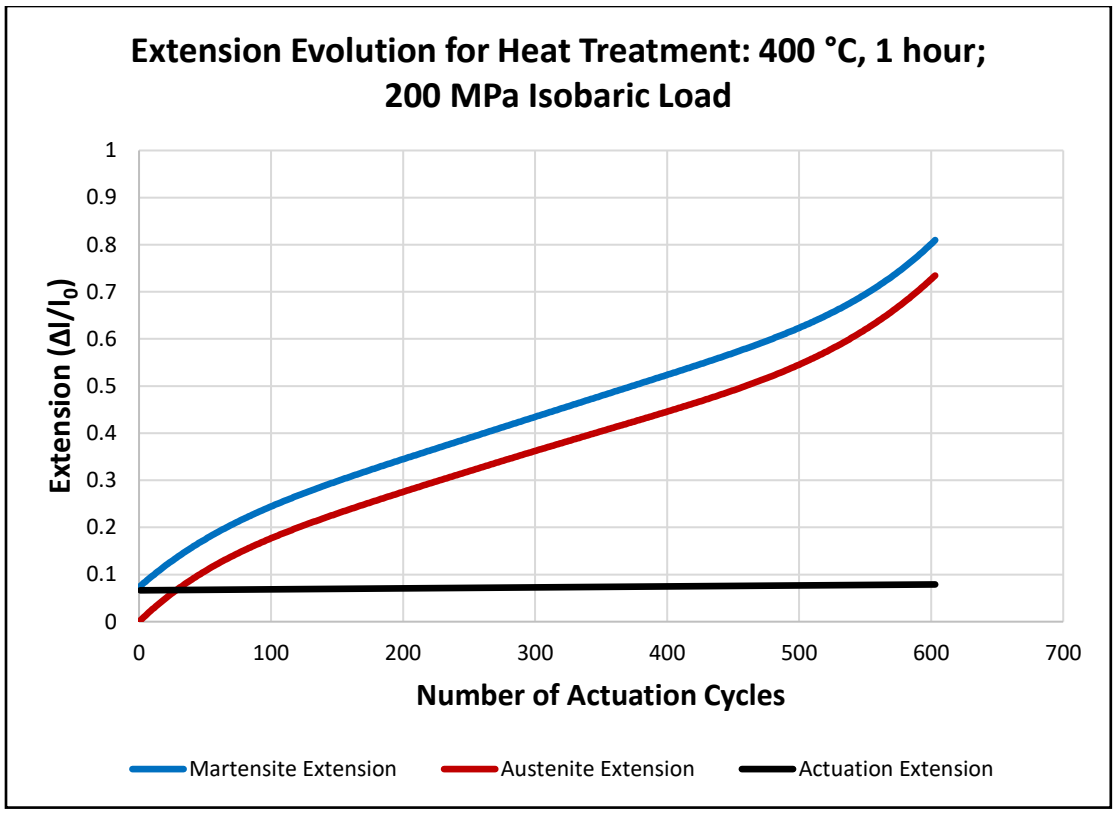

Figure 3.14: Engineering strain evolution for specimen E11; 200 MPa isobaric loading.

When loaded with a spring array, specimens with the E1 heat treatment showed small fatigue improvements. Irrecoverable strain generation was slightly slower and the final irrecoverable strain was marginally lower. Their failure mechanisms were also consistent as they fell victim to necking towards the end of their fatigue lives. This minor improvement can be seen in Figure 3.15.

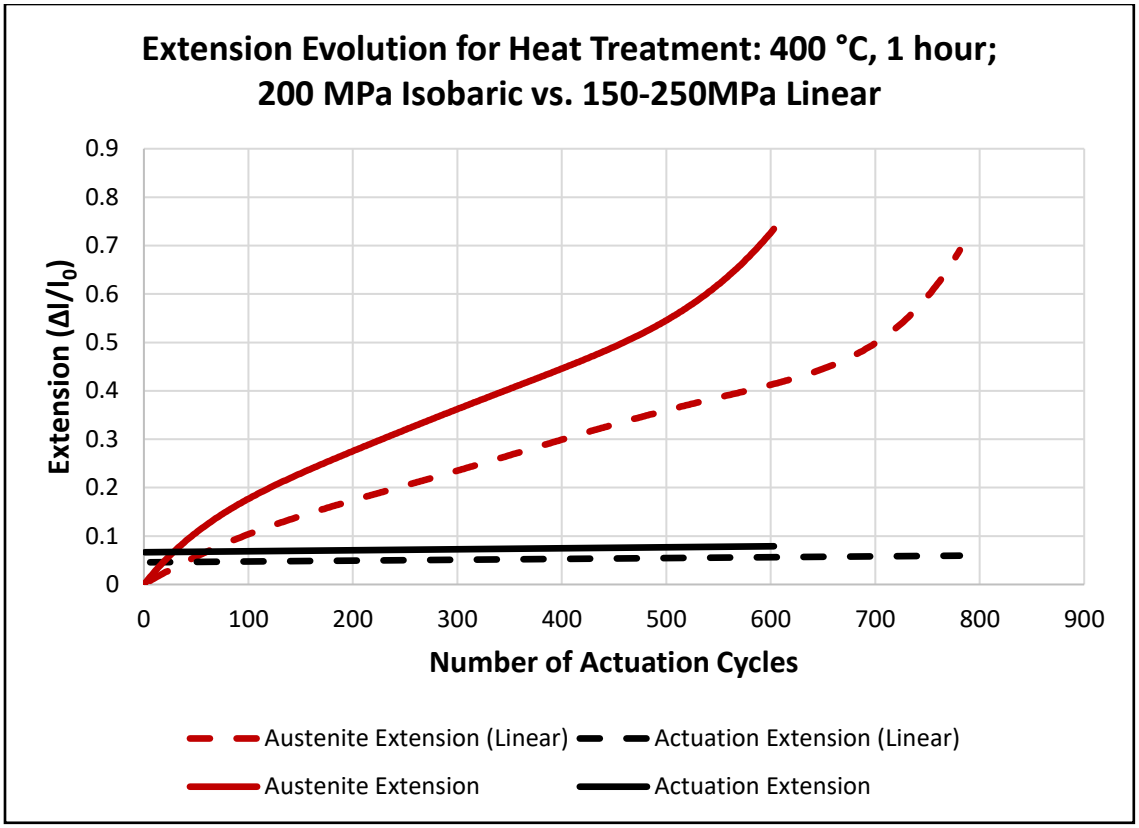

Figure 3.15: Engineering strain evolution for specimen C31 compared with C38; 200 MPa isobaric loading compared with 150-250MPa linearly varying loading.

400°C for 2 hours (E2x)

Specimens with the highest heat treatment exhibited the most ductile response. They were characterized by very large strains and fast irrecoverable strain generation. The actuation strains were also unstable for all tests. Due to the high irrecoverable strain generation per cycle (1-1.5%), the actuation strains were inflated since the actuation strain is defined as the difference between the austenite strain and the following martensite strain. From Figure 3.16, it is clear that actuators produced by this heat treatment are not promising for applications requiring large actuation forces.

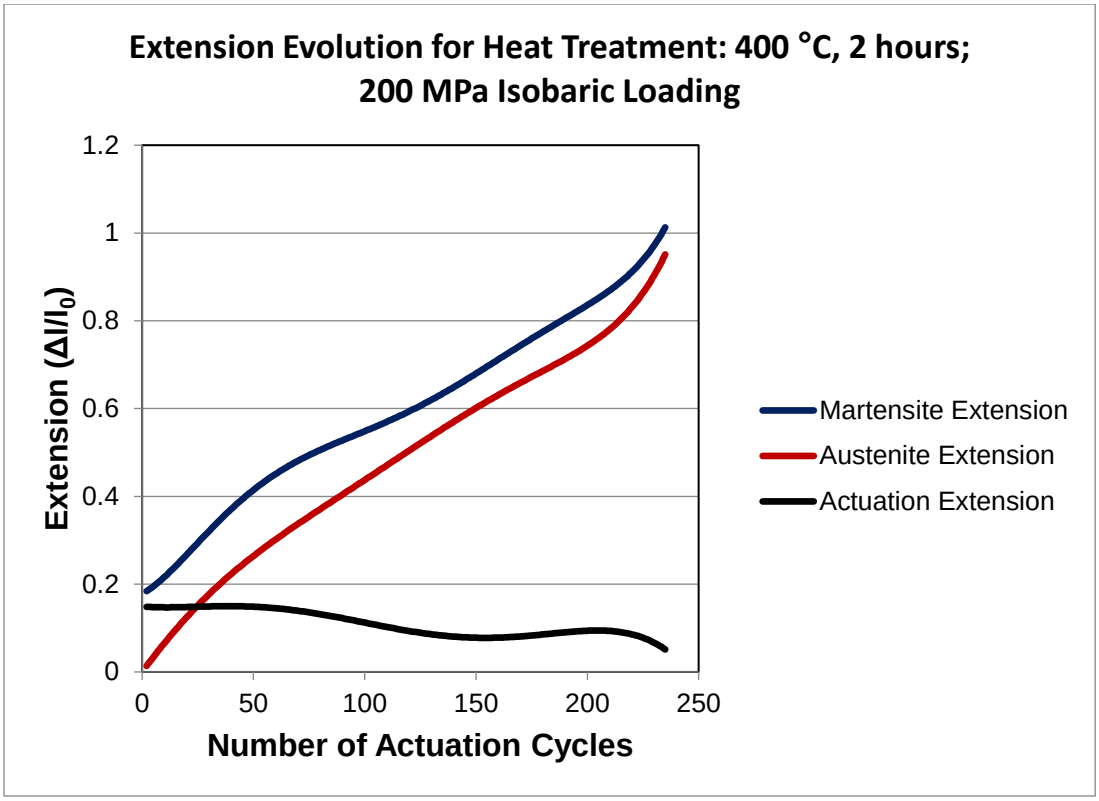

Figure 3.16: Engineering strain evolution for specimen E22; 200 MPa isobaric loading.

As expected, specimens with the E2 heat treatment showed small fatigue improvements when loaded with a spring array, as shown in Figure 3.17. Irrecoverable strain generation was slightly slower and the final irrecoverable strain was nearly equivalent. Their failure mechanisms were also consistent as they fell victim to necking towards the end of their fatigue lives. The rate of irrecoverable strain generation near the end of the fatigue lives was nearly equivalent and thus the final strains were similar. The only major difference between specimens of the varying loading paths was that the actuation strain was more stable for the linear loading cases.

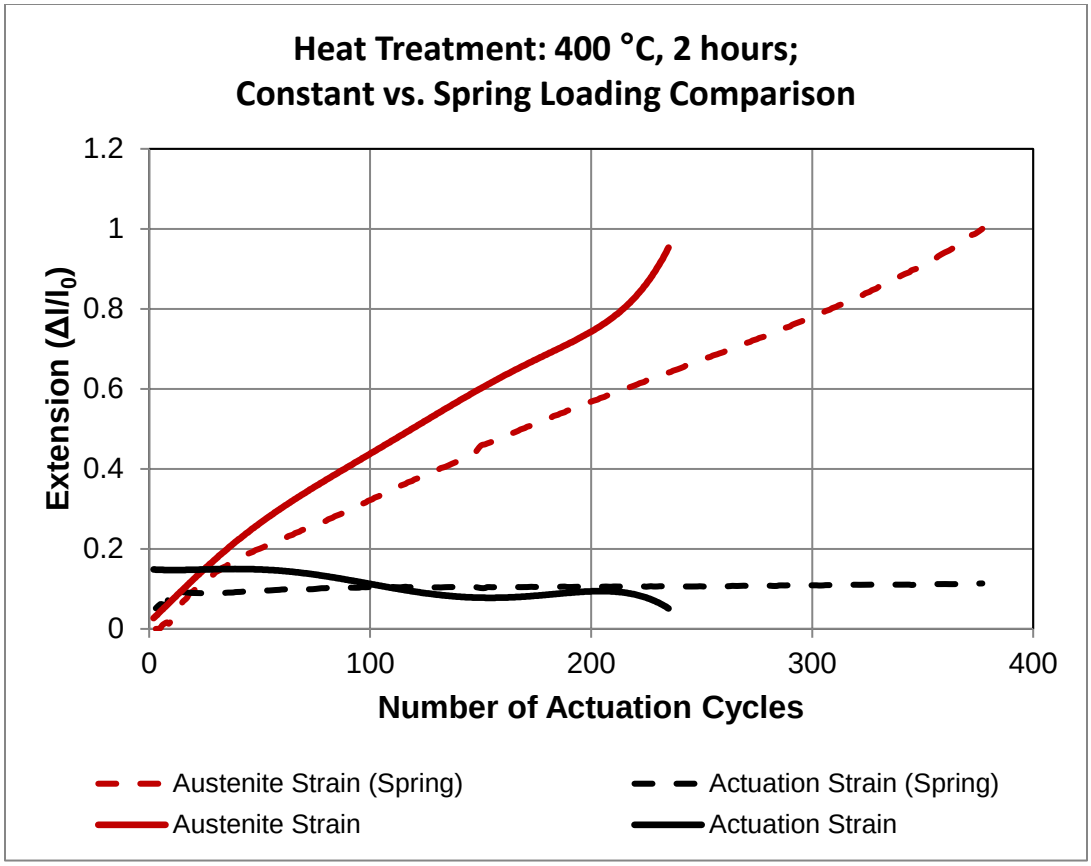

Figure 3.17: Engineering strain evolution for specimen E22 compared with E28; 200 MPa isobaric loading compared with 150-250MPa linearly varying loading.

In order to quantify the amount of necking which occurred prior to failure, the visual extensometry methods described in [66] were utilized. Figure 3.18 is a contour plot which shows the evolution of the engineering strain in five regions throughout the dogbone. The austenite data is plotted in Figure 3.19, where it is clear that the engineering strain begins to localize just prior to cycle 200.

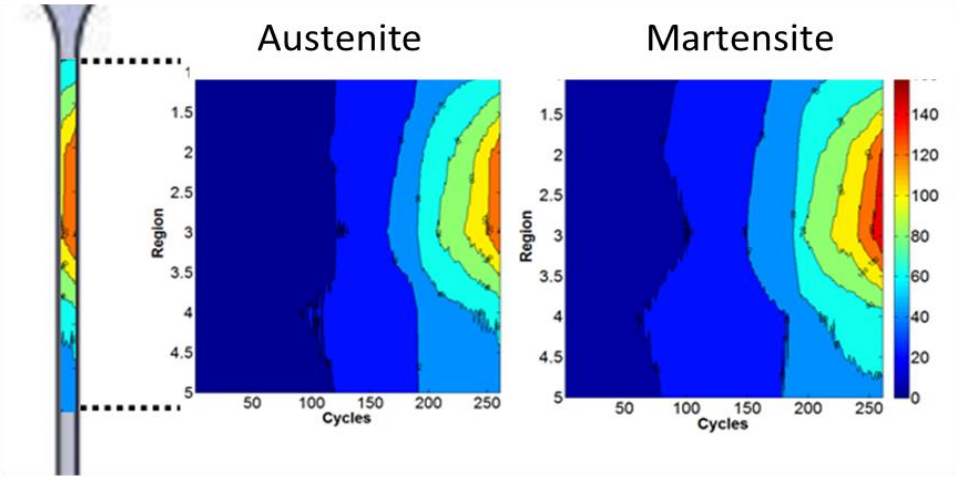

Figure 3.18: Engineering strain evolution for test E23 as detected by visual extensometry.*

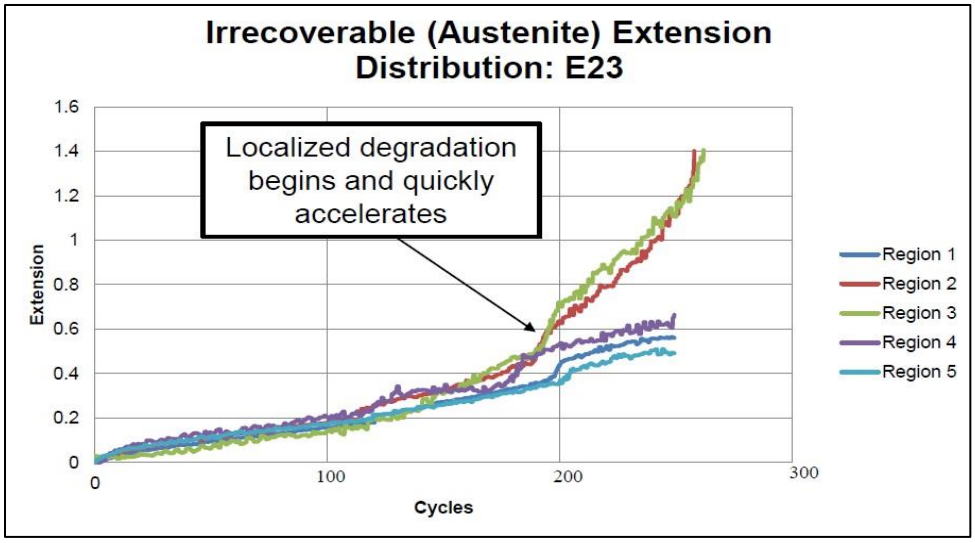

Figure 3.19: TRIP (engineering strain) evolution for test E23 as detected by visual extensometry.

* Figure 3.18 is reprinted with permission from Effect of processing and loading on equiatomic NiTi fatigue life and localized failure mechanisms by Wheeler RW, Santa-Cruz J, Hartl DJ, Lagoudas DC, 2013. Vol. 2 Mech. Behav. Act. Mater. Integr. Syst. Des. Implementation; Bioinspired Smart Mater. Syst. Energy Harvest., Copyright 2013 by ASME.

3.1.3 The Effect of Heat Treatment Parameters and Variable Loading

In the strain evolution plots in the previous section, it is clear there are a few types of responses: Specimens which had heat treatments with lower temperatures and less time exhibited a brittle response (e.g. A2), where the austenite and martensite extension slowly increased and failure occurred at or below 20% irrecoverable engineering strain. Specimens which had heat treatments at higher temperatures or average temperatures for longer periods of time exhibited a ductile response (e.g. E1), where irrecoverable engineering strains were quickly generated; however, failure did not occur until irrecoverable extensions exceeded 75%. Specimens which were heat treated for two hours at 375°C exhibited a favorable fatigue response (C2) with a much longer fatigue life with irrecoverable extensions between 35% and 37%.

The fatigue responses for specimens with equivalent heat treatments and loading conditions were very similar. There was also no distinguishable trend between thick and thin specimens. This repeatability can be seen in Figure 3.20 for two C2 heat treated specimens which both underwent isobaric actuation fatigue at 200MPa. In order to quantify the degree of repeatability for all tests and characteristics, the average values, along with the standard deviations, are reported in the following tables.

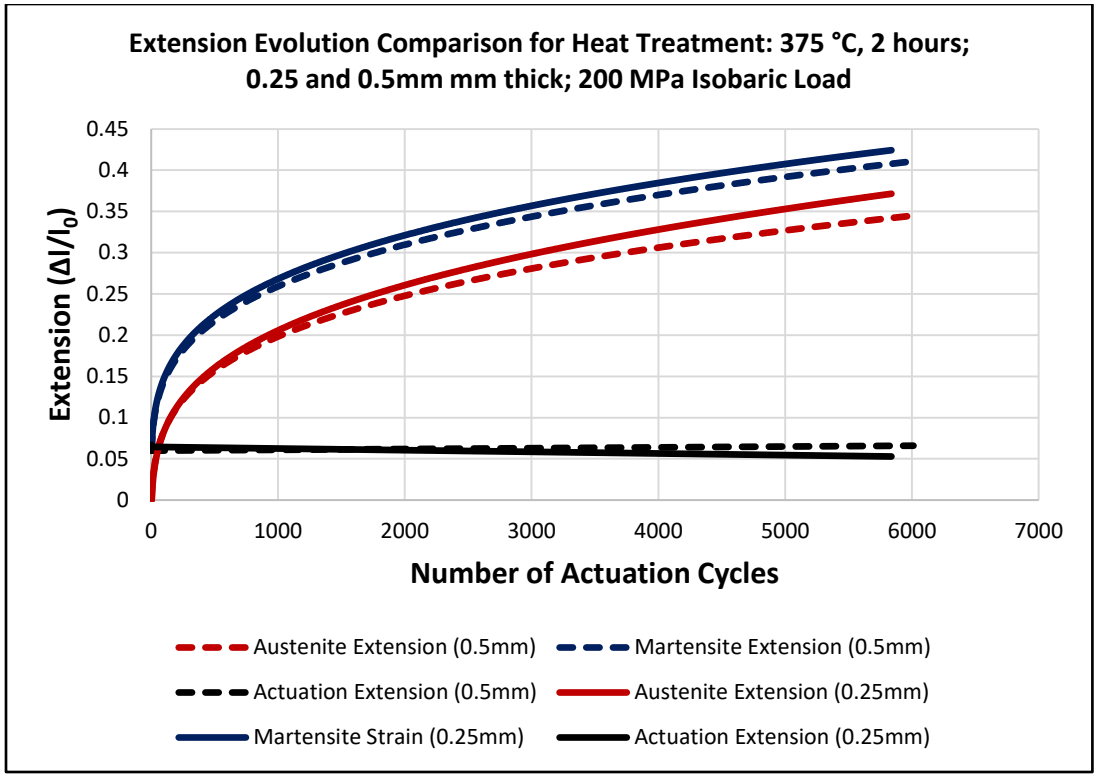

Figure 3.20: Engineering strain evolution comparison between 0.25mm and 0.5mm thick specimens with a heat treatment of 375°C for 2 hours (C2).

In Table 3-2, the average cycles to failure are listed for each of the heat treatments. Due to the relatively large average variance of the cycles to failure (approximately 10%), the standard deviation is also listed (in parenthesis) for each data point. The other fatigue characterization parameters had a much lower relative standard deviation (RSD), so only the averages are listed in Tables 3-3 through 3-6.

From Table 3-2, it is clear that the fatigue lives tended to decrease as specimens received heat treatments with more time and at higher temperatures than 375°C for two

hours. Equivalently, the fatigue lives also decreased as the specimens received heat treatments with lower temperatures and less time than 375°C at two hours.

Table 3-2: Cycles to Failure (Standard Deviation)

Heat Treatment	*1 hour*	*2 hours*	*3 hours*
350°C (A)		1195 (20.4)	1471 (29.9)
365°C (B)		1535 (79.5)	
375°C (C)	1125 (100.8)	5607 (388.3)	496 (41.9)
385°C (D)		1335 (7.1)	
400°C (E)	612 (8.1)	178 (62.1)	

The engineering strain in the austenite phase just prior to failure, or the final irrecoverable engineering strain, is shown in Table 3-3. As specimens were heat treated for more time or at higher temperatures, the final irrecoverable extension increased. As expected, there was a clear increase in the ductility of the specimens as the heat treatment parameters were increased.

Two new non-dimensional parameters were defined in order better characterize and quantify the effect of heat treatments on equiatomic NiTi. The necking ratio (NR) indicates how much the cross-sectional area (A) at the failure location decreased or by how much the original stress was amplified at the failure location. The strain localization factor (SLF) modifies the necking ratio by factoring the isochoric elongation out and

yielding a ratio purely indicative of strain localization at the failure location. They are defined in Equations 3.1 and 3.2.

Table 3-3: Overall Specimen Extension at Failure[5]

Heat Treatment	*1 hour*	*2 hours*	*3 hours*
350°C (A)		0.171	0.185
365°C (B)		0.278	
375°C (C)	0.301	0.349	0.641
385°C (D)		0.596	
400°C (E)	0.765	1.01	

$$NR = \frac{A_f}{A_0} \tag{3.1}$$

$$SLF = \frac{A_f}{A_0} * \frac{l_f}{l_0} \tag{3.2}$$

Tables 3-4 and 3-5 contain the necking ratios and extension localization factors, respectively. The necking ratio indicates the factor by which the 200MPa initial load increased at the failure location. The trend follows expectations, based on Tables 3-2 and 3-3, since specimens with higher overall extensions exhibited larger necking ratios. The SLF (Table 3-5) indicates whether or not strain localization contributed to actuator failure. Specimens which had ratios near unity exhibited little evenly distributed extensions over

[5] Note: Normalized variance was below 3% for all data points in the test matrix.

their length. On the other hand, specimens with higher heat treatment parameters exhibited larger amounts of strain localization at the failure point. It should also be noted that all specimens failed at the location of minimum cross-sectional area.

Table 3-4: Necking Ratio[6]

Heat Treatment	*1 hour*	*2 hours*	*3 hours*
350°C (A)		1.19	1.23
365°C (B)		1.31	
375°C (C)	1.31	1.35	2.47
385°C (D)		1.77	
400°C (E)	2.94	3.85	

Table 3-5: Strain Localization Factor[7]

Heat Treatment	*1 hour*	*2 hours*	*3 hours*
350°C (A)		1.02	1.04
365°C (B)		1.03	
375°C (C)	1.01	1.00	1.51
385°C (D)		1.11	
400°C (E)	1.67	1.92	

[6] Note: Normalized variance was below 3% for all data points in the test matrix.
[7] Note: Normalized variance was below 1% for all data points in the test matrix.

The transformation (or actuation) extension is shown for each specimen in Table 3-6. Specimens with higher actuation extension tended to have shorter fatigue lives. Specimens with longer or hotter heat treatments tended to have a higher actuation extension, with the exception being the heat treatment which produced the longest fatigue lives (375°C for two hours).

Table 3-6: Actuation Strain

Heat Treatment	*1 hour*	*2 hours*	*3 hours*
350°C (A)		5.00%	5.00%
365°C (B)		6.40%	
375°C (C)	7.40%	5.50%	8.20%
385°C (D)		7.20%	
400°C (E)	8.60%	12.10%	

In order to ensure that specimen failure location was not solely dependent on the experimental process, six initially equidistant markers were placed along six different specimens for each of the three fatigue frames. While specimens tended to fail within 8mm of the center of the specimen 65% of the time[8], there were no other discernable trends regarding the failure location for a specific heat treatment or frame. Due to the nature of

[8] Note: the gage section was 31.75mm, therefore being within 8mm of the center corresponds to being within the center 50% of the gage section.

joule or resistive heating, this slight bias towards failing in the center half of the gage section was expected.

3.1.4 The Effect of Loading Path on Actuation Fatigue of Equiatomic NiTi

In addition to studying the effect of the heat treatment on isobaric fatigue, actuators for seven of the heat treatments were also subjected to 150-250MPa loading. The actuation fatigue characteristics of these tests are summarized in Tables 3-7 through 3-12. For each of the heat treatments, an increase in the fatigue life was seen when the 200MPa isobaric load was replaced with a linearly varying 150-250MPa load. The average number of cycles to failure is shown in Table 3-7 for each heat treatment.

Table 3-7: Average Cycles to Failure: 150-250MPa Linear Loading

Heat Treatment	*1 hour*	*2 hours*	*3 hours*
350°C (A)		2575	3104
375°C (C)	1729	7124	627
400°C (E)	817	271	

In Table 3-8, the final irrecoverable engineering strain is shown for each heat treatment. In general, the amount of irrecoverable deformation was lower or approximately equivalent for the linear loading. The change in the average final irrecoverable engineering strain is also noted in parenthesis (e.g. -0.15 indicates the final irrecoverable engineering strain was 15% lower for linear loading).

Table 3-8: Average Final Irrecoverable Engineering Strain: 150-250MPa Linear Loading

Heat Treatment	*1 hour*	*2 hours*	*3 hours*
350°C (A)		0.165 (-0.006)	0.179 (-0.006)
375°C (C)	0.248 (-0.212)	0.349 (0.000)	0.645 (+0.004)
400°C (E)	0.791 (+.0260)	1.02 (+0.010)	

Following the same trend observed in the total irrecoverable engineering strain, the necking ratio increased with heat treatment time and temperature; however, the experimental value did not vary significantly for many of the heat treatments. The values of the necking ratio are shown in Table 3-9, and the change is indicated in parenthesis.

Table 3-9: Necking Ratio: 150-250MPa Linear Loading

Heat Treatment	*1 hour*	*2 hours*	*3 hours*
350°C (A)		1.17 (-0.02)	1.18 (-0.05)
375°C (C)	1.25 (-0.06)	1.35 (0.00)	2.42 (-0.05)
400°C (E)	3.01 (+0.07)	3.87 (+0.02)	

The strain localization factor for each of the heat treatments is listed in Table 3-10. Interestingly, when the isochoric expansion is taken into account, the response of the material appears to be very similar for both isobaric and linear loading. As in the previous

tables, the change, when replacing an isobaric 200MPa load with a linearly varying load ranging between 150-250MPa, is noted in parenthesis.

Table 3-10: Strain Localization Factor: 150-250MPa Linear Loading

Heat Treatment	*1 hour*	*2 hours*	*3 hours*
350°C (A)		1.00 (-0.02)	1.00 (-0.04)
375°C (C)	1.00 (-0.01)	1.00 (0.00)	1.50 (-0.01)
400°C (E)	1.68 (+0.01)	1.92 (0.00)	

For all of the heat treatments, the average actuation extension was lower when loaded via the spring array. This is a result of the spring relaxing as the actuator finishes transforming into martensite, thus decreasing the applied mechanical load. The actuation strain was shown to generally increase with heat treatment time and temperature. These trends are captured in Table 3-11. The change from the isobaric values for the actuation engineering strain is reported in parenthesis in Table 3-11, as well.

Table 3-11: Average Actuation Engineering Strain: 150-250MPa Linear Loading

Heat Treatment	*1 hour*	*2 hours*	*3 hours*
350°C (A)		4.5% (-0.5%)	4.6% (-0.4%)
375°C (C)	5.8% (-1.6%)	5.2% (-0.3%)	5.9% (-2.3%)
400°C (E)	8.1% (-0.5%)	9.9% (-2.2%)	

By switching from an isobaric to a linear loading scheme, actuators from every heat treatment showed an increase in the total work output (Table 3-12). The actuators with the slowest irrecoverable strain generation rate, A2 and A3, benefitted the most from mechanical loading via spring array.

Table 3-12: Average Increase in Total Work: 150-250MPa Linear Loading

Heat Treatment	*1 hour*	*2 hours*	*3 hours*
350°C (A)		194%	192%
375°C (C)	120%	137%	121%
400°C (E)	125%	123%	

3.1.5 Equiatomic NiTi: Further Characterization of Selected Heat Treatments

From the results obtained while analyzing the effects of heat treatment and load path on the actuation fatigue response of equiatomic NiTi, two heat treatments were selected due to their appealing characteristics: 350°C for two hours was selected due to its low irrecoverable deformation, and 375°C for two hours was selected since it had the longest fatigue life for both loading paths. The additional isobaric calibration tests are summarized in Tables 3-13 and 3-14 for 350°C/two hours and 375°C/two hours, respectively. These additional tests also allowed for the calibration of the phenomenological model developed by Lagoudas *et al.* [1].

Table 3-13: 350°C, Two Hours Additional Isobaric Calibration Tests

Load (MPa)	*Actuation Strain*	*Cycles to Failure*
100	4.12%	3052
100	4.05%	3601
150	4.30%	1745
150	4.26%	1820
200	4.35%	1226
200	5.00%	1166
200	5.02%	1048
200	4.19%	1642
300	5.20%	650
300	5.05%	698

Table 3-14: 375°C, Two Hours Additional Isobaric Calibration Tests

Load (MPa)	*Actuation Strain*	*Cycles to Failure*
150	5.20%	12000
150	5.10%	13336
200	6.05%	3209
200	5.37%	5841
200	6.05%	3211
200	5.65%	4734
200	5.27%	6012
250	6.12%	2536
250	5.94%	2745

Table 3-14: Continued

Load (MPa)	*Actuation Strain*	*Cycles to Failure*
300	5.51%	1643
350	5.72%	1237

The actuation strain, which evolves with the applied load is described by Equation 3.3, where H^{cur} is the transformation strain as a function of the applied load, σ, H^{min} is the minimum transformation strain (determined to be zero for these untrained materials), σ^{crit} is the critical stress for developing transformation strain when the material is martensite, H^{sat} is the maximum transformation strain for very large loads, and k is a fitting parameter.

$$H^{cur}(\sigma) = \begin{cases} H^{min} & , \ \sigma \leq \sigma^{crit} \\ H^{sat}(1 - \exp[-k(\sigma)]) & , \ \sigma > \sigma^{crit} \end{cases} \tag{3.3}$$

The resulting calibration for both heat treatments can be seen in Figure 3.21, and the values are summarized in Table 3-15.

Table 3-15: H^{cur} Parameters for Equiatomic NiTi

Parameter	*375°C, 2 Hours*	*350°C, 2 Hours*
H^{sat}	6.1%	5.3%
k	0.015	.013
σ^{cr}	25MPa	25MPa

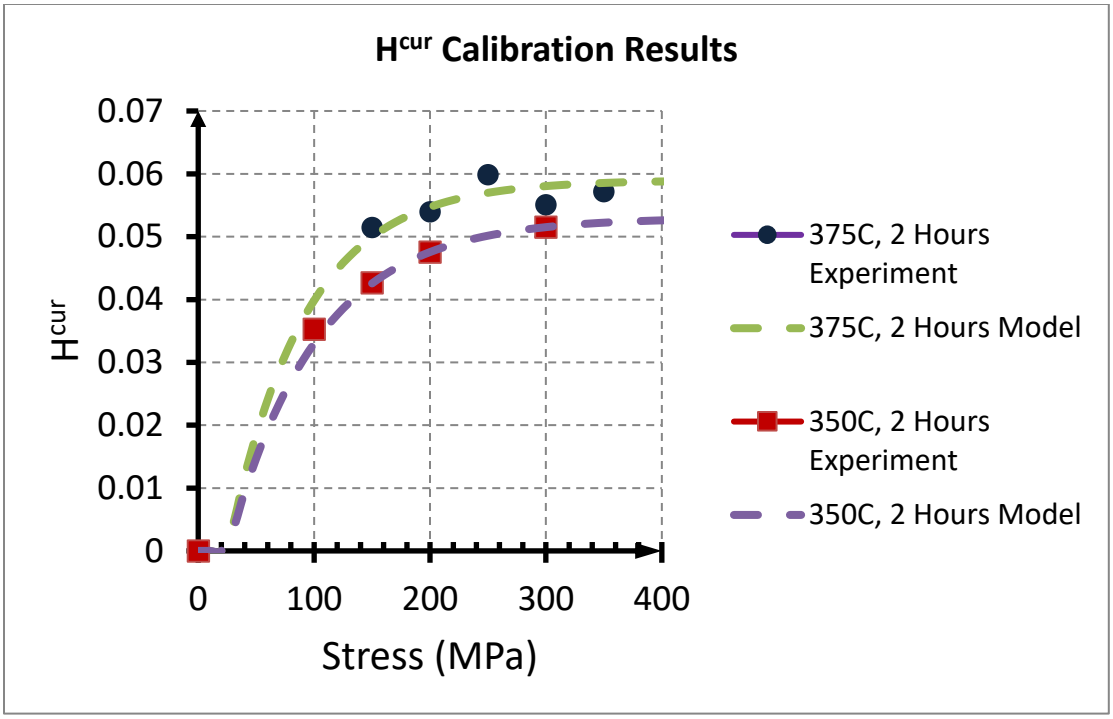

Figure 3.21: $H^{cur}(\sigma)$ model and experiments for equiatomic NiTi.

3.2 Nickel-Rich $Ni_{60}Ti_{40}$ (wt%) Actuation Fatigue Characterization

The $Ni_{60}Ti_{40}$ material system was selected for the initial testing due to availability of material, previously collected data, and the similarity of some of the fatigue characteristics (relatively low transformation and irrecoverable strain) with those of NiTiHf.

The test matrix, which can be seen in Table 3-16, was completed in order to collect data to assist in the calibration and evaluation of fatigue life prediction methods for variable geometries. Isobaric dogbone testing was utilized to characterize the material with stresses ranging between 150 and 300MPa; in total, ten isobaric tests were conducted.

Table 3-16: $Ni_{60}Ti_{40}$ Test Matrix

Specimen Geometry	*Load Path*	*Load (MPa)*	*Specimen Nomenclature*
Dogbone	Isobaric	150	A1, A2
Dogbone	Isobaric	200	B1, B2, B3
Dogbone	Isobaric	250	C1, C2, C3
Dogbone	Isobaric	300	D1, D2
Notched Plate	Constant Load	400MPa initial max	NP1, NP2
Plate with centered Hole	Constant Load	400MPa initial max	CH1, CH2
Plate with Eccentric Hole	Constant Load	400MPa initial max	EH1, EH2

3.2.1 $Ni_{60}Ti_{40}$: 150 MPa Isobaric Loading

When loaded with 150MPa, specimen A2 achieved an actuation strain of about 1%, which can be seen in Figure 3.22. The maximum actuation strain observed was 1.17% and the minimum was 0.70%. The irrecoverable strain generation rate appeared to stabilize after approximately 1,200 cycles.

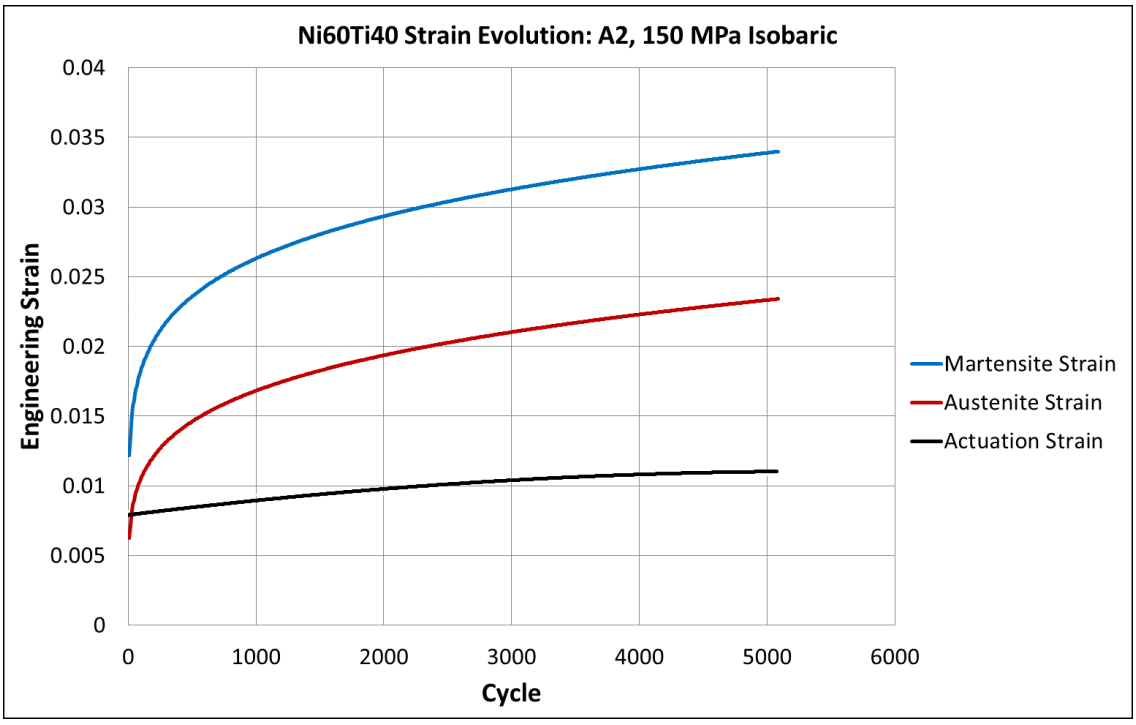

Figure 3.22 Strain evolution for specimen A2 – 150 MPa isobaric loading.

The hysteresis evolution for this test can be seen in Figure 3.23. From this figure, it is apparent that the transformation temperatures are nearly constant throughout the fatigue life. This test was repeated with an upper cycle temperature of 100°C and produced similar results.

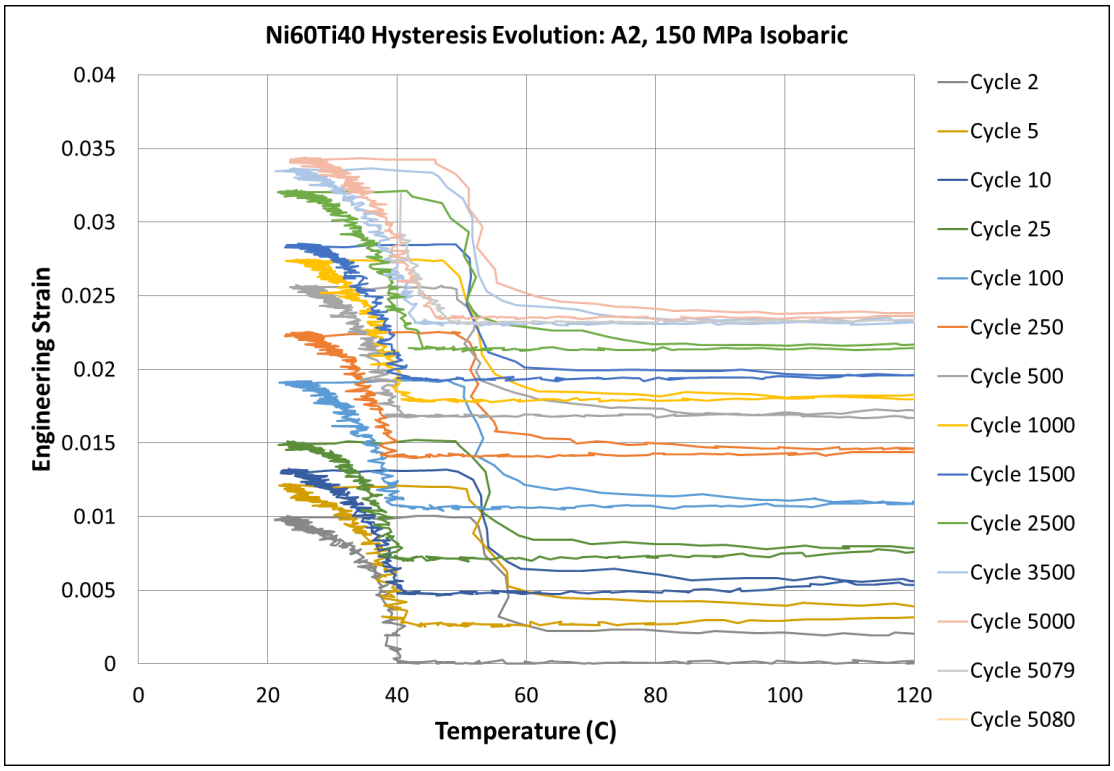

Figure 3.23: Hysteresis evolution for specimen A2 – 150 MPa isobaric loading.

3.2.2 $Ni_{60}Ti_{40}$: 200 MPa Isobaric Loading

When mechanically loaded with 200MPa, the Nickel-rich actuators generated approximately 1.5% actuation strain. A representative strain evolution can be seen in Figure 3.24. Similar to the 150MPa fatigue response, the strain evolution is very stable; however, the actuation strain and fatigue life are relatively low and short, respectively. As expected, the transformation temperatures were nearly constant throughout the fatigue life. This can be observed in the hysteresis evolution, shown in Figure 3.25.

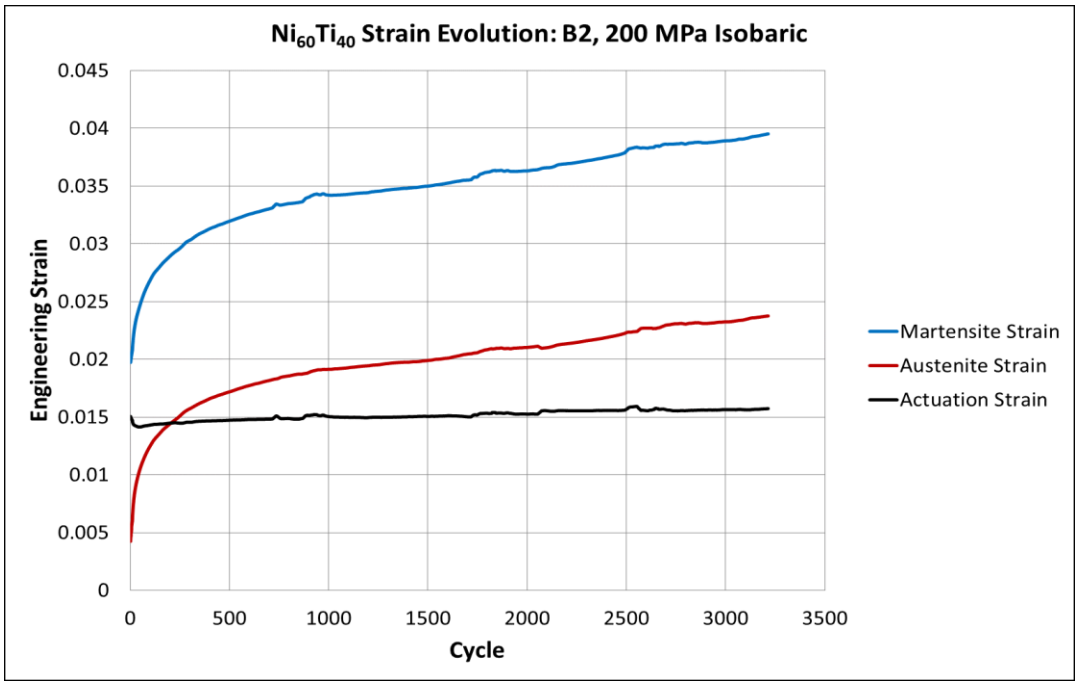

Figure 3.24: Strain evolution for specimen B2 – 200 MPa isobaric loading.

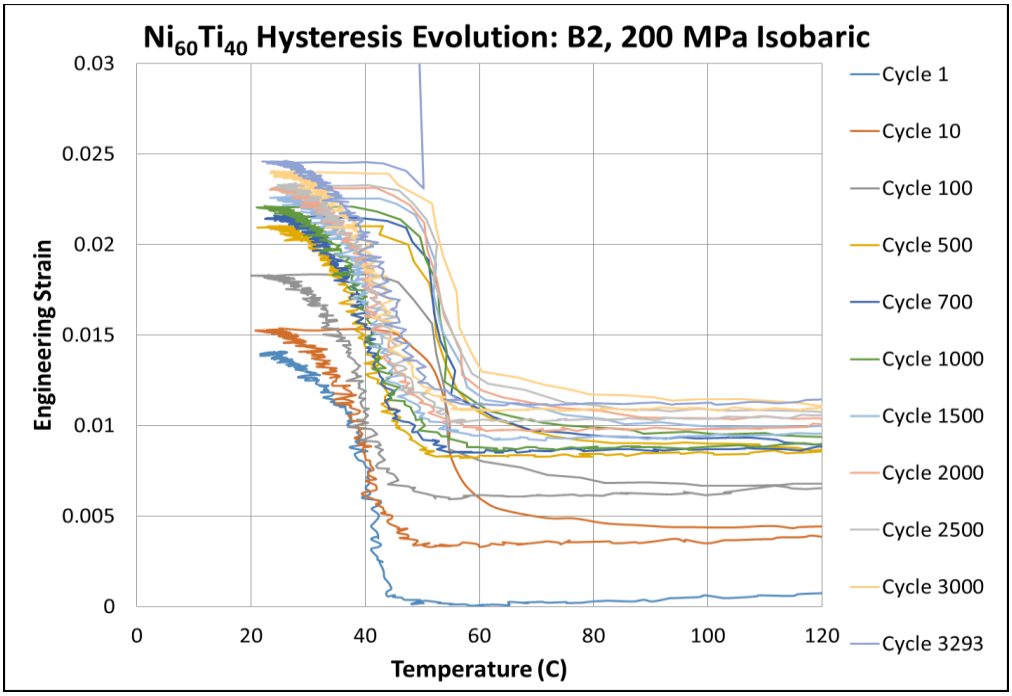

Figure 3.25: Hysteresis evolution for specimen B2 – 200 MPa isobaric loading.

For the 200MPa loading condition, DIC analysis was also performed. Similar to the equiatomic NiTi material system, the region which would ultimately fail was detectable approximately halfway through the fatigue life. However, unlike the equiatomic system, this localized deformation was only detectable through DIC and not visually apparent; this localized region reached strains between 2% and 4% in Nickel-rich NiTi, while it reached values several orders of magnitude higher in the equiatomic system. An example of this result can be seen in Figure 3.26, where the final austenite and martensite images are shown for specimen B2.

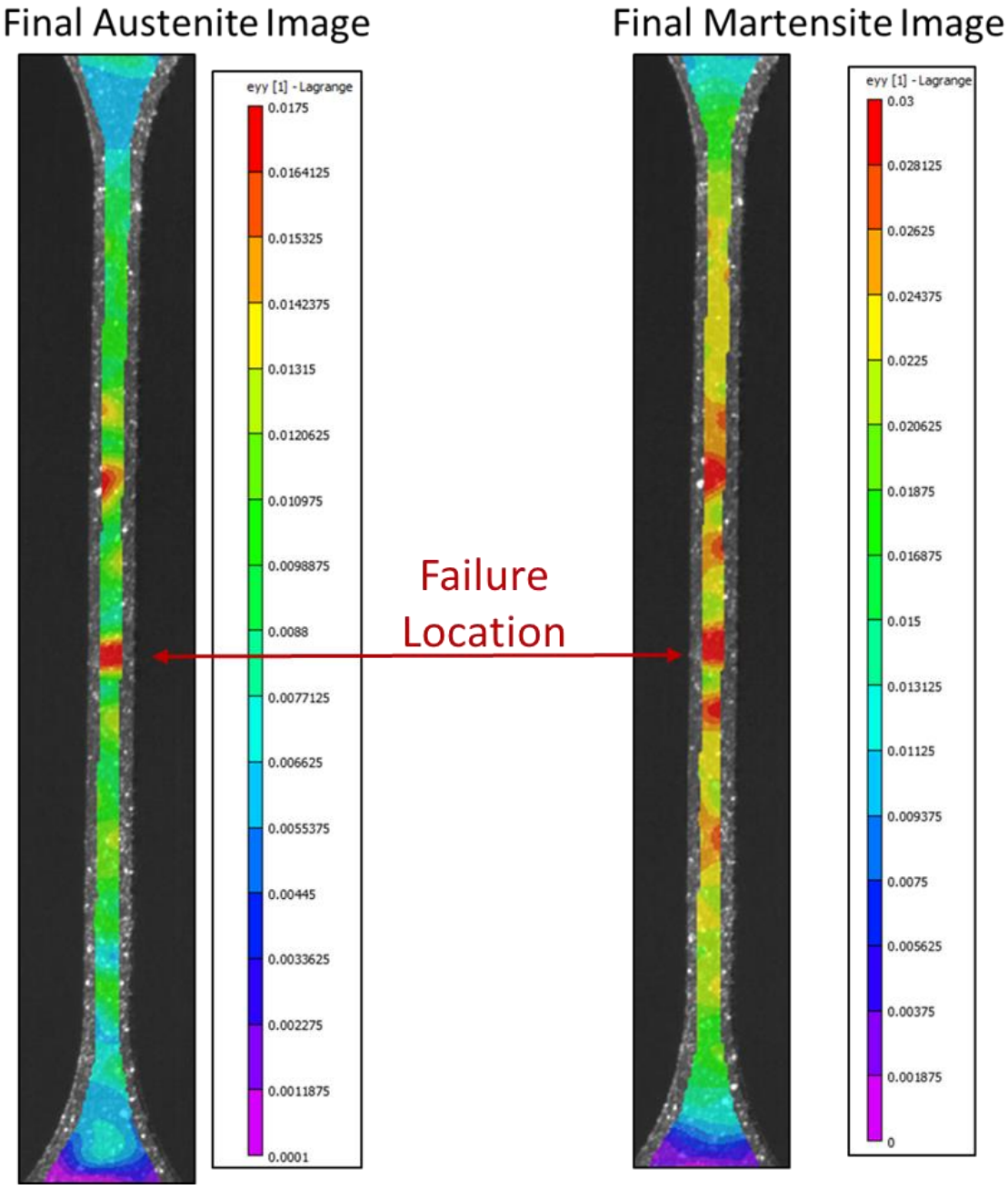

Figure 3.26: Final austenite (left) and martensite (right) images for specimen B2. DIC results were obtained through VIC2D (a commercially available software).

3.2.3 $Ni_{60}Ti_{40}$: 250 MPa Isobaric Loading

The third loading group, denoted with the letter C, consisted of three isobaric actuation fatigue tests at 250MPa. The strain evolution, shown in Figure 3.27, appears to be very similar to the 200MPa result, with the exception of a shorter fatigue life. However, from the hysteresis evolution, shown in Figure 3.28, it is clear that the actuator needs significantly more heating to complete transformation due to the increased load.

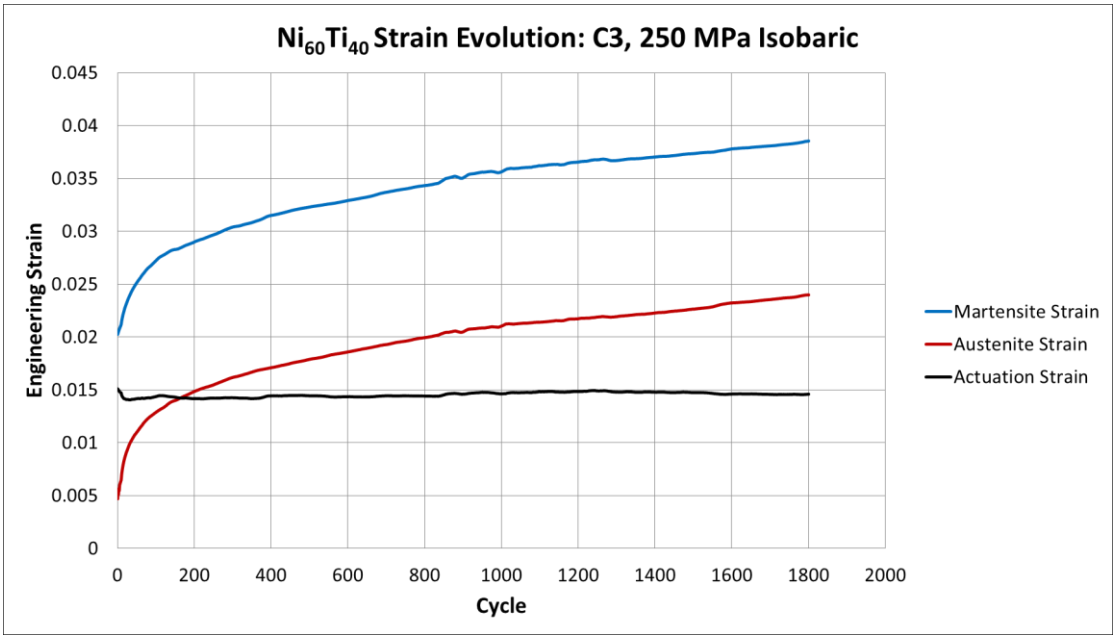

Figure 3.27: Strain evolution for specimen C2 – 250 MPa isobaric loading.

One interesting result when comparing the strain evolution for the 200MPa and 250MPa load is that, despite the fatigue life of the 250MPa case being 1200 cycles short, both fail at nearly the same austenite strain or accumulated TRIP. However, when the

tests were repeated, they were found to fail between 1.4% and 2.7%, and no trend was evident relating the final austenite strain to load or cycles to failure. This small variation, or critical range for failure, was not expected due to the large variation in final austenite strains seen when testing equiatomic NiTi.

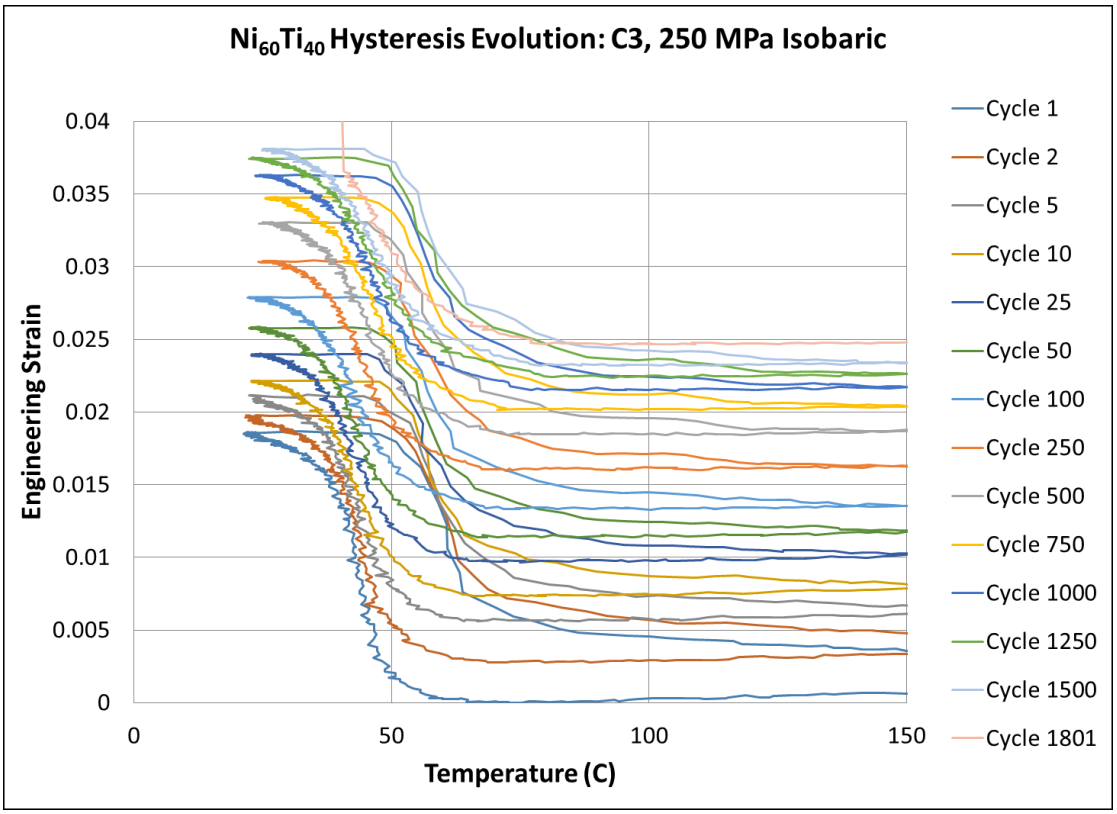

Figure 3.28: Hysteresis evolution for specimen C3 – 250 MPa isobaric loading.

3.2.4 $Ni_{60}Ti_{40}$: 300 MPa Isobaric Loading

The highest load of the calibration tests, 300MPa, produced the most stable strain evolution, as can be seen in Figure 3.29. The actuation strain was nearly constant at 1.5%

throughout the fatigue life. Similarly, the hysteresis evolution, shown in Figure 3.30, was very stable. The final austenite strain, approximately 1.4%, was found to be lower than the final austenite strains of tests conducted at lower stress levels.

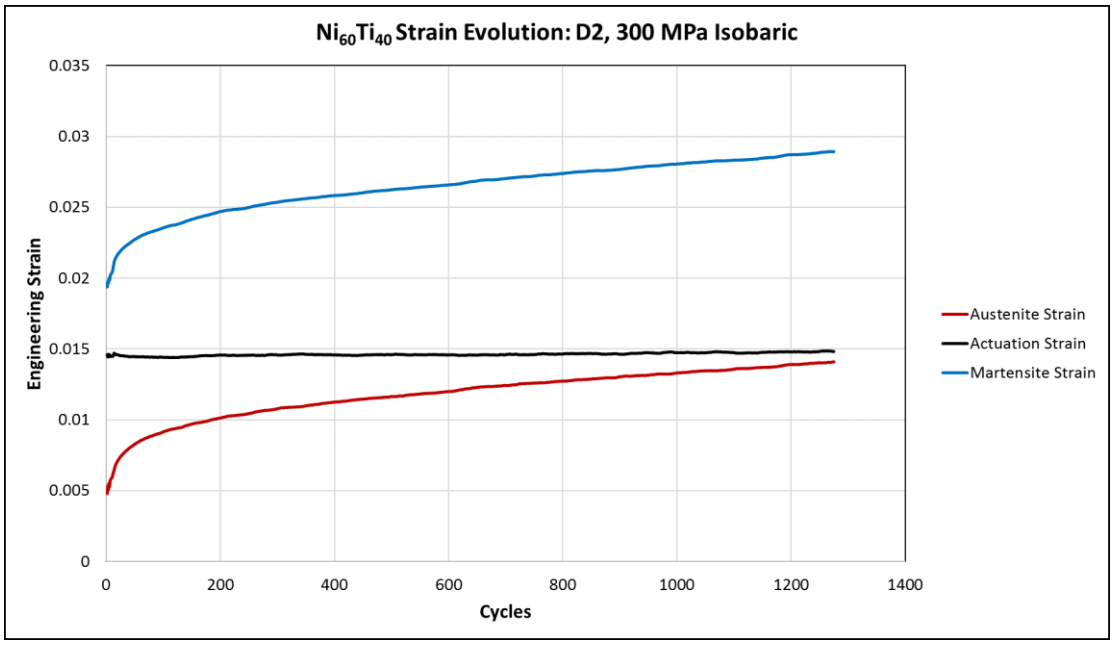

Figure 3.29: Strain evolution for specimen D1 – 300 MPa isobaric loading.

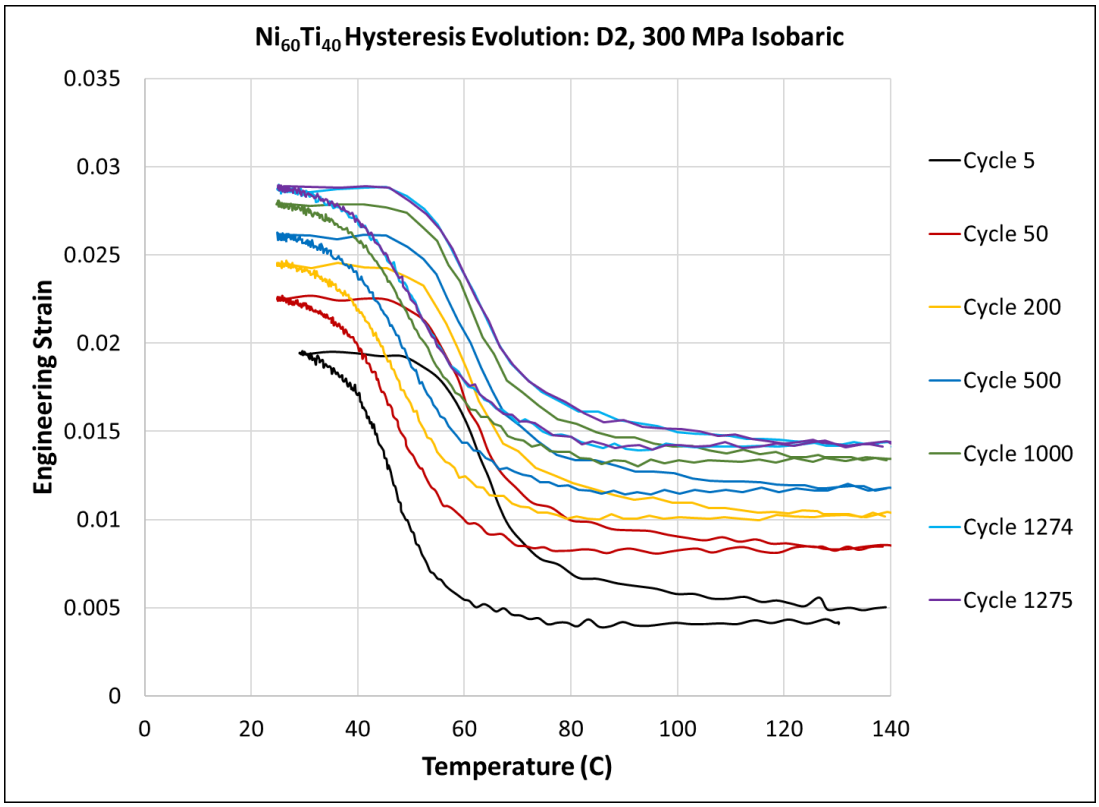

Figure 3.30: Hysteresis evolution for specimen D1 – 300 MPa isobaric loading.

3.2.5 Calibration Results Summary

The test matrix described in Table 3-16 was completed in order to collect data to calibrate the phenomenological model proposed by Lagoudas *et al*. [1]. The averaged results are summarized in Table 3-17. From these results, it is clear that the transformation strain saturates very quickly and that the final austenite strain does not seem to correlate well with either cycles to failure or applied load.

Table 3-17: Averaged Isobaric Test Results for $Ni_{60}Ti_{40}$

Load [MPa]	*Actuation Strain*	*Cycles to Failure*	*Final Austenite Strain*	*Final Martensite Strain*
150	0.99%	5078	2.21%	3.38%
200	1.41%	3255	1.67%	3.10%
250	1.48%	2051	2.22%	3.74%
300	1.50%	1275	1.42%	2.90%

The resulting calibration parameters from the data presented are summarized in Table 3-18. Note: the calibration methodology utilized was developed by Lagoudas *et al.* [1]. The transformation strain as a function of the applied stress, or H^{cur}, is shown in Figure 3.31.

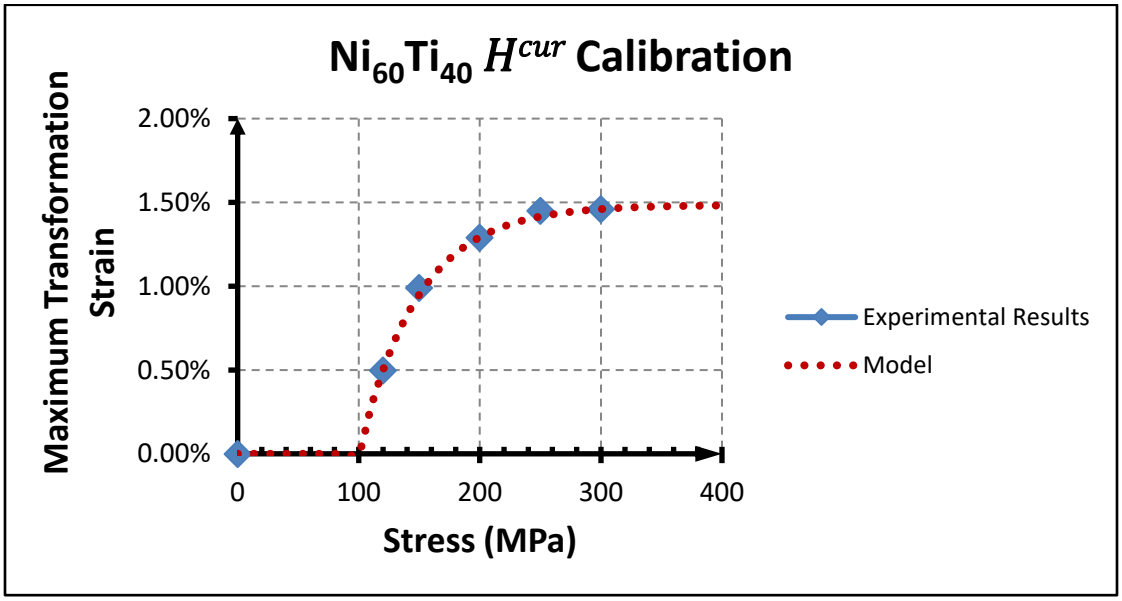

Figure 3.31: H^{cur} calibration results.

Table 3-18: Material Parameters Determined from Isobaric Testing

Material Parameter	*Value*
H^{sat}	1.485%
H^{min}	0
k	.0204
σ^{crit}	100MPa
$E_M = E_A$	70GPa
$\nu_M = \nu_A$	0.33
$C_M = C_A$	22MPa/K
M_s	318K
M_f	298K
A_s	332K
A_f	352K

3.2.6 Fatigue Testing of $Ni_{60}Ti_{40}$ Plate Actuators

Once the dogbone characterization tests were completed, the results were utilized to calibrate the SMA model developed by Lagoudas *et al.* and the material properties (listed in Table 3-18) were input in an ABAQUS user material subroutine [1] . The resulting simulations were used to determine the operational load which would induce 400MPa at the stress concentration. These loads are listed in Table 3-19, and the transformation strain resulting from these loads can be seen in Figure 3.32 for each geometry.

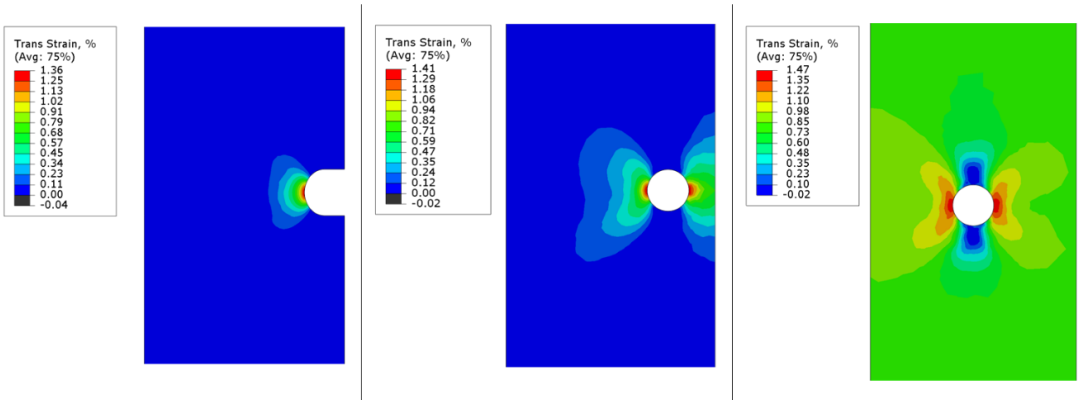

Figure 3.32: Transformation strain predicted by the standard SMA model.

Table 3-19: Nominal Loads for Plate Actuators

Geometry	*Stress*
Centered Hole	136 MPa
Eccentric Hole	118 MPa
Notched Plate	86 MPa

While these nominal stresses were selected to induce 400MPa at the stress concentration, which is sufficient to nearly fully saturate the transformation strain, they did not cause the entirety of the plate actuator to develop transformation strain. This result is particularly interesting for the notched plate actuators due to the fact that the determined load is lower than the critical stress found during the characterization. Because of this, the majority of the notched plate does not develop transformation strain, as can be seen in Figure 3.32.

For each of the three plate geometries, two tests were conducted and monitored with DIC. As expected, the forward transformation (into martensite) initiated at the stress concentration and propagated outwards for nominal stress levels ranging between 75 and 400MPa. In Figure 3.33, the initial transformation strain is shown for each geometry. This was calculated by taking the difference between the fully austenite and martensite positions.

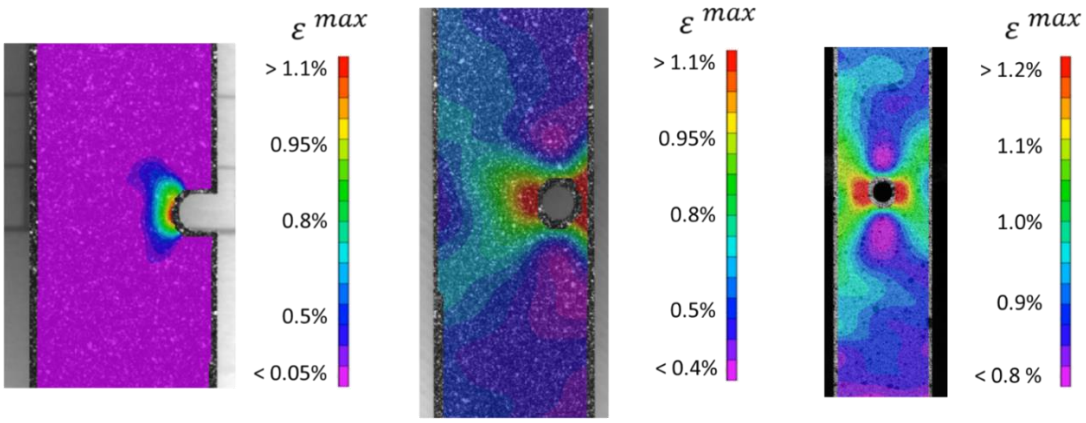

Figure 3.33: Initial transformation strains for each actuator design.

Prior to failure, images captured showed crack growth until catastrophic failure occurred. As the material cooled, the crack could be seen to open and grow during each forward transformation; upon heating, the crack would close and only remain visible during the last two or three cycles. This cyclic opening and closing of a macroscopic crack was detected once the crack reached a length of 0.2mm and was observed during the final 10, 25, and 60 cycles for the single notch, eccentric hole, and centered hole specimens,

respectively. The final austenite and martensite images can be seen in Figure 3.34 for each of the three geometries. All tests failed during cooling (after the final austenite picture). Final martensite strains for all tests exceeded 5% at the failure location. An example of this result can be seen in Figure 3.35.

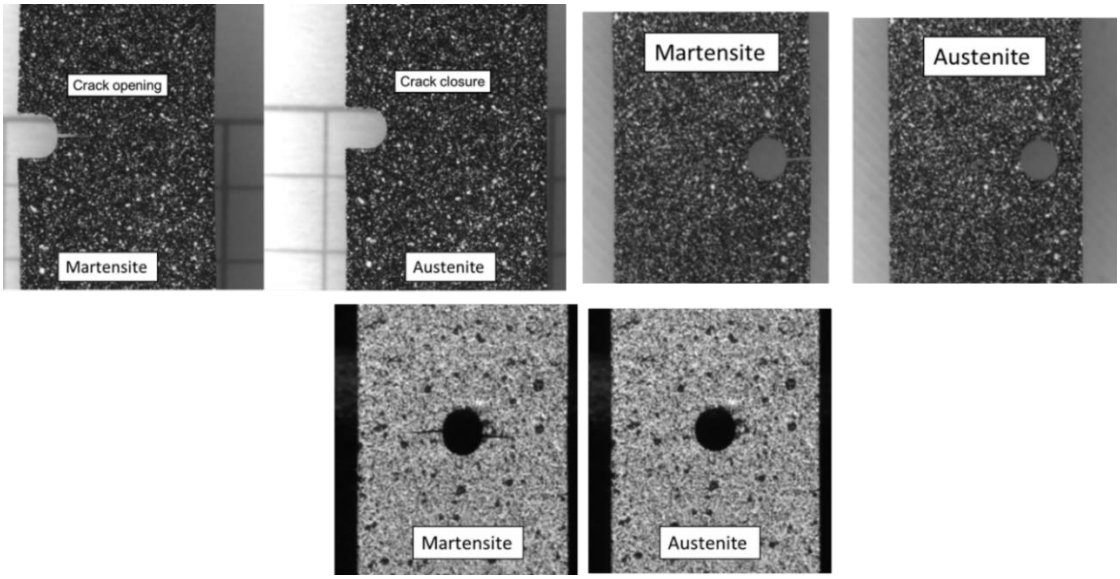

Figure 3.34: Final pictures prior to failure. Note: Crack(s) close completely after heating/actuation cycle.

From Figure 3.34, it can be seen that the ligament in the plate actuator with an eccentric hole has already failed, while the bulk of the actuator is damaged, but has yet to catastrophically fail. This was observed for all plate actuators tested with this geometry. Despite this fractured ligament, the actuator survived approximately 40 more actuation cycles. Even during the final heating cycle, the actuator managed to close the failed ligament. Based on the simulations, the actuation strain was expected to be higher in the

ligament. Therefore, it was not surprising that it failed prior to the catastrophic failure of the entire actuator.

Due to the stress concentrations in the plate actuators, the regions which are expected to dictate the actuator lifecycles are in the immediate vicinity of the holes/notches. Since these regions consistently led to failure, this region was selected for further comparison between simulation and experimental results. From Figures 3.32 and 3.33, it is clear that the actuation strains qualitatively agree, and, from Table 3-20, it is clear that they quantitatively agree in the critical regions.

Due to the asymmetric geometry of the plates with eccentric holes, two values of actuation strain are listed in Table 3-20. Similarly, there are two reported cycles to failure for each of the eccentric tests in Table 3-21.

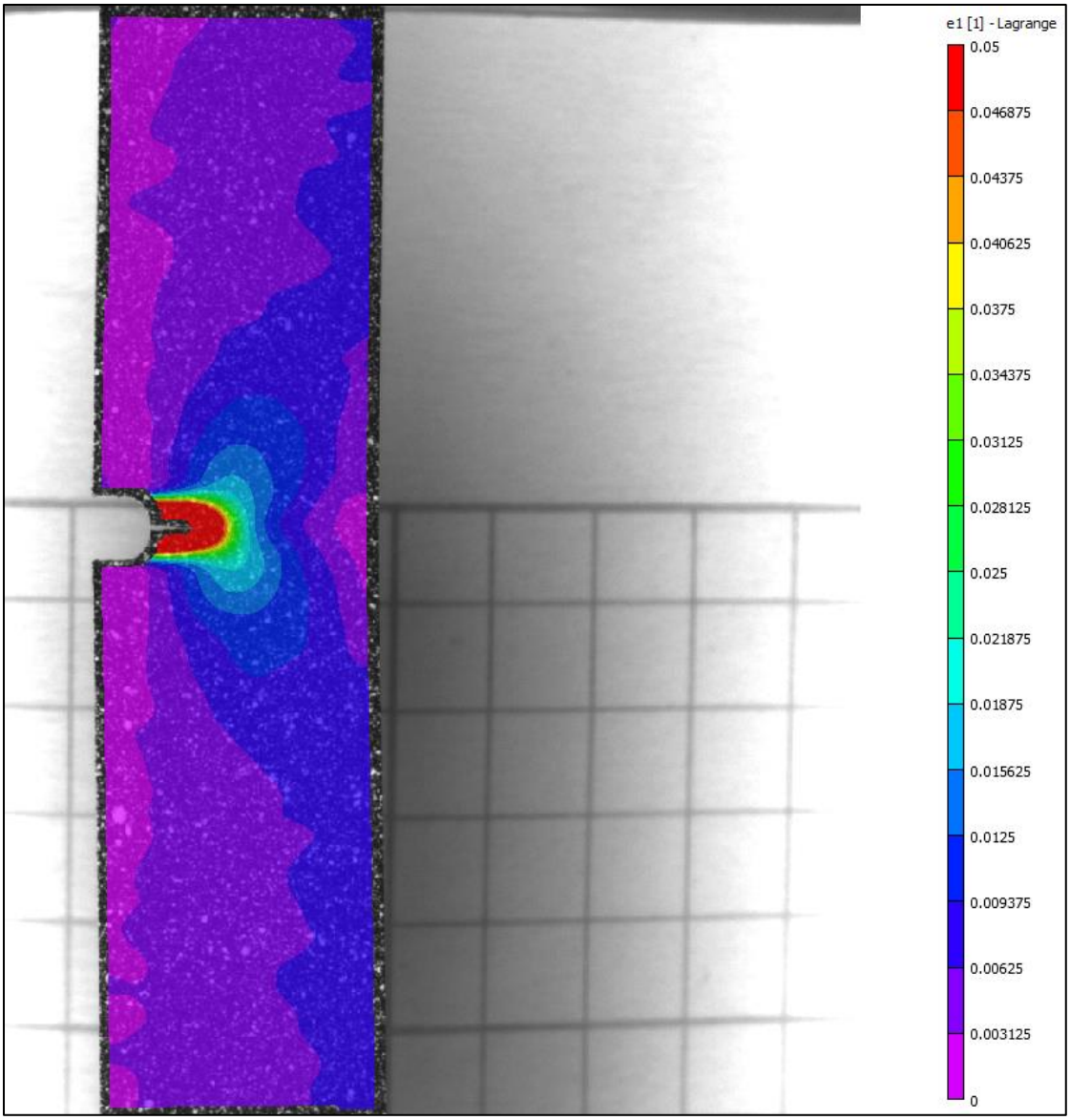

Figure 3.35: Final martensite strain for NP1.

Table 3-20: Experimental and Simulation Comparison of Actuation Strains near the Stress Concentrations

Specimen	*Actuation Strain (DIC)*	*Predicted Actuation Strain*
Centered 1	1.34%	1.31%
Centered 2	1.52%	1.31%
Notched 1	0.98%	0.98%
Notched 2	0.96%	0.98%
Eccentric 1	1.25%	1.21% (ligament)
	0.99%	1.05% (bulk)
Eccentric 2	1.23%	1.21% (ligament)
	1.06%	1.05% (bulk)

Table 3-21: Cycles to Failure for Plate Actuators with Stress Concentrations

Specimen	*Cycles to Failure*	*Average*
Centered 1	973	923
Centered 2	872	923
Notched 1	1523	1548
Notched 2	1573	1548
Eccentric 1	1062	1042
	1086	1075
Eccentric 2	1021	1042
	1063	1075

4 ACTUATION FATIGUE CHARACTERIZATION AND DATABASE OF NICKEL-TITANIUM SMAS OF NITIHF HTSMAS*

4.1 High Temperature SMAs: Nickel-Titanium-Hafnium Characterization

Due to the high operational temperatures of many aerostructures, system requirements for SMA actuators have encouraged the development and characterization of high temperature shape memory alloys (HTSMAs). One of the primary candidates for HTSMA-based actuator design is Nickel-Titanium-Hafnium, in particular $Ni_{50.7}Ti_{29.3}Hf_{20}$ (atomic percentage), which has been used in several applications [14].

In order to subject the NiTiHf specimens to actuation fatigue, the experimental methods described in Chapter 2 were utilized. Three material lots, which were produced separately by the same metallurgical supplier, underwent preliminary characterization performed by Karaman *et al.* [67]. Two of the three material lots, the 200 and 500 series, were found to be nearly identical in overall composition, stiffness, and transformation temperatures.

The DSC analysis for the three material lots, after solutionizing for one hour at 900°C, is shown in Figure 4.1a and the zero-stress transformation temperatures are listed in Table 4-1. From these DSC results, it is clear that the 200 and 500 series were very similar compositionally, and that the 300 series was Nickel-lean. This was later confirmed with

* Part of the data reported in this chapter is reprinted with permission from Modeling of thermo-mechanical fatigue and damage in shape memory alloy axial actuators by Wheeler RW, Hartl DJ, Chemisky Y, Lagoudas DC, 2015. International Society for Optics and Photonics, Copyright 2015 by Society of Photo Optical Instrumentation Engineers.

EDS. Due to this significant difference, only the 200 and 500 series were studied further in this work. As shown in Figure 4.1b, the post heat treated materials were also found to have very similar transformation temperatures.

Table 4-1: Zero-stress Transformation Temperatures for each NiTiHf Material Lot

Material Lot	*Mf (°C)*	*Ms (°C)*	*As (°C)*	*Af (°C)*
200	76	95	110	128
300	139	158	172	185
500	83	95	121	131

In order to further characterize the materials and find the cause of the difference in sharpness of the DSC response, Karakoc *et al*. [68] collected SEM images to determine the purity of the materials. These images were then analyzed through visual techniques, and it was found that the 200 series had approximately 0.4% impurities while the 500 series had less than 0.08%[9]. For this reason, the 200 series is referred to as "low purity" while the 500 series is referred to as "high purity." Two example SEM images can be seen in Figure 4.2.

[9] Discussion of the visual analysis methods can be found in Appendix A.

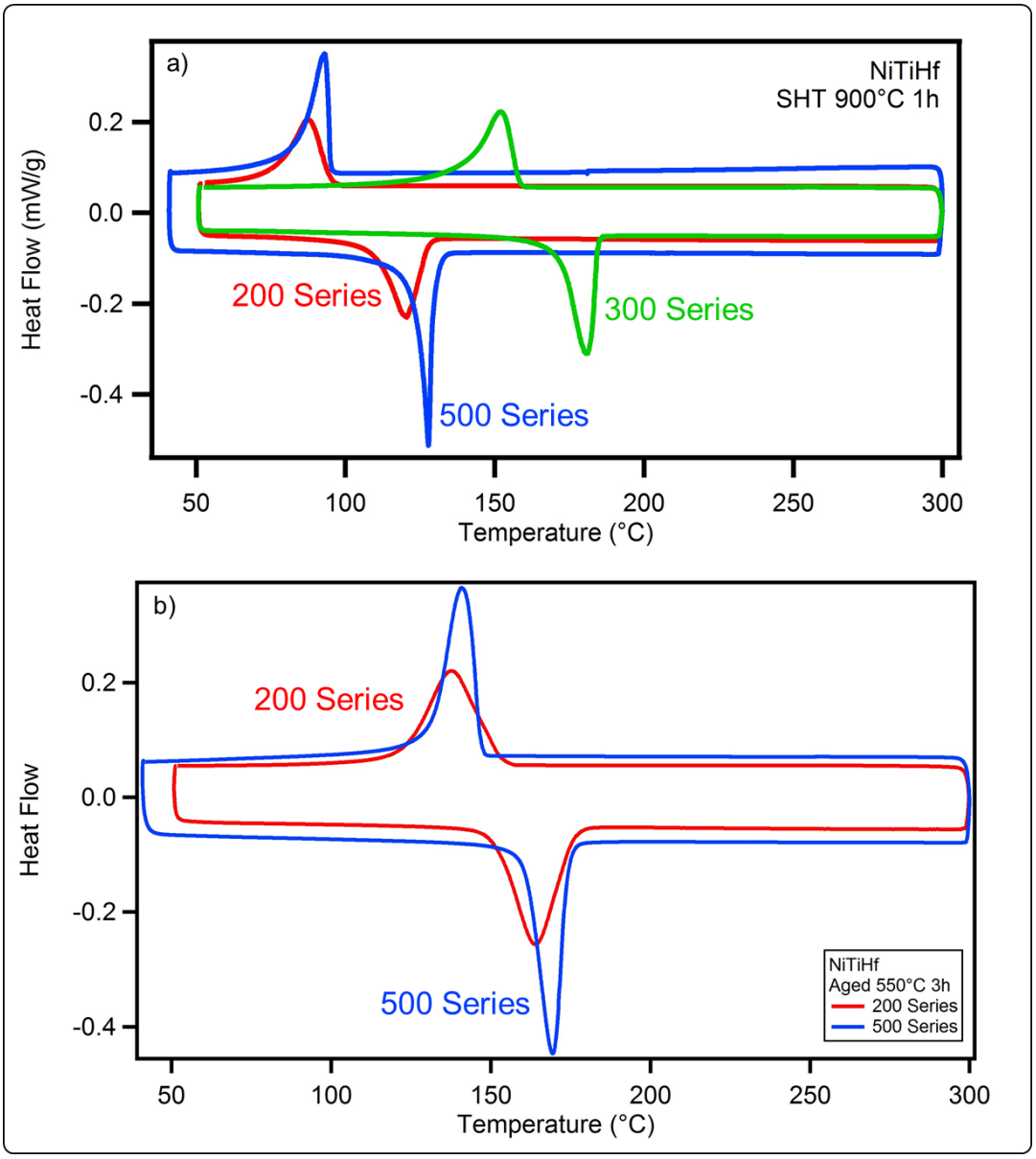

Figure 4.1: a) DSC curves for all material lots after solutionizing. b) DSC curves for the two material lots chosen to study, 200 and 500 series [67].

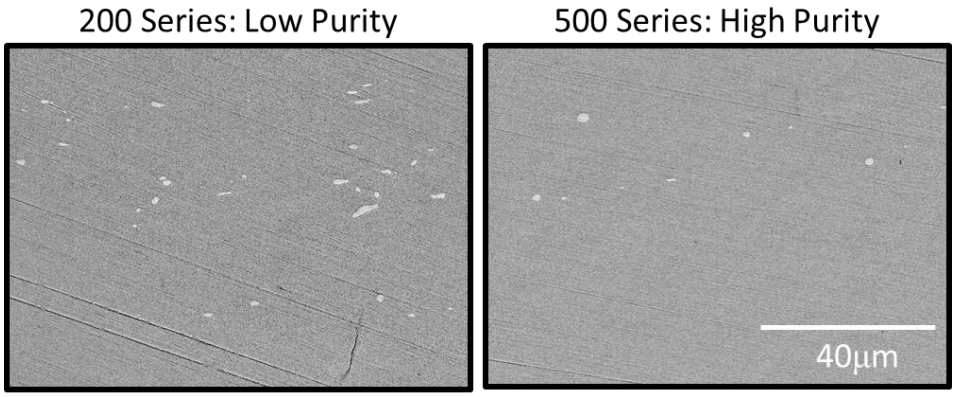

Figure 4.2: 200 Series and 500 Series NiTiHf SEM images [68].

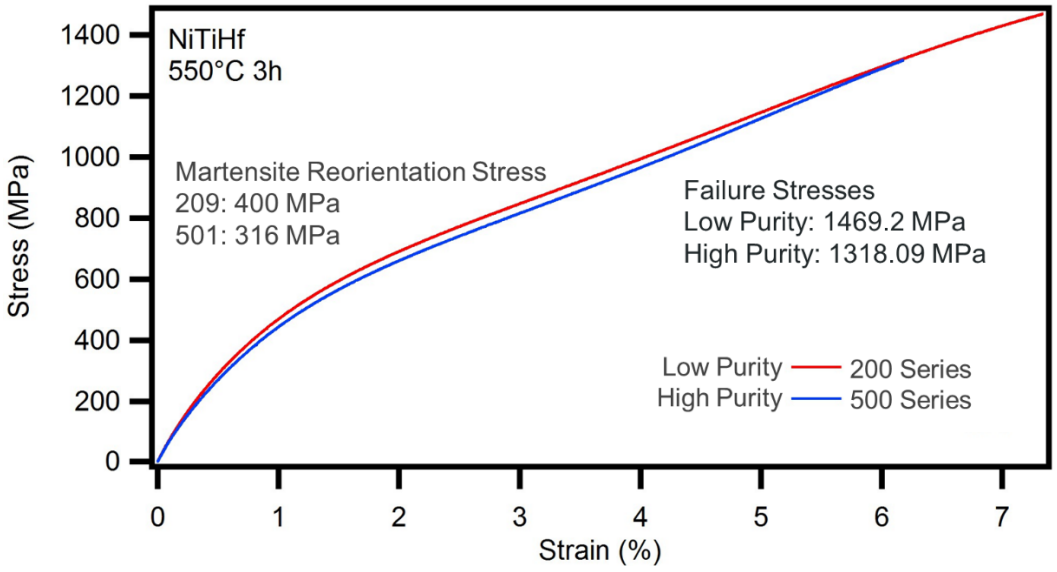

Figure 4.3: Ultimate tensile test of high and low purity NiTiHf [67].

The final portion of the preliminary testing consisted of ultimate tensile tests and pseudoelastic characterization of dogbone test samples. The ultimate tensile tests were performed at room temperature, and can be seen in Figure 4.3. While these results appear

similar, their pseudoelastic responses, Figure 4.4, better illustrate the difference in the material.

Although the low purity (200 series) NiTiHf failed at higher strains and loads during the ultimate tensile and the pseudoelastic characterization tests, the pseudoelastic response of the high purity material is clearly more stable. For comparison, after being strained to 6%, the high purity system had accumulated approximately 0.3% irrecoverable strain while the low purity system was over 1%. In order to induce pseudoelasticity, the test chamber was kept to a constant 50°C above the austenite finish temperature, or 178°C and 181°C for the low and high purity systems, respectively.

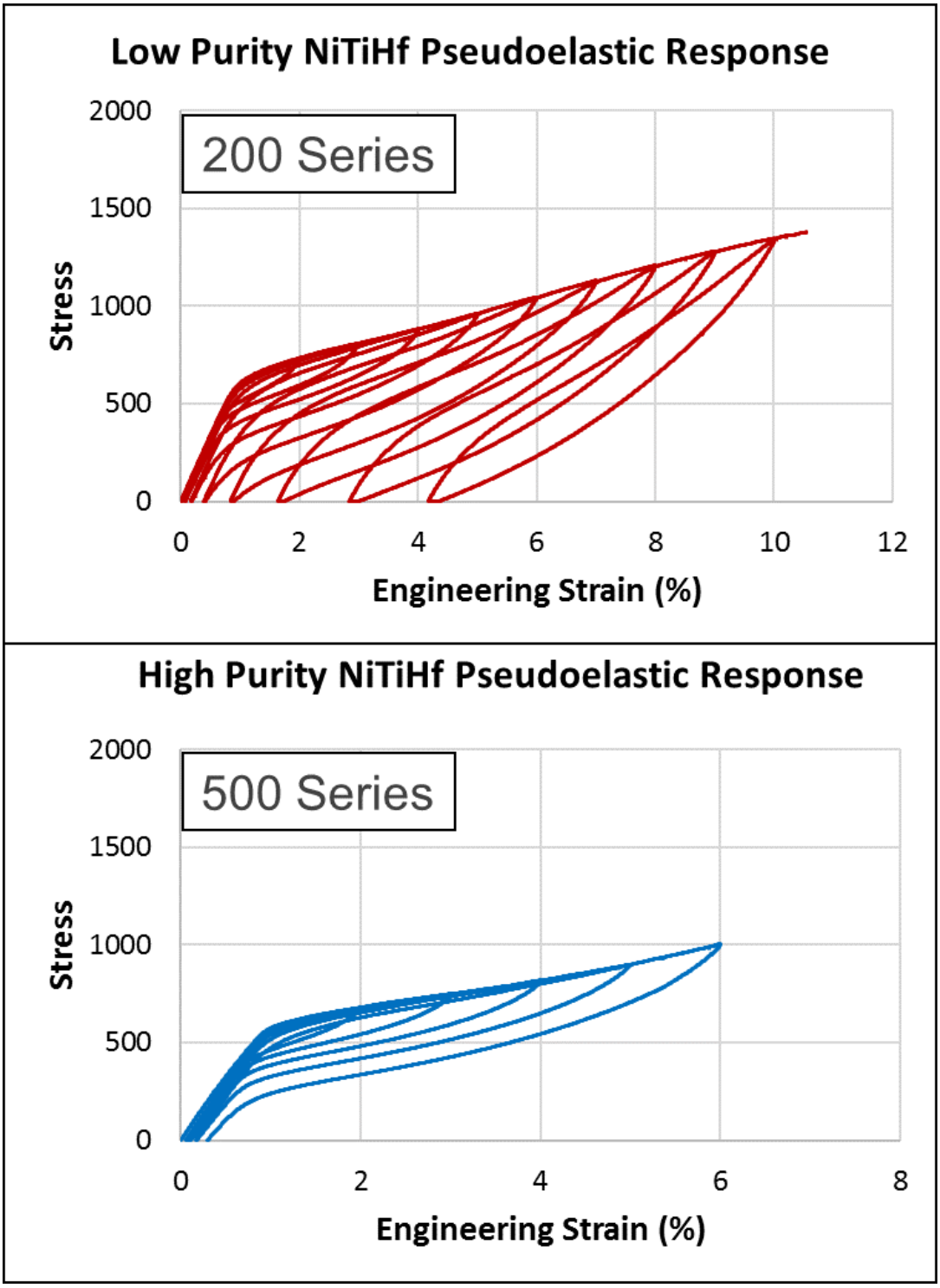

Figure 4.4: Pseudoelastic comparison of low (left) and high (right) purity NiTiHf material systems.

4.2 Low Purity NiTiHf: 200 Series Characterization

Prior to the main characterization of the NiTiHf material system, a scoping study was performed to select material processing steps. These results are summarized in Appendix C. From these results, it was found that polishing (mechanical or electrochemical) reduced the actuation fatigue life and performance. Additionally, allowing the actuators to exceed 300°C was found to significantly shorten the fatigue life; therefore, a temperature limit was imposed on the cycle control. The study of the low purity NiTiHf series consists of two parts: isobaric characterization and the effects of variable loading.

All isobaric characterization test specimens were loaded with a constant weight which was determined by the original cross-section and target load. The linear and stepwise loading paths were also held constant throughout the test and calibrated with the original cross-sectional area. To account for the transformation induced plasticity and ensure consistent mechanical loading for the stepwise and linear loading paths, adjustments were made throughout the test utilizing a turnbuckle connected in series with a load cell.

4.2.1 Isobaric Characterization: Low Purity NiTiHf

The isobaric characterization test matrix consisted of seven isobaric tests with stresses ranging from 200-600MPa. The individual tests are listed in Table 4-2.

Table 4-2: Isobaric Characterization Test Matrix

Test Number	*Loading*	*Load (MPa)*
A1	Isobaric	200
A2	Isobaric	300
A3	Isobaric	300
A4	Isobaric	400
A5	Isobaric	400
A6	Isobaric	500
A7	Isobaric	600

The strain evolutions are shown in Figure 4.5-4.7 for the 200, 400, and 600MPa loading conditions. It was found that the 600MPa loading condition significantly reduced the fatigue life and resulted in increasing rates of plastic deformation (dimensional instability). The actuation strain was stable for the 200MPa case, while it decreased for the 300-500MPa cases.

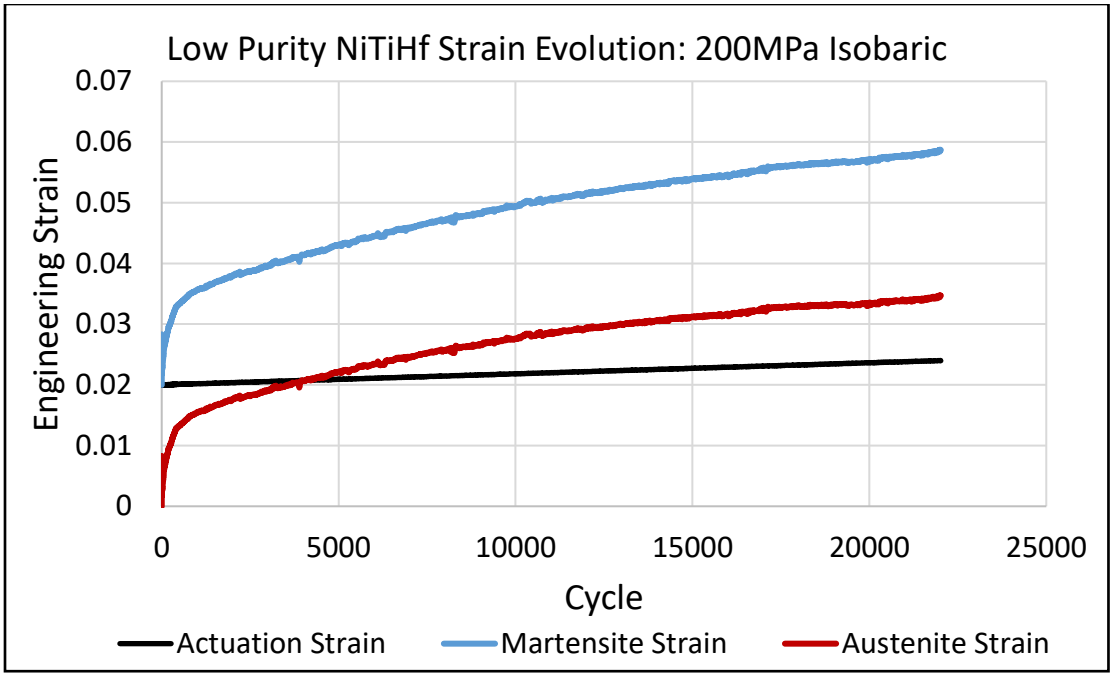

Figure 4.5: Strain evolution of low purity NiTiHf actuator under 200MPa isobaric load.

This decrease in actuation strain can be seen in Figure 4.6, where the actuation strain for the first cycle was above 3% and decreased to approximately 2.2% by the final cycle. It was found that this decrease in actuation strain was due to partial cycle resulting from shifting transformation temperatures. While tests which did not limit the temperature of the actuator maintained consistent actuation strain throughout their fatigue life, the number of cycles to failure decreased drastically and damage was visible on the surface of the actuators.

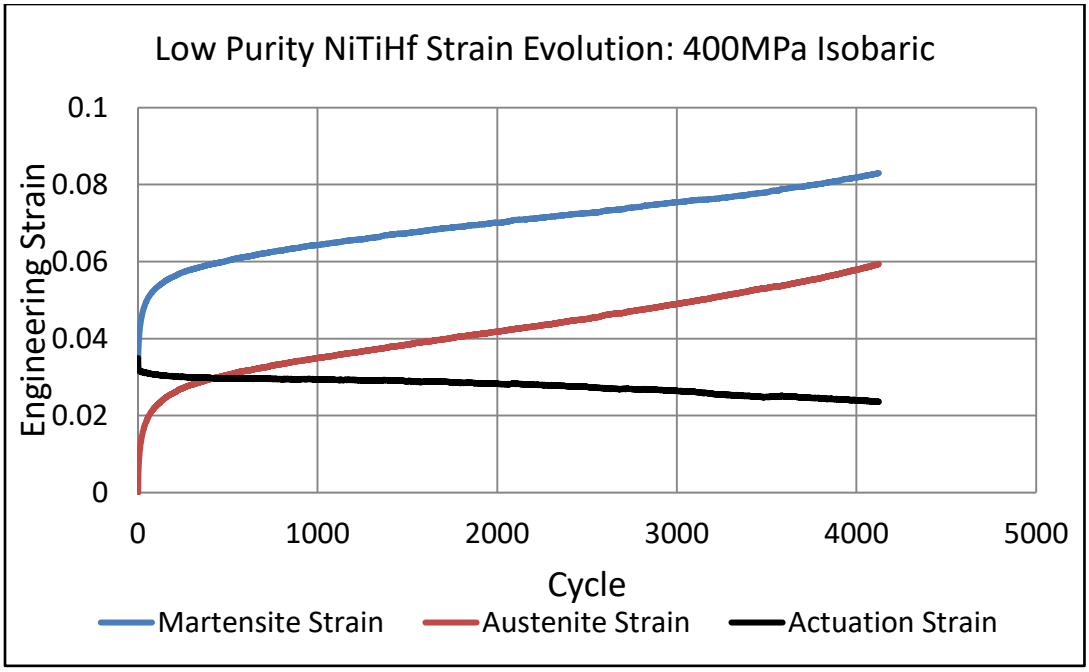

Figure 4.6: Strain evolution of low purity NiTiHf actuator under 400MPa isobaric load.

While the actuation strain initially began to decrease in the 600MPa test, similar to the response seen in the 300-500MPa tests, it began to increase once the actuator became dimensionally unstable, as shown in Figure 4.7. Due to the extremely poor fatigue response at 600MPa, it was determined to be outside of the operating range of this material.

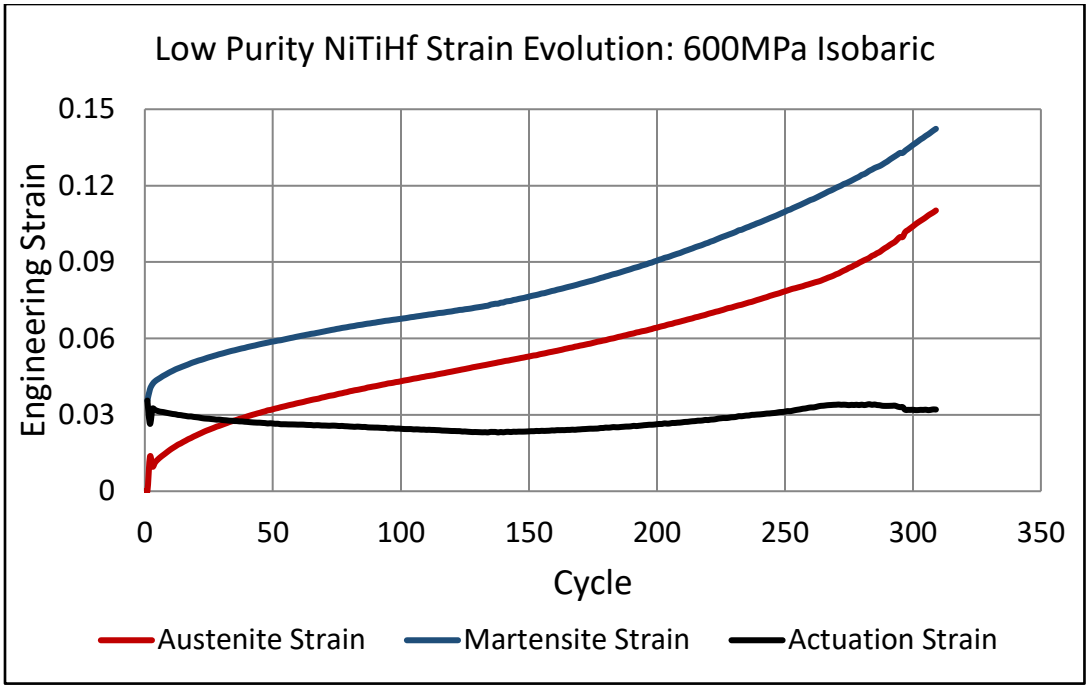

Figure 4.7: Strain evolution of low purity NiTiHf actuator under 600MPa isobaric load.

The isobaric results from the test matrix in Table 4-2 are summarized in Table 4-3, and the actuation strain as a function of the applied stress (H^{cur}) is shown in Figure 4.8. Due to the evolution of the transformation temperatures and the material temperature limit, only partial cycles were achievable for portions of the fatigue life in each of the 300-500MPa tests. Therefore, only the initial transformation strain was utilized for the isobaric tests when calibrating H^{cur}.

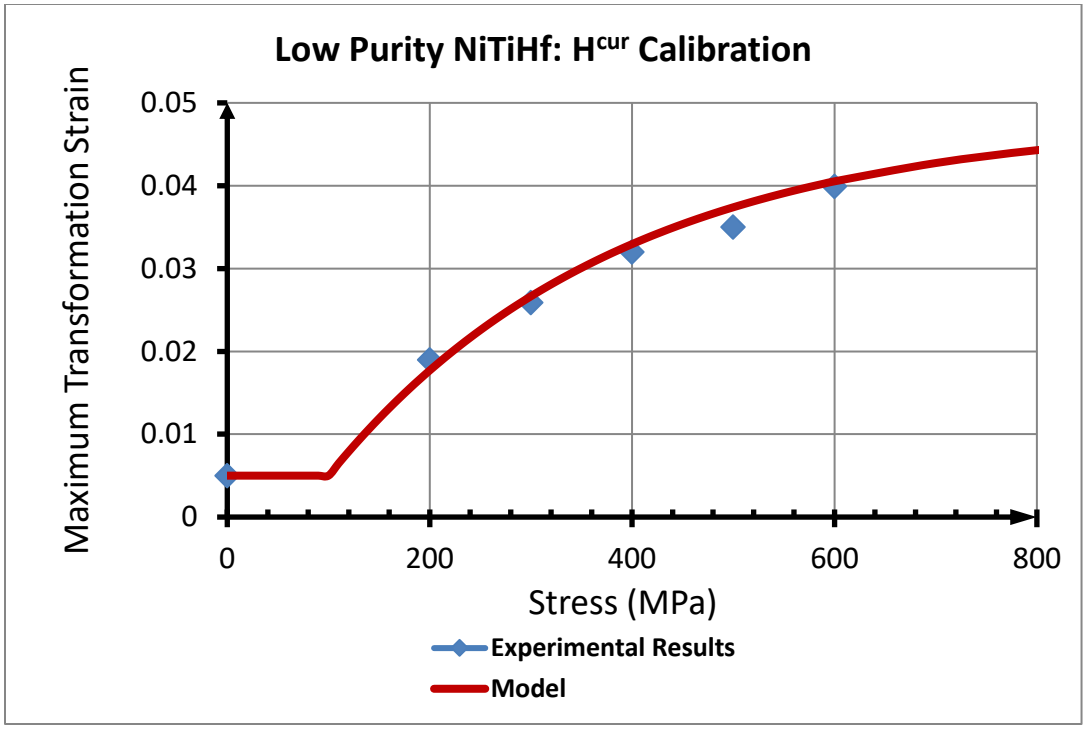

Figure 4.8: H^{cur} calibration for low purity NiTiHf (200 series).

Table 4-3: Summary of Low Purity NiTiHf Isobaric Test Results.

Test	*Load [MPa]*	*Cycles to Failure*	*Avg. Actuation Strain*
A1	200	21258	2.12%
A2	300	11396	2.23%
A3	300	9742	2.54%
A4	400	4889	2.80%
A5	400	3507	3.29%
A6	500	7388	1.38%
A7	600	309	2.99%

4.2.2 Effect of Loading Path on Low Purity NiTiHf Actuation Fatigue

After the isobaric characterization tests were completed, tests with variable loading conditions were performed in order to gauge the response of the material to variable loading, as well as provide the data necessary to validate fatigue lifetime prediction methods. The variable loading test matrix for the low purity NiTiHf is shown in Table 4-4. Four different loading paths were considered, and two tests were performed at each stepwise loading condition to ensure repeatability for the experimental methods which induced stepwise loading.

Table 4-4: Variable Loading Test Matrix for Low Purity NiTiHf

Test Nomenclature	*Loading*	*Load Max [MPa]*	*Load Min [MPa]*
SW1, SW2	Stepwise	300	0
SW3, SW4	Stepwise	400	0
L1	Linear	400	300
L2	Linear	500	300

As seen with the equiatomic NiTi characterization, the linear loading increased the fatigue life. The actuators with stepwise loading paths also saw an increase in fatigue life, however, not to the same extent. These results are summarized in Table 4-5. Due to the fact that, for NiTiHf, the transformation strain increased very slowly with the applied

load, relative to equiatomic NiTi, the increase in fatigue life resulting from linear loading paths was smaller than what was observed with the equiatomic NiTi material system.

Table 4-5: Summary of Low Purity NiTiHf Variable Loading Tests

Test	*Loading Path*	*Load Max [MPa]*	*Load Min [MPa]*	*Cycles to Failure*
SW1	Stepwise	300	0	17354
SW2	Stepwise	300	0	16572
SW3	Stepwise	400	0	6127
SW4	Stepwise	400	0	6706
L1	Linear	400	300	6605
L2	Linear	500	300	5263

4.3 High Purity NiTiHf: 500 Series Characterization

Due to the differences noted in Section 3.3 between the low and high purity NiTiHf material lots, the isobaric characterization was repeated to better understand the material, as well as quantify the differences between the two material systems. Two linear loading tests were completed in addition to the isobaric characterization. As with the low purity system, the load range of the linear loading was kept within load range explored by the isobaric characterization.

Based on material availability, additional isobaric characterization tests were performed on the high purity NiTiHf. The isobaric characterization test matrix can be seen in Table 4-6. Due to the inability of the low purity NiTiHf series to sustain 600MPa

and the improbability of an actuator application requiring or being designed for that load, the maximum load studied was 550MPa. A temperature limit of 300°C was also implemented to prevent temperature induced damage to the actuators for the isobaric characterization study.

Table 4-6: Isobaric Characterization Test Matrix: High Purity NiTiHf

Test Condition Nomenclature	*Loading*	*Load (MPa)*	*Number of Tests*
Iso200	Isobaric	200	2
Iso300	Isobaric	300	3
Iso400	Isobaric	400	3
Iso500	Isobaric	500	2
Iso550	Isobaric	550	2

Similar to the low purity NiTiHf, the dogbone actuators exhibited very stable strain evolutions as well as decreasing transformation strains. Representative strain evolutions can be seen for 300 and 400MPa in Figures 4.9 and 4.10, respectively. When loaded with 300MPa, the dogbone actuators lasted approximately 15,000 cycles and exhibited initial actuation strains between 3% and 3.5%. Increasing the mechanical load to 400MPa resulted in initial actuation strains of 3.5% to 4%; however, due to the increased load, the actuation strain decreased more quickly over a shorter fatigue life.

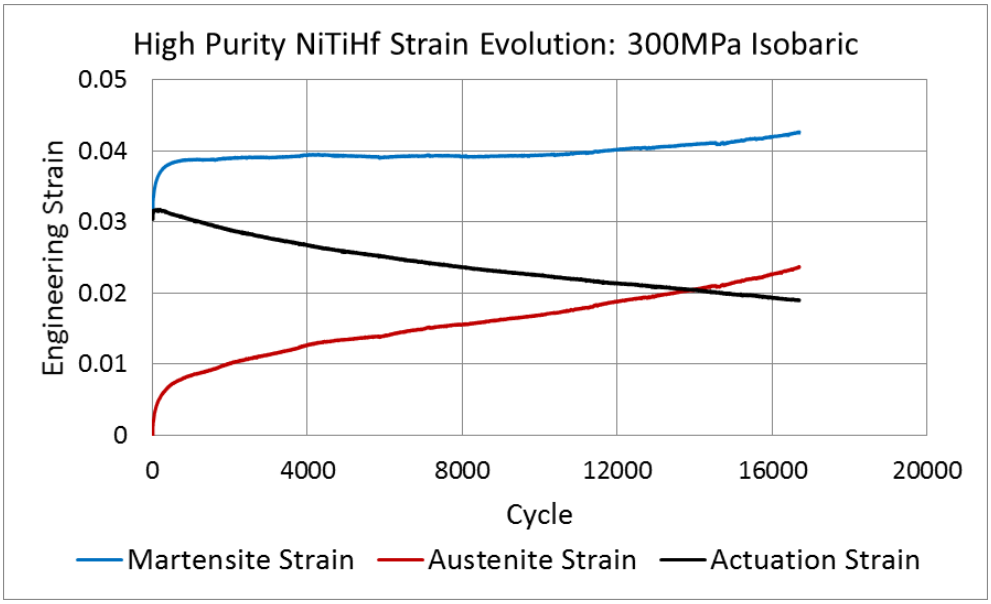

Figure 4.9: High purity NiTiHf strain evolution for 300MPa isobaric loading.

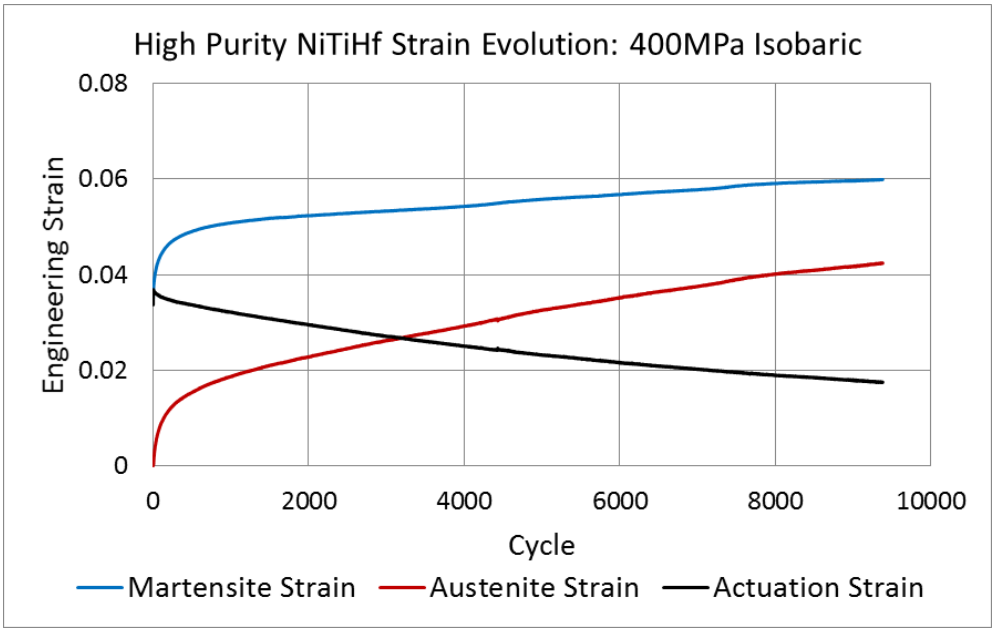

Figure 4.10: High purity NiTiHf strain evolution for 400MPa isobaric loading.

This decrease in actuation strain due to increasing transformation temperatures can also be seen in the hysteresis evolution, shown in Figure 4.11 for a 300MPa test, as the recovered strain decreases and the reverse transformation is no longer as abrupt.

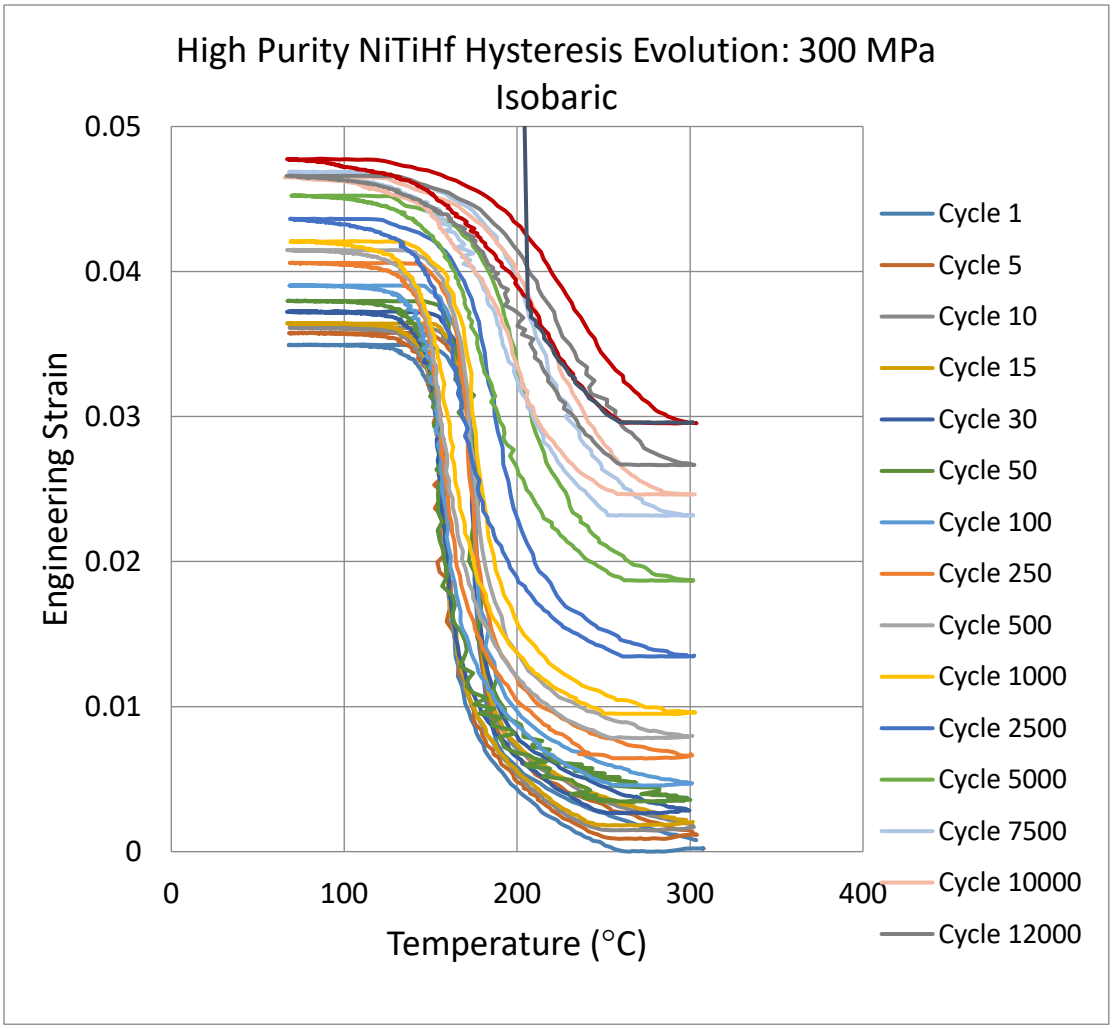

Figure 4.11: High purity NiTiHf hysteresis evolution for 300MPa isobaric loading; failure occurred at approximately 200°C and 4% engineering strain and is shown in figure by sharp increase in strain during cycle 14,607.

A decrease in transformation strain was observed to a much more severe extent in the 500 and 550MPa isobaric tests. In Figure 4.12, the actuation strain for the 500MPa test shown begins at 4.3%; however, towards the end of the fatigue life, it is observed to be around 1.9%.

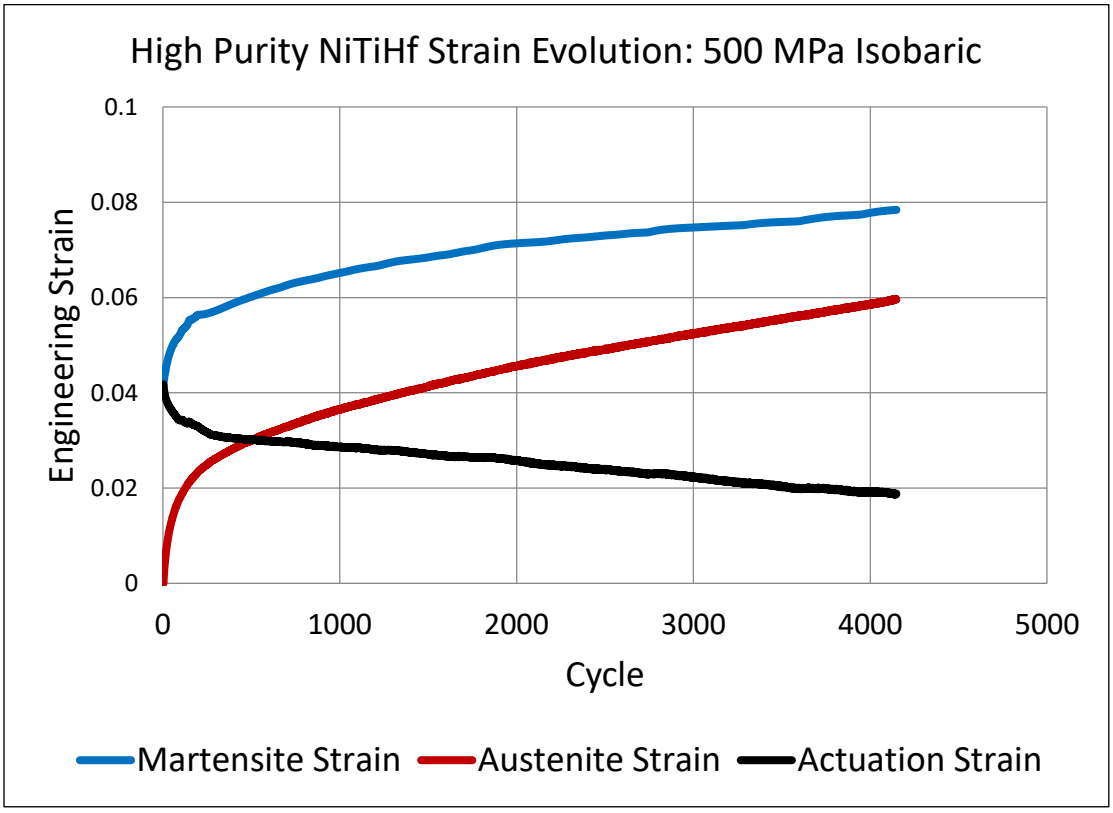

Figure 4.12: High purity NiTiHf strain evolution for 500 MPa isobaric loading.

Similar to the 400MPa case, the increase in the austenite finish temperature can be seen more clearly in the hysteresis evolution, which is shown in Figure 4.12 for the

500MPa test. Once the material had completed the training phase, approximately cycle 500 in Figure 4.13, the rate of actuation strain decrease appeared to stabilize.

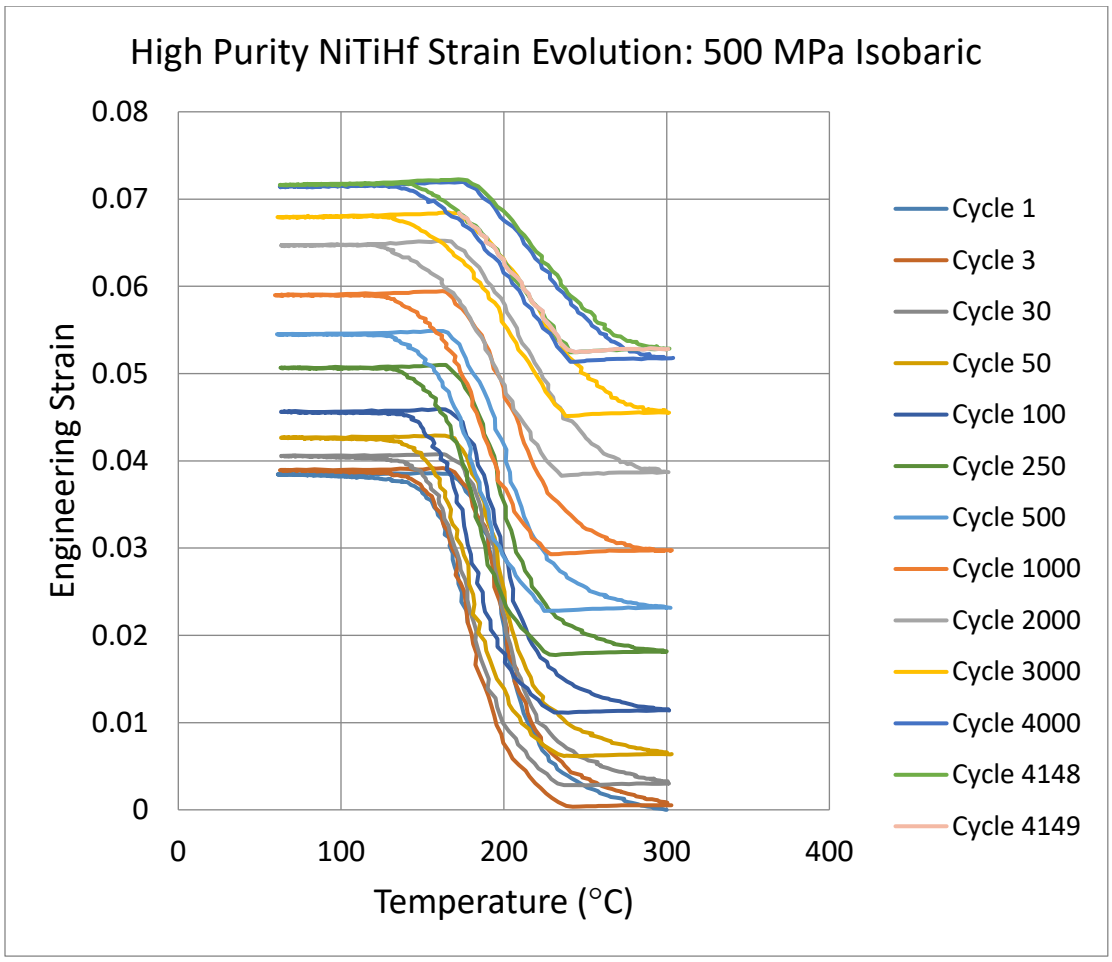

Figure 4.13: High purity NiTiHf strain evolution for 500 MPa isobaric loading.

Two actuation fatigue tests with linear loading were performed with loads of 200-400MPa and 300-400MPa. These tests are listed in Table 4-7. The 200-400MPa case

achieved an average actuation strain of 1.85% while the 300-400MPa test achieved an average actuation strain of 2%.

Table 4-7: Linear Loading Tests for High Purity NiTiHf

Test	*Loading Path*	*Initial Load Max*	*Initial Load Min*	*Cycles to Failure*
HPL 1	Linear	200	400	17650
HPL 2	Linear	300	400	8914

4.4 Comparison of Low and High Purity NiTiHf

Based on the preliminary observations between the two material lots, the high purity series was expected to outperform the low purity material system in terms of fatigue life and resistance to transformation induced plasticity. This expectation was confirmed when the strain evolutions were compared for the two material lots from the isobaric characterization. An example of this direct comparison can be seen in Figure 4.14 where a high and low purity NiTiHf dogbone were subjected to identical loads. Furthermore, the transformation strains for both actuators were consistent as well; however, the low purity actuator failed shortly after four thousand cycles while the high purity actuator exceeded nine thousand cycles.

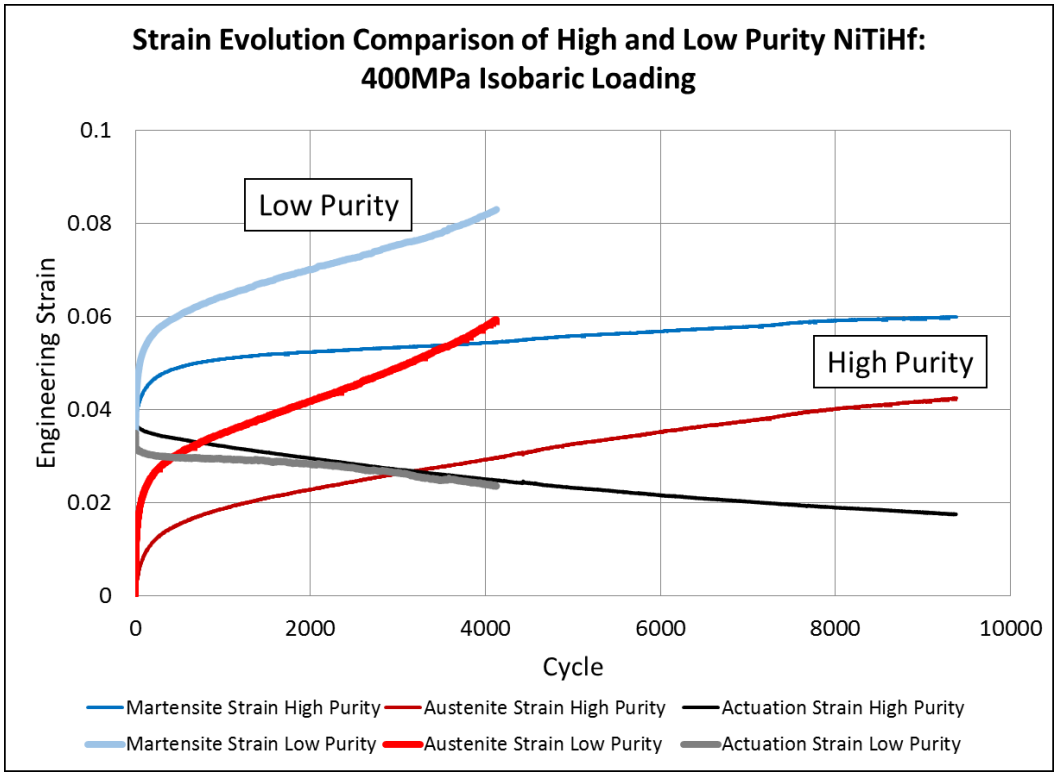

Figure 4.14: Strain evolution comparison between high and low purity NiTiHf dogbones which were subjected to 400MPa isobaric loading. The low purity data (shorter fatigue life) are shown in thick, lighter colored lines while the high purity data are shown in darker, thin lines (longer).

In the preliminary study performed by Karaman *et al.* [68], the main macroscopic and measurable difference between the high and low purity material systems was development of approximately 300% more irrecoverable strain after several pseudoelastic cycles. Although both material systems eventually stabilize their irrecoverable strain generation rate under actuation loading, the amount of austenite strain is much high when the stabilization occurs and the constant rate is also steeper. This stabilization occurs at approximately one thousand cycles in Figure 4.14, and the austenite rates are

approximately 10^{-5} and $3*10^{-6}$ for the low and high purity systems, respectively. While the development of the austenite strains in these two fatigue tests is due in part to the partial transformation, since their transformation strains decrease at approximately the same rate, the majority of this difference can be attributed to transformation induced plasticity. This same trend can also be observed in Figure 4.15, which compares the strain evolutions for high and low purity NiTiHf subjected to 300MPa isobaric loading.

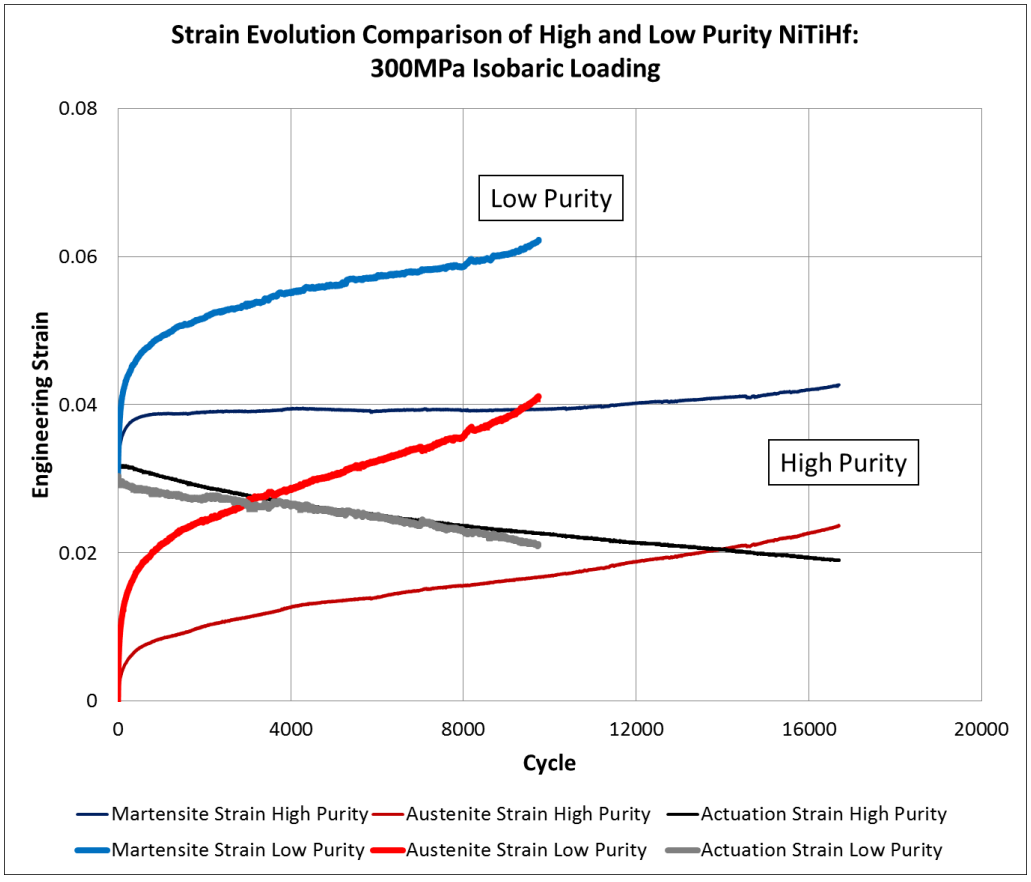

Figure 4.15: Strain evolution comparison between high and low purity NiTiHf dogbones which were subjected to 300MPa isobaric loading. The low purity data are shown in thick, lighter colored lines while the high purity data are shown in darker, thin lines.

4.4.1 DIC Comparison of Low and High Purity Actuation Fatigue Response

While there were measurable differences in the preliminary characterization and the macroscopic actuation fatigue response between the two NiTiHf lots, the most apparent difference was found when analyzing the DIC results. When analyzing the visual extensometry results of the equiatomic NiTi material and the DIC results of the Nickel-rich system, it can be concluded that localized deformation plays an important role in failure and determining where failure will occur. This was seen to be true also for the NiTiHf material systems, which tended to failure at localized strains between 5%-15% for the high purity and 10%-25% for the low purity material system.

In addition to the increased macroscopic and localized irrecoverable deformation, localized transformation strain was also observed in the low purity series. An example of this response can be seen in Figure 4.16, where the transformation strain is shown for a low purity NiTiHf sample under 400MPa with an upper cycle temperature of 350°C. Approximately 70% of the way through the fatigue life, localized transformation strain begins to develop, and, during the final two cycles, the transformation strain near the failure location was approximately 5.2% while the macroscopic strain (averaged over the gage section) was below 4%.

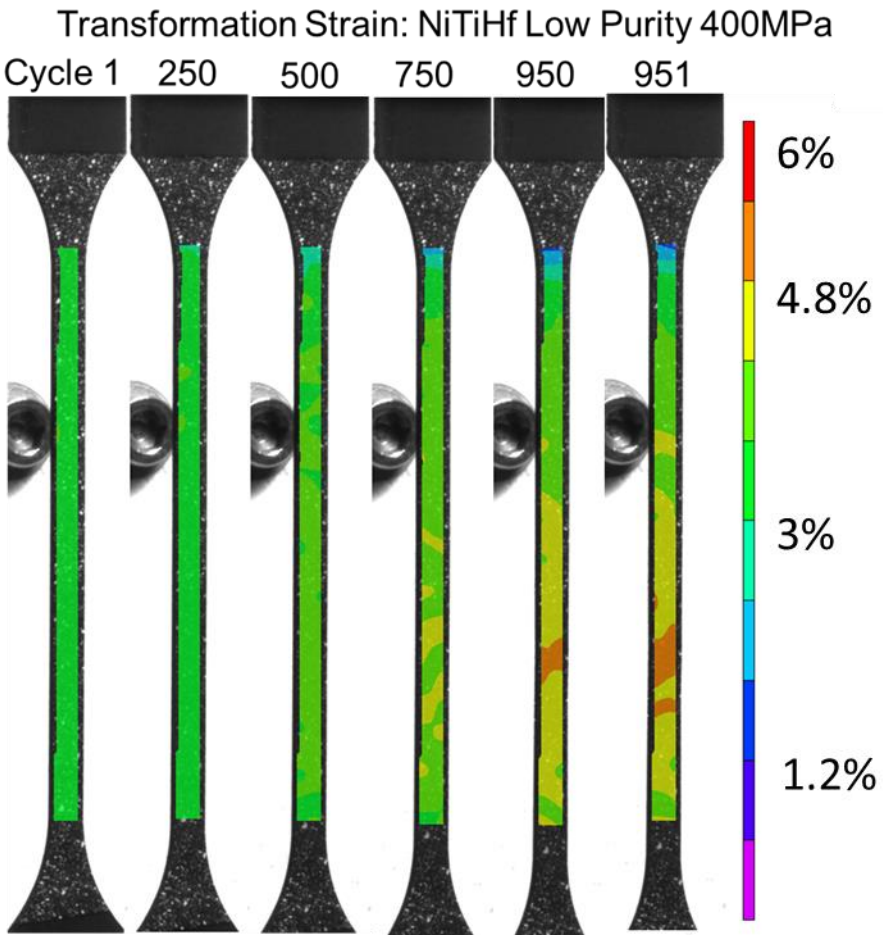

Figure 4.16: DIC results showing transformation strain for low purity NiTiHf subjected to 400MPa isobaric loading with a 350°C upper cycle temperature.

5 DEVELOPMENT AND IMPLEMENTATION OF FATIGUE LIFE PREDICTION METHODS

5.1 Overview of Actuation Fatigue Life Prediction Methods

This chapter consists of three sections: First, implementations for two fatigue life prediction methods based on available literature and data collected during this work are developed. These fatigue life prediction methods utilize both irrecoverable strain and actuation work based criteria. Second, these methods are calibrated for each of the data sets presented in Chapters 3 and 4, and then used to simulate the isobaric characterization experimental results. Finally, the most promising fatigue life prediction methods are used to determine the actuation fatigue lives for actuators with variable loads and geometries.

5.1.1 Irrecoverable Strain Criteria

In Lagoudas *et al.* [58], it was noted that there was a correlation between accumulated plastic strain and cycles to failure. A method similar to the Coffin-Manson law was implemented to describe this relationship:

$$\varepsilon^{tr} = \alpha N_f^{\beta} \tag{5.1}$$

In Equation 5.1, α and β are fitting parameters; they are referred to as the fatigue ductility coefficient and fatigue ductility exponent, respectively, in classical low-cycle mechanical fatigue of metals. An example of this correlation can be seen in Figure 5.1 where $\alpha = 1.6$ and $\beta = -.308$.

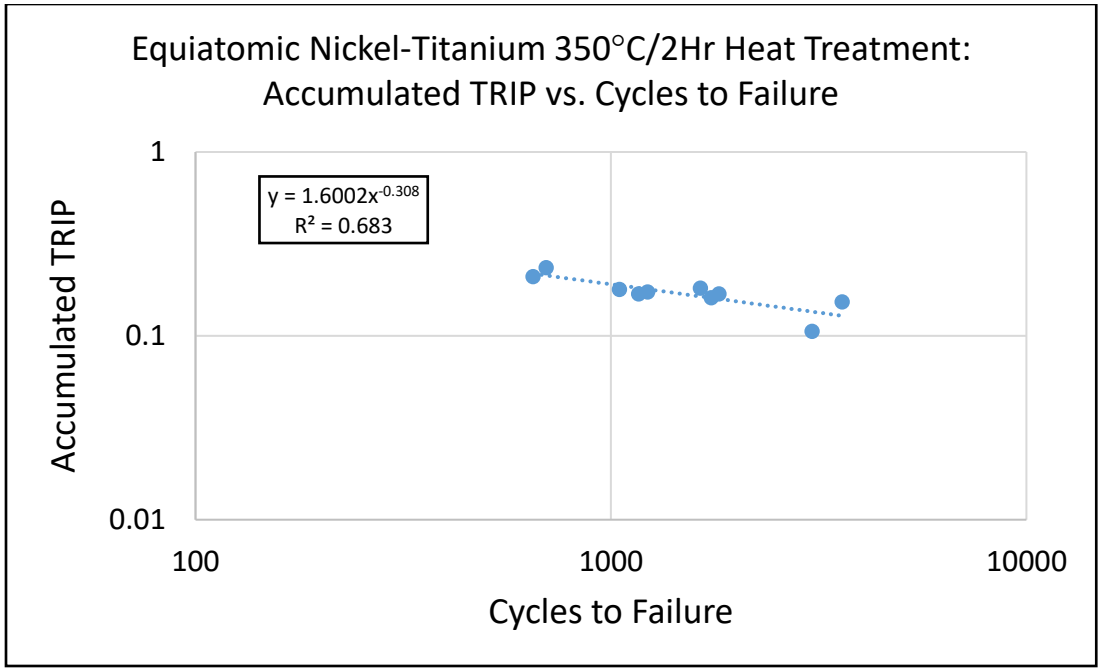

Figure 5.1: Accumulated TRIP (engineering strain) correlated with cycles to failure for equiatomic NiTi with a 350°C/2Hr heat treatment.

While this relationship does not directly lend itself to the prediction of the actuation fatigue life for a given loading condition, it can be utilized in conjunction with the transformation induced plasticity (TRIP) model proposed by Lagoudas *et al.* [64,65] in order to determine the expected fatigue life of an actuator. Additionally, it can be used as a fatigue limit during the monitoring of live testing; during each cycle, the actuator accrues more TRIP and the cycle count increases, thus moving the actuator closer to the line captured in Equation 5.1.

5.1.2 Actuation Work Criteria

Early actuation fatigue studies noted the relationship between applied stress and cycles to failure, as well as the relationship between transformation strain and cycles to failure. These methods are similar to well-established models in classical mechanical fatigue for standard metals (e.g. steel and aluminum), such as the Wöhler S-N curve, which relates applied stress to fatigue life in high cycle fatigue, and the Coffin-Manson relationship, which relates plastic strain amplitude to fatigue life in low cycle fatigue.

Based on these well-established fatigue lifetime prediction methods, the next step would be to analyze the actuation work extracted from the SMA system. Many previous studies have noted the strong correlation between actuation work density and cycles to failure [35–41]. Due to the strength of the correlation between cycles to failure and actuation work density, a power-law equation, as shown in Equation 5.2, can be used to accurately determine the fatigue life of dogbones subjected to actuation loading under isobaric loading.

$$\mathrm{N}_f = \left(\frac{\widehat{\Phi}}{a}\right)^{-b} \tag{5.2}$$

In Equation 5.2, $\widehat{\Phi}$ is the actuation work density, N_f represents the cycles to failure, a and b are fitting parameters determined through isobaric testing. The actuation work density can be experimentally determined by multiplying the actuation strain by the applied load for isobaric loading conditions. To utilize this relationship as a predictive method, the actuation strain and loading path must be determined. For a given load, the actuation strain as a function of stress, or H^{cur}, can be determined through isobaric

actuation cycles using the phenomenological model developed by Lagoudas *et al.* [1] and discussed in Chapters 3 and 4. The actuation work can be predicted for a given isobaric load by multiplying the actuation strain by the applied load, as shown in Equation 5.3.

$$\widehat{\Phi} = \sigma * H^{cur} \tag{5.3}$$

5.2 Implementation, Evaluation, and Calibration of Lifetime Prediction Methods

The actuation fatigue characteristics of five material systems were studied: Equiatomic NiTi (two heat treatments), Nickel-Rich NiTi, a low purity NiTiHf, and a high purity NiTiHf. The experimental results for these material systems was summarized in an actuation fatigue database for both material characterization, as well as evaluation for fatigue lifetime prediction methods. In this section, each of the prediction methods are discussed and evaluated utilizing the collected actuation fatigue data.

5.2.1 Accumulated Transformation Induced Plasticity Criterion Calibration

As noted, by Lagoudas et al. [58] there is a strong correlation between cycles to failure and accumulated plastic strain (TRIP) for certain material systems. This correlation can be seen in four of the five material systems which were studied. In Figures 5.2 and 5.3, this relationship is shown for both the 350°C/2hr and 375°C/2hr heat treatment, respectively.

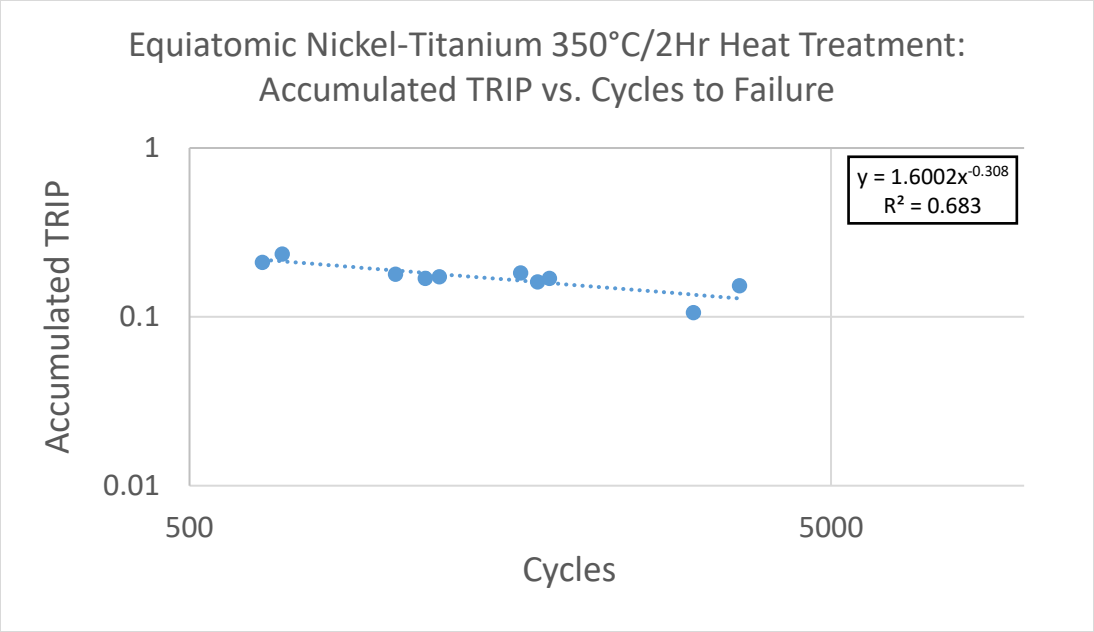

Figure 5.2: Accumulated TRIP (engineering strain) correlated with cycles to failure for equiatomic NiTi with a 350°C/2Hr heat treatment under isobaric loading of 100-300MPa.

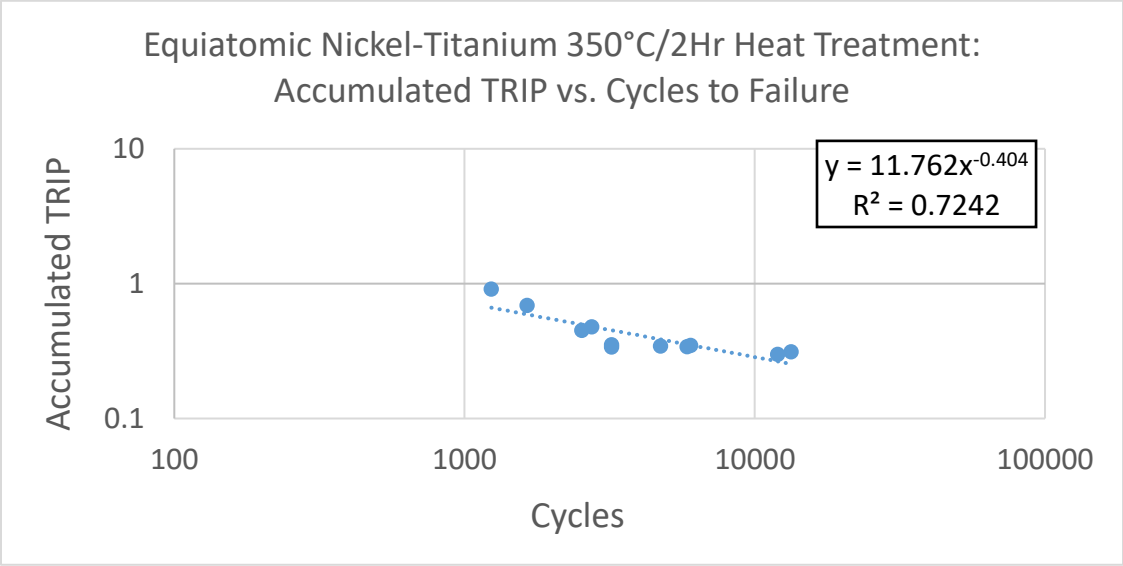

Figure 5.3: Accumulated TRIP (engineering strain) correlated with cycles to failure for equiatomic NiTi with a 375°C/2Hr heat treatment under isobaric loading of 150-350MPa.

For both heat treatments of Equiatomic NiTi, there was shown to be a correlation between accumulated TRIP and cycles to failure. The strength of this correlation is extremely significant, as it represents the predictive limits of an accumulated TRIP-based prediction method. Figures 5.4 and 5.5 demonstrate that a similar relationship can be determined for both the low and high purity NiTiHf.

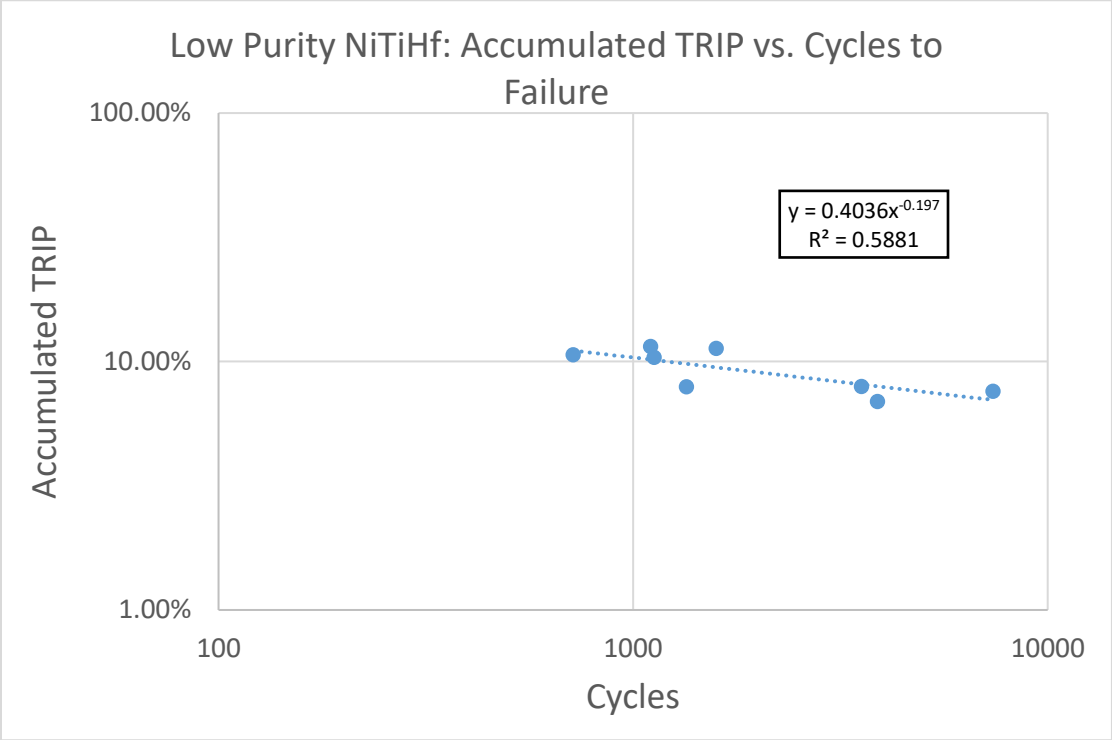

Figure 5.4: Accumulated TRIP (engineering strain) correlated with cycles to failure for low purity NiTiHf under 200-500MPa isobaric loading.

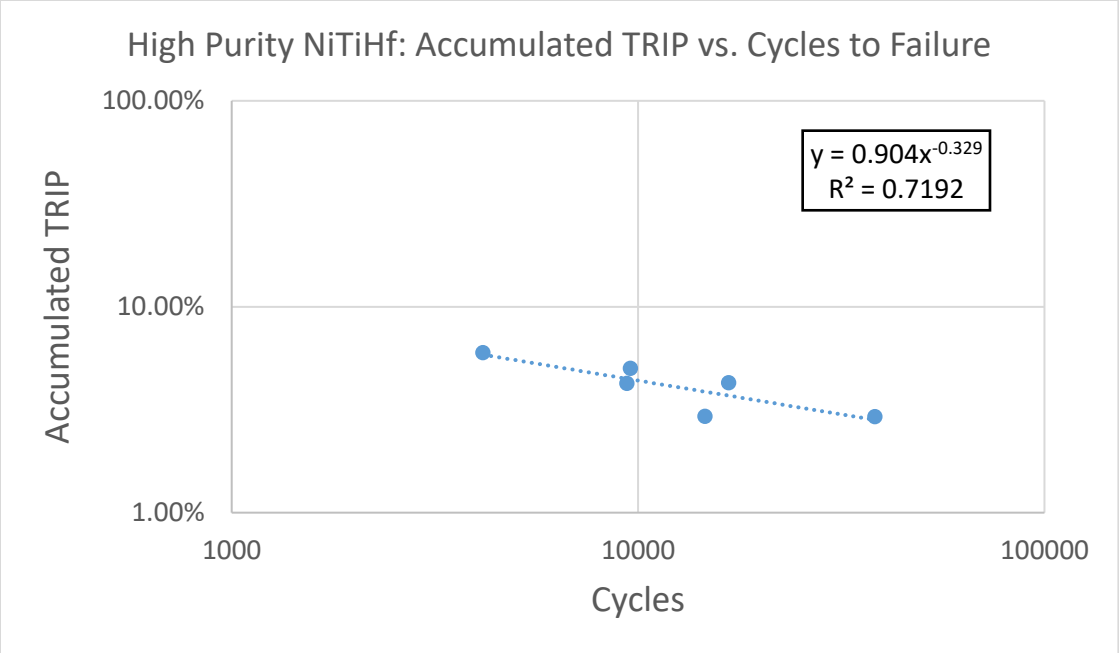

Figure 5.5: Accumulated TRIP (engineering strain) correlated with cycles to failure for high purity NiTiHf under 200-500MPa isobaric loading.

One of the discernable trends between these two sets of data for equiatomic NiTi and NiTiHf is that the correlation is stronger for the material systems with higher accumulated TRIP; the 375°C/2hr heat treatment has more accumulated TRIP and a stronger correlation than the material system with the 350°C/2hr heat treatment, and the low purity NiTiHf has a stronger correlation than the high purity, which has significantly lower accumulated TRIP. However, for the material system with the lowest TRIP, there is almost no correlation between accumulated TRIP and cycles to failure; this is illustrated in Figure 5.6, which contains the characterization data for the Nickel-Rich NiTi material system presented in Section 3.2.2.

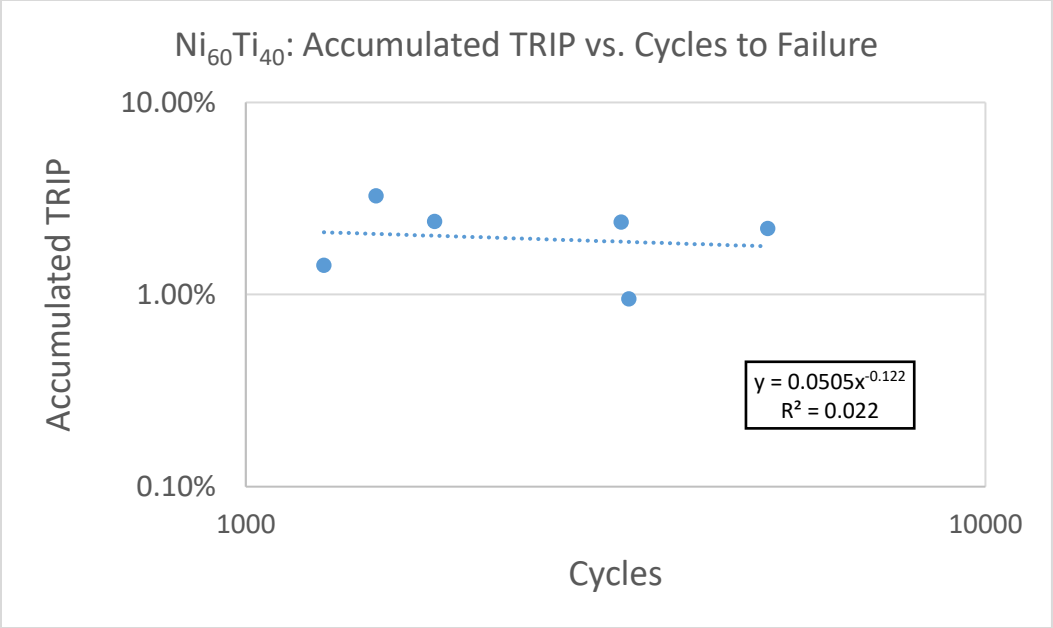

Figure 5.6: Accumulated TRIP (engineering strain) correlated with cycles to failure for $Ni_{60}Ti_{40}$ under 150-300MPa isobaric loading.

In order to develop a predictive method based on this experimental observation, the TRIP model developed by Lagoudas *et al.* [64, 65, 69] was utilized in conjunction with the failure curve relating TRIP to cycles to failure. The solution method for predicting failure with this TRIP-based criterion consists of finding the intersection between the failure curve (Equation 5.1) and the predicted cyclic TRIP evolution. This method is shown graphically in Figure 5.7.

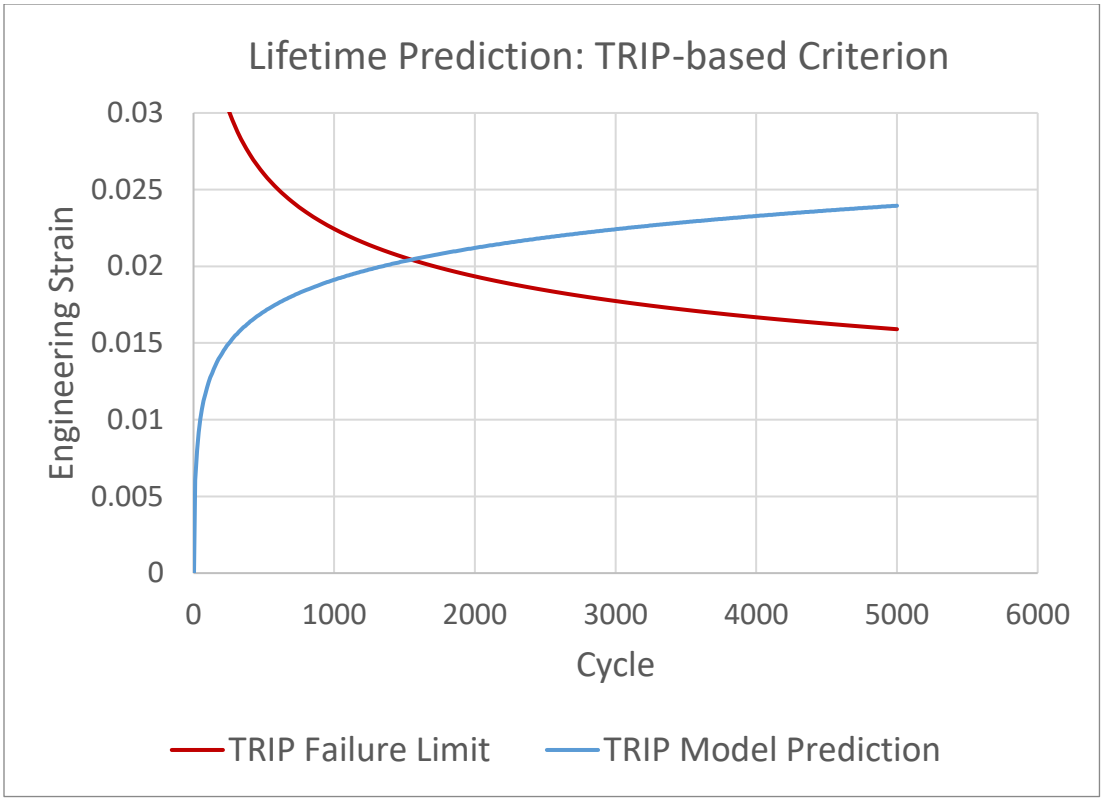

Figure 5.7: Graphical representation of implementation of TRIP-based criterion for actuation fatigue lifetime prediction. Failure is predicted when the accumulated TRIP reaches the TRIP failure limit (Equation 5.1), approximately cycle 1,500 as shown. Parameters from $Ni_{60}Ti_{40}$ system were utilized.

From Figure 5.7, it is clear that the error can be interpreted in either accumulated TRIP or cycles to failure. Due to the fact that the goal of this implementation was to accurately predict the actuator life, the error is expressed relative to the experimental cycles to failure. In the following tables, the simulation error of this prediction method is listed for each of the six data sets, starting with equiatomic NiTi. It should be noted that the data in these tables were utilized to calibrate the prediction method, so these are simulations rather than predictions.

Table 5-1: TRIP Criterion Predictions for Equiatomic NiTi 350°C/2 hours Heat Treatment

Heat Treatment	*Mechanical Load*	*Accumulated TRIP*	*Cycles to Failure*	*TRIP Criterion Simulation*	*Error (%)*	*Absolute Error (%)*
350°C, 2 hours	100	0.106	3052	6722	120%	120%
350°C, 2 hours	100	0.153	3601	2042	-43%	43%
350°C, 2 hours	150	0.161	1745	1731	-1%	1%
350°C, 2 hours	150	0.169	1820	1479	-19%	19%
350°C, 2 hours	200	0.173	1226	1371	12%	12%
350°C, 2 hours	200	0.169	1166	1479	27%	27%
350°C, 2 hours	200	0.179	1048	1227	17%	17%
350°C, 2 hours	200	0.182	1642	1163	-29%	29%
350°C, 2 hours	300	0.21	650	731	12%	12%
350°C, 2 hours	300	0.235	698	507	-27%	27%
Average					***7%***	***31%***

Table 5-2: Equiatomic: TRIP Criterion Predictions for Equiatomic NiTi 375°C/2 hours Heat Treatment

Heat Treatment	*Mechanical Load*	*Accumulated TRIP*	*Cycles to Failure*	*TRIP Criterion Simulation*	*Error (%)*	*Absolute Error (%)*
375°C, 2 hours	150	0.299	12000	7977	-34%	34%
375°C, 2 hours	150	0.312	13336	5918	-56%	56%
375°C, 2 hours	200	0.352	3209	6448	101%	101%
375°C, 2 hours	200	0.34	5841	6495	11%	11%
375°C, 2 hours	200	0.339	3211	6219	94%	94%
375°C, 2 hours	200	0.345	4734	6045	28%	28%
375°C, 2 hours	200	0.349	6012	3222	-46%	46%
375°C, 2 hours	250	0.45	2536	2761	9%	9%
375°C, 2 hours	250	0.479	2745	1119	-59%	59%
375°C, 2 hours	300	0.69	1643	564	-66%	66%
Average					***-2%***	***50%***

From Tables 5-1 and 5-2, it is apparent that utilizing this TRIP-based criterion does not accurately capture the cycles to failure. Based on the strength of the correlation between cycles to failure, significant error was expected. While the average absolute error is significantly large, the averaged error in the prediction is relatively low, indicating that the fitting parameters determined during the calibration were properly calculated. Similar

results can be seen in Tables 5-3 and 5-4, which contain the low and high purity NiTiHf datasets, respectively.

Table 5-3: TRIP Criterion Predictions for Low Purity NiTiHf

Specimen Nomen-clature	*Mecha-nical Load*	*Upper Cycle Temp.*	*Accum-ulated TRIP*	*Cycles to Failure*	*TRIP Criterion Simulation*	*Error (%)*	*Absolute Error (%)*
HF207-15	300	350	0.0795	3561	3798	7%	7%
HF208-11	300	350	0.069	3890	7340	89%	89%
HF207-9	400	350	0.104	1124	1089	-3%	3%
HF207-10	400	350	0.113	1589	741	-53%	53%
HF207-17	400	350	0.1065	717	975	36%	36%
HF208-9	400	350	0.115	1103	683	-38%	38%
HF208-25	400	350	0.0792	1347	3866	187%	187%
HF207-7	500	350	0.076	7388	4683	-37%	37%
HF208-6	600	350	0.1423	309	254	-18%	18%
Average						**19%**	**52%**

Table 5-4: TRIP Criterion Predictions for High Purity NiTiHf

Specimen Nomen-clature	*Mecha-nical Load*	*Upper Cycle Temp.*	*Accum-ulated TRIP*	*Cycles to Failure*	*TRIP Criterion Simulation*	*Error (%)*	*Absolute Error (%)*
HF500-4	200	300	3.83%	38256	33632	-12%	12%
HF500-7	300	300	4.76%	14606	33286	128%	128%
HF500-10	300	300	2.38%	16698	10706	-36%	36%
HF500-8	400	300	6.00%	9378	10860	16%	16%
HF500-6	400	300	7.24%	9566	6547	-32%	32%
HF500-16	500	300	7.87%	4148	3846	-7%	7%
Average						**10%**	**39%**

Of all the material systems studied, the Nickel-Rich NiTi had the weakest correlation between cycles to failure and accumulated TRIP. As there is almost no correlation between the two experimental values, the slope of the fit shown in Figure 5.6 is nearly zero. For this reason, the error for prediction grows significantly for actuator specimens which had very low accumulated TRIP. This can be seen in Table 5-5:

Table 5-5: TRIP Criterion Predictions for $Ni_{60}Ti_{40}$

Specimen Nomen-clature	*Mecha-nical Load*	*Upper Cycle Temp.*	*Accum-ulated TRIP*	*Cycles to Failure*	*TRIP Criterion Simulation*	*Error (%)*	*Absolute Error (%)*
A2	150	150C	0.0221	5078	1074	-79%	79%
B2	200	150C	0.0095	3293	55496	1585%	1585%
B3	200	150C	0.0238	3217	760	-76%	76%
C3	250	150C	0.024	1800	731	-59%	59%
D1	300	150C	0.0142	1275	8483	565%	565%
D2	300	150C	0.0327	1500	173	-88%	88%
Average						**308%**	**409%**

5.2.2 Actuation Work Parameter Calibration

As discussed in Section 5.1.2, a simple relationship can be utilized to describe the correlation between actuation work density and cycles to failure for isobaric testing. The expected accuracy of the prediction method can be determined by examining the strength of the correlation on which the method is based. For this reason, the actuation energy-based method appears to be significantly more promising, as there is clearly a very strong correlation between cycles to failure and actuation energy density for all of the material

systems studied. In Figures 5.8 and 5.9, the actuation work vs. cycles to failure are shown for the two equiatomic NiTi data sets.

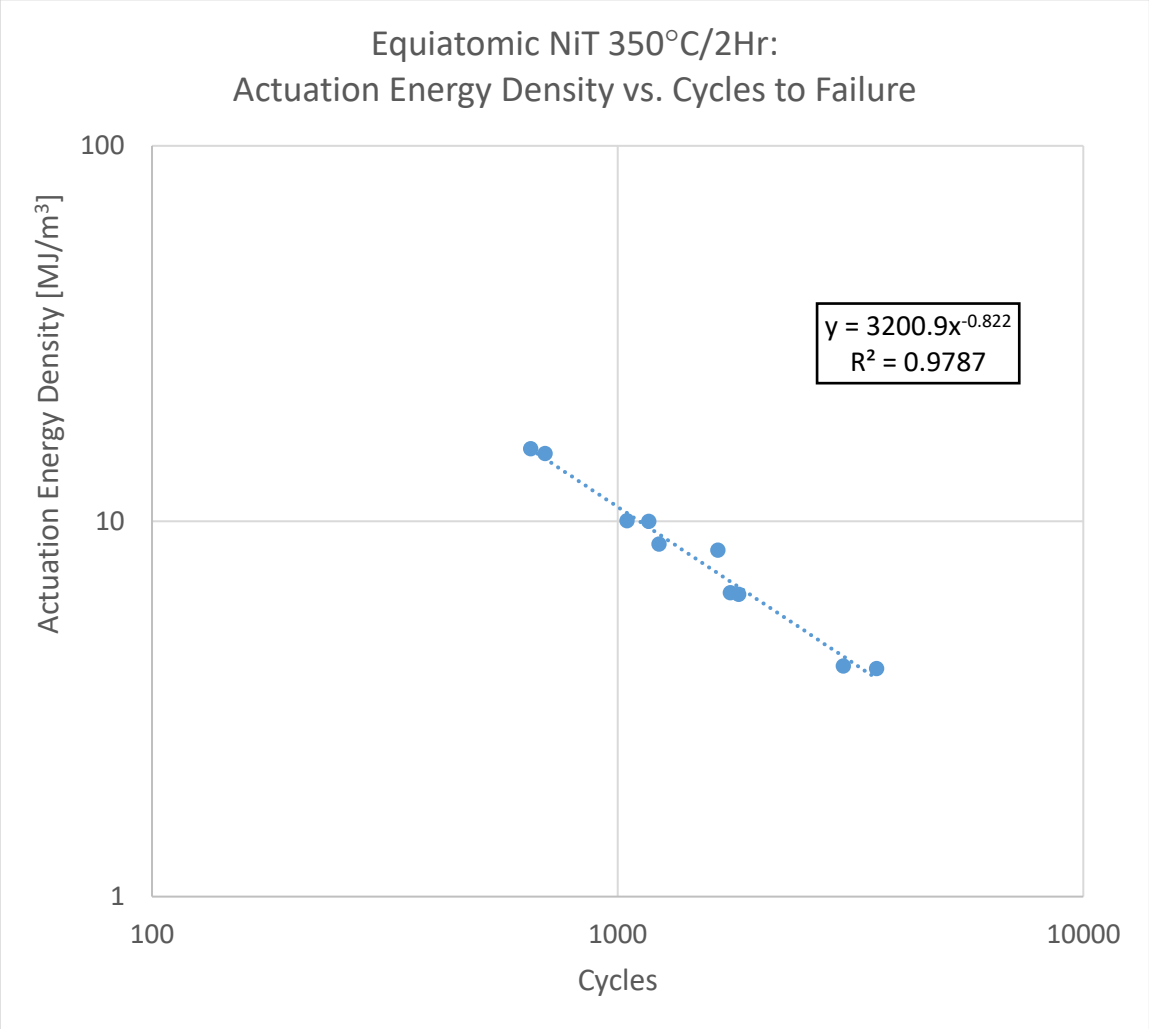

Figure 5.8: Actuation energy density correlated with cycles to failure for equiatomic NiTi with a 350°C/2Hr heat treatment under 100-300MPa isobaric loading.

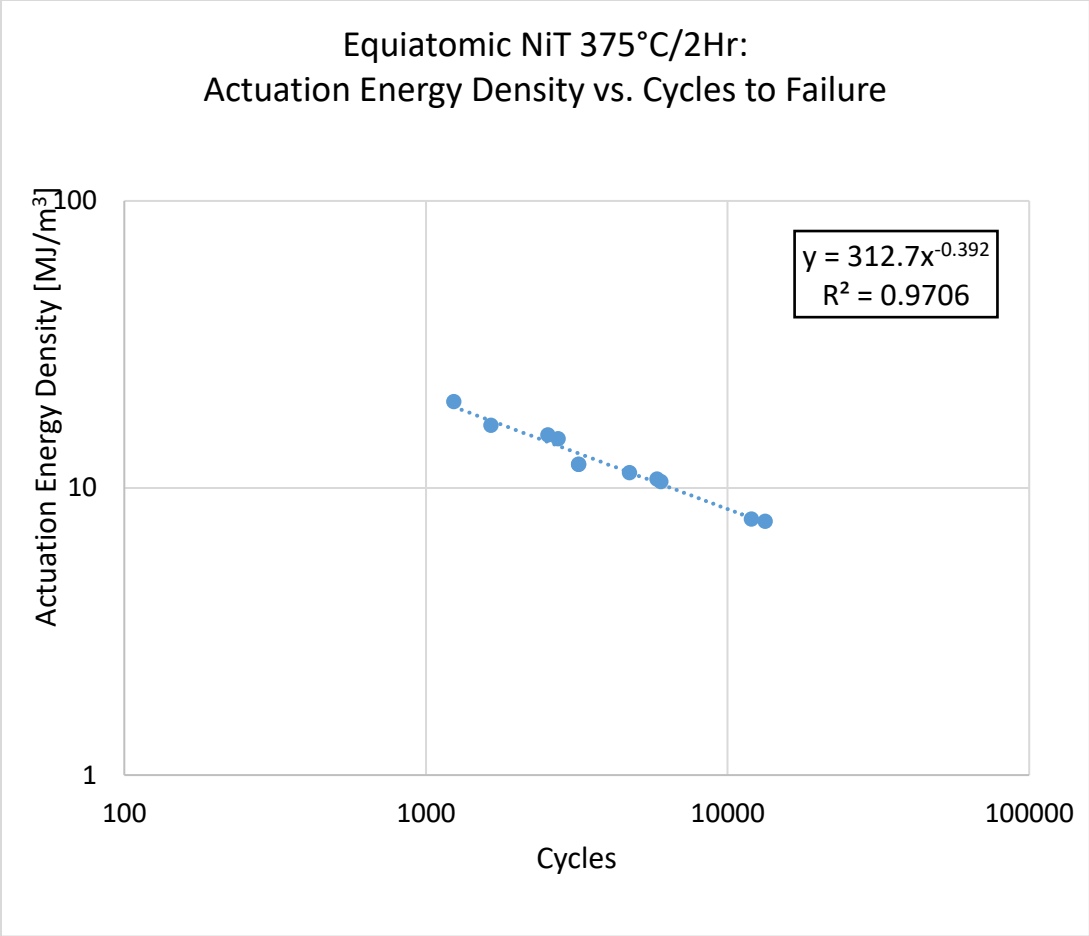

Figure 5.9: Actuation energy density correlated with cycles to failure for equiatomic NiTi with a 350°C/2Hr heat treatment under 100-300MPa isobaric loading.

While equiatomic NiTi, with both a 350°C, 2 hour and a 375°C, 2 hour heat treatment, can achieve very high actuation work densities, they have significantly different fatigue lives as the actuation energy density is varied. Unlike the equiatomic NiTi, the $Ni_{60}Ti_{40}$ has significantly lower actuation energy density. This can be seen in Figure 5.10.

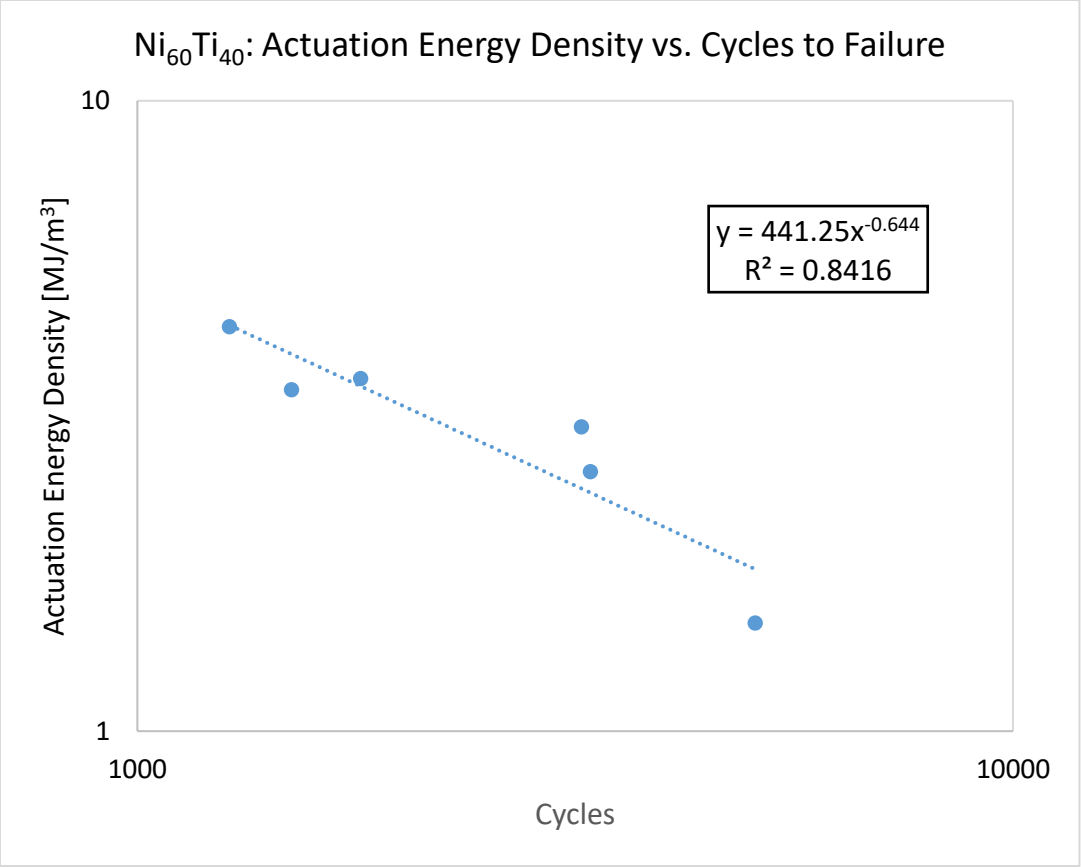

Figure 5.10: Actuation energy density correlated with cycles to failure for $Ni_{60}Ti_{40}$ under 100-300MPa isobaric loading.

As expected, both NiTiHf material systems outperform the binary systems at high stress levels. However, there was a detectable increase in performance for the high purity NiTiHf. The relationship between cycles to failure and actuation energy density can be seen for both the low and high purity systems in Figures 5.11 and 5.12, respectively.

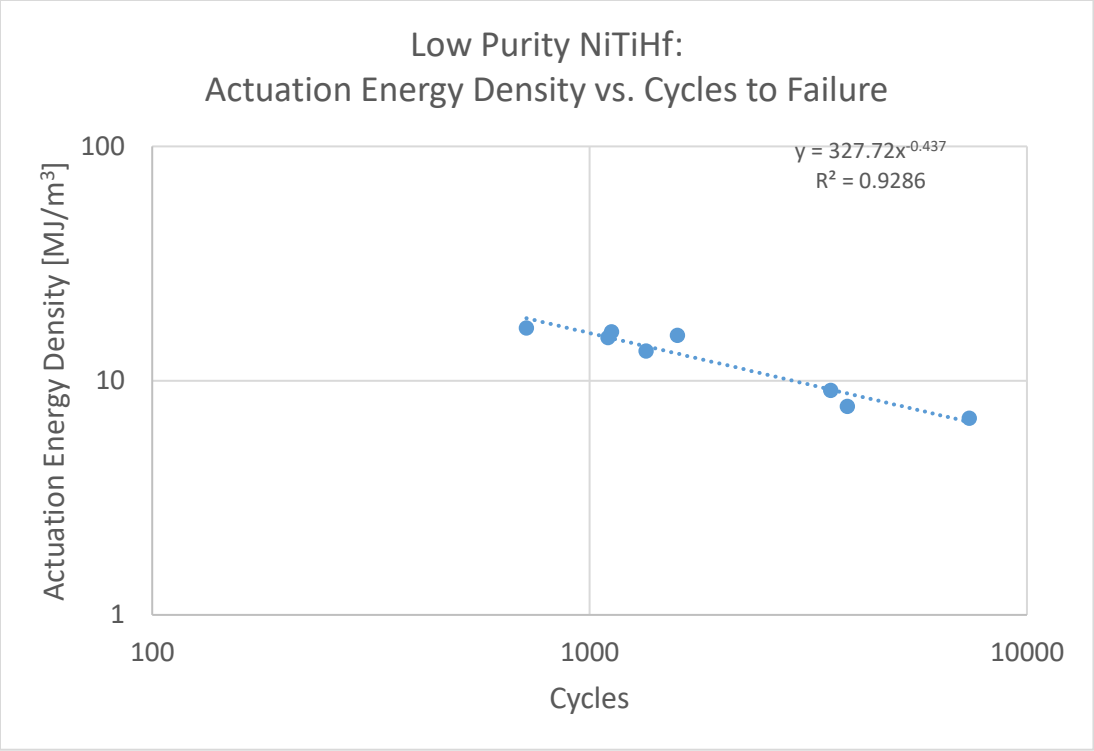

Figure 5.11: Actuation energy density correlated with cycles to failure for low purity NiTiHf under 200-500MPa isobaric loading.

When the actuation energy density is used to determine the cycles to failure, the actuation energy density can either be obtained from experimental results (measuring the load and actuation strain) or as shown in Equation 5.3 for isobaric loading. In order to be predictive, the actuation strain predicted by the model must be utilized. However, when calibrating the energy-based fatigue life prediction methods, the experimentally measured results can be used to better gage how well the material parameters were calibrated.

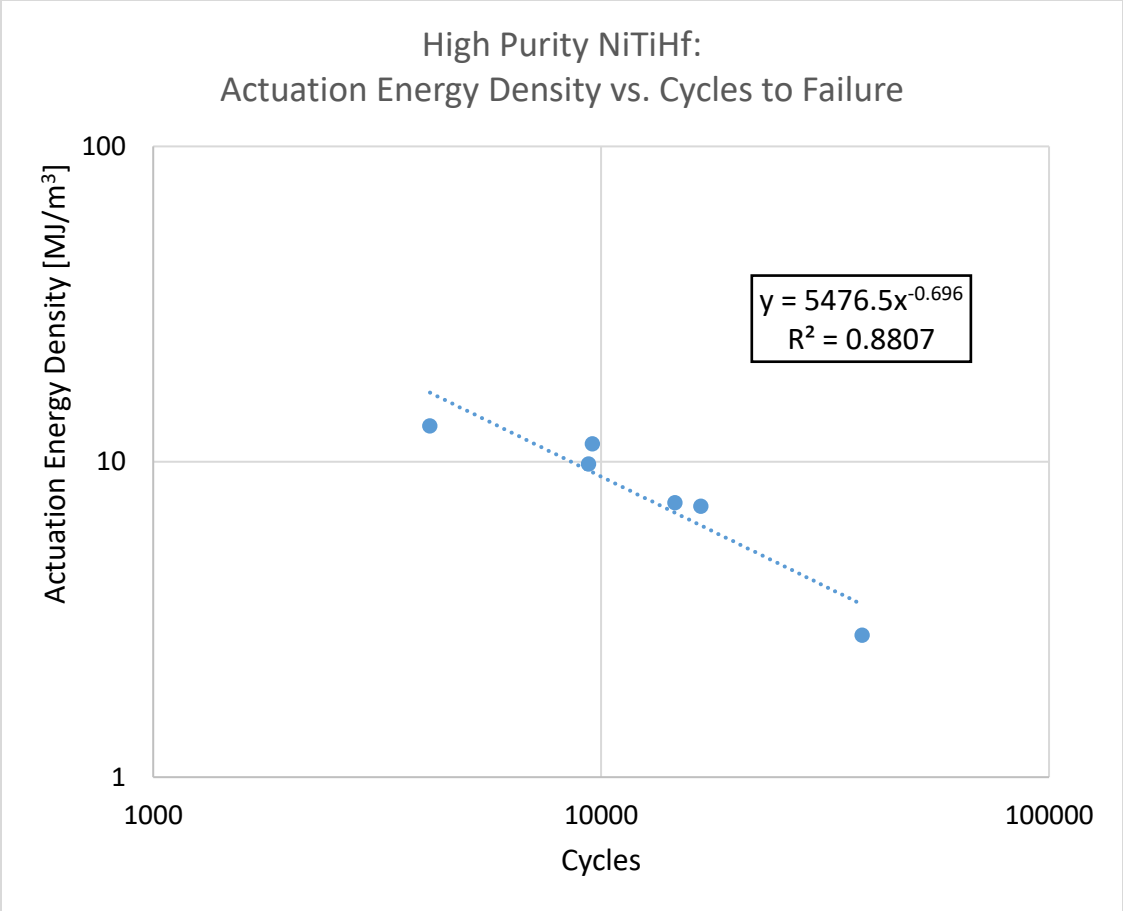

Figure 5.12: Actuation energy density correlated with cycles to failure for high purity NiTiHf under 200-500MPa isobaric loading.

In Tables 5-6 through 5-10, the actuation energy density and simulated cycles to failure are presented for the calibration tests for each of the material systems. From the extremely low simulation error in Table 5-6, it is apparent that actuation energy-based criterion accurately captures the cycles to failure for isobaric tests with loads between 100 and 300MPa. This method also captures the cycles to failure for a similar loading range with the higher temperature heat treated NiTi, as can be seen in Table 5-7.

Table 5-6: Actuation Energy Density Predictions for Equiatomic NiTi 350°C, 2 Hours

Heat Treatment	*Mechanical Load*	*Energy Density*	*Cycles to Failure*	*Energy Criterion Prediction*	*Simulation Error (%)*	*Absolute Error (%)*
350°C, 2 hours	100	4.12	3052	3284	8%	8%
350°C, 2 hours	100	4.05	3601	3353	-7%	7%
350°C, 2 hours	150	6.45	1745	1904	9%	9%
350°C, 2 hours	150	6.39	1820	1925	6%	6%
350°C, 2 hours	200	8.702	1226	1323	8%	8%
350°C, 2 hours	200	9.994	1166	1118	-4%	4%
350°C, 2 hours	200	10.04	1048	1111	6%	6%
350°C, 2 hours	200	8.37	1642	1387	-16%	16%
350°C, 2 hours	300	15.6	650	650	0%	0%
350°C, 2 hours	300	15.15	698	674	-3%	3%
Average					***0%***	***6%***

Table 5-7: Actuation Energy Density Predictions for Equiatomic NiTi 375°C, 2 Hours

Heat Treatment	*Mechanical Load*	*Energy Density*	*Cycles to Failure*	*Energy Criterion Prediction*	*Simulation Error (%)*	*Absolute Error (%)*
375°C, 2 hours	150	7.8	12000	12285	2%	2%
375°C, 2 hours	150	7.65	13336	12909	-3%	3%
375°C, 2 hours	200	12.1	3209	4008	25%	25%
375°C, 2 hours	200	10.74	5841	5433	-7%	7%
375°C, 2 hours	200	12.1	3211	4008	25%	25%

Table 5-7: Continued

Heat Treatment	*Mechanical Load*	*Energy Density*	*Cycles to Failure*	*Energy Criterion Prediction*	*Simulation Error (%)*	*Absolute Error (%)*
375°C, 2 hours	200	11.3	4734	4772	1%	1%
375°C, 2 hours	200	10.54	6012	5700	-5%	5%
375°C, 2 hours	250	15.3	2536	2203	-13%	13%
375°C, 2 hours	250	14.8525	2745	2376	-13%	13%
375°C, 2 hours	300	16.53	1643	1809	10%	10%
Average					***2%***	***10%***

As expected, the low and high purity NiTiHf have significantly different responses when analyzed in terms of actuation energy density vs. cycles to failure; however, both material systems show strong correlations between cycles to failure and actuation energy density, with the low purity system having a detectable decline in the fatigue performance. This correlation can be seen in Tables 5-8 and 5-9 for the low and high purity NiTiHf systems, respectively.

Table 5-8: Actuation Energy Density Predictions for Low Purity NiTiHf

Specimen Nomen-clature	*Mechanical Load*	*Upper Cycle Temperature*	*Energy Density [MJ/m^3]*	*Cycles to Failure*	*Energy Criterion Simulation*	*Error (%)*	*Absolute Error (%)*
HF207-15	300	350	9.09	3561	3539	-1%	1%
HF208-11	300	350	7.77	3890	5092	31%	31%
HF207-9	400	350	16.16	1124	932	-17%	17%
HF207-10	400	350	13.6	1589	1390	-13%	13%
HF207-17	400	350	16.76	717	856	19%	19%
HF208-9	400	350	15.28	1103	1061	-4%	4%
HF208-25	400	350	13.36	1347	1448	7%	7%
HF207-7	500	350	6.9	7388	6708	-9%	9%
Average						***2%***	***13%***

Table 5-9: Actuation Energy Density Predictions for High Purity NiTiHf

Specimen Nomen-clature	*Mechanical Load*	*Upper Cycle Temperature*	*Energy Density [MJ/m^3]*	*Cycles to Failure*	*Energy Criterion Simulation*	*Error (%)*	*Absolute Error (%)*
HF500-4	200	300	2.82	38256	42032	10%	10%
HF500-7	300	300	7.41	14606	14524	-1%	1%
HF500-10	300	300	7.23	16698	14127	-15%	15%
HF500-8	400	300	9.84	9378	10257	9%	9%
HF500-6	400	300	11.4	9566	8687	-9%	9%
HF500-16	500	300	20.9	4148	4383	6%	6%
Average						***0%***	***8%***

While the actuation work density criterion show significantly more accuracy when dealing with the isobaric fatigue response of the NiTi and NiTiHf systems, the largest difference is observed when analyzing the response of the Nickel-rich system. The experimental data for the Ni60Ti40 system is summarized in Table 5-10.

Table 5-10: Actuation Energy Density Predictions for $Ni_{60}Ti_{40}$

Specimen Nomen-clature	*Mechanical Load*	*Upper Cycle Temperature*	*Energy Density [MJ/m^3]*	*Cycles to Failure*	*Energy Criterion Simulation*	*Error (%)*	*Absolute Error (%)*
A2	150	150C	1.5	5078	6582	30%	30%
B2	200	150C	2.58	3293	2986	-9%	9%
B3	200	150C	3.04	3217	2351	-27%	27%
C3	250	150C	3.625	1800	1819	1%	1%
D1	300	150C	4.4	1275	1372	8%	8%
D2	300	150C	4	1500	1576	5%	5%
Average						***1%***	***13%***

5.3 Comparison and Discussion of Actuation Fatigue Lifetime Prediction Methods

In the previous section, the isobaric fatigue tests for five material systems were used to calibrate fatigue life criteria based on accumulated plastic strain (TRIP) and actuation work density. These calibrations are summarized in Table 5-11. Both sets of calibration parameters indicate the dependence of an actuator's fatigue life on different factors. The constant TRIP parameter indicates how much TRIP would theoretically be required for failure under a single cycle, while the exponent captures the sensitivity of the material's fatigue life to TRIP. Similarly, for the actuation energy density parameters, the constant represents the theoretical actuation energy required for single cycle failure, while the exponent for the power fit indicates the sensitivity to increased actuation energy density. For full-cycle isobaric fatigue, this exponent indicates a sensitivity to increased mechanical loads. It is important to note that since this method is not able to capture ultra-low cycle fatigue (below 100 cycles), these values should be interpreted as indicators rather than physically accurate values.

Table 5-11: Fatigue Lifetime Prediction Material Parameters

Material	*TRIP Criterion Parameters*		*Actuation Energy Density Parameters*	
NiTi 350°C	1.6	-0.308	3200.9	-0.822
NiTi 375°C	11.762	-0.404	312.7	-0.392
NiTiHf Low Purity	1.285	-0.359	3231.3	-0.672
NiTiHf High Purity	0.904	-0.329	35216	-0.886
$Ni_{60}Ti_{40}$	0.505	-0.322	624.4	-0.686
	Constant	*Exponent*	*Constant*	*Exponent*

The experimental results which were used to calibrate these material parameters were also compared with the calibrated lifetime prediction methods. These results, which are detailed in Tables 4-1 through 4-10, allow for initial analysis and the simulation error indicates a minimum expected prediction error[10] for additional tests. The results of the simulations can be seen in Table 5-12.

The results in Table 5-12 make it clear the actuation energy density-based criteria are significantly more promising. For this reason, only the actuation work density criteria proposed in Section 5.1 was pursued further.

[10] This assumes the sample size of the calibration results is sufficient. For reference, an experimental variation of 10% requires seven independent tests for five-sigma level certainty of variations between data sets.

Table 5-12: Average Simulation Error for TRIP and Energy-based Criteria for each Material System

Material	*Accumulated TRIP Criterion Average Absolute Error (%)*	*Actuation Energy Density Criterion Average Absolute Error (%)*
NiTi 350°C	31%	6%
NiTi 375°C	50%	8%
NiTiHf Low Purity	52%	13%
NiTiHf High Purity	39%	10%
$Ni_{60}Ti_{40}$	409%	13%
Average Error	***116%***	***10%***

5.4 Predictive Capabilities of Actuation Energy Density-Based Methods

In order to develop a predictive method for determining the actuation fatigue life, the implementations calibrated and analyzed in the previous sections must be able to determine the fatigue life of actuators prior to testing or without taking data from the tests. This was accomplished by utilizing the calibrated methods to predict the fatigue lives for additional isobaric dogbone experiments, actuator parts with stress concentrators, which simulated attachment points or rivet holes, and variable loading paths, which simulated two common variable loading actuation paths.

As expected, the prediction errors for the additional isobaric dogbone experiments, shown in Table 5-13, are nearly equivalent to the simulation errors listed in Table 5-12. These tests were conducted within the same stress ranges as the calibration tests for all materials systems.

Table 5-13: Actuation Energy Density Predictions for Additional $Ni_{60}Ti_{40}$ Isobaric Dogbone Tests

Load (MPa)	*Experimental Cycles to Failure*	*Predicted Cycles to Failure*	*Error (±%)*
150	5061	5069	+0.2%
200	3255	3041	-6%
250	1800	1875	+4%
300	1275	1379	-7%

5.4.1 Prediction of Failure in Actuator Parts with Spatially Varying Stresses

Most large-scale actuator applications will require an SMA to actuate under non-uniform loads due to attachment points, system integration, or other design considerations/restrictions. In order to develop actuator parts with the fatigue response of the material system in mind, a model or method for predicting the fatigue life must be work for dogbone test specimens or more complex actuator parts. However, the prediction method must be geometry independent, otherwise redesigns would necessitate repeating fatigue testing. For this reason, the calibration data, which was collected from dogbone specimens, was used to predict the failure of the actuator parts shown in Figure 5.13 and reported in Section 3.2.3.

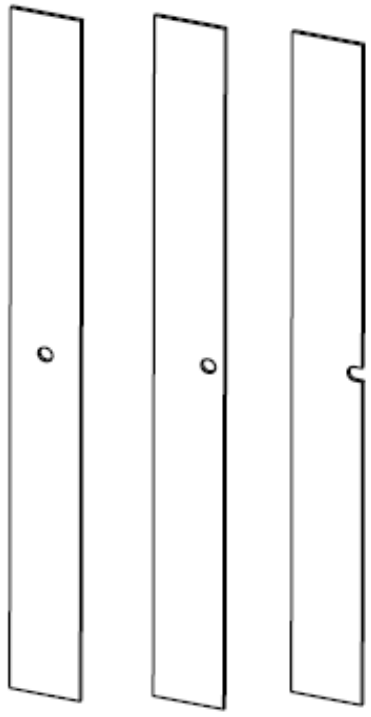

Figure 5.13: Plate actuator geometries considered. Centered hole, eccentric hole, and notched plate (from left to right).

Due to the complex geometry of the actuator parts in Figure 5.13, additional material parameters were required to fully model the system. These parameters, which are summarized in Table 5-14, were also obtained from the same set of isobaric experiments. The evolution of the transformation strain, as a function of the applied stress, or H^{cur}, is shown in Figure 5.14. These parameters were input into an ABAQUS simulation, which utilizes the phenomenological model develop by Lagoudas *et al.* [1]in order to accurately capture the evolution of the transformation strain.

Table 5-14: Material Parameters Utilized in Fatigue Life Predictions

MATERIAL PARAMETER	VALUE
a	731.75
b	1.418
H^{sat}	1.485%
H^{min}	0
k	.0204
σ^{crit}	100MPa
$E_M = E_A$	70GPa
$v_M = v_A$	0.33
$C_M = C_A$	22MPa/K
M_s	318K
M_f	298K
A_s	332K
A_f	352K

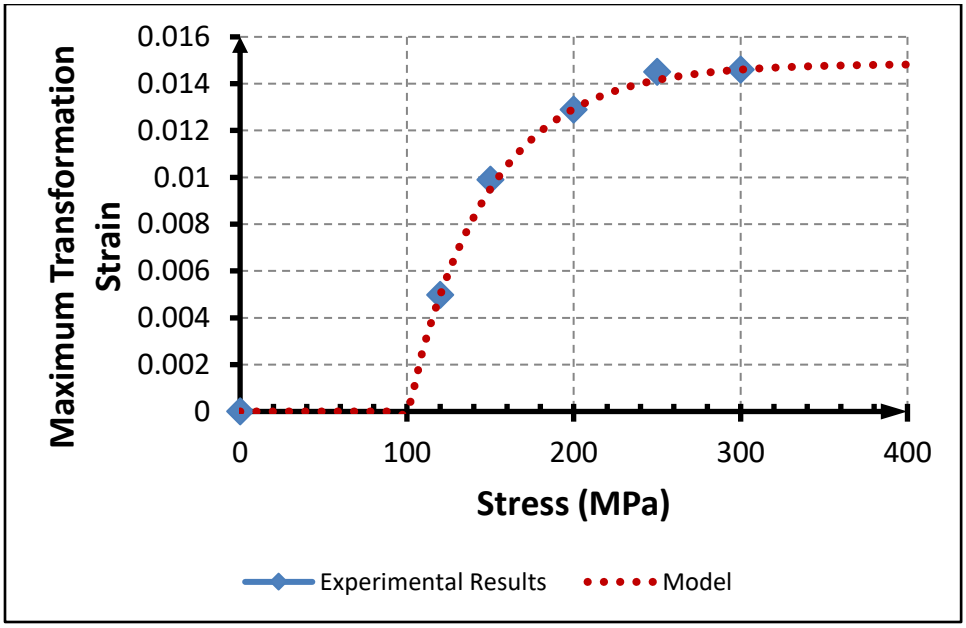

Figure 5.14: Evolution of the transformation strain as a function of the applied stress.

The number of actuation cycles each geometry could survive was predicted by using the material properties derived from the isobaric tests in simulations and the stress states and transformation strains near the notch/hole were utilized by the damage model. Due to the fact that the material survives a number of cycles after a macroscopic crack is formed, the weighted equivalent actuation work density method was applied to the critical region on both sides of the eccentric and centered hole plates and on one side of the notched plate. The transformation strain from the simulations can be seen in Figure 5.15.

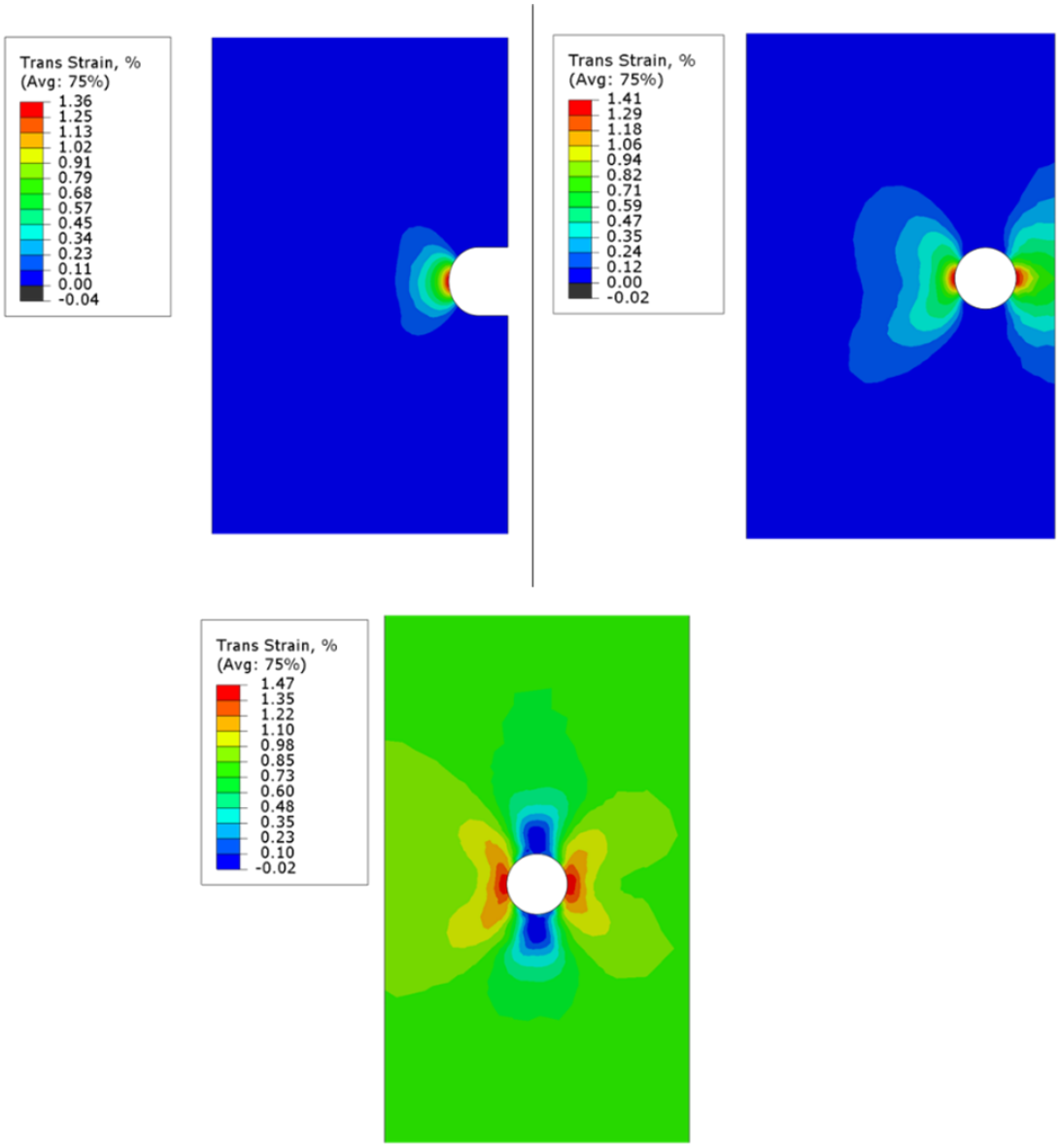

Figure 5.15: Abaqus Simulations for each design; transformation strain shown.

This critical region, which was used to analyze the material response and predict the fatigue life, was selected based on observed critical crack lengths. These critical crack

lengths were found during the initial analysis, described in Section 3.2.3. The experimental results can be seen in Figure 5.16.

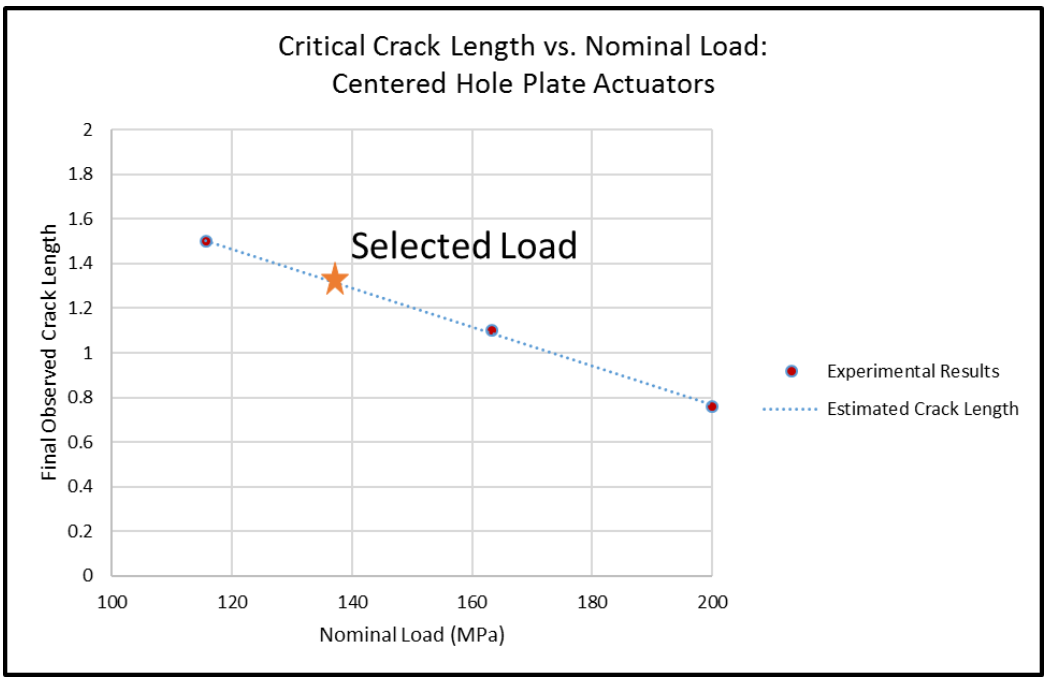

Figure 5.16: Critical crack length vs. applied load for plate actuators with centered holes.

These actuation work values were utilized in the damage model in order to predict the lifetime of each actuator geometry. These lifetime predictions can be seen in Table 5-15 for the centered and notched specimens.

Table 5-15: Actuation Lifetime Predictions for Centered Hole and Single Notched Specimens

Specimen	***Actuation Strain (DIC)***	***Predicted Actuation Strain***	***Experimental Cycles to Failure***	***Predicted Cycles to Failure***	*Error (±%)*
Centered 1	1.34%	1.313%	973	1099	+11.5%
Centered 2	1.52%	1.313%	872	1099	+20.6%
Notched 1	0.98%	0.98%	1523	1673	+8.97%
Notched 2	0.96%	0.98%	1573	1673	+5.98%

Due to the lack of symmetry in the plates with an eccentric hole, lifetime predictions were carried out for both the smaller ligament (right side in Figure 5.15) and the larger (left) side. The predictions based on the values obtained from both sides are shown in Table 5-16 and compared with the experimental values. It can be seen that the failure of the right ligament is predicted well by the damage model while the ultimate failure of the sample is not. It should be noted that the predicted failure of the left side does not take into consideration the increase in stress resulting from the failure of the right ligament.

Table 5-16: Actuation Lifetime Predictions for Eccentric Hole Specimens

Specimen	*Actuation Strain (DIC)*	*Predicted Actuation Strain*	*Experimental Cycles to Failure*	*Predicted Cycles to Failure*	*Error (±%)*
Eccentric 1	1.25%	1.210% (right)	1062	1139	6.76%
	0.99%	1.055% (left)	1086	1400	22.40%

Table 5-16: Continued

Specimen	*Actuation Strain (DIC)*	*Predicted Actuation Strain*	*Experimental Cycles to Failure*	*Predicted Cycles to Failure*	*Error (±%)*
Eccentric 2	1.23%	1.210% (right)	1021	1139	10.30%
	1.06%	1.055% (left)	1063	1400	24.10%

5.4.2 Variable Loading Paths: Defining an Equivalent Actuation Work Density

For isobaric tests, only the applied load is required to predict the number of cycles to failure for an SMA actuator, as shown in the previous sections. However, for more complex loading schemes which evolve during the cycle, an equivalent actuation work density must be defined in order to use the relationship between actuation work density and cycles to failure for isobaric loading (Equation 5.2). Due to the increase in fatigue life when an isobaric load is replaced with an energetically equivalent linear load (as shown in Chapters 3 and 4), four approaches for determining an equivalent actuation work density were considered: First, the unmodified actuation work density, which is the average mechanical work per cycle normalized by the volume of the gage section, was considered. Second, a modified form of the Smith-Watson-Topper criteria was utilized. Finally, an equivalent actuation work density motivated by a continuum damage model developed by Hartl *et al.* [61] and a modified form with a weighting function motivated by experimental results were developed. While each of these approaches differs for linear

and set-down loading, it is important to note that they are defined such that they predict the same result for isobaric loading.

Smith-Watson-Topper Convex Cutting Plane Criteria

Smith, Watson, and Topper [70] suggested a critical plane model for the low and intermediate-cycle fatigue life of conventional elastic-plastic materials. Unlike the SWT parameter, the modified form presented in Equation 5.4 only considers transformation strain contributions.

$$\sigma_\alpha \varepsilon_\alpha = a\, N_f^b \tag{5.4}$$

In Equation 5.4, ε_α is the maximum principal strain amplitude, σ_α is the maximum normal stress on the plane of ε_α. In this adapted form of the SWT parameter, $\sigma_\alpha \varepsilon_\alpha$ is the actuation work density. Similar to the TRIP criteria, a and b are fitting parameters which can be obtained from uniaxial fatigue testing. The motivation for this modified form of the actuation work criteria was to better capture both evolving thermomechanical loading. The equivalent actuation work can be calculated by taking the maximum of $\sigma_\alpha \varepsilon_\alpha$ for a variable loading path.

Equivalent Actuation Work Density

In order to capture an evolving thermomechanical load, Equation 5.5 can be utilized, which allows H^{cur} to evolve with the applied load. This method for selecting an equivalent actuation work density is based on the model proposed by Hartl *et al.* [61].

$$\widehat{\Phi}^* = \int_0^1 (H^{cur} * \sigma)\, d\xi \tag{5.5}$$

The main benefit of utilizing this definition for the equivalent actuation work density is that it takes the evolution of the maximum transformation strain into account as the load evolves. For example, a linear loading scheme, such as those tested in Chapters 3 and 4, will result in the majority of the material transforming prior to the SMA reaching the average load. Once the equivalent actuation work density, $\widehat{\Phi}^*$, is calculated, it can be utilized to predict the actuation fatigue life through Equation 5.2.

Additionally, this definition of an equivalent actuation work density provides flexibility for further improvement through the use of a weighting function. As illustrated by the increase in fatigue life when an isobaric load is replaced with an energetically equivalent linear load, higher stresses when the material is fully martensite decrease the expected fatigue life. To account for this reduction in fatigue life, a linear weighting function, such as the one shown in Equation 5.6 can be utilized to account for this effect.

$$\widehat{\Phi}' = \int_0^1 (2\xi * H^{cur} * \sigma)\, d\xi \tag{5.6}$$

It should be noted that any weighting function can be selected as long as the integral reduces to the actuation work density for isobaric loading; however, a linear weighting function was selected as it provides an additional penalty for large loads as the forward transformation is nearing completion.

5.4.3 Predictions for Variable Loading Paths

For isobaric fatigue tests, the adapted form of the Smith-Watson-Topper convex-cutting plane, actuation work criterion, and the equivalent actuation work density method all predict the same fatigue life as they utilize the same actuation work density. However,

for more complex loading paths, such as those seen by most actuator applications, these predictions differ significantly: the SWT method utilizes a single, critical value for each cycle; the actuation work method is based on the specific work generated during the entire actuation cycle; and the equivalent actuation work density method evolves with the state of the material by taking the actuation response into account.

In order to determine the optimal method for monitoring and predicting failure independent of the selected thermomechanical loading path, two variable loading paths were studied for the NiTiHf and equiatomic NiTi material systems. These additional loading paths, shown schematically in Figure 5.17, better simulate loading scenarios SMA actuator applications will undergo and allow for the actuation energy density-based to be further analyzed and validated.

In Figure 5.17, the standard, isobaric loading path is shown in red. The calibration tests discussed in section 5.2 were all performed with this loading. This calibrated model was then utilized to predict the actuator lifetime for a given linear (blue in Figure 5.17) or set-down (purple) loading path. For both NiTi heat treatments and high/low purity NiTiHf, several variable loading tests were completed and compared with modeling predictions.

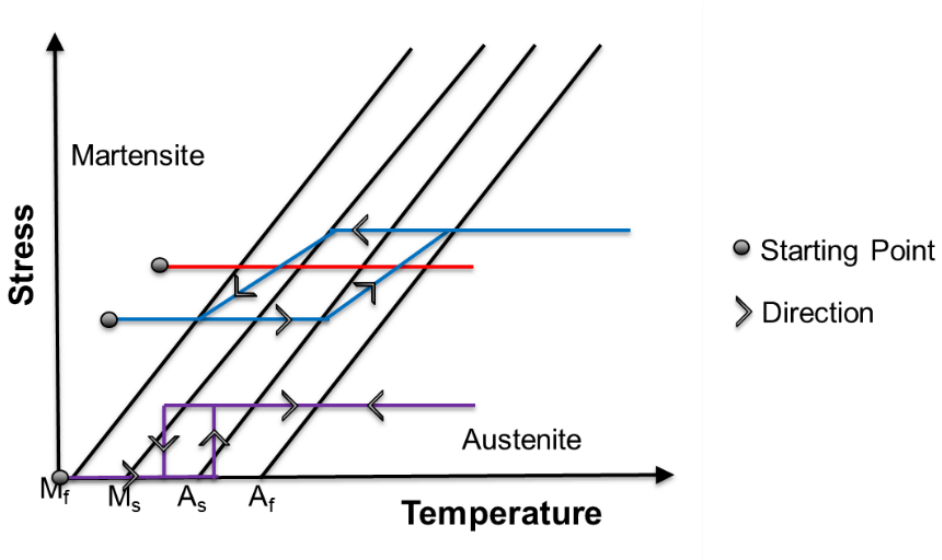

Figure 5.17: Variable loading paths which were studied in Chapter 3 and are used to evaluate the actuation energy density-based fatigue criteria.

Each energy density-based method has a different method for determining the equivalent actuation work density for a given thermomechanical cycle. For the variable loading paths, these differences result in largely varying predictions. The simplest to determine is the modified SWT parameter as it utilizes the maximum of the dot product of the transformation strain and stress; for linear or setdown dogbone tests, the SWT method maximizes Equation 5.7. For linear loading tests, this frequently occurs at the lowest stress, when the transformation strain is maximized.

$$SWT = MAX\,\langle \sigma * \varepsilon^t \rangle \tag{5.7}$$

The actuation work criterion (AWC) can be determined by integrating the mechanical work density performed by the system over the course of the cycle, as shown in Equation 5.8.

$$AWC = \frac{\int_{cycle} Force * displacement}{Volume} = \int_{cycle} \sigma(t) * \varepsilon^t(t)\, dt \tag{5.8}$$

For isobaric cycles, this reduces to product of the stress and actuation strain. Similar simplifications can be made for the linear loading, which reduces to the average stress multiplied by the actuation strain, and the set-down test, which reduces to the actuation strain prior to the set-down multiplied by the actuation strain.

The SWT parameter and actuation work criteria are easier to evaluate than the equivalent actuation work density (E) and the modified equivalent actuation work density (E') since they do not evolve with the state of the material.

In many actuator applications, the load on the SMA will be directly tied to the actuation strain; e.g. an axial SMA actuator moving a control surface will see an increase in the load as the control surface is moved further into the flow. Similarly, the load on actuators during the variable loading tests is dependent on the actuation strain of the material. For the linear loading path, this relationship can be seen in Equation 5.9 where K_{eff} is the effective spring constant of the spring array and L is the gage length. This can be simplified for a given loading range, R, which is the difference between the maximum and minimum loads. The simplified form is shown in Equation 5.10. When the material is fully martensite ($\xi = 1$), the load is at its minimum and, as the actuator is heated and

undergoes reverse transformation, the load increases. This change in loads is shown schematically in Figure 5.17.

$$\sigma(\xi) = \sigma^{max} - K_{eff} * \varepsilon^{t} * L * \xi \tag{5.9}$$

$$\sigma(\xi) = \sigma^{max} - R * \xi \tag{5.10}$$

Similarly, the stress on the actuator when it is subjected to stepwise loading can be defined in terms of the MVF. This is shown in Equation 5.11 for a load path where the weight is lifted after one fourth of the actuation stroke is achieved, as was the case with the stepwise fatigue tests.

$$\sigma(\xi) = \begin{cases} \sigma^{applied}, \xi \leq 0.75 \\ 0 \quad\quad , \xi > 0.75 \end{cases} \tag{5.11}$$

For a given linear loading path with stress range R and max stress σ^{max}, the predicted cycles to failure for the equivalent actuation work density method and modified form are shown in Equations 5.12 and 5.13, respectively.

$$N_f = \left[\int_0^1 \left(\frac{(\sigma^{max} - R\xi) * H^{sat} \left(1 - \exp\left[-k\left(\sigma^{max} - R\xi - \sigma^{crit}\right)\right]\right)}{\mathrm{a}} \right)^{\mathrm{b}} d\xi \right]^{-1} \tag{5.12}$$

$$N_f = \left[\int_0^1 \left(\frac{2\xi(\sigma^{max} - R\xi) * H^{sat} \left(1 - \exp\left[-k\left(\sigma^{max} - R\xi - \sigma^{crit}\right)\right]\right)}{\mathrm{a}} \right)^{\mathrm{b}} d\xi \right]^{-1} \tag{5.13}$$

With the fatigue lifetime prediction methods implemented for both linear and stepwise loading paths, the material parameters obtained from the isobaric characterization testing were used to predict the fatigue lives for each of the variable loading tests. In Table 5-17, the experimental cycles to failure are compared with the predicted cycles to failure for the actuation work criteria (AWC), the modified SWT method, and the weighted equivalent actuation work density (E'). In Table 5-18, the error (relative to the experimental value) is shown for each variable loading test and prediction method.

While all three prediction methods are based on some function of the actuation energy density and predict the same actuator life for isobaric loading, their predictions differ drastically when non-constant loads are considered. From the results in Tables 5-17 and 5-18, it is clear that the weighted equivalent actuation work density provides the best prediction method. For the linear loading paths, the SWT method overpredicts while the actuation work underestimates the fatigue life. This is likely due to the fact that neither fully capture the behavior of the material: The SWT method only considers the state of the material when the stress is the lowest and the actuation strain is the highest for these cases, which results in the over prediction. Conversely, the AWC utilizes the average stress and fails to account for the evolution of the actuation strain, or H^{cur}, as the load increases, thus underestimating the fatigue life.

Table 5-17: Actuation Fatigue Lifetime Prediction Results Compared for Variable Loading Tests

Material	*Load Path*	*Target (Initial) Stress Range (MPa)*	*Cycles to Failure*	*SWT*	*Work (AWC)*	*E'*
NiTi 350°C	Linear	150-250	2494	4107	1891	2311
NiTi 350°C	Linear	150-250	2652	4107	2007	2425
NiTi 350°C	Linear	150-292	2278	2850	1605	2408
NiTi 350°C	Linear	208-284	1555	2138	1390	1630
NiTi 375°C	Linear	150-250	7124	15457	5504	7004
NiTi 375°C	Linear	150-250	7586	20292	6544	8445
NiTiHf (Low)	Stepwise	0-300	17354	11696	11696	15565
NiTiHf (Low)	Stepwise	0-300	16572	11696	11696	15565
NiTiHf (Low)	Stepwise	0-400	6127	3903	3903	5927
NiTiHf (Low)	Stepwise	0-400	6706	3903	3903	5927
NiTiHf (Low)	Linear	300-400	6605	7865	5600	6357
NiTiHf (Low)	Linear	300-500	5263	7118	3903	4787
NiTiHf (High)	Linear	200-400	17650	58859	11013	15150
NiTiHf (High)	Linear	300-400	8914	11013	6679	7690

Table 5-18: Actuation Fatigue Lifetime Prediction Error Compared for Variable Loading Tests

Material	*Load Path*	*Target (Initial) Stress Range (MPa)*	*Cycles to Failure*	*SWT*	*Work (AWC)*	*E'*
NiTi 350°C	Linear	150-250	2494	59.5%	-26.6%	-10.3%
NiTi 350°C	Linear	150-250	2652	43.4%	-29.9%	-15.3%
NiTi 350°C	Linear	150-292	2278	25.1%	-29.5%	5.7%
NiTi 350°C	Linear	208-284	1555	37.5%	-10.6%	4.8%
NiTi 375°C	Linear	150-250	7124	128.4%	-18.7%	3.5%
NiTi 375°C	Linear	150-250	7586	184.8%	-8.1%	18.5%
NiTiHf (Low)	Stepwise	0-300	17354	-32.6%	-32.6%	-10.3%
NiTiHf (Low)	Stepwise	0-300	16572	-29.4%	-29.4%	-6.1%
NiTiHf (Low)	Stepwise	0-400	6127	-36.3%	-36.3%	-3.3%
NiTiHf (Low)	Stepwise	0-400	6706	-41.8%	-41.8%	-11.6%
NiTiHf (Low)	Linear	300-400	6605	19.1%	-15.2%	-3.8%
NiTiHf (Low)	Linear	300-500	5263	35.2%	-25.8%	-9.0%
NiTiHf (High)	Linear	200-400	17650	233.5%	-37.6%	-14.2%
NiTiHf (High)	Linear	300-400	8914	23.5%	-25.1%	-13.7%
Average Error				**53.5%**	**-23.4%**	**-4.6%**
Average Absolute Error				***72.2%***	***25.5%***	***9.29%***

For each of the variable loading tests, the AWC and the SWT have clear trends in their prediction errors: the AWC underestimates both linear and stepwise loading, and the SWT overestimates linear loading tests while underestimating stepwise loading. For linear loading, the weighted equivalent actuation work density method overestimated 40% of the tests, while underestimating the stepwise loading by an average of 10%, which is nearly equivalent to the expected experimental variability based on the material characterization. The unweighted version underestimated nearly all of the linear loading tests, however, resulted in an average absolute error of 22%. This trend illustrates that taking the non-linear evolution of H^{cur} into account increases the accuracy of the prediction. Additionally, the weighted version of the equivalent actuation work density method further improves this prediction. From these results, it is clear that the weighted equivalent actuation work density method represents the most accurate method for predicting the fatigue life for dogbone actuators with variable thermomechanical loading paths and for plate actuators with spatially varying stress fields.

6 DISCUSSION AND SUMMARY OF RESULTS

The main goal of this dissertation was to study the actuation fatigue process of five SMAs and HTSMAs in order to improve the design process of SMA-based actuation systems, especially those pertaining to aerospace engineering challenges. This was accomplished through actuation fatigue characterization of several SMA and HTSMA material systems, the development of a fatigue database and improved testing methods, and the development of fatigue lifetime prediction methods based on experimental observations.

One of the main advantages of SMA-based actuation systems is that the materials are highly tunable for specific applications; as seen in this and many other studies, the actuation fatigue life, transformation temperatures, and actuation stroke of Nickel-Titanium based systems can be altered to fit a certain design by modifying Nickel content, microstructural properties, or adding a third constituent such as Hafnium or Zirconium. However, over the course of hundreds to tens of thousands of thermomechanical cycles, these differences are severely exaggerated. This was evident during the equiatomic NiTi phase of the study, where fatigue lives ranged between 200 and 12,000 cycles to failure and actuation strain at working loads ranged between 5% and 12% for the same material with varying heat treatments. The irrecoverable strain evolution for three of the fatigue tests can be seen in Figure 6.1, where the engineering strain at failure was observed to be between 20% and 80%.

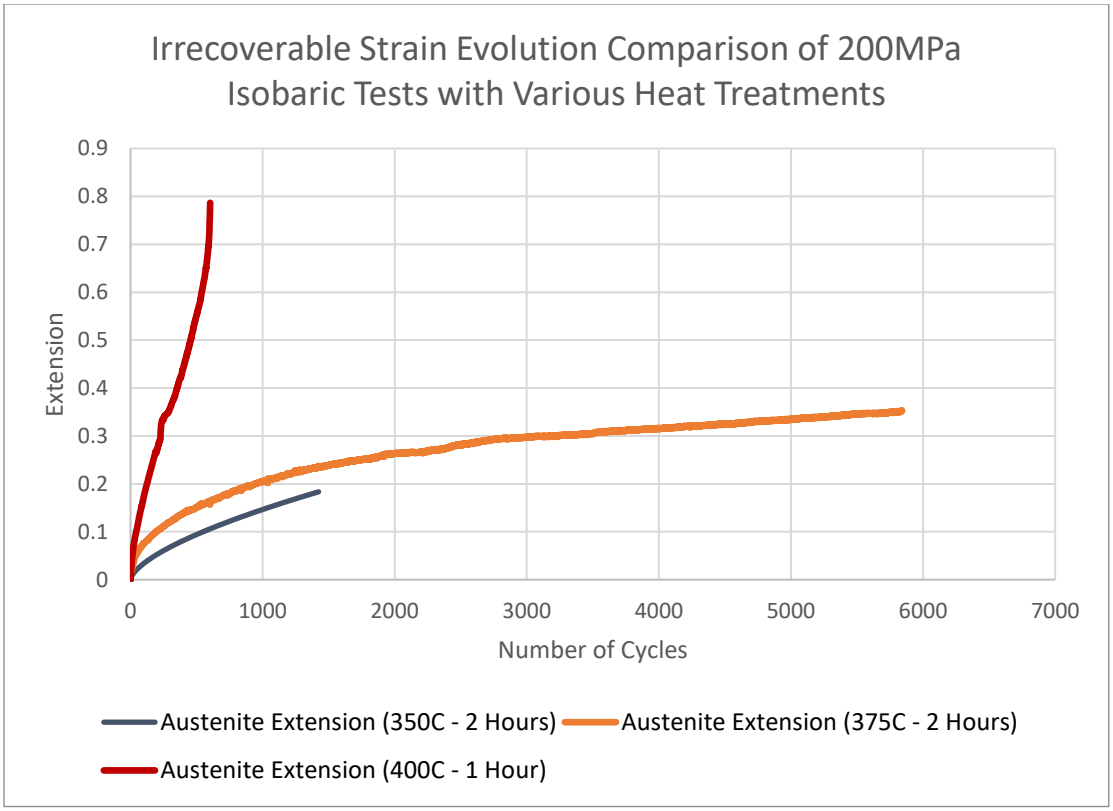

Figure 6.1: Irrecoverable or austenite extension evolution for equiatomic NiTi with various heat treatments: 200MPa isobaric loading.

Due to this sensitivity of the actuation fatigue response, several alloys were selected for characterization over the course of this work. In order to develop a baseline response, equiatomic NiTi was selected for the initial study. A scoping study was completed to determine optimal heat treatments. Further characterization was carried out on two heat treatments: 350°C for two hours and 375°C for two hours. These two heat treatments each exhibited a desirable trait, low irrecoverable deformation and long fatigue life, respectively. In addition to determining the optimal heat treatments, the effects of variable loading paths were also investigated, and it was found that replacing an isobaric load with

an energetically equivalent linear loading path significantly increased the fatigue life. This increase in fatigue performance can be seen in Figure 6.2, where two equiatomic NiTi fatigue tests are compared: one was subjected to a constant load of 200MPa (solid line), while the second was subjected to a load varying between 150 and 250MPa. Since both tests produced approximately the same amount of actuation work per cycle, these two loading paths are referred to as being energetically equivalent. Despite the actuation cycles being approximately energetically equivalent, actuation fatigue lives were observed to be significantly longer when loaded with a spring array.

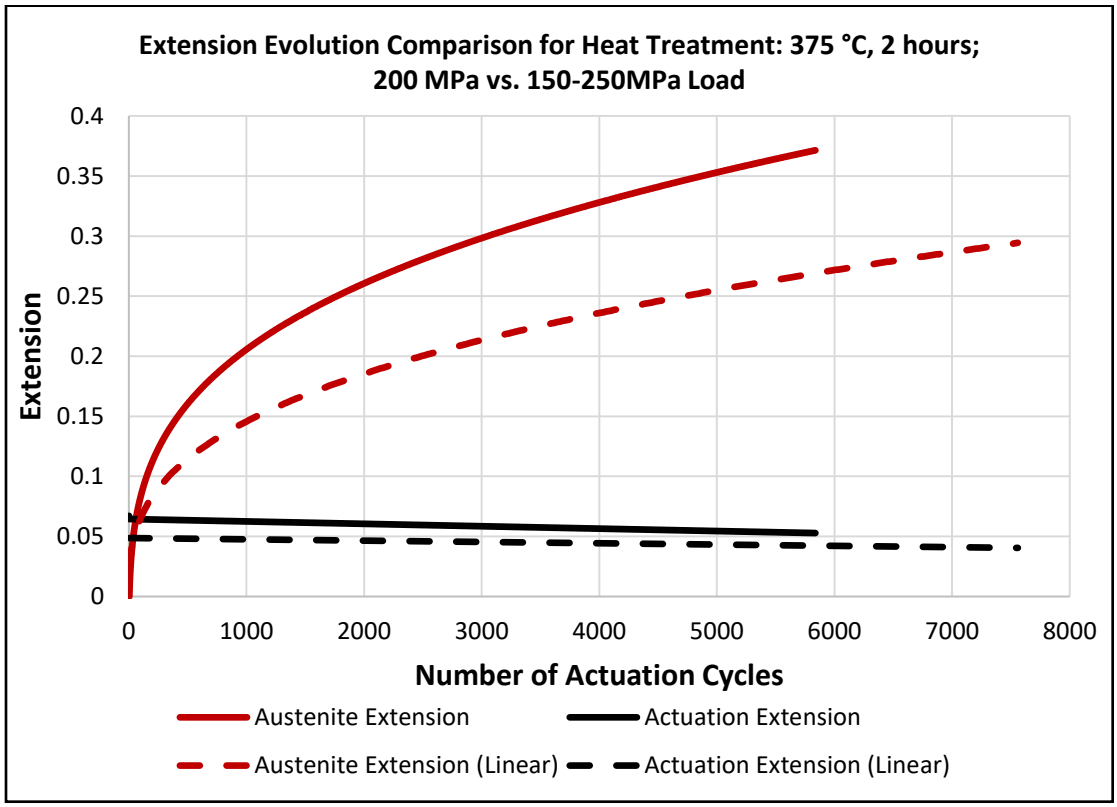

Figure 6.2: Strain evolution for specimen C21 compared with C27; 200 MPa isobaric loading compared with 150-250MPa linearly varying loading.

With the extremely large levels of irrecoverable extension observed in the equiatomic NiTi fatigue tests, it was not surprising that localized deformation was observed in many of the heat treatments. The test specimen shown in Figure 6.1 which sustained nearly 80% extension (red line) prior to failure can be seen in Figure 6.3 after fatigue testing. When compared to a virgin sample, the localized deformation was visibly apparent.

Figure 6.3: Comparison of equiatomic NiTi dogbone actuators; virgin specimen on left, fatigued specimen on right.

After a baseline fatigue response was developed through the characterization of equiatomic NiTi, Nickel-rich $Ni_{60}Ti_{40}$ (Ni60Ti40 atomic weight %) was studied. $Ni_{60}Ti_{40}$ was chosen due to its previous use in aerospace applications[12]and very high resistance to irrecoverable deformation or transformation induced plasticity (TRIP).

Many largescale SMA-based actuation systems will require the SMA component to actuate under a spatially varying stress field due to stress concentrations from attachment points or mechanisms, imperfect machining, or additional system requirements. Therefore, in addition to the characterization of $Ni_{60}Ti_{40}$, the fatigue of plate actuator parts was also studied. This allowed for the proposed fatigue life prediction methods to be validated for dogbone specimens as well as more complex geometries. Collected data includes full field deformation through the use of Digital Image Correlation (DIC) and was compared with ABAQUS simulations which utilized the phenomenological framework developed by Lagoudas *et al.*[1]. Three geometries were considered: notched plates, plates with eccentric holes, and plates with centered holes. An example of the DIC results obtained from this phase of the study can be seen in Figure 6.4, which shows the transformation strain during the first cycle.

While the actuation strain after the first cycle was captured in the simulations, DIC analysis revealed that the actuation strain evolved continuously over the fatigue life of the notched plate actuator. This increase in transformation strain, which appeared to result from the development of TRIP, was observed in all plate actuator geometries. However, this phenomenon was most noticeable in the notched plates due to the fact that the nominal

load was below the critical stress for developing actuation strain. This evolution of transformation strain can be seen in Figure 6.5 for a $Ni_{60}Ti_{40}$ notched plate actuator.

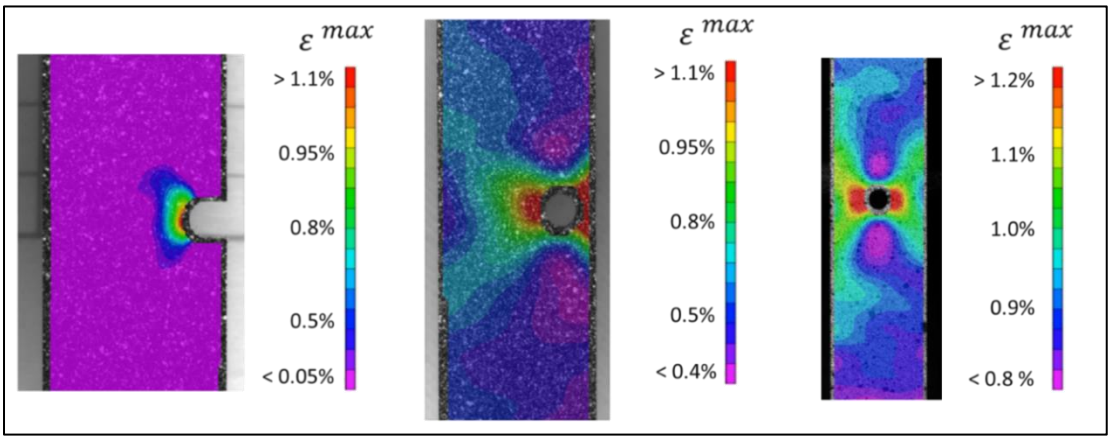

Figure 6.4: Initial transformation strain for each plate actuator geometry.

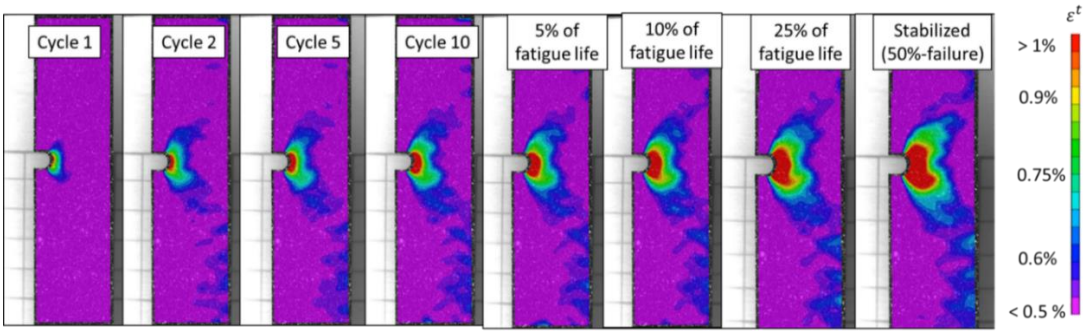

Figure 6.5: Evolution of transformation strain in notched plate actuator due to TRIP.

During the experimental stage of this study, cracks were observed to form and propagate during the final stages of the fatigue life for each of the three geometries

considered. Each of these geometries can be seen in Figure 6.6. It was also observed that these cracks would close during reverse transformation (heating) and open further after each consecutive cooling cycle.

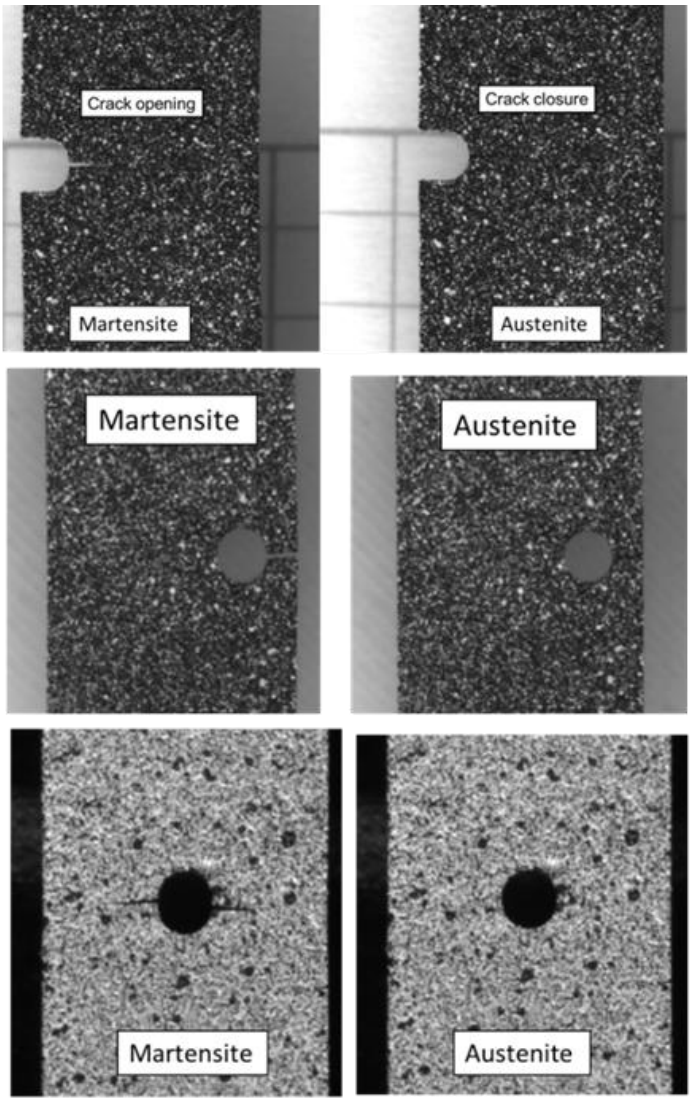

Figure 6.6: Plate actuator geometries with DIC speckle pattern and visibly open cracks post cooling (left) and closed cracks after heating (right). Images on left were taken approximately thirty seconds before images on right; critical failure occurred shortly after these images were captured.

Due to the extreme environments many aerostructures must endure, high temperature SMAs (HTSMAs) can be attractive candidates as their critical temperatures for transformation can be either tuned for high temperature applications or tuned such that they do not run the risk of actuating under extreme operating conditions.

In this work, two material lots of NiTiHf were studied – one with low purity and one with a higher purity. The high purity material system was found to have 400% fewer defects via SEM imaging. While DSC and ultimate tensile testing did not reveal large differences in the material response, pseudoelastic characterization indicated the low purity system was significantly more susceptible to TRIP. While both NiTiHf material lots were found to significantly outperform any of the binary, low temperature SMA systems studied, the low purity material system exhibited a reduction in fatigue life and increase in observable microstructural damage. SEM imaging of post-mortem fatigue specimens indicated that the low purity system had significantly higher crack density, despite having short fatigue lives.

During the isobaric characterization, two key trends were noted: the transformation induced plasticity and actuation energy density both correlated with cycles to failure for most of the material systems. In previous studies by Lagoudas [49] and Calhoun [36] these trends were also noted and discussed. Two examples of these trends can be seen in Figure 6.7, which features the TRIP vs. cycles to failure for equiatomic NiTi heat treated at 350°C for two hours, and Figure 6.8, which shows the actuation energy density vs. cycles to failure for equiatomic NiTi heat treated at 375°C for two hours.

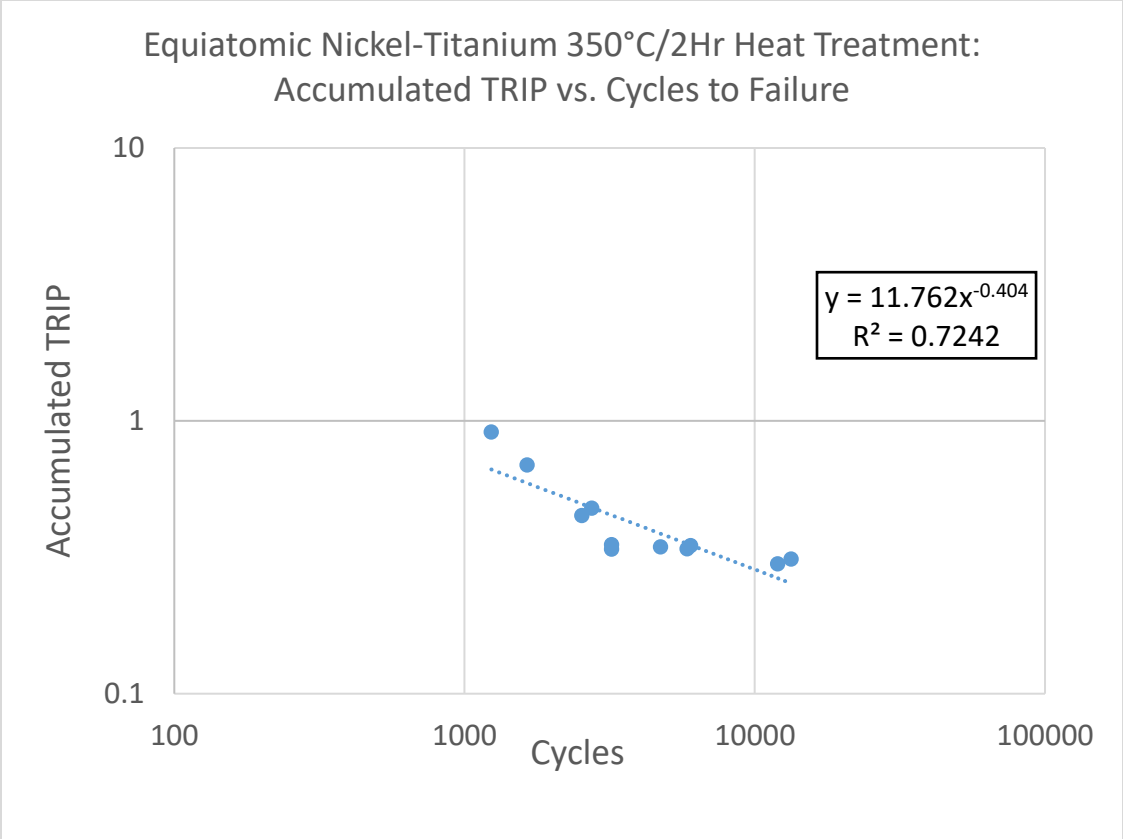

Figure 6.7: Accumulated TRIP (engineering strain) correlated with cycles to failure for equiatomic NiTi with a 375°C/2Hr heat treatment under isobaric loading of 150-350MPa.

Based on these observable trends, four methods for predicting the actuation fatigue life were developed and implemented. First, an accumulated TRIP-based criterion was implemented based on the modified form of the Manson-Coffin relationship proposed by Lagoudas [49] and the TRIP model developed by Lagoudas [64,65], an implementation was developed which both determined simulated fatigue lives for experimental data used to calibrate the material models and predicted fatigue lives for additional tests. The

modified Manson-Coffin relationship was used to develop a theoretical fatigue limit, which is a function of accumulated plastic strain or TRIP and cycles to failure.

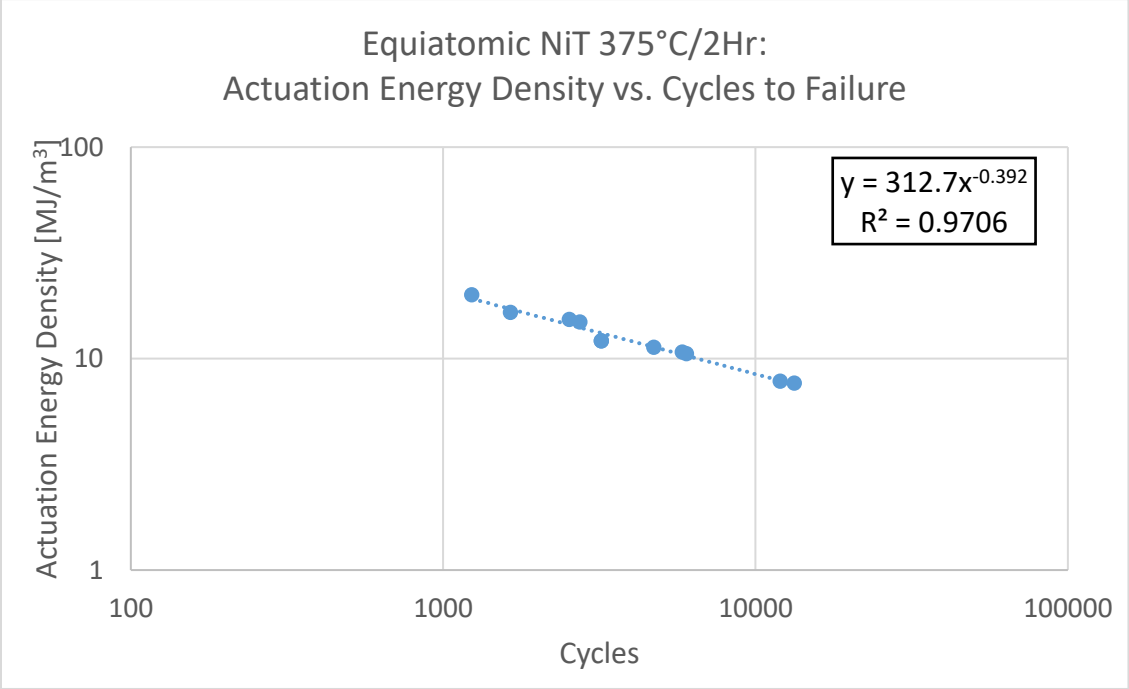

Figure 6.8: Actuation energy density correlated with cycles to failure for equiatomic NiTi with a 350°C/2Hr heat treatment under 100-300MPa isobaric loading.

The three remaining fatigue life prediction methods were developed based on the actuation energy density's correlation with cycles to failure. Similar to the TRIP criterion implementation, each selects a fatigue criteria based on the actuation energy density: the actuation work method utilizes the macroscopic work performed by the actuator, the modified form of the Smith-Watson-Topper convex cutting plane utilizes a maximum value of mechanical stress projected onto the plane of maximum transformation strain,

and the equivalent actuation work density method utilizes an actuation work density that evolves with the state of the actuator. The key difference between these three fatigue life prediction methods is that the actuation work and SWT method both select different critical values for a given cycle, while the equivalent actuation work density method incorporates the actuation loading into the prediction method.

While the actuation energy density-based lifetime prediction methods differ in the way they handle complex thermomechanical loading paths, they all reduce to the same form for isobaric fatigue tests. In order to select actuation fatigue lifetime prediction methods for further evaluation, the actuation fatigue data collected during the experimental phase of the work was used to calibrate the TRIP and actuation energy density-based fatigue criteria. Then, these calibrated models were used to simulate the actuation fatigue life of the tests which were used to calibrate the material parameters. The results are summarized in Figure 6.9, where the average simulation error is shown for each of the five material systems studied. From these results, it is clear the energy density-based criteria show more promise as the average simulation error is nearly an order of magnitude higher for each of the material systems. For this reason, the Actuation Work Criteria (AWC), modified Smith-Watson-Topper (SWT) method, and the Equivalent Actuation Work Density method were studied and envaulted for more complex thermomechanical loading paths.

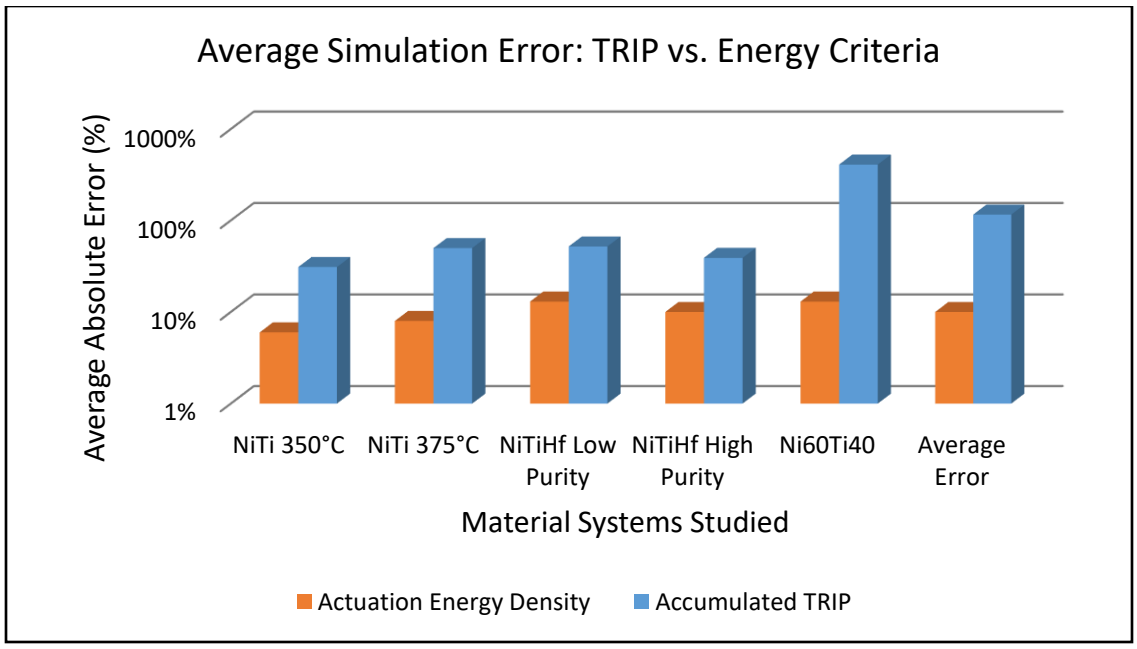

Figure 6.9: Comparison of average simulation error for actuation energy density and accumulated TRIP-based criteria.

During the characterization phase of this work, non-isobaric data were collected for each of the material systems. For the equiatomic NiTi and NiTiHf systems, variable loading paths were studied, and, for the Nickel-rich system, the fatigue of plate actuators was characterized for three different geometries. Since the three work density-based methods differ for how they treat variable loading paths, these tests were used to validate each of the methods. The summary of the validation can be seen in Figure 6.10, where the average error is reported for each material system and loading path. Based on the accuracy of the predictions determined by using the weighted equivalent actuation work density, it is clear that this method provides the most accurate fatigue life estimation method.

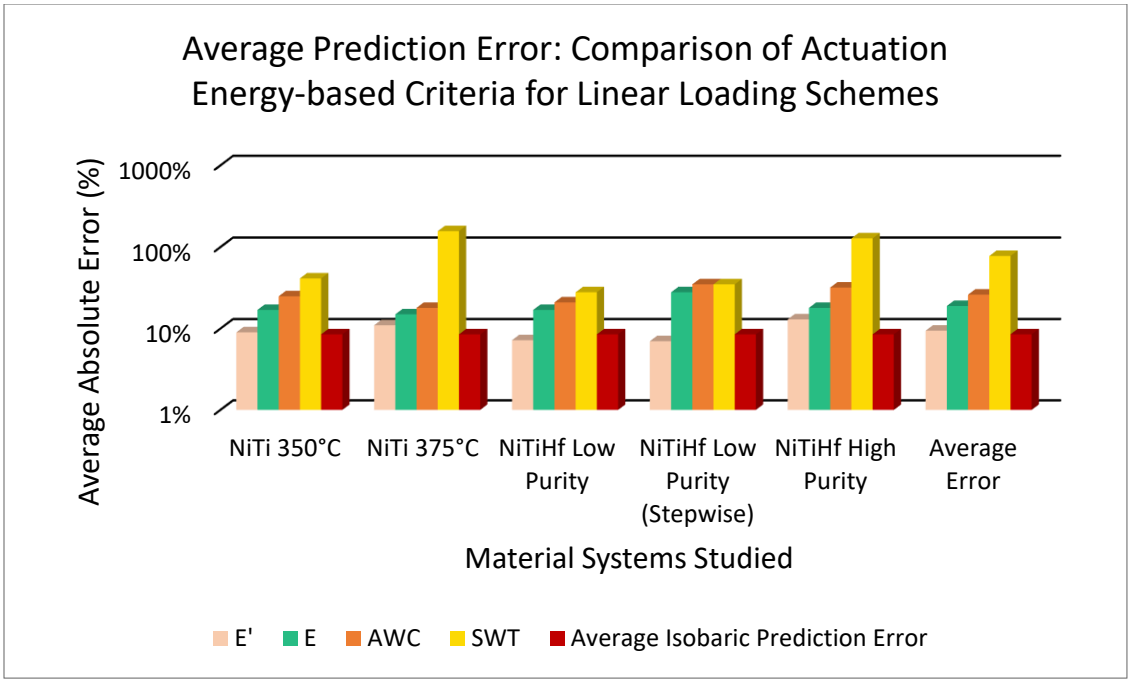

Figure 6.10: Comparison of average prediction error for the weighted and unweighted equivalent actuation work density method (E' and E, respectively), the actuation work criteria (AWC), and the modified Smith-Watson-Topper (SWT) method. Data is compared against the average isobaric prediction error to indicate expected error due to experimental variability.

In addition to studying variable loading paths that better simulate the thermomechanical loading which actuators undergo, the fatigue response of actuator parts with variable geometries was also studied to characterize the effect of stress concentrations as well as validate the fatigue life prediction methods for actuators with spatially varying stress fields. For each of the three geometries, which are shown in Figure 6.3, the equivalent actuation work density method was utilized to predict the fatigue life. In order to predict the fatigue life of a part subjected to thermal cycling and a spatially varying stress field, one actuation cycle was simulated in ABAQUS and the actuation work density

was determined. The error of the resulting predictions, which are shown in Figure 6.11, was found to be nearly equivalent to the simulation error, which was obtained by simulating the calibration tests.

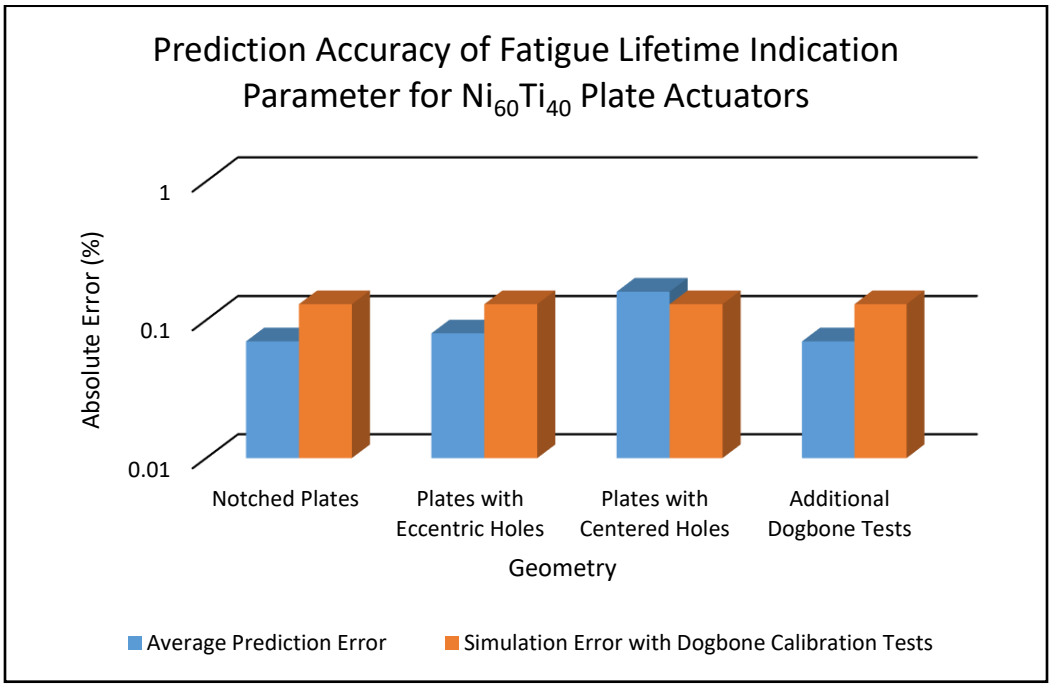

Figure 6.11: Summary of prediction error for Nickel-rich plate actuators with stress concentrations.

Although there is approximately 10% average deviation from the predicted cycles to failure in the isobaric dogbone tests, all of the modeling predictions for the plate actuators overestimated the fatigue life. This trend is likely a result of the fact that the predictions were based on a single simulated thermomechanical cycle and did not take irrecoverable deformation into account. From the DIC results, it was evident that the development of

TRIP played a large role in the reduction of the fatigue life, due to the increase in transformation strain.

6.1 Impact on the Actuation Fatigue Testing of SMA Actuators

Over the course of this study, the testing procedures and experimental methods were continuously improved through the implementation of better testing software and the addition of several non-contact sensors. The new testing software suite, which is outlined in Chapter 2 and discussed in Appendix A, significantly improved cycle control and reduced the expected value for testing failures from over four per ten thousand cycles, to under one per hundred thousand cycles. Additional "stress testing" of the software was performed by a National Instruments LabVIEW engineer for each iteration of the software, and edits to the software were made until it successfully completed 10^6 simulated cycles without error. While the previously conducted experiments on dogbone actuators by Calhoun et al. and Agboola *et al*. [35, 36] were performed on the same loading frames, the experimental variability was reduced significantly with the implementation of a state-space control scheme. The average relative standard deviation (RSD) of the actuation fatigue lives for a given stress level was found to be between 30-80% for previous studies [35, 36] (conducted on Nickel-rich NiTi), while it was always below 20% for equiatomic NiTi, 12% for Nickel-rich NiTi, and 10% for NiTiHf. The average RSD (normalized by experimentally determined fatigue life) was between 5% and 8% for each of these material systems.

While the actuation fatigue testing software had the largest effect on reducing the experimental variability in terms of fatigue life, the cyclic repeatability was improved

most significantly by the addition of an infrared thermometer (once intelligent feedback control had been implemented). Due to the increase in resistivity of an SMA actuator (resulting from TRIP and microcracks) over its fatigue life, an open-loop, time-based control scheme frequently leads to inconsistent cycling (e.g. over-heating, partial cycling, necessary manual adjustments of the power supply, etc.). When the testing results presented in Section 3.2 are compared with previous studies [35, 36, 56], it is clear that an intelligent feedback control scheme must be utilized in order to ensure repeatability and reliably collect data to be used for actuation fatigue modeling.

In Chapter Four, it was shown that a relatively small difference in impurities can have very large effects on the fatigue life of NiTiHf actuators. While two material lots, which were produced by the same manufacturer, had very similar transformation temperatures and compositions, the low purity material lot had up to a 50% reduction in fatigue life. This decrease in performance could be noted when comparing equivalent tests or when comparing the actuation work density vs. fatigue life plots. During testing, the material lot of an actuator could be quickly identified through DIC by examining the rate of TRIP accumulation, amount of TRIP localization, or analyzing the transformation strain and looking for localization. As new SMA and HTSMA compositions are developed and used, quantifying and detecting batch to batch variation becomes vital. The experimental techniques developed herein make offer a very reliable way to determine this variation.

6.2 Impact on the Modeling and Design of SMA Actuators

Several tasks have been completed over the course of this study: In Chapter Two, improved experimental methods and testing standards were developed for studying the

actuation fatigue response of SMAs and HTSMAs. The actuation response and fatigue behavior of five material systems were characterized in Chapter Three. The data from these characterization studies led to the implementation of four fatigue life prediction methods which were calibrated and tested in Chapter Four. One of the main outcomes of this work is the process of taking an SMA material system and developing design guidelines such that an actuator application can be developed while taking the actuation fatigue response of the material into account.

One common place to begin the design process is selecting a material. From the characterization studies, it is clear there are many different facets of the fatigue response which can be influence the material selection; these include dimension stability or resistance to TRIP, transformation temperatures, operational stress limits, actuation energy density, and fatigue life. If the actuation energy density and fatigue life were selected, the data summary shown in Figure 6.12 would be utilized. While the data shown is for isobaric loading, a similar graph could be developed for additional, variable thermomechanical loading paths through the use of the equivalent actuation work density.

An example of what a design space might look like is shown in Figure 6.13, where the characterization data has been utilized to determine zones where each material system could satisfy the combination of energy density and cycles to failure. Note: the smaller regions are shown on top of the larger regions; e.g. the high purity NiTiHf area encompasses all of the area shared by the other material systems.

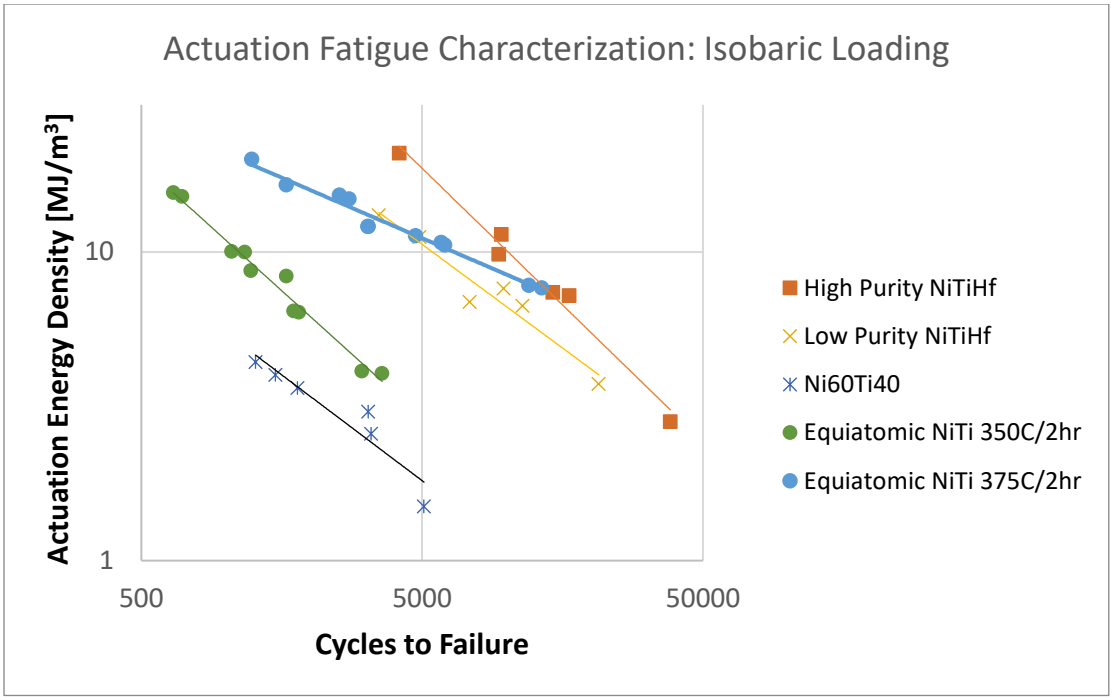

Figure 6.12: Actuation energy density correlated with cycles to failure for all characterized material systems. Data shown are from isobaric testing only.

The bounds in Figure 6.13 were determined from the characterization tests and the equivalent actuation work density method predictions. Based on the experimental results and fatigue life predictions, an actuator which falls within the bounds would be a successful design. Further refinement of these design spaces could include limiting irrecoverable deformation, which would significantly reduce the area which the equiatomic NiTi systems inhabit, or limiting the operational temperatures which could lower the obtainable actuation energy density for the NiTiHf material systems. The actuation energy density and fatigue life is just one combination of actuation fatigue characteristics that can be analyzed. The weighted equivalent actuation work method,

when combined with the TRIP model and characterization data, can be used to develop a first order design of an actuator.

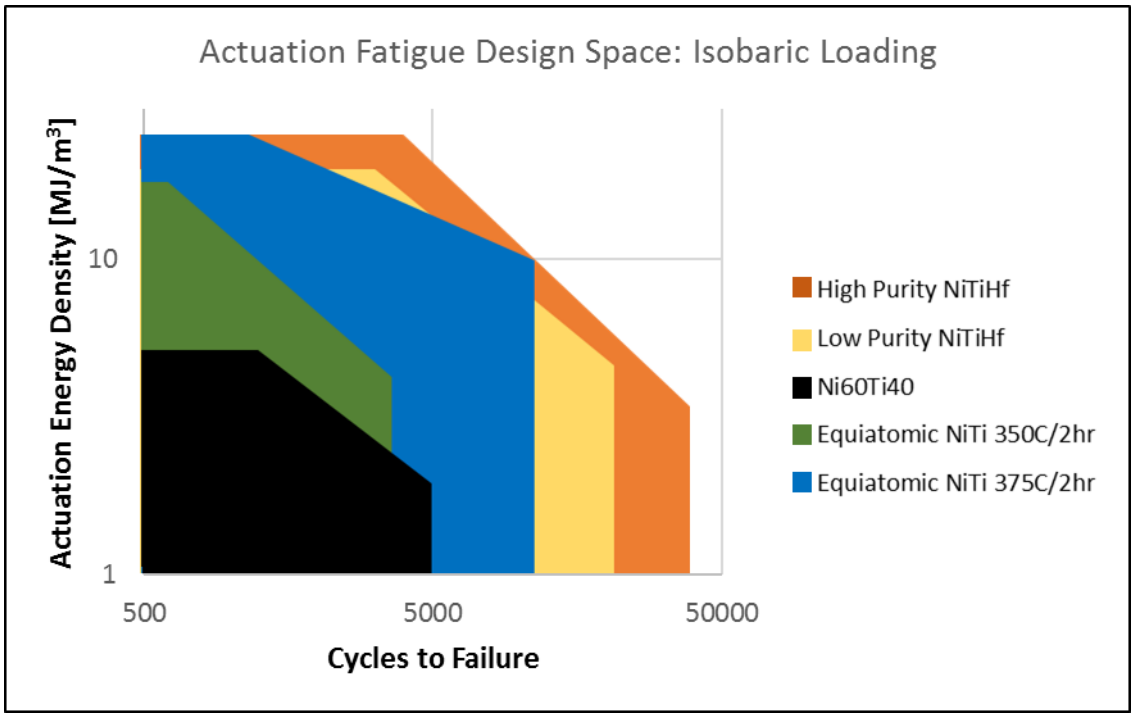

Figure 6.13: Actuation energy density and cycles to failure design space for all characterized material systems. Area shown was determined for isobaric loading conditions.

Additionally, with the use of the weighted equivalent actuation density method, this design space can be adapted for any variable loading path. Since the main goal of utilizing this technique was to adapt the actuation work density from a variable loading path to utilize the relationship between isobaric actuation energy density and cycles to failure, the equivalent actuation work can be utilized to place a design in Figure 6.13. While the

weight function used in Chapter Five was selected to capture the effect of linear and set-down loading, the framework developed can utilize additional weighting functions for other variable loading paths. Finally, a weighting function can also be selected based on other principles such as fracture mechanics.

7 CONCLUSIONS AND FUTURE WORK

As the aerospace, civil, automotive, and biomedical industries advance, and products and systems become smaller, lighter, and more integrated, the potential applications for shape memory alloys and other multifunctional materials will only increase. However, the actuation fatigue phenomenon must be better understood before the full benefits of SMA-based actuation systems can be realized.

In this work, experimental methods were developed to study and characterize the actuation fatigue response of equiatomic NiTi, Nickel-rich NiTi, and NiTiHf, a high temperature SMA. The majority of the experimental improvements made during the course of this study were related to the development and implementation of non-contact sensing. Due to the complex nature of the SMA actuation response, having continuous temperature information from infrared sensors not only helps characterize the fatigue response, but also significantly improves repeatability.

One of the main impediments to studying actuation fatigue is the time investment required to collect sufficient data. When preparing to characterize a material, several tradeoffs must be considered, such as the actuator size and heating and cooling methods. The testing methods developed for this work were designed to strike a balance between cost, time investment, material usage, and repeatability. With the incorporation of a state-space control scheme and high instrument read rates, cycle times for HTSMAs were reduced to approximately forty seconds while the maximum temperature gradient was

reduced to five degrees Celsius. The experimental methods for this study were also designed with the long-term goal of developing industry-wide testing standards, and future work will focus on refining these methods as this research continues.

Over the course of this study, five material systems underwent isobaric characterization and many other systems were explored during scoping studies. The experimental results presented in Chapter Three and Four summarize the characterization data collected from over one hundred actuation fatigue tests. When studying equiatomic NiTi, it was demonstrated that small changes to heat treatments can have large effects on the fatigue characteristics. While the equiatomic NiTi actuators tested were able to achieve very large actuation strains and could potentially provide a large amount of actuation work in a system, the design would have to account for the extremely large irrecoverable extensions the actuators experienced. Even though it was seen that the Nickel-rich NiTi generally produced less actuation strain and lower fatigue lives than the more promising equiatomic NiTi actuators, the Nickel-rich system would most likely be more useful in applications due to its much lower irrecoverable deformation.

In addition to the binary systems, two material lots of the HTSMA NiTiHf were also characterized. While their DSC and ultimate tensile responses were similar, the low purity system (0.4% volume fraction) had a detectably worse fatigue performance than the high purity system (0.08%). Future work for the HTSMA systems will seek to include these differences in the modeling techniques as well as develop requirements which ensure the performance does not degrade past a designed amount.

For many large-scale SMA-based actuation systems, the current design process requires prohibitively expensive and lengthy fatigue testing and certification. This is largely due to the lack of design tools or methods which can provide accurate predictions for the fatigue life of actuator components. In this study, several implementations were developed in order to predict the number of actuation cycles a part can withstand prior to catastrophic failure. Of the prediction methods investigated, the simplified implementation of a continuum damage model proposed by Hartl *et al.* was calibrated with dogbone isobaric actuation fatigue tests and used to predict the failure of dogbone actuators subjected to variable thermomechanical loading paths and plate actuators with sections removed to induce spatially varying stress fields.

While the weighted equivalent actuation work density method showed significantly lower simulation and prediction error than the other methods, the less accurate methods still have useful applications. For example, the actuation work criterion provides a lower limit for the predicted fatigue life for variable loading under the condition that the load decreases as the actuator is cooling.

The DIC results obtained from the plate actuator study indicated that TRIP plays a larger role in the fatigue life of actuator parts or components when the geometry is non-uniform. The transformation strain for each of the plate actuators increased over the course of the fatigue life, which accelerated the actuation fatigue process. Continuation of the design tool and modeling efforts will need to incorporate the TRIP behavior in order to improve the fidelity of fatigue life predictions.

REFERENCES

[1] Lagoudas DC, editor. Shape memory alloys modeling and engineering applications. Springer US; 2008. doi:10.1007/978-0-387-47685-8.

[2] Hartl DJ, Lagoudas DC. Aerospace applications of shape memory alloys. J Aerosp Eng 2007;221:535–52. doi:10.1243/09544100JAERO211.

[3] Hartl DJ, Lagoudas DC, Calkins FT, V B, Song G MN and LH-N, B MN, et al. Advanced methods for the analysis, design, and optimization of SMA-based aerostructures. Smart Mater Struct 2011;20:94006. doi:10.1088/0964-1726/20/9/094006.

[4] Mabe J, Calkins F, Butler G. Boeing's variable geometry chevron, morphing aerostructure for jet noise reduction. 47th AIAA/ASME/ASCE/AHS/ASC Struct. Struct. Dyn. Mater. Conf. 14th AIAA/ASME/AHS Adapt. Struct. Conf. 7th, Reston, Virginia: American Institute of Aeronautics and Astronautics; 2006. doi:10.2514/6.2006-2142.

[5] Strelec JK, Lagoudas DC, Khan MA, Yen J. Design and implementation of a shape memory alloy actuated reconfigurable airfoil. J Intell Mater Syst Struct 2003;14:257–73. doi:10.1177/1045389X03034687.

[6] Mabe JH, Ruggeri RT, Rosenzweig E, Yu C-JM. NiTinol performance characterization and rotary actuator design. In: Anderson EH, editor., International Society for Optics and Photonics; 2004, p. 95. doi:10.1117/12.539008.

[7] Roh J-H, Kim K-S, Lee I. Shape adaptive airfoil actuated by a shape memory alloy and its aerodynamic characteristics. Mech Adv Mater Struct 2009;16:260–74. doi:10.1080/15376490902746996.

[8] McNichols JL, Brookes PC, Cory JS. NiTi fatigue behavior. J Appl Phys 1981;52:7442. doi:10.1063/1.328738.

[9] Barbarino S, Saavedra Flores EI, Ajaj RM, Dayyani I, Friswell MI, Abdullah E J BC and WS, et al. A review on shape memory alloys with applications to morphing aircraft. Smart Mater Struct 2014;23:63001. doi:10.1088/0964-1726/23/6/063001.

[10] Ataalla T, Leary M, Subic A. Functional fatigue of shape memory alloys. Sustain. Automot. Technol. 2012, Berlin, Heidelberg: Springer Berlin Heidelberg; 2012, p. 39–43. doi:10.1007/978-3-642-24145-1_6.

[11] Mabe J, Cabell R, Butler G. Design and control of a morphing chevron for takeoff and cruise noise reduction. 11th AIAA/CEAS Aeroacoustics Conf., Reston, Virginia: American Institute of Aeronautics and Astronautics; 2005. doi:10.2514/6.2005-2889.

[12] Hartl D, Volk B, Lagoudas DC, Calkins F, Mabe J. Thermomechanical characterization and modeling of Ni60Ti40 SMA for actuated chevrons. ASME Int. Mech. Eng. Congr. Expo. Aerosp., vol. 2006, ASME; 2006, p. 281–90. doi:10.1115/IMECE2006-15029.

[13] Saunders RN, Hartl DJ, Boyd JG, Lagoudas DC. Modeling and development of a twisting wing using inductively heated shape memory alloy actuators. In: Liao W-H, editor., International Society for Optics and Photonics; 2015, p. 94310U. doi:10.1117/12.2175692.

[14] Calkins FT. FAA continuous lower energy, emissions and noise (CLEEN) 176 technologies, Boeing program overview, Atlanta, GA, USA.: CLEEN Consortium Conference; 2014.

[15] Pitt D, Dunne J, White E, Garcia E. SAMPSON smart inlet SMA powered adaptive lip design and static test. 19th AIAA Appl. Aerodyn. Conf., Reston, Virginia: American Institute of Aeronautics and Astronautics; 2001. doi:10.2514/6.2001-1359.

[16] Rey N, Tillman G, Miller RM, Wynosky T, Larkin MJ, Flamm JD, et al. Shape memory alloy actuation for a variable area fan nozzle. In: McGowan A-MR, editor., International Society for Optics and Photonics; 2001, p. 371–82. doi:10.1117/12.429677.

[17] Hartl DJ, Lagoudas DC. Characterization and 3-D modeling of Ni60Ti SMA for actuation of a variable geometry jet engine chevron. In: Tomizuka M, Yun C-B, Giurgiutiu V, editors., International Society for Optics and Photonics; 2007, p. 65293Z. doi:10.1117/12.715764.

[18] Wheeler RW, Benafan O, Gao X, Calkins FT, Ghanbari Z, Hommer G, et al. Engineering Design Tools for Shape Memory Alloy Actuators: CASMART Collaborative Best Practices and Case Studies. Vol. 1: Multi. Mater.; Mech. Behav. of Act. Mater., ASME; 2016, p. V001T04A010. doi:10.1115/SMASIS2016-9183.

[19] Blum U, Voshage G, Lammer J, Beyersdorf F, Töllner D, Kretschmer G, et al. Endoluminal stent–grafts for infrarenal abdominal aortic aneurysms. N Engl J Med 1997;336:13–20. doi:10.1056/NEJM199701023360103.

[20] Pelton AR, Dicello J, Miyazaki S. Optimisation of processing and properties of medical grade Nitinol wire. Minim Invasive Ther Allied Technol 2000;9:107–18. doi:10.3109/13645700009063057.

[21] Shayan M, Chun Y. An overview of thin film nitinol endovascular devices. Acta Biomater 2015;21:20–34. doi:10.1016/j.actbio.2015.03.025.

[22] Chun Y, Lin P-Y, Chang H-Y, Emmons MC, Mohanchandra KP, Levi DS, et al. Modeling and experimental analysis of the hyperelastic thin film nitinol. J Intell Mater Syst Struct 2011;22:2045–51. doi:10.1177/1045389X11422105.

[23] Ng CH, Chan CW, Man HC, Waugh DG, Lawrence J. NiTi shape memory alloy with enhanced wear performance by laser selective area nitriding for orthopaedic applications. Surf Coatings Technol 2016. doi:10.1016/j.surfcoat.2016.10.042.

[24] El Medawar L, Rocher P, Hornez JC, Traisnel M, Breme J, Hildebrand HF. Electrochemical and cytocompatibility assessment of NiTiNOL memory shape alloy for orthodontic use. Biomol Eng 2002;19:153–60. doi:10.1016/S1389-0344(02)00041-2.

[25] Falk V, Diegeler A, Walther T, Löscher N, Vogel B, Ulmann C, et al. Endoscopic coronary artery bypass grafting on the beating heart using a computer enhanced telemanipulation system. Heart Surg Forum 1999;2:199–205.

[26] Konh B, Datla N V., Hutapea P. Feasibility of shape memory alloy wire actuation for an active steerable cannula. J Med Device 2015;9:21002. doi:10.1115/1.4029557.

[27] Konh B, Honarvar M, Hutapea P. Design optimization study of a shape memory alloy active needle for biomedical applications. Med Eng Phys 2015;37:469–77. doi:10.1016/j.medengphy.2015.02.013.

[28] Farooq MU, Khalid FA, Zaigham H, Abidi IH. Superelastic behaviour of Ti-Nb-Al ternary shape memory alloys for biomedical applications. Mater Lett 2014;121:58–61. doi:10.1016/j.matlet.2014.01.148.

[29] Fischer H, Vogel B, Welle A. Applications of shape memory alloys in medical instruments. Minim Invasive Ther Allied Technol 2004;13:248–53. doi:10.1080/13645700410018046.

[30] Duerig T, Pelton a, Stöckel D. An overview of nitinol medical applications. Mater Sci Eng A 1999;273–275:149–60. doi:10.1016/S0921-5093(99)00294-4.

[31] Sakai Y, Kitagawa Y, Fukuta T, Iiba M. Experimental study on enhancement of self-restoration of concrete beams using SMA wire. In: Liu S-C, editor., International Society for Optics and Photonics; 2003, p. 178. doi:10.1117/12.482680.

[32] McGavin GL, Guerin G. Real-time seismic damping and frequency control of steel structures using nitinol wire. In: Liu S-C, Pines DJ, editors., International Society for Optics and Photonics; 2002, p. 176–85. doi:10.1117/12.472553.

[33] Song G, Ma N, Li HN. Applications of shape memory alloys in civil structures. Eng Struct 2006;28:1266–74. doi:10.1016/j.engstruct.2005.12.010.

[34] Saadat S, Salichs J, Noori M, Hou Z, Davoodi H, Bar-on I, et al. An overview of vibration and seismic applications of NiTi shape memory alloy. Smart Mater Struct 2002;11:218–29. doi:10.1088/0964-1726/11/2/305.

[35] Agboola BO, Hartl DJ, Lagoudas DC. A study of actuation fatigue of shape memory alloy. Vol. 2 Mech. Behav. Act. Mater. Integr. Syst. Des. Implementation; Bio-Inspired Mater. Syst. Energy Harvest., ASME; 2012, p. 287. doi:10.1115/SMASIS2012-8222.

[36] Calhoun C. A. Effect of Ni3Ti precipitates on actuation fatigue of Ni60Ti40 (wt. %) shape memory alloys. Texas A&M University, 2011. Thesis.

[37] Pelton AR. Nitinol fatigue: a review of microstructures and mechanisms. J Mater Eng Perform 2011;20:613–7. doi:10.1007/s11665-011-9864-9.

[38] Wheeler R, Santa-Cruz J, Hartl D, Lagoudas D. Effect of processing and loading on equiatomic NiTi fatigue life and localized failure mechanisms. Vol. 2 Mech. Behav. Act. Mater. Struct. Heal. Monit. Bioinspired Smart Mater. Syst. Energy Harvest., ASME; 2013, p. V002T02A010. doi:10.1115/SMASIS2013-3163.

[39] Miller DA. Thermomechanical characterization of plastic deformation and transformation fatigue in shape memory alloys. Texas A&M University, 2000.

[40] Wheeler RW, Hartl DJ, Chemisky Y, Lagoudas DC. Characterization and modeling of thermo-mechanical fatigue in equiatomic NiTi actuators. Vol. 2 Mech. Behav. Act. Mater. Integr. Syst. Des. Implementation; Bioinspired Smart Mater. Syst. Energy Harvest., ASME; 2014, p. V002T02A009. doi:10.1115/SMASIS2014-7591.

[41] Calhoun C, Wheeler R, Baxevanis T, Lagoudas DC. Actuation fatigue life prediction of shape memory alloys under the constant-stress loading condition. Scr Mater 2015;95:58–61. doi:10.1016/j.scriptamat.2014.10.005.

[42] Melton K., Mercier O. Fatigue of NITI thermoelastic martensites. Acta Metall 1979;27:137–44. doi:10.1016/0001-6160(79)90065-8.

[43] Mammano GS, Dragoni E. Functional fatigue of NiTi Shape Memory wires for a range of end loadings and constraints. Fract Struct Integr 2013;23:25–33. doi:10.3221/IGF-ESIS.23.03.

[44] Wheeler RW, Hartl DJ, Chemisky Y, Lagoudas DC. Modeling of thermo-mechanical fatigue and damage in shape memory alloy axial actuators. In: Goulbourne NC, editor., International Society for Optics and Photonics; 2015, p. 94320K. doi:10.1117/12.2175747.

[45] Tobushi H, Hachisuka T, Hashimoto T, Yamada S. Cyclic deformation and fatigue of a TiNi shape-memory alloy wire subjected to rotating bending. J Eng Mater Technol 1998;120:64. doi:10.1115/1.2806839.

[46] Young JM, Van Vliet KJ. Predicting in vivo failure of pseudoelastic NiTi devices under low cycle, high amplitude fatigue. J Biomed Mater Res B 2005;72:17–26. doi:10.1002/jbm.b.30113.

[47] Miyazaki S, Mizukoshi K, Ueki T, Sakuma T, Liu Y. Fatigue life of Ti–50 at.% Ni and Ti–40Ni–10Cu (at.%) shape memory alloy wires. Mater Sci Eng A 1999;273:658–63. doi:10.1016/S0921-5093(99)00344-5.

[48] Gall K, Maier H. Cyclic deformation mechanisms in precipitated NiTi shape memory alloys. Acta Mater 2002;50:4643–57. doi:10.1016/S1359-6454(02)00315-4.

[49] Bertacchini OW, Lagoudas DC, Patoor E. Fatigue life characterization of shape memory alloys undergoing thermomechanical cyclic loading. In: Lagoudas DC, editor., International Society for Optics and Photonics; 2003, p. 612. doi:10.1117/12.508207.

[50] Bigeon MJ, Morin M. Thermomechanical study of the stress assisted two way memory effect fatigue in TiNi and CuZnAl wires. Scr Mater 1996;35:1373–8. doi:10.1016/S1359-6462(96)00228-X.

[51] Scirè Mammano G, Dragoni E. Effects of loading and constraining conditions on the thermomechanical fatigue life of NiTi shape memory wires. J Mater Eng Perform 2014;23:2403–11. doi:10.1007/s11665-014-0945-4.

[52] Bhaumik SK, Saikrishna CN, Ramaiah KV, Venkataswamy MA. Understanding the fatigue behaviour of NiTiCu shape memory alloy wire thermal actuators. Key Eng Mater 2008;378–379:301–16. doi:10.4028/www.scientific.net/KEM.378-379.301.

[53] Pappas P, Bollas D, Parthenios J, Dracopoulos V, Galiotis C, C B, et al. Transformation fatigue and stress relaxation of shape memory alloy wires. Smart Mater Struct 2007;16:2560–70. doi:10.1088/0964-1726/16/6/060.

[54] Maletta C, Sgambitterra E, Furgiuele F, Casati R, Tuissi A. Fatigue of pseudoelastic NiTi within the stress-induced transformation regime: a modified Coffin–Manson approach. Smart Mater Struct 2012;21:112001. doi:10.1088/0964-1726/21/11/112001.

[55] Karhu M, Lindroos T. Microstructure analysis and damage patterns of thermally cycled Ti-49.7 Ni (at.%) wires. Smart Mater Struct 2012;21.

[56] Bertacchini OW. Characterization and modeling of transformation induced fatigue of shape memory alloy. Texas A&M University, 2009. Dissertation.

[57] Lagoudas DC, Bo Z. Thermomechanical modeling of polycrystalline SMAs under cyclic loading, Part II: material characterization and experimental results for a stable transformation cycle. Int J Eng Sci 1999;37:1141–73. doi:10.1016/S0020-7225(98)00114-1.

[58] Rong LJ, Miller DA, Lagoudas DC. Thermo-mechanical fatigue and transformation behavior of TiNiCu SMA. Mater Sci Forum 2002;394–395:329–32. doi:10.4028/www.scientific.net/MSF.394-395.329.

[59] Lagoudas DC, Miller DA, Rong L, Kumar PK, M WC, Miyazaki S ITIY and OK, et al. Thermomechanical fatigue of shape memory alloys. Smart Mater Struct 2009;18:85021. doi:10.1088/0964-1726/18/8/085021.

[60] Lagoudas DC, Bertacchini OW, Patoor E. Surface crack development in transformation induced fatigue of SMA actuators. Residual Stress Its Eff. Fatigue Fract., Dordrecht: Springer Netherlands; 2006, p. 209–22. doi:10.1007/1-4020-5329-0_18.

[61] Hartl DJ, Chemisky Y, Meraghni F. Three-dimensional constitutive model considering transformation-induced damage and resulting fatigue failure in shape memory alloys, San Diego, California, United States: SPIE, Behavior and Mechanics of Multifunctional Materials and Composites; 2014, p. 905805. doi:10.1117/12.2046668.

[62] Schick JR. Transformation induced fatigue of Ni-rich NiTi SMA actuators. Texas A&M University, College Station TX, USA, 2009.

[63] Scirè Mammano G, Dragoni E. Effects of loading and constraining conditions on the thermomechanical fatigue life of NiTi shape memory wires. J Mater Eng Perform 2014;23:2403–11. doi:10.1007/s11665-014-0945-4.

[64] Entchev PB, Lagoudas DC. Modeling of transformation-induced plasticity and its effect on the behavior of porous shape memory alloys. Part II: porous SMA response. Mech Mater 2004;36:893–913. doi:10.1016/j.mechmat.2003.08.005.

[65] Lagoudas DC, Entchev PB. Modeling of transformation-induced plasticity and its effect on the behavior of porous shape memory alloys. Part I: constitutive model for fully dense SMAs. Mech Mater 2004;36:865–92. doi:10.1016/j.mechmat.2003.08.006.

[66] Santa Cruz J, Hartl D, Shryock K, Lagoudas D. In-situ strain localization measurements of shape memory alloy actuators during a research experience for undergraduates program: American Society for Engineering Education. ASEE 120th Annu. Conf. Expo. Div. Aerosp., Atlanta, GA, USA.: ASEE; 2013, p. 7779.

[67] Sam, J, Karaman, I. Material characterization of NiTiHf material lots. Unpublished report. Texas A&M University, 2016.

[68] Karakoc, O, Karaman, I. Microstructural characterization of NiTiHf material lots. Unpublished report. Texas A&M University, 2016.

[69] Qidwai MA, Lagoudas DC. On thermomechanics and transformation surfaces of polycrystalline NiTi shape memory alloy material. Int J Plast 2000;16:1309–43. doi:10.1016/S0749-6419(00)00012-7.

[70] Smith, K. N., Topper, T. H., & Watson, P. A stress-strain function for the fatigue of metals (Stress-strain function for metal fatigue including mean stress effect). Journal of Materials 1970, 5, 767-778.

[71] Miller DA, Lagoudas DC. Influence of cold work and heat treatment on the shape memory effect and plastic strain development of NiTi. Mater Sci Eng A 2001;308:161–75. doi:10.1016/S0921-5093(00)01982-1.

[72] Mitwally ME, Farag M. Effect of cold work and annealing on the structure and characteristics of NiTi alloy. Mater Sci Eng A 2009;519:155–66. doi:10.1016/j.msea.2009.04.057.

[73] Gall K, Maier H. Cyclic deformation mechanisms in precipitated NiTi shape memory alloys. Acta Mater 2002;50:4643–57. doi:10.1016/S1359-6454(02)00315-4.

APPENDIX A: SOFTWARE DEVELOPMENT FOR ACTUATION FATIGUE TESTING

The software suite developed for this research is discussed in additional detail in this appendix.

Control Scheme and State-Space Machine

As discussed in Chapter Two, the primary testing software was developed in LabVIEW. The state-space machine was implemented through a case structure with a numerical input for state selection. In total, there are 11 unique states, as shown in Table A-1, which correspond to different states the system can inhabit.

Table A-1: Unique States for LabVIEW Control Scheme

State Name - Number	*Description*	*Exit Condition*
Initialize – 0	Reference state, no output from DAQ board	Test initiated by user; proceeds to Off
Off – 1	System resting state, no output from DAQ, data recording	Start command from user once all necessary inputs are registered; proceeds to Heating if no errors.
Heating – 2	DAQ supplies power to trigger SSR; actuator is heated	Proceeds to Austenite if time, temperature, displacement, or resistance criteria met. Error checking.
Austenite – 3	DAQ triggers DIC camera	State executes once, proceeds to Cooling if no errors.

Table A-1: Continued

State Name - Number	*Description*	*Exit Condition*
Cooling – 4	No output from DAQ	Proceeds to Martensite if time, temperature, or displacement criteria met.
Martensite – 5	DAQ triggers DIC camera	State executes once, proceeds to Data Writing if no errors.
Data Writing – 6	Cyclic parameters calculated and written to cyclic text file	State executes once, proceeds to Heating if no errors or wait commands.
Over Extension – 7	Enters state if LVDT outside of user defined range	Remains in state until manually exited. Sends notification to user.
Cooling Timeout – 8	Enters state if cooling time outside of user defined range	Remains in state until manually exited. Sends notification to user.
Heating Timeout – 9	Enters state if heating time outside of user defined range	Remains in state until manually exited. Sends notification to user.
Over Heating – 10	Enters state if specimen temperature outside of user defined range	Remains in state until manually exited. Sends notification to user.

The cyclic process is shown in Figure A.1. The error states are not shown due to the fact that they are continuously checked at every processing step.

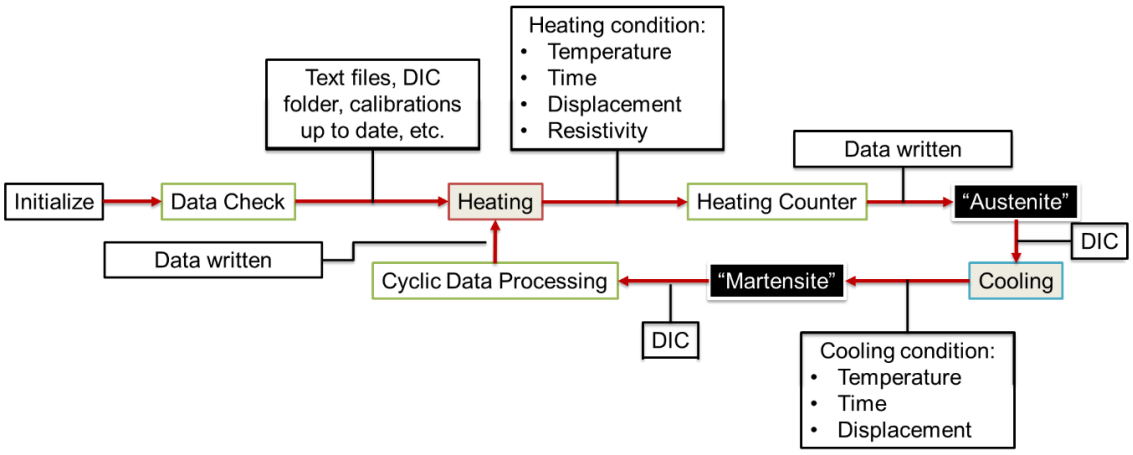

Figure A.1: Flow chart for cyclic control implemented in LabVIEW.

The code for the baseline of the fatigue testing software is shown in Figure A.2. This framework allows for any condition (e.g. the temperature of the specimen reaches 350°C) or set of conditions to be used as a control for the cycling.

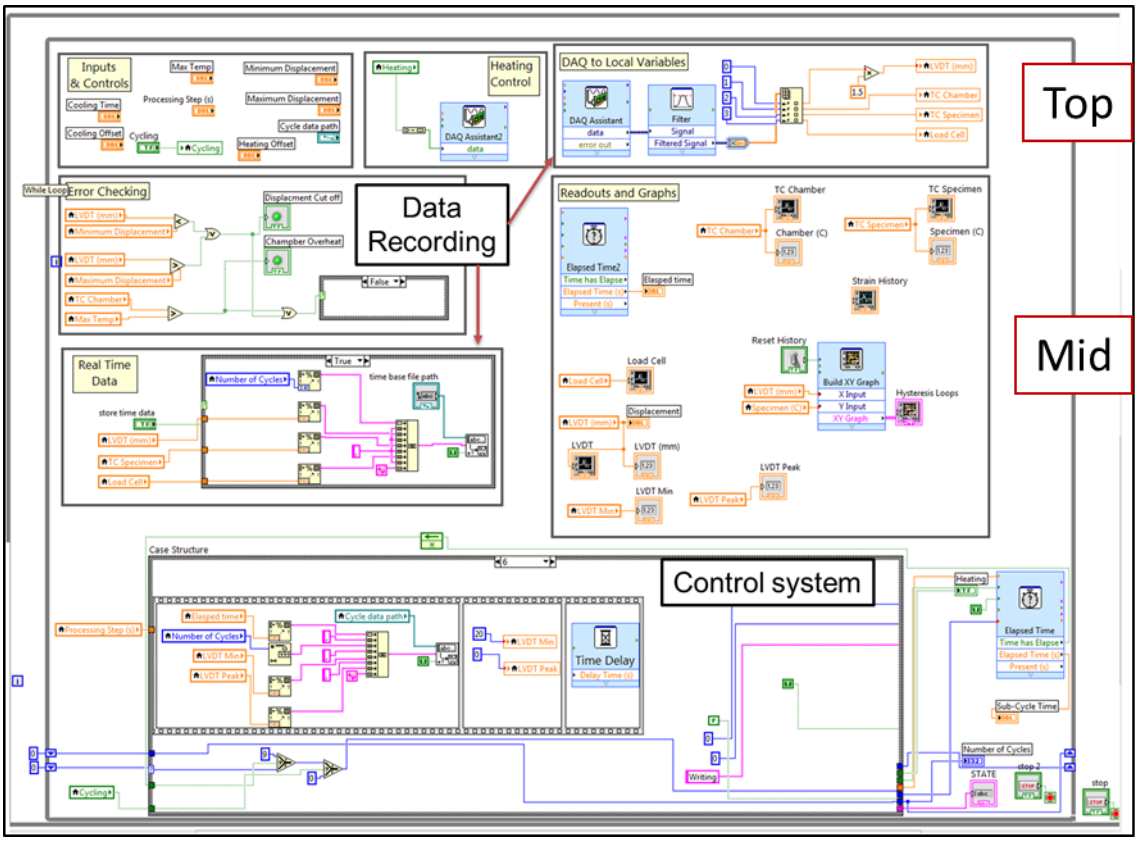

Figure A.2: Baseline of Fatigue Testing Software; coded in LABVIEW.

The code is divided into sections with specific functions. In the top row (from left to right), there is the Input & Controls section which takes user inputs and writes them to local variables, a heating control which converts a Boolean to an output signal which controls the power supply system through an SSR, and a data acquisition block which filters the input from sensors and writes the values to local variables.

In the middle row, on the top left is the Error Checking code block, which continuously runs inequality tests to ensure the testing halts if any operational parameters (e.g. specimen temperature) are exceeded. Continuous data is written in the LabVIEW

code block immediately below Error Checking in the block labeled Real Time Data. As implemented for the tests in Chapter 3, this portion of the code writes a line of data (including values such as specimen temperature and grip displacement) at a rate of 10hz. The right half of the Mid portion of the baseline code takes local variables and displays them as graphs and readouts in the front panel of the software, which can be seen in Figures 2.12 and 2.13. The lower portion of the code, labeled Control System, houses the state space machine responsible for the overall operation of the fatigue testing software and is discussed in Chapter 2.

Data Processing Scripts

Depending on the fatigue life of an actuator specimen, between 10^5 and 10^8 data points are collected in addition to high-contrast images for visual analysis for each fatigue test. In order to process the large amount of data collected during each test, several scripts were developed and utilized to produce the data presented in Chapter 3.

Three different types of data are collected: *cyclic data* which captures the maximum and minimum grip displacements (LVDT), cycle temperatures (IR thermometer), and mechanical loads (load cell); *real-time data* which records sensor inputs at a frequency of 10hz, and visual data which consists of high-contrast images that provide localized deformation values.

Cyclic Data Processing

Cyclic data is collected during the data writing state of each cycle and provides much of the critical information which describes the individual cycle. For each cycle, the LVDT maxima and minima are collected and converted to extension or engineering strain. Additional recorded data includes heating and cycle time, maximum and minimum temperatures, and ambient temperatures. The cyclic data processor takes the raw data written during the Data Writing state and develops the engineering strain evolutions shown in Chapter 3. The script generates an excel report for each test, which includes the testing information, statistics, and graphs. In the event of strain discontinuities or extremely low actuation strokes, the user is also notified of the problematic cycles. For tests which contain numerous discontinuities in the raw data, a Savitzky-Golay filter was utilized. To ensure consistency of the data, raw and processed data were required to have a correlation coefficient of 0.999 or higher, and the martensite displacement was held equal to the sum of the actuation stroke and austenite displacement. First through sixth order polynomials were investigated for data smoothing, and the order which provided the best correlation constant was selected. The cyclic data processor was initially implemented in python and was later converted to MATLAB.

Real-time Data Processing

Since the real-time data files are generally too large to process directly, a MATLAB script was developed to take user inputs and read selected portions of the data files. After the test operator inputs a vector containing the cycles of interest, several plots are

generated, including Engineering Strain vs. Temperature and Resistivity vs. Temperature, which are shown in Figures A.3 and A.4, respectively.

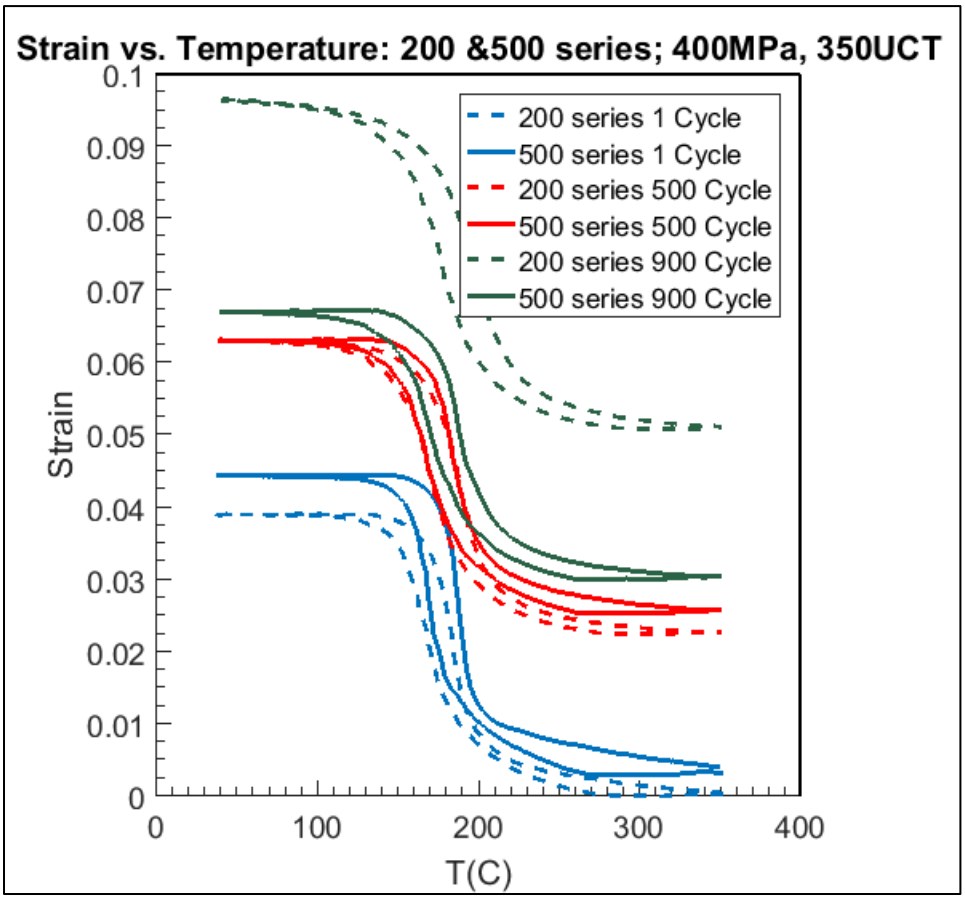

Figure A.3: Engineering Strain vs. Temperature output from data processing script. As shown, two tests are compared.

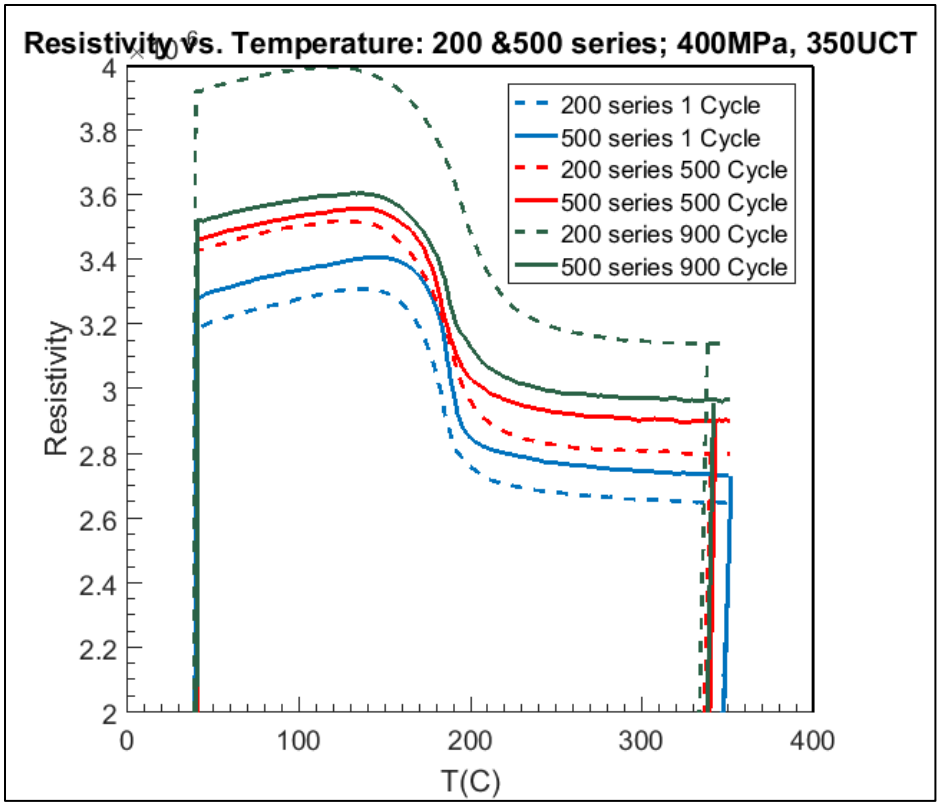

Figure A.4: Resistivity vs. Temperature output from data processing script. As shown, two tests are compared.

In addition to analyzing the evolution of the hysteresis loops and resistance of the material, the transformation temperatures are also determined for the cycles of interest. The script accomplishes this by applying the tangent method, which can be seen graphically in Figure A.5.

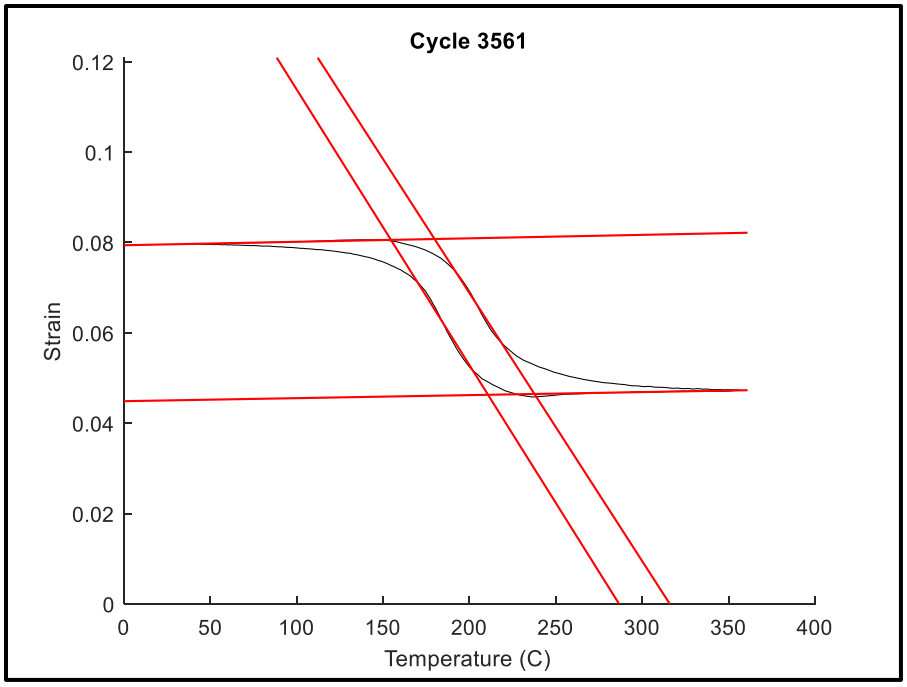

Figure A.5: Example output for transformation temperature analysis utilizing the tangent method.

Visual Data Processing

Due to the extremely large irrecoverable strains observed in the equiatomic NiTi material system, DIC analysis was not feasible. For this reason, visual extensometry was chosen instead to characterize the material and quantify the degree of strain localization. The visual extensometry method developed by Santa-Cruz et al. is described in [66]. Similar analysis was performed utilizing the National Instruments Vision Assistant suite to approximate the volume fraction of impurities and cracks in post-mortem samples. This process can be seen in Figure A.6.

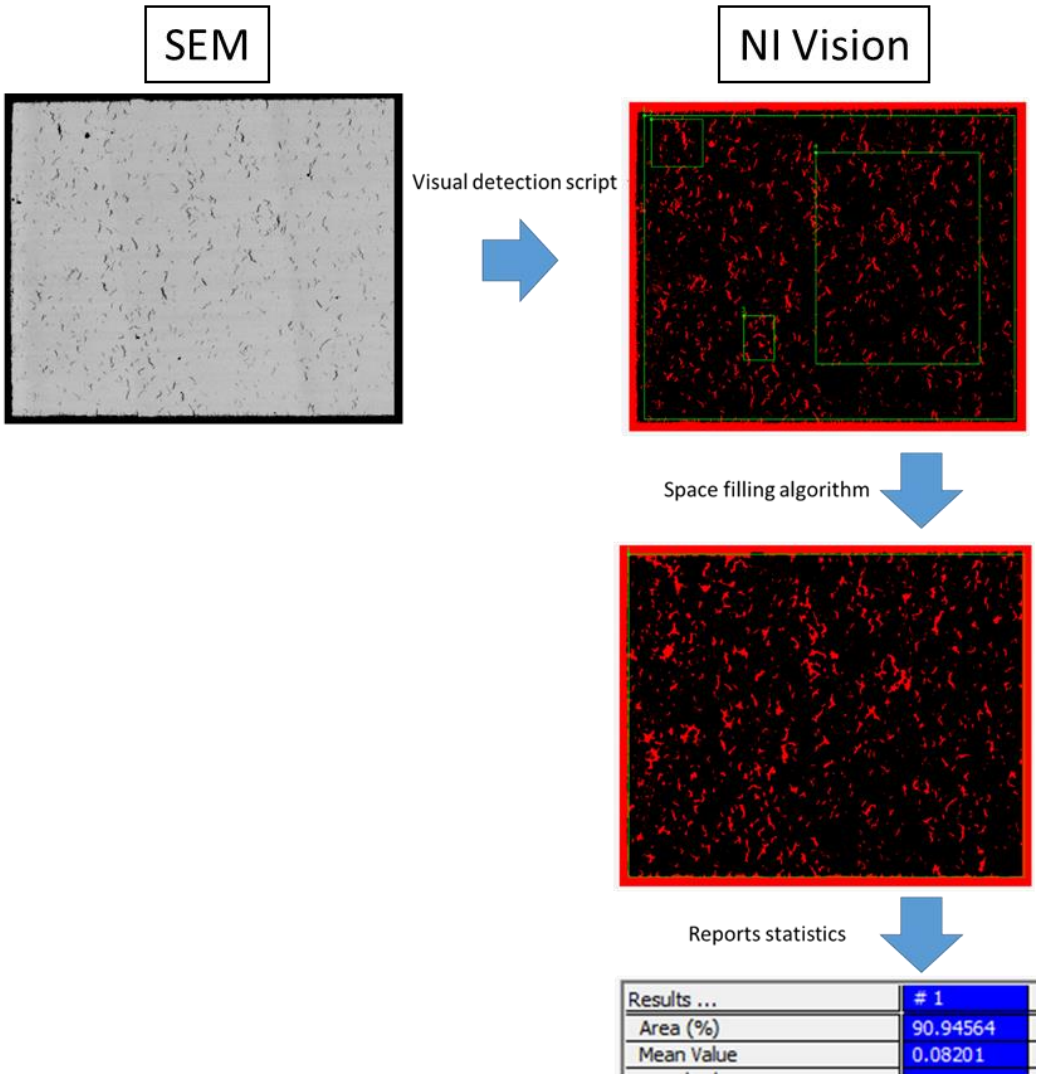

Figure A.6: Schematic of showing area determination through Vision Assistant.

Comparison and Validation of Extensometry Methods

In order to ensure accurate extensometry measurements, LVDT results were compared with laser extensometer, DIC, visual extensometry, and caliper measurements. Several cylinders with a 10mm diameter were 3D printed with lengths ranging between 5mm and 15mm; the lengths were found to be within 0.1mm of the target length for all

cases through laser extensometry and caliper measurements. The LVDT system was found to be accurate within the same bounds (±0.1mm). The DIC and visual extensometry measurements were found to be within 0.25mm and 0.5mm, respectively, of the LVDT measurements for low displacements, and within 1.5% and 0.5% for displacements exceeding 5mm. It should be noted that the LVDT was measuring grip displacement while the visual/DIC methods were only analyzing the gage section.